



# The 2004 NASA Faculty Fellowship Program Research Reports

*Program Co-Directors:*

*J.R. Pruitt, Marshall Space Flight Center, Marshall Space Flight Center, Alabama*

*G. Karr, The University of Alabama in Huntsville, Huntsville, Alabama*

*L.M. Freeman, The University of Alabama, Tuscaloosa, Alabama*

*R. Hassan, Alabama A&M University, Normal, Alabama*

*J.B. Day*

*Compiler and Editor*

*Marshall Space Flight Center, Marshall Space Flight Center, Alabama*

Prepared for Marshall Space Flight Center  
under Contract NNM04AA08G

## The NASA STI Program Office...in Profile

Since its founding, NASA has been dedicated to the advancement of aeronautics and space science. The NASA Scientific and Technical Information (STI) Program Office plays a key part in helping NASA maintain this important role.

The NASA STI Program Office is operated by Langley Research Center, the lead center for NASA's scientific and technical information. The NASA STI Program Office provides access to the NASA STI Database, the largest collection of aeronautical and space science STI in the world. The Program Office is also NASA's institutional mechanism for disseminating the results of its research and development activities. These results are published by NASA in the NASA STI Report Series, which includes the following report types:

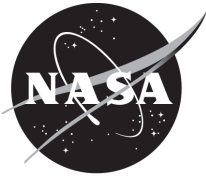
- **TECHNICAL PUBLICATION.** Reports of completed research or a major significant phase of research that present the results of NASA programs and include extensive data or theoretical analysis. Includes compilations of significant scientific and technical data and information deemed to be of continuing reference value. NASA's counterpart of peer-reviewed formal professional papers but has less stringent limitations on manuscript length and extent of graphic presentations.
- **TECHNICAL MEMORANDUM.** Scientific and technical findings that are preliminary or of specialized interest, e.g., quick release reports, working papers, and bibliographies that contain minimal annotation. Does not contain extensive analysis.
- **CONTRACTOR REPORT.** Scientific and technical findings by NASA-sponsored contractors and grantees.

- **CONFERENCE PUBLICATION.** Collected papers from scientific and technical conferences, symposia, seminars, or other meetings sponsored or cosponsored by NASA.
- **SPECIAL PUBLICATION.** Scientific, technical, or historical information from NASA programs, projects, and mission, often concerned with subjects having substantial public interest.
- **TECHNICAL TRANSLATION.** English-language translations of foreign scientific and technical material pertinent to NASA's mission.

Specialized services that complement the STI Program Office's diverse offerings include creating custom thesauri, building customized databases, organizing and publishing research results...even providing videos.

For more information about the NASA STI Program Office, see the following:

- Access the NASA STI Program Home Page at <http://www.sti.nasa.gov>
- E-mail your question via the Internet to [help@sti.nasa.gov](mailto:help@sti.nasa.gov)
- Fax your question to the NASA Access Help Desk at 301-621-0134
- Telephone the NASA Access Help Desk at 301-621-0390
- Write to:  
NASA Access Help Desk  
NASA Center for AeroSpace Information  
7121 Standard Drive  
Hanover, MD 21076-1320  
301-621-0390



# The 2004 NASA Faculty Fellowship Program Research Reports

*Program Co-Directors:*

*J.R. Pruitt, Marshall Space Flight Center, Marshall Space Flight Center, Alabama*

*G. Karr, The University of Alabama in Huntsville, Huntsville, Alabama*

*L.M. Freeman, The University of Alabama, Tuscaloosa, Alabama*

*R. Hassan, Alabama A&M University, Normal, Alabama*

*J.B. Day*

*Compiler and Editor*

*Marshall Space Flight Center, Marshall Space Flight Center, Alabama*

Prepared for Marshall Space Flight Center  
under Contract NNM04AA08G

National Aeronautics and  
Space Administration

Marshall Space Flight Center • MSFC, Alabama 35812

## **TRADEMARKS**

Trade names and trademarks are used in this report for identification only. This usage does not constitute an official endorsement, either expressed or implied, by the National Aeronautics and Space Administration.

Available from:

NASA Center for AeroSpace Information  
7121 Standard Drive  
Hanover, MD 21076-1320  
301-621-0390

National Technical Information Service  
5285 Port Royal Road  
Springfield, VA 22161  
703-487-4650

## INTRODUCTION

This is the administrative report for the 2004 NASA Faculty Fellowship Program (NFFP) held at the George C. Marshall Space Flight Center (MSFC) for the 40th consecutive year. The NFFP offers science and engineering faculty at U.S. colleges and universities hands-on exposure to NASA's research challenges through summer research residencies and extended research opportunities at participating NASA research Centers. During this program, fellows work closely with NASA colleagues on research challenges important to NASA's strategic enterprises that are of mutual interest to the fellow and the Center. The nominal starting and finishing dates for the 10-week program were June 1 through August 6, 2004. The program was sponsored by NASA Headquarters, Washington, DC, and operated under contract by The University of Alabama, The University of Alabama in Huntsville, and Alabama A&M University. In addition, promotion and applications are managed by the American Society for Engineering Education (ASEE) and assessment is completed by Universities Space Research Association (USRA).

The primary objectives of the NFFP are to:

- Increase the quality and quantity of research collaborations between NASA and the academic community that contribute to the Agency's space aeronautics and space science mission.
- Engage faculty from colleges, universities, and community colleges in current NASA research and development.
- Foster a greater public awareness of NASA science and technology, and therefore facilitate academic and workforce literacy in these areas.
- Strengthen faculty capabilities to enhance the STEM workforce, advance competition, and infuse mission-related research and technology content into classroom teaching.
- Increase participation of underrepresented and underserved faculty and institutions in NASA science and technology.

Questions about any report should be addressed to Dr. L. Michael Freeman, Aerospace Engineering Department, The University of Alabama, Box 870280, Tuscaloosa, AL 35487-0280.  
Email: [mike.freeman@ua.edu](mailto:mike.freeman@ua.edu)

## TABLE OF CONTENTS

### **Mechanical Characterization of a Multifunctional Composite Material and Preliminary Design of a Lunar Habitat**

Felipe Acosta-Costa, University of Puerto Rico-Mayaguez

### **The Technology and Art of Aerocapture**

Mary Bangs, SUNY Empire State College

### **A Threefold Treatise on HOSC Performance Metrics, Implementing Full Cost Analysis, and a Competition Matrix for Future Business Planning**

Gregory Battle, Morehouse College

### **Reliability Assessment of Conceptual Launch Vehicles**

Lisa Bloomer, Middle Tennessee State University

### **Fiber Reinforced Composites for Insulation and Structures**

Roy Broughton, Auburn University

### **Sub-Grid Modeling of Electrokinetic Effects in Micro Flows**

Chien-Pin Chen, The University of Alabama in Huntsville

### **Incorporation of a Chemical Equilibrium Equation of State Into LOCI-Chem**

Carey Cox, Louisiana Technological University

### **Fiber-Reinforced Composite Materials Used for Tankage**

Christy Cunningham, Auburn University

### **Integration of Launch Vehicle Simulation/Analysis Tools and Lunar Cargo Lander Design (Part 2/2)**

George Brian DeJean, Christian Brothers University

### **Coupled Electromagnetic Resonators for Enhanced Communications and Telemetry**

John Dimmock, The University of Alabama in Huntsville

### **Enhancement and Analysis of Real-Time Radiography Images**

Edward Doering, Minnesota State University

### **Controls for Reusable Launch Vehicles During Terminal Area Energy Management**

Brian Driessen, The University of Alabama in Huntsville

### **Optical Cryogenic Tank Level Sensor**

Amanda Duffell, The University of Alabama in Huntsville

**Control of Combustion Instabilities Through Various Passive Devices**

Kader Frendi, The University of Alabama in Huntsville

**Local Intensity Enhancements in Spherical Microcavities: Implications for Photonic Chemical and Biological Sensors**

Kirk Fuller, The University of Alabama in Huntsville

**Analysis of Upper Air, Ground, and Remote Sensing Data for the Atlas Field Campaign in San Juan, Puerto Rico**

Jorge González-Cruz, Santa Clara University

**Specific Impulse and Mass Flow Rate Error**

Don Gregory, The University of Alabama in Huntsville

**A Theoretical Investigation of Oxidation Efficiency of a Volatile Removal Assembly Reactor Under Microgravity Conditions**

Boyun Guo, University of Louisiana at Lafayette

**Optimal Configuration of Human Motion Tracking Systems: A Systems Engineering Approach**

Steven Henderson, U.S. Military Academy

**Learning Effectiveness of the NASA Digital Learning Network**

Billy Hix, Motlow College

**Effects of Piezoelectric (PZT) Sensor Bonding and the Characteristics of the Host Structure on Impedance-Based Structural Health Monitoring**

Abdul Jalloh, Alabama A&M University

**Study of a 30-m Boom for Solar Sailcraft: Model Extendibility and Control Strategy**

Leeyun Keel, Tennessee State University

**Modeling and Testing of Non-Nuclear, High-Power Simulated Nuclear Thermal Rocket Reactor Elements**

Daniel Kirk, Florida Institute of Technology

**In Situ Resource Utilization Experiments for Mars Exploration**

Matt Marone, Mercer University

**Convergence Acceleration and Documentation of CFD Codes for Turbomachinery Applications**

Jed Marquart, Ohio Northern University

**The Plunge Phase of the Friction Stir Welding**

John McClure, University of Texas-El Paso

**Visualization Methods for Viability Studies of Inspection Modules for the Space Shuttle**

Amir Mobasher, Alabama A&M University

**Elemental Analysis of the JSC Mars-1 Soil Simulant Using Laser Ablation and Magnetic Separation**

Ahad Nasab, Middle Tennessee State University

**Whispering-Gallery Mode at MSFC: Excitation of Fused-Silica Micro-Resonators Via Tapered Optical Fiber**

Jamiu Odutola, Alabama A&M University

**Mechanical Characterization of a Multifunctional Composite Material**

Juan Román Pagán, University of Puerto Rico

**Investigation of Integrated Vehicle Health Management Approaches**

Deidre Paris, Clark Atlanta University

**CFD Multiphysics Tool**

Eric Perrell, Embry-Riddle Aeronautical University

**On Structural Design of a Mobile Lunar Habitat With Multi-Layered Environmental Shielding**

Masoud Rais-Rohani, Mississippi State University

**Analysis of Piezoelectric Structural Sensors With Emergent Computing Techniques**

Douglas Ramers, University of North Carolina-Charlotte

**Lightning Detection Efficiency Analysis Process: Modeling Based on Empirical Data**

John Rompala, University of Wisconsin-Stout

**Development of a Modeling Framework to Support Control Investigations of Sailcraft Missions: A First Cut ABLE Sailcraft Dynamics Model**

Sriprakash Sarathy, Clark Atlanta University

**Java-Based Graphical User Interface for MAVERIC-II**

Suk Seo, Middle Tennessee State University

**NASA Integrated Vehicle Health Management (NIVHM)—New Simulation Architecture: An Investigation PART I**

Gene Sheppard, Georgia Perimeter College

**Integration of Launch Vehicle Simulation/Analysis Tools and Lunar Cargo Lander Design (Part 1 of 2)**

Yeu-Sheng Paul Shiue, Christian Brothers University

**An Open Source Simulation System**

Thomas Slack, The University of Memphis

**Fabrication of 3-D Photonic Band Gap Crystals Via Colloidal Self-Assembly**

Girija Subramaniam, Pennsylvania State University, Hazleton

**The Effect of Infrastructure Sharing in Estimating Operations Cost of Future Space Transportation Systems**

Meenakshi Sundaram, Tennessee Technological University

**Rack Distribution Effects on MPLM Center of Mass**

John Tester, Northern Arizona University

**A Summary of NASA Summer Faculty Fellowship Work in the E.O. Office and in the Educator Resources Center**

Hubert Wendell Thompson, Alabama A&M University

**Electroformed Nickel-Graphite Composite**

Pei Xiong-Skiba, Austin Peay State University

**2004**

**NASA FACULTY FELLOWSHIP PROGRAM**

**MARSHALL SPACE FLIGHT CENTER**

**THE UNIVERSITY OF ALABAMA  
THE UNIVERSITY OF ALABAMA IN HUNTSVILLE  
ALABAMA A&M UNIVERSITY**

**MECHANICAL CHARACTERIZATION OF A  
MULTIFUNCTIONAL COMPOSITE MATERIAL AND  
PRELIMINARY DESIGN OF A LUNAR HABITAT**

Prepared By:	Felipe J. Acosta Costa
Academic Rank:	Associate Professor
Institution and Department:	University of Puerto Rico Mayagüez Campus Department of Civil Engineering and Surveying
NASA/MSFC Directorate:	Engineering
MFSC Colleague:	Dr. Raj K. Kaul

2004

**NASA FACULTY FELLOWSHIP PROGRAM**

**MARSHALL SPACE FLIGHT CENTER  
THE UNIVERSITY OF ALABAMA  
THE UNIVERSITY OF ALABAMA IN HUNTSVILLE  
ALABAMA A&M UNIVERSITY**

**THE TECHNOLOGY & ART OF  
AEROCAPTURE**

Prepared by:	Mary C Bangs
Academic Rank:	Instructor
Institution and Department:	Empire State College Art Department/SUNY
NASA/MSFC Directorate:	In-Space Propulsion Technology Projects
MSFC Colleague:	Les Johnson Jack Hood

## **Introduction**

Aerocapture is a type of aero-assist technology in which an interplanetary spacecraft is equipped with a device shaped to optimize atmospheric drag during a pass through a planet's upper atmosphere. An aerocapture maneuver alters the spacecraft's trajectory so that it is captured as a satellite of that planet.

Aerocapture is related to aerobraking. In aerobraking, a spacecraft lowers its orbit around a planet by repeated passes through that planet's upper atmosphere.

As part of the public outreach effort of the NASA MSFC In-Space Propulsion research effort, a poster is being constructed relating to the new technology of aerocapture. Entitled "The Technology & Art of Aerocapture," this poster will speak to three groups of people. The first and broadest audience is the general public who may or may not be familiar with aerocapture as a concept. The second group is the scientifically educated and informed public that is familiar with the concept of aerocapture but may or may not know the finer points about it. Finally, the third audience consists of the group that has worked with and is familiar with aerocapture. The poster is designed to educate and inspire all these audiences.

## **Poster Construction**

My working drawing (Fig. 1) focused on the airflow pattern the aerocapture device would make upon entering a planetary atmosphere. Around and behind it is a representation of surface heating and stress patterns. Included within these patterns are equations from NASA AFE's (Aeroassist Flight Experiment's) guidance, atmosphere defining, lift to drag and the aerodynamic flow of gases. The equations were included as an acknowledgement to the work that provided the base for aerocapture studies and ideas that have been developed since the 1980's.

Terry White of Media Fusion constructed the CAD-CAM images working off my initial drawing after Bonnie James of MSFC approved the use of historical and proposed images. The CAD-CAM images took on jewel-like clarity and are easy to manipulate because of the great care with which they were constructed.

Beneath the featured aeroshell are four examples of historical hard- body aerocapture shells. These include AFE, CNES, the Attached Ballute developed and launched in 1996 by Russia and the Slender Body. Above the featured aeroshell are three examples of inflatable ballutes. Along the bottom of the poster are the planets and satellite that aerocapture missions could travel to. On the bottom left side are the Neptune and Titan aeroshroud. On the bottom right side is a diagram of the planet-centered orbit that aerocapture will enable. Text was edited from earlier aerocapture CDs.



**Fig. 1. Working Drawing for Aerocapture Poster**

### **Aerocapture History**

Application of aerocapture-related techniques began with the Apollo Program in the 1960's when astronauts used aerobraking as the maneuver that would enable their return to Earth. Aerocapture continued to develop in the 1970's when the Pioneer Venus Multipurpose used aerobraking to explore Venus. Although it was not expected to survive the descent through the atmosphere, one probe continued to operate for 45 minutes after reaching the surface. Pioneer Venus-Orbiter was inserted into an elliptical orbit around Venus on December 4, 1978. It carried 17 experiments and operated until the fuel used to maintain its orbital position was exhausted; atmospheric entry destroyed the spacecraft in August 1992.

During the 1980's, aeroassist was applied to AFE (Aeroassist Flight Experiment) and the Galileo Probe. On December 7, 1995 Galileo began its prime mission: a two-year study of the Jovian system. Galileo traveled around Jupiter in an elongated oval-shaped orbit lasting about two months. By observing at different distances from Jupiter, Galileo's experiments could sample different parts of the planet's extensive magnetosphere. The orbits were designed for close flybys of Jupiter's largest satellites. On the 7<sup>th</sup> of December, the Galileo atmospheric subprobe entered the Jovian atmosphere, making a 75-minute fiery descent, before all contact was lost. The probe sliced into Jupiter's atmosphere at one-hundred-six thousand miles per hour. It slowed, released its parachute, and dropped its heat shield. As the probe descended through 95 miles of the top layers of the atmosphere, it collected 58 minutes of data on the local weather.

AFE was developed in the 1980's. This NASA mission was originally planned for the 1990's but has not yet flown. The sub-scale AFE vehicle was intended to perform an aeroassist maneuver

similar to that of a full-scale vehicle. Bonnie James suggested that I contact, Mark Seaford of MSFC who had worked on AFE. He spoke with me at length about AFE and provided technical reports. This information was used by Terry White to construct the 3D computer models of aerocapture vehicles.

Most recently in the 2000's, aerobraking was applied to the Mars Sample Return and CNES Orbiter. After hitting the Martian atmosphere at 12,000 mph, an aeroshell, parachute and retro-rockets will bring the Sample-Return spacecraft to a near standstill during a harrowing six-minute drop to the surface. CNES is a French-designed Mars orbiter.

### **Aerocapture-Maneuver Details**

At 400,000 feet or 75.76 miles above Earth's surface, a returning spacecraft encounters the entry interface. This is where heating caused by atmospheric drag becomes observable. Heat from the spacecraft is radiated back into space from the elevated-temperature thermal-protection system.

Aeroassist equipment may experience damage to the fabric on the ballute or solar sail during atmospheric entry. Heat is conducted quickly through the material, which requires a nonablativ surface that remains aeroelastic and continues to offer lightweight and efficient thermal protection. Aeroshell development and intergration is necessary to optimize both aerocapture and aerobraking.

An aerocapture maneuver can take approximately one hour while an aerobraking maneuver can take as long as weeks or months. NASA missions utilizing this technology are under consideration for Venus, Earth, Mars, Jupiter, Saturn, Titan, Uranus and Neptune.

An important concept is "Living off the Land" that enables the craft to carry less fuel to it's destination. Aerocapture allows a spacecraft to use the available atmosphere to achieve orbit around its destination, reducing the need for deceleration fuel. This important concept utilizes available materials, thereby enabling the vehicle to adapt readily to whatever environment it is traveling in and to.

### **Conclusions: The Poster as an Outreach Tool**

Bonnie James concluded that the poster with airflow and incorporated equations is superior to the alternative approach of showing an image of fire coming off the aerocapture device. This proved to be the main feature of the poster and also the "selling point" to help viewers realize the dynamics instead of the theatrics of aerocapture. Erin Richardson of MSFC also viewed the poster and noted that the inflatables shown present a progression from the most to least advanced.

Jack Hood of MSFC suggested using a hologram-like process as a handout to accompany the poster. The "hologram" would function to show different objects at different angles and show limited animation. This could serve as an alternative visual to use in educational outreach to the variety of audiences.

Les Johnson of MSFC reviewed the poster midway through the process and suggested that there should be both a back and front side to it (Fig: 2). This would insure that the front would not be overloaded with text and give an additional opportunity to highlight the three-dimensional models constructed with engineering specifications as well as reference to earlier CAD-CAM models.

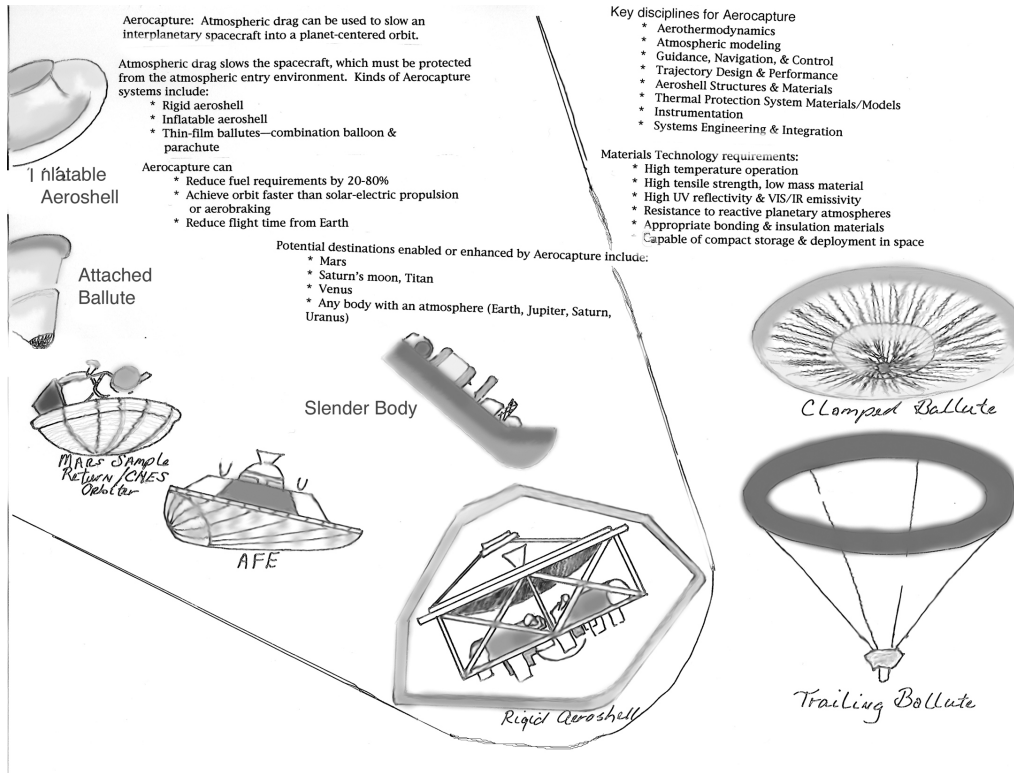


**Fig. 2: Working drawing for the back of the Aerocapture poster**

Other aerocapture sources included Claude A. Graves and Chris Cerimele from NASA Johnson Space Flight Center. Dick Powell and Eric Queen of Langley Space Flight Center provided information on the CNES. Kevin Miller of Ball Aerospace gave additional input on the ballute CAD-CAM images. The 3D models were e-mailed to these sources to insure their accuracy.

As the poster became nearly complete, the title was added, “The Technology & Art of Aerocapture with the subtext “How atmospheric drag can be used to slow an interplanetary spacecraft into a planet-centered orbit.” The text was blurred slightly and an atmospheric effect was included to reflect the idea of aerocapture and atmosphere.

The back of the poster is the place where the technological ideas are featured along with the titles of the individual models. Partial wire frames with the other areas fully built will be shown along with text to highlight the construction of the vehicles. The airflow will be shown with a diagrammatic view.

In my opinion, the finished poster will serve as an effective tool in communicating aerocapture fundamentals to a wide audience.

**2004**

**NASA FACULTY FELLOWSHIP PROGRAM**

**MARSHALL SPACE FLIGHT CENTER**

**THE UNIVERSITY OF ALABAMA  
THE UNIVERSITY OF ALABAMA IN HUNTSVILLE  
ALABAMA A&M UNIVERSITY**

**A THREEFOLD TREATISE ON  
HOSC PERFORMANCE METRICS, IMPLEMENTING  
FULL COST ANALYSIS,  
AND A COMPETITION MATRIX FOR FUTURE  
BUSINESS PLANNING**

Prepared By:	Gregory Battle
Academic Rank:	Professor
Institution and Department:	Morehouse College Atlanta, GA
NASA/MSFC Directorate:	FD43
MSFC Colleague:	Lisa Watson-Morgan

## STAR ODYSSEY

He plots an astronomical course  
Into a swirl of stars;  
Dark matter oozing blacker than molasses  
And galaxies as round as pancakes  
Bubbling on a gaseous griddle;  
Dense nebulas foaming up to thunderheads  
Curved by supernovas  
Bursting in the volcanic cosmos;  
His intelligent gaze glaring redder than Martian hematite;  
And senses stunned by a stellar eruption that wind gusts  
His lone, exploring soul stretched as wide  
As a catamaran sailing slowly by an asteroid reef;  
Suddenly, a brief trail of comet glitter  
Is slung into an elliptical path on  
A phantom gravitational string;  
Now metronomes ticking from blue screens  
Looked upon by the giant god  
Whose furious and molten passions  
Attract a courtship of lunar maidens.  
None ever noticing this quiet messenger  
Pregnant with hope and awe,  
Approaching with reverent precision,  
On slowing engines of molecular propulsion;  
The cautious wanderer  
Extends an optical basket to gather the apples  
Of astral destiny,  
Then opens a cyber portal to watch  
Microcircuits rubbing their probes  
across the Braille  
Of new constellations  
Erected by the Architect of glory.

◆BATTLE◆

## **Introduction**

This paper is an analysis and narrative of the qualitative business parameters of the Huntsville Operations and Support Center (HOSC), Building 4663 at the Marshall Space Flight Center (MSFC) in which the NASA faculty researcher was assigned the twofold tasks of analyzing HOSC Operations and Support Metrics (which measure a portion of Mission Systems Operations performances), as well as developing a comprehensive spreadsheet to rank possible future competition which will arise from the “*New Vision*” under the new NASA Exploration Program initiative as espoused by NASA Director Sean O’Keefe. More information of the future missions of NASA may be found at the website: [http://www.nasa.gov/missions/solarsystem/explore\\_main.html](http://www.nasa.gov/missions/solarsystem/explore_main.html) . The restructuring of MSFC will change to some degree the cost/budgeting strategies of all its bureaucracy by changing over from traditional accounting procedures to full-cost accounting. The context of this research in relations to the daily business flow within FD43, Mission Systems Operations Group under the Flight Projects Directorate, FD01 is explained in the following directives:

MSFC is the first NASA center to really embrace full cost accounting. This means MSFC put all center overhead and G&A (dollars to pay for salaries, programs like the one this summer researcher was in, administration personnel, cafeteria, etc.) as a burden on the projects MSFC support. Not all of NASA has communicated thoroughly enough from headquarters to the Centers about impending changes in its bureaucratic landscape to make project operations more efficient and aligned with the “*New Vision*”. Code U (out of headquarters in DC) who pays for MSFC projects is screaming because of the increase to them due to MSFC being one of the first to use *full cost dollars*. So part of the problem of implementing bureaucratic changes is due to adopting a new cost/budgeting strategy which is completely out of the control of HOSC. Since associative projects are threatening to pull funds, HOSC is in the process of strategic planning and posturing itself to meet challenges raised by the Exploration Initiative (Code T out of headquarters.) The reason is that Code T is the next large project and HOSC really wants a piece of it. So some of the research this summer faculty endeavored to do was to work on a HOSC competition matrix to go into a possible draft of a business plan. Pursuant to this mandate, the summer faculty researcher had to compose from meticulous investigation a list of HOSC competitors, then manifest tentatively how much they cost versus HOSC (at somewhat of a high level marketing analysis) . This included the designation of potential customers for future business. All of these systematic efforts tied into measuring how well HOSC, Mission Systems Operations Group executed its functions, i.e., how well it optimized, in its diurnal dealings, the metrics that characterize its overall mission performances. Thus, the summer faculty researcher had the task to develop a HOSC competition matrix, as well as to research what would be quality metrics (not quantity/throughput necessarily) that HOSC could use in an ops organizational genre. The NASA government has never had to work this way before. So this summer researcher had to do *path-finding* work to find a way to parameterize the key performance measures that would allow for prototyping a robust HOSC business plan to keep Mission Systems Operations thriving into the distant and cosmic future. Initially, this research paper will give a brief narrative on the concept of full cost accounting which in the business literature is known as “activity-based” cost accounting. The subsequent pages will feature a “HOSC NASA Information Competitors Chart” composed in EXCEL. The latter sections will consist of an “HPR Stats Sheet”, composed in EXCEL as well (and based upon the Enhanced HOSC Systems

Operations and Maintenance Backup Charts) which does some statistical hypothesis testing on management directed questions, and a final section on some suggested metrics to incorporate into future HOSC business evaluation.

### **Full Cost Accounting**

A brief treatise on full-cost accounting is provided below:

Activity-based costing, or full-cost accounting is an accounting technique that allows an organization like HOSC to determine the actual cost associated with each product and service produced by the organization without regard to the organizational structure. The five activities that need to occur in order to determine activity costs are:

- Analyze Activities
- Gather Costs
- Trace Costs to Activities
- Establish Output Measures
- Analyze Costs

Now the knowledge of the true cost of an object is important for three reasons:

- To Discover Opportunities For Cost Improvement
- To Prepare And Actualize A Business Plan
- To Improve Strategic Decision Making

Overall, the formula to remember is that:

Total Cost = Direct Cost (Labor, Materiel) + Overhead Cost

As a matter of comparison, traditional cost accounting : (a) allocates overhead to the cost object (b) total company's overhead is allocated to the products based on volume based on measure, e.g., labor hours, computer central processing unit time (c) an assumed relationship between the overhead and volume-based measure . On the other hand, activity based cost accounting: (a) has a more accurate cost management methodology (b) focuses on indirect costs (overhead) (c) traces rather than allocates each expense category to the particular cost object (d) makes "indirect" expenses "direct". Again, the basic principles of activity based costing are: (a) cost objects consume activities (b) activities consume resources (c) the consumption of resources drives costs (d) understanding this relationship is critical to managing overhead. The best business conditions under which to use activity based cost accounting is when: (a)overhead is high (b) products are diverse: complexity, volume, amount of direct labor (c) making costly errors (d) the competition is seeming insurmountable. In HOSC, two vital activities are 1. Data Processing (measured in CPU, or MB) and 2. Customer Support (measured in hourly response time, or number of calls processed) . The best aspect of activity based cost accounting is that activity based cost allows indirect overhead to be shifted to those products that actually consume



World Class. A list of competitors was fashioned consisting of other NASA Centers, prime and subordinate contractors, as well as collaborative groups of pursuing lucrative NASA space business. The reference section of this research paper contains details of each competitor listing its capabilities, location and an enumeration of its supportive customers. The categories of evaluation of the HOSC competition matrix are (left to right)

- (a) Entity (foreign or domestic competitor)
- (b) Remote Operations
- (c) Command and Control
- (d) Planning Systems
- (e) Scheduling
- (f) Flight Dynamics/Trajectory
- (g) Systems Engineering
- (h) Interoperability
- (i) Information Management
- (j) Simulation
- (k) Payload Test/Check Out
- (l) Deep Space Network/Telemetry Data Retrieval Satellite Systems
- (m) Artificial Intelligence
- (n) Man versus Unmanned
- (o) Technical Innovation
- (p) Central Configuration

The rightmost column contains the average of all the designated rankings. Provided below is the entire matrix over several pages:

### HOSC NASA Information Competitors Chart

Competitor	Entity	Remote Operations	C <sup>2</sup> Cmmd&Cntrl	Planning Systems	Scheduling
1 GSD	US	3.00	1.00	2.00	2.00
2 ESA/ESOC	Foreign	3.00	3.00	2.00	2.00
3 RHEA Group	Foreign	3.00	0.00	2.00	2.00
4 GMV	Foreign	3.00	0.00	2.00	2.00
5 MRC	US	0.00	0.00	1.00	3.00
6 Lockheed-Martin Astronautics	US	2.00	0.00	3.00	2.00
6 Support JPL Mars Program	US	3.00	0.00	2.00	2.00
6 Built HST-Initial Control Center Operator	US	3.00	0.00	1.00	2.00
6 CSOC	US	2.00	0.00	2.00	2.00
6 USA	US	2.00	0.00	3.00	3.00
7 CSA	Foreign	3.00	2.00	3.00	3.00
8 BOEING	US	3.00	0.00	3.00	2.00
9 GSFC	US	2.00	0.00	3.00	3.00
9 Explorer Program	US	2.00	0.00	3.00	3.00
9 Geostationary Operations Environmental Satellite (GOES)	US	0.00	0.00	3.00	3.00
9 Earth Observing System (EOS)	US	3.00	0.00	3.00	3.00
9 Hubble Space Telescope (HST at Space Telescope Science Institute (STScI))	US	3.00	0.00	3.00	3.00
10 KSC	US	3.00	3.00	3.00	3.00
10 Launch Control	US	3.00	3.00	3.00	3.00
10 Space Shuttle	US	3.00	3.00	3.00	3.00
10 International Space Station (ISS)	US	3.00	3.00	3.00	3.00
11 JSC	US	3.00	3.00	3.00	3.00
11 International Space Station (ISS)	US	3.00	3.00	3.00	3.00
11 Space Shuttle	US	3.00	3.00	3.00	3.00
12 LRC	US	1.00	0.00	0.00	0.00
13 ARC	US	1.00	0.00	1.00	1.00
14 SSC	US	1.00	1.00	3.00	3.00
15 JPL	US	2.50	3.00	3.00	3.00
15 Earth Observing Missions (Jason, Topex, AcrimSat)	US	3.00	3.00	3.00	3.00
15 Mars (Orbit Surveyor, Odyssey, MER)	US	3.00	3.00	3.00	3.00
15 Solar System (Genesis, Stardust, Deep Impact, Cassini, Voyager)	US	3.00	3.00	3.00	3.00

Systems Engineering	InterOps	Info Management	Simulation	P/L Test--CheckOut	DSN/TDRSS	AI	Man Vs. Unmanned
2.00	3.00	3.00	3.00	2.00	2.00	1.00	3.00
2.00	1.00	3.00	2.00	2.00	3.00	2.00	2.00
3.00	1.00	2.00	2.00	1.00	0.00	1.00	1.00
3.00	1.00	3.00	3.00	2.00	2.00	2.00	3.00
2.00	1.00	2.00	2.00	0.00	0.00	2.00	1.00
3.00	1.00	2.00	3.00	2.00	2.00	2.00	3.00
3.00	2.00	3.00	3.00	3.00	3.00	1.00	1.00
2.00	3.00	3.00	1.00	3.00	1.00	2.00	2.00
2.00	2.00	2.00	2.00	3.00	1.00	2.00	2.00
2.00	1.00	3.00	3.00	3.00	1.00	2.00	1.00
3.00	3.00	3.00	3.00	3.00	2.00	2.00	2.00
3.00	2.00	3.00	3.00	3.00	2.00	2.00	3.00
3.00	1.75	3.00	0.00	0.50	2.25	0.00	2.25
3.00	2.00	3.00	0.00	2.00	3.00	0.00	3.00
3.00	2.00	3.00	0.00	0.00	2.00	0.00	2.00
3.00	0.00	3.00	0.00	0.00	2.00	0.00	2.00
3.00	3.00	3.00	0.00	0.00	2.00	0.00	2.00
0.00	3.00	2.33	3.00	2.00	1.00	1.00	3.00
0.00	3.00	3.00	3.00	2.00	1.00	1.00	3.00
0.00	3.00	2.00	3.00	2.00	1.00	1.00	3.00
0.00	3.00	2.00	3.00	2.00	1.00	1.00	3.00
3.00	2.50	3.00	3.00	3.00	3.00	1.00	3.00
3.00	3.00	3.00	3.00	3.00	3.00	1.00	3.00
3.00	2.00	3.00	3.00	3.00	3.00	1.00	3.00
2.00	0.00	0.00	1.00	0.00	0.00	0.00	2.00
3.00	2.00	3.00	3.00	0.00	0.00	1.00	2.00
3.00	2.00	2.00	3.00	2.00	1.00	0.00	3.00
3.00	2.67	3.00	2.17	1.83	2.00	1.00	2.17
3.00	3.00	3.00	3.00	2.00	1.00	1.00	2.00
3.00	3.00	3.00	3.00	2.00	2.00	1.00	2.00
3.00	3.00	3.00	3.00	2.00	2.00	1.00	2.00

Techno-Innovation	Central/Config	Ranking
1.00	3.00	2.13
2.00	3.00	2.33
3.00	3.00	1.80
1.00	2.00	2.13
3.00	3.00	1.40
3.00	3.00	2.27
3.00	3.00	2.33
3.00	2.00	1.93
2.00	2.00	1.87
3.00	3.00	2.20
3.00	3.00	2.73
3.00	2.00	2.47
3.00	3.00	1.98
3.00	3.00	2.20
3.00	3.00	1.80
3.00	3.00	1.87
3.00	3.00	2.07
2.67	3.00	2.40
2.00	3.00	2.40
3.00	3.00	2.40
3.00	3.00	2.40
3.00	3.00	2.83
3.00	3.00	2.87
3.00	3.00	2.80
2.00	0.00	0.53
3.00	0.00	1.53
1.00	1.00	1.93
2.67	2.17	2.48
3.00	2.00	2.53
3.00	2.00	2.60
3.00	2.00	2.60

15	Space Shuttle payloads (SRTM)	US	0.00	3.00	3.00	3.00
15	Deep Space Network	US	3.00	3.00	3.00	3.00
15	Astrophysics-operates Lyman Spitzer Infrared Telescope	US	3.00	3.00	3.00	3.00
16	SSL (Berkeley)	Contractor	0.00	0.00	0.00	0.00
17	Rockwell Intl(Boeing Df&SpGp)	US	0.00	3.00	2.00	1.00
18	ViaSat, Inc.	Contractor	2.00	3.00	0.00	0.00
19	Northrop Grumman	Contractor	2.00	3.00	2.00	3.00
19	Bought TRW in 2002. TRW built Chandra and was initial control center operator at Cambridge; SAO operates Chandra.	Contractor	2.00	3.00	2.00	3.00
20	Aastra Aerospace	ForeignCctr	1.00	3.00	1.00	1.00
21	Aerocorp Tech.	ForeignCctr	1.00	2.00	1.00	2.00
22	Bristol Aerospace Ltd.(Magellan)	ForeignCctr	3.00	3.00	2.00	3.00
23	Space Systems/Loral	Contractor	1.00	2.00	2.00	2.00
24	Honeywell (& Allied Signal)	Contractor	3.00	2.00	3.00	2.00
25	United Technologies	Contractor	0.00	0.00	0.00	0.00
26	Raytheon	Contractor	1.00	1.00	2.00	1.00
27	Altair Aerospace Company	Contractor	0.00	0.00	2.00	0.00
28	Visage, Applenet, Inc.	Contractor	0.00	0.00	2.00	0.00
29	Image2000 : Lockheed MMS in Sunnyvale	US	2.00	3.00	2.00	2.00
30	GMSEC	US	2.00	3.00	2.00	2.00
31	JASON-1 (JPL developed the ground control system; CNES operates it.)	US	2.00	3.00	2.00	2.00
32	Harris Corporation	Contractor	2.00	3.00	3.00	3.00
33	SESS (NOAA)--ITT	US	3.00	3.00	3.00	3.00
34	SENTEL / EPIC	US	3.00	3.00	3.00	3.00
35	Davidson Technologies	Contractor	0.00	0.00	3.00	2.00
36	Digital Operations Corporation	Contractor	0.00	3.00	0.00	0.00
37	General Dynamics	Contractor	1.00	3.00	1.00	1.00
38	L3 Communications	Contractor	0.00	1.00	0.00	1.00
39	SAIC	Contractor	0.00	1.00	1.00	1.00
40	Space Vector Corporation	Contractor	2.00	1.00	2.00	2.00
41	SRS Technologies	Contractor	0.00	2.00	3.00	3.00
42	Tanner Labs	Contractor	0.00	0.00	1.00	1.00
43	Teledyne Brown Engineering	Contractor	2.00	1.00	2.00	2.00
44	Z Microsystems, Inc.	Contractor	1.00	1.00	2.00	1.00

3.00	3.00	3.00	3.00	1.00	3.00	2.00	1.00	3.00
3.00	3.00	2.00	3.00	2.00	1.00	3.00	1.00	2.00
3.00	3.00	2.00	3.00	1.00	1.00	2.00	1.00	2.00
2.00	3.00	0.00	2.00	2.00	0.00	1.00	1.00	0.00
0.00	3.00	1.00	2.00	2.00	0.00	0.00	0.00	0.00
0.00	0.00		2.00	0.00	2.00	1.00	1.00	0.00
3.00	3.00	2.00	3.00	2.00	2.00	1.00	1.00	0.00
3.00	3.00	2.00	3.00	2.00	2.00	1.00	1.00	0.00
1.00	1.00	0.00	1.00	0.00	0.00	0.00	1.00	0.00
3.00	3.00	3.00	2.00	2.00	0.00	1.00	1.00	0.00
3.00	3.00	3.00	2.00	2.00	0.00	0.00	1.00	1.00
0.00	2.00	0.00	1.00	2.00	2.00	1.00	0.00	1.00
3.00	3.00	0.00	2.00	3.00	2.00	1.00	2.00	3.00
3.00	0.00	2.00	0.00	2.00	1.00	0.00	0.00	0.00
3.00	2.00	2.00	3.00	2.00	3.00	1.00	1.00	2.00
0.00	2.00	1.00	3.00	0.00	0.00	0.00	1.00	0.00
0.00	2.00	1.00	2.00	1.00	0.00	0.00	0.00	0.00
3.00	2.00	2.00	2.00	2.00	1.00	0.00	1.00	1.00
3.00	2.00	3.00	2.00	3.00	2.00	3.00	1.00	2.00
3.00	3.00	3.00	3.00	2.00	0.00	3.00	0.00	2.00
2.00	3.00	1.00	3.00	1.00	0.00	2.00	0.00	3.00
3.00	3.00	3.00	3.00	2.00	0.00	2.00	1.00	3.00
0.00	3.00	0.00	3.00	0.00	0.00	0.00	0.00	0.00
0.00	3.00	3.00	3.00	0.00	0.00	0.00	0.00	0.00
3.00	3.00	3.00	3.00	1.00	0.00	0.00	0.00	0.00
0.00	3.00	1.00	3.00	0.00	0.00	1.00	1.00	0.00
0.00	3.00	2.00	3.00	1.00	0.00	0.00	0.00	0.00
3.00		2.00	3.00	3.00	3.00	1.00	0.00	2.00
1.00	3.00	3.00	3.00	3.00	2.00	2.00	1.00	1.00
0.00	3.00	2.00	3.00	1.00	0.00	0.00	2.00	0.00
3.00	3.00	3.00	3.00	3.00	1.00	1.00	1.00	2.00
1.00	3.00	1.00	2.00	1.00	0.00	0.00	1.00	0.00

2.00	3.00	2.40
3.00	2.00	2.47
2.00	2.00	2.27
2.00	0.00	0.87
3.00	0.00	1.13
1.00	0.00	0.86
3.00	1.00	2.07
3.00	1.00	2.07
2.00	1.00	0.87
3.00	2.00	1.73
3.00	2.00	2.07
1.00	0.00	1.13
3.00	0.00	2.13
3.00	1.00	0.80
3.00	2.00	1.93
2.00	0.00	0.73
2.00	0.00	0.67
3.00	2.00	1.87
2.00	3.00	2.33
2.00	3.00	2.33
2.00	2.00	2.27
3.00	2.00	2.13
3.00	3.00	2.53
1.00	0.00	0.80
1.00	0.00	0.87
3.00	0.00	1.47
3.00	0.00	0.93
2.00	1.00	1.00
3.00	1.00	2.00
3.00	2.00	2.13
3.00	1.00	1.13
3.00	2.00	2.13
2.00	1.00	1.13

**Column Explanation:**

<b>Competitor:</b>	<b>List of current &amp; potentially competing contractors</b>
<b>Niche:</b>	<b>Command Control (C2), Remote Operations (Rm/Ops)</b>
<b>Planning Systems:</b>	<b>Mission Planning (MP), Payload Planning (P/L P), Crew Planning (CP)</b>
<b>Systems Engineering:</b>	<b>Functional Requirements Document (FRD), Cost (C ), Schedule (S), Risk (R )</b>
<b>Information Management:</b>	<b>Portals (P), Data Mining (DM),Adv. Architect&amp;Automa(AAA), Micro-tronics (ME)</b>
<b>Simulation:</b>	<b>Cybernetics (C), Robotics(R ), Supercomputing (SC)</b>
<b>P/L Test Checkout:</b>	<b>Remote Facility Testing (RFT), Closed Loop Test (CLT)</b>
<b>DSN/TDRSS: (Deep Space Network/Telemetry Data Relay Satellite System)</b>	<b>Radio &amp; Radar Astronomy (RRA), Telescope (T), Dish (D), Antenna (A)</b>
<b>Artificial Intelligence (AI):</b>	<b>Animation Research (AR), Image Processing (ImP), Neural Networks (NN)</b>
<b>Manned Vs. Unmanned:</b>	<b>Mobile Robotics(MbRb), Adv Telecomm(AT), Superarchitecture Software(SaSw)</b>
<b>Remote Operations:</b>	<b>Video/Voice/Cmmd:Cntrl</b>
<b>InterOps</b>	<b>Interoperability = Tech xchange among NASA Centers, or space industry</b>
<b>CSOC</b>	<b>Consolidated Space Operations Contract</b>

**A LIST OF CONTRACTOR ACRONYMS:**

**COLSA CORPORATION**  
**MORGAN RESEARCH CORPORATION (MRC)**  
**COMPUTER SCIENCES CORPORATION (CSC)**  
**LOCKHEED MARTIN Astronautics**  
**CSA (Canadian Space Agency)**  
**GMV (Spanish Aerospace)**  
**RHEA (Rheatech Ltd, UK)**  
**MRC (Mission Research Corp)**  
**Boeing (Teledyne)**  
**GOSC (Goddard Space Ctr)**  
**KSC (Kennedy Space Ctr)**  
**JSC (Johnson Space Ctr)**  
**LRC (Langley Research Ctr)**  
**ARC (Ames Research Ctr)**  
**SSC (Stennis Space Ctr)**  
**JPL (Jet Propulsion Laboratory)**  
**SSL (Berkeley) Space Science Lab**  
**CNES = Centre National d'Etudes Spatiales**  
**USA = United Space Alliance**

The next chart is just some statistical variance between different columns of the HOSC Competitors Matrix using the paired F-tests that measure variance to note if there were any correlations between any specific two of interest. The objective of doing these variance tests was to determine what columns acting a variable could be eliminated from any linear estimating model equation based upon all the matrix columns.

Statistical Metrics	
0.53	Statistical F-Test Between Sys. Eng. And Simulation
0.68	Statistical F-Test Between Sys. Eng. And P/L Test
0.05	Statistical F-Test Between Sys. Eng. And Info Management
0.02	Statistical F-Test Between DSN/TDRSS And AI
0.42	Statistical F-Test Between Tech Niche And Planning Systems
0.05	Statistical F-Test Between Sys. Eng. And Man Vs. Unmanned
0.67	Statistical F-Test Between Sys. Eng. And Planning Systems
0.70	Statistical F-Test Between Sys. Eng. And Technical Niche
0.40	Statistical F-Test Between Planning Systems And P/L Test--Check Out
0.02	Statistical F-Test Between Technical Niche And Info Management
0.87	Statistical F-Test Between Technical Niche And Simulation
0.97	Statistical F-Test Between Technical Niche And P/L Test -- CheckOut
0.05	Statistical F-Test Between Sys. Eng. And Info Management
0.88	Statistical F-Test Between Technical Niche And Manned vs. Unmanned
0.00	Statistical F-Test Between Technical Niche And AI
0.37	Statistical F-Test Between Technical Niche And DSN--TDRSS
0.82	Statistical F-Test Between Sys. Eng. And Man vs. Unmanned
0.16	Statistical F-Test Between DSN/TDRSS And Info Management
0.30	Statistical F-Test Between AI And Info Management
0.03	Statistical F-Test Between Manned Vs. Unmanned And Info Management
0.02	Statistical F-Test Between P/L Test--CheckOut And Info Management
0.46	Statistical F-Test Between DSN--TDRSS And Simulation
0.52	Statistical F-Test Between Simulation And Planning Systems
0.03	Statistical F-Test Between Simulaton And Info Management
0.51	Statistical F-Test Between Planning Systems And Man vs. Unmanned
0.92	Statistical F-Test Between Planning Systems And DSN--TDRSS

Finally, a ranking of all the competitors is given in the columnar format that follows:

Sorted Competitors List Ranked Highest-To-Lowest	Rank
JSC	2.83
CSA	2.73
SENTEL / EPIC	2.53
JPL	2.48
BOEING	2.47
KSC	2.40
ESA/ESOC	2.33
GMSEC	2.33
Lockheed-Martin Astronautics	2.27
Harris Corporation	2.27
GMV	2.13
GSD	2.13
Teledyne Brown Engineering	2.13
SRS Technologies	2.13
SESS (NOAA)--ITT	2.13
Honeywell (& Allied Signal)	2.13
Northrop Grumman	2.07
Bristol Aerospace Ltd.(Magellan)	2.07
Space Vector Corporation	2.00
GSFC	1.98
SSC	1.93
Raytheon	1.93
Image2000 : Lockheed MMS in Sunnyvale	1.87
RHEA Group	1.80
Aerocorp Tech.	1.73
ARC	1.53
General Dynamics	1.47
MRC	1.40
Rockwell Intl(Boeing Df&SpGp)	1.13
Space Systems/Loral	1.13
Tanner Labs	1.13
Z Microsystems, Inc.	1.13
SAIC	1.00
L3 Communications	0.93
SSL (Berkeley)	0.87
Aastra Aerospace	0.87
Digital Operations Corporation	0.87
ViaSat, Inc.	0.86
United Technologies	0.80
Davidson Technologies	0.80
Altair Aerospace Company	0.73
Visage, Applenet, Inc.	0.67
LRC	0.53

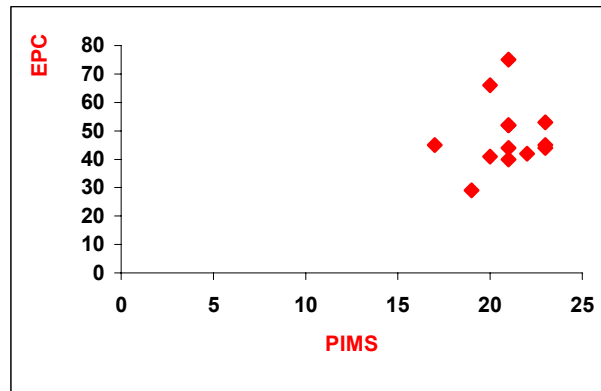
### **HPR Statistical Analysis**

A year long study was conducted on Payload Operations with an emphasis of charting performance metrics to measure facility and system readiness as well as responsiveness to mission systems operations problems that are an integral part of diurnal business. The data used in the statistical charts and matrices were taken from a document entitled, "*HOSC Metrics/DRD 1016MA-003 (part B)/NASA Contract NNM04AA07C, May 2004*". The first chart on the next page charts the HOSC Problems Reports per subsystem (Commanding, Database, Telemetry, PDSS, Services & Utilities, PIMS and EPC) over a one-year interval from May 2003 to May 2004. A scatter diagram of EPC (Enhanced HOSC PC) to PIMS (Payload Integration Management System) is given to see if the problems arising in these subsystems share a dependency. The subsequent hypothesis testing inquires into whether or not the average Database HPR exceeds a given threshold (in this case 50 per year). Both the Student T-Test and Normal Test statistics were used as a matter of which ever set of valid assumptions could be defended, or promoted by management, to ascertain their respective validity. Either test accepted the null hypothesis that the Database HPR tends to average more than 50 per month. The subsequent hypothesis tests whether or not the PDSS subsystem HPR exceeded 10 per year with a conclusion to fail to accept this hypothesized notion.

**HPR STATS SHEET** (HOSC Problem Report Statistical Sheet)

	May-03	Jun-03	Jul-03	Aug-03	Sep-03	Oct-03	Nov-03	Dec-03	Jan-04	Feb-04	Mar-04	Apr-04	May-04	avg	std dev
Commanding	20	25	24	23	28	32	32	27	29	42	46	42	43	31.77	8.34
Database	54	56	60	61	59	60	60	71	75	66	67	66	70	63.46	5.98
Telemetry	79	82	74	70	71	74	74	69	71	72	73	64	63	72.00	4.98
PDSS	29	7	8	8	8	9	11	12	13	13	13	10	12	11.77	5.39
Services & Utilities	46	42	43	37	38	43	49	57	60	55	57	50	50	48.23	7.20
PIMS	19	17	20	23	21	21	23	20	23	21	21	21	22	20.92	1.64
EPC	29	45	66	44	44	75	45	41	53	52	52	40	42	48.31	11.33

average	39.43	39.14	42.14	38.00	38.43	44.86	42.00	42.43	46.29	45.86	47.00	41.86	43.14		
std dev	20.12	23.56	23.57	20.49	20.19	23.94	20.10	22.05	22.73	20.43	20.82	19.25	19.20		



**Hypothesis Testing**

1 Does the average Database HPR exceed 50 per year?

54	56	60	61	59	60	60	71	75	66	67	66	70
50	50	50	50	50	50	50	50	50	50	50	50	50

t-value: 4.90E-06 accept  
Answer: Yes, with a statistical significance at the 0.0001 level  
z-value 1.11E-16 accept

2 Does the average PDSS HPR exceed 10 per year?

10	10	10	10	10	10	10	10	10	10	10	10	10
29	7	8	8	8	9	11	12	13	13	13	10	12

t-value: 0.278 reject  
Answer: No, with a statistical significance at the 0.05 level  
z-value 0.500 reject

Finally, the last series of statistical matrices and charts looks at the monthly percentage changes in open HPR's , then test the hypothesis that the average monthly percentage change in the Database HPR exceeds 5% (a management-directed threshold). They are given on the following pages.

**MONTHLY PERCENTAGE CHANGE IN OPEN HPR's**

	May-Jun	Jun-Jul	Jul-Aug	Aug-Sep	Sep-Oct	Oct-Nov	Nov-Dec	Dec-Jan	Jan-Feb	Feb-Mar	Mar-Apr	Apr-May
Commanding	25.00%	-4.00%	-4.17%	21.74%	14.29%	0.00%	-15.63%	7.41%	44.83%	9.52%	-8.70%	2.38%
Database	3.70%	7.14%	1.67%	-3.28%	1.69%	0.00%	18.33%	5.63%	-12.00%	1.52%	-1.49%	6.06%
Telemetry	3.80%	-9.76%	-5.41%	1.43%	4.23%	0.00%	-6.76%	2.90%	1.41%	1.39%	-12.33%	-1.56%
PDSS	-75.86%	14.29%	0.00%	0.00%	12.50%	22.22%	9.09%	8.33%	0.00%	0.00%	-23.08%	20.00%
Services & Utilities	-8.70%	2.38%	-13.95%	2.70%	13.16%	13.95%	16.33%	5.26%	-8.33%	3.64%	-12.28%	0.00%
PIMS	-10.53%	17.65%	15.00%	-8.70%	0.00%	9.52%	-13.04%	15.00%	-8.70%	0.00%	0.00%	4.76%
EPC	55.17%	46.67%	-33.33%	0.00%	70.45%	-40.00%	-8.89%	29.27%	-1.89%	0.00%	-23.08%	5.00%

May-Jun	Jun-Jul	Jul-Aug	Aug-Sep	Sep-Oct	Oct-Nov	Nov-Dec	Dec-Jan	Jan-Feb	Feb-Mar	Mar-Apr	Apr-May
3.70%	7.14%	1.67%	3.28%	1.69%	0.00%	18.33%	5.63%	12.00%	1.52%	1.49%	6.06%

**MONTHLY PERCENTAGE CHANGE IN OPEN HPR's**

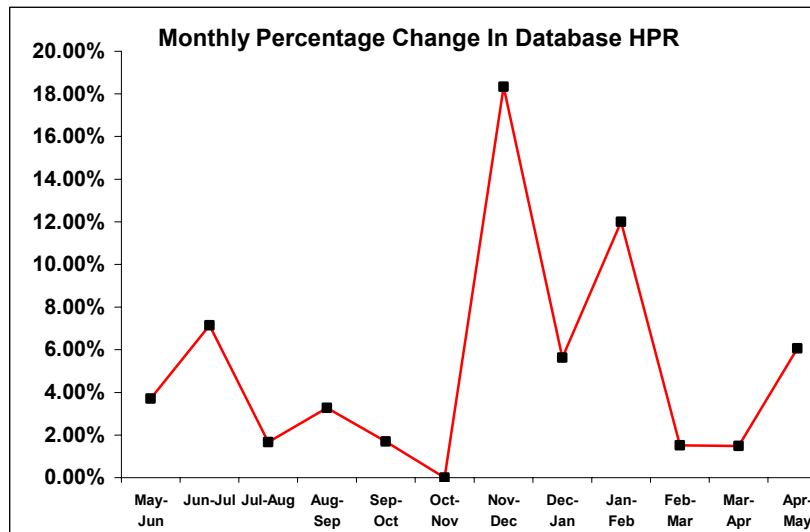
	May-Jun	Jun-Jul	Jul-Aug	Aug-Sep	Sep-Oct	Oct-Nov	Nov-Dec	Dec-Jan	Jan-Feb	Feb-Mar	Mar-Apr	Apr-May	avg	std dev
Commanding	25.00%	4.00%	4.17%	21.74%	14.29%	0.00%	15.63%	7.41%	44.83%	9.52%	8.70%	2.38%	13.14%	0.13
Database	3.70%	7.14%	1.67%	3.28%	1.69%	0.00%	18.33%	5.63%	12.00%	1.52%	1.49%	6.06%	5.21%	0.05
Telemetry	3.80%	9.76%	5.41%	1.43%	4.23%	0.00%	6.76%	2.90%	1.41%	1.39%	12.33%	1.56%	4.25%	0.04
PDSS	75.86%	14.29%	0.00%	0.00%	12.50%	22.22%	9.09%	8.33%	0.00%	0.00%	23.08%	20.00%	15.45%	0.21
Services & Utilities	8.70%	2.38%	13.95%	2.70%	13.16%	13.95%	16.33%	5.26%	8.33%	3.64%	12.28%	0.00%	8.39%	0.06
PIMS	10.53%	17.65%	15.00%	8.70%	0.00%	9.52%	13.04%	15.00%	8.70%	0.00%	0.00%	4.76%	8.57%	0.06
EPC	55.17%	46.67%	33.33%	0.00%	70.45%	40.00%	8.89%	29.27%	1.89%	0.00%	23.08%	5.00%	26.15%	0.24

**Hypothesis Testing**

1 Does the average monthly percentage change of the Database HPR exceed 5%?

0.04	0.07	0.02	0.03	0.02	0.00	0.18	0.06	0.12	0.02	0.01	0.06
0.05	0.05	0.05	0.05	0.05	0.05	0.05	0.05	0.05	0.05	0.05	0.05

t-value: 0.893 reject  
 Answer: No, reject at the .05 level  
 z-value 0.445 reject



Comment: The peak percentage changes occur in the 1st and 2nd quarters of the new fiscal year.

And the next statistical graphics and testing attempt to determine if the monthly percentage carryover of Incident Reports

**Hypothesis Testing**

1 Does the average monthly percentage change of the Incident Reports carryover exceed 5%?

0.10	0.04	0.06	0.07	0.03	0.06	0.05	0.12	0.07	0.05	0.06	0.07	0.02
0.05	0.05	0.05	0.05	0.05	0.05	0.05	0.05	0.05	0.05	0.05	0.05	0.05

t-value: 0.150 **reject** Answer: No, reject at the 0.1 level

z-value 0.025 **accept** Answer: Yes, accept at the .025 level

More decision weight should be given to the Z - Test.

## **Formulations of New Metrics**

The following is a list of Proposed HOSC Metrics:

1. Create a standard to measure real time Customer Service performance in dollar amount: CPU, or other processing time equated to “Cost Per Byte”, or “Cost Per Second” as examples based upon the service entity.

Narrative: This would allow for a dollar measure on amount of money needed to support additional personnel or materiel to keep the various service areas: telemetry, commanding, database, PIMS, Web, etc. supported and running without time-consuming and performance-degrading stoppages. The NASA initiative to reorient its budgeting and planning to “full-cost accounting”, or “activity-based” accounting is driving the need to start associating to each service activity some metric that yields cost of the service product to input into such accounting models. The objective is to predict amounts of O & S dollars on a given project when negotiating contract costs.

2. Flowchart per daily hour, or other unit time measure, the volume or capacity of service flow per HOSC service item, then map these numbers to do statistical measures: perhaps a multivariate Poisson distribution will allow for the probability of a given workload at a given time of interest.
3. Measure the backlog of Lost Cadre Support in terms of dollar per unit-time amount as well with the focus being what amount of dollars is lost daily, or monthly on services that are never performed. Lost Cadre Support may be due to system failure, or software integrity issue, in either case some measure is warranted to systematically predict the amount of such flow lost, either by interpolation of flow amount per unit time, or trending benchmarks of activity amounts that lead to a Lost Cadre Support. The twofold idea is to measure the decrement in profit from lost of providing a service, or to acquire statistical data to improve the formulation of reliability statistics such as MTTR (meantime to repair) to better predict when additional support may be needed to minimize such lost service.
4. Given Internal Total Service Outages, take each one and parameterize a failure distribution (from the exponential-parameter family of distributions) such as a Weibull, or Exponential one to create a sum of distributions with distinctive service measure (outages per unit time, or dollars) to use to predict future outages in magnitude or cost accumulation.
5. Maintain a regular measure of existing HOSC service capacity to actual or predicted incoming capacity to determine as a preventive plan, where to maximize critical services availability---to keep equipment and personnel on board to maintain more cost-effective operations.
6. Create a mean Incident Reports (ISS only) stat (either percentage or maximum) beyond which management decisions will be made to allocate available additional

resources and personnel to maintain service operations at an acceptable standard: this metric should be categorized (and updated as configurations changes are made) for each HOSC service and used as a quality performance measure standard, such as, the number of requests per hour per service for maximum or minimum work processing.

7. Take various metrics, for example, Critical Service Availability, say on a per month basis, then determine a parameter threshold between operating green, yellow or red, then run hypothesis tests on whether a monthly average basis if Critical Service Availability exceed, or not exceed a management targeted threshold for smooth work flow.

## **Summary**

The Huntsville Operations Support Center which encompasses the Mission Systems Operations Group will have to reformat its business processes due to the adaptation of the full cost accounting methodology being systematically implemented at all NASA centers. This change in daily procedural transactions has led to the requirement of composing a business plan for HOSC and its payload operations constituents to optimize its striving for a sizeable share of the projects associated with the new Exploration Initiative conceived by NASA Headquarters in Washington, DC. This paper summarized the numerical schematics of a full cost accounting procedure; also, the space industry data base was canvassed to composed eventually a HOSC competitors matrix to give payload operations an idea of how to assemble a business plan to rival, or incorporate prospective ventures of competing entities for NASA futuristic projects to advance its mission into the depth of the cosmos, as well as guardianship of the planet Earth. Some statistical analyses were performed on the HOSC Problem Reports (HPR's) just to key management to possible issues that could benefit from new metrics formulation. The latter section contained some suggested new metrics to characterize future HOSC performance readiness or responsiveness.

## **Acknowledgements**

Foremost, I extend abundant gratitude to Mr. Nathaniel Bocclair, III (Group Leader, Mission Systems Operations Group) for coordinating and accepting me to perform under his management leadership in my first NASA research job. His clear goal setting and his giving generously of payload operations technical expertise coupled with encouragement to set and achieve a high standard of accomplishment will be ever cherished warmly. Also, much accolades I extend to Ms. Lisa Watson-Morgan for creating a unique project for me to endeavor with to enhance the composition of a business plan to direct the Mission Systems Operations Group to a more profitable future in its vital role to support the Space Shuttle and the International Space Station. Ms. Brenda Wade, Ms. Margaret Hanson, Ms. Cynthia Frost, Mr. Doug FooShee, and Mr. Steve Cavelage and the diligent denizens (COLSA) of Room A182, Bldg. 4663, along with other personnel in the Flight Projects Directorate and external support I encountered, are all regarded with much appreciation for their assistance and rapport in my sometimes capricious efforts to conduct creditable research while I endured challenging issues. Undoubtedly, the future of space exploration belongs to a

talented, adventuresome, and techno-savvy group of youthful pioneers who will take NASA deeper into the unknown cosmos seeking fundamental truths that will help enrich human life and illuminate universal truths. In this spirit, I hope to return again next summer under the auspices of the NASA Faculty Fellowship Program to research in mathematical areas such as full-cost accounting, computational fluid dynamics, helioseismology, or modeling and simulation to advance space exploration in some academic ways to greater frontiers.

### **HOSC Competition References**

1. <http://www.mission.com/tech.html>
2. [http://www.ast.lmco.com/cgi-bin/websearch\\_ssc2.pl](http://www.ast.lmco.com/cgi-bin/websearch_ssc2.pl)
3. [http://www.space.gc.ca/asc/eng/csa\\_sectors/technology/development/csa\\_labs/expertise/expertise.asp](http://www.space.gc.ca/asc/eng/csa_sectors/technology/development/csa_labs/expertise/expertise.asp)
4. <http://www.gsfc.nasa.gov>
5. <http://spaceflightnow.com/news/n0101/22jscfd>
6. <http://ase.arc.nasa.gov/vv2000/kortenxamp.pdf>
7. [http://www-space.arc.nasa.gov/ann\\_report.cfm](http://www-space.arc.nasa.gov/ann_report.cfm)
8. <http://www.larc.nasa.gov/research/research.htm>
9. <http://www.ffc.arc.nasa.gov/vast/vast.html>
10. <http://www.ames.technology.org/ames/success-story.amp?NAME=spectrum.html>
11. <http://www.asc.nasa.gov/aatt/rto/tutorial21.pdf>
12. [http://www.jacobssverdup.com/eis/ss\\_ames.html](http://www.jacobssverdup.com/eis/ss_ames.html)
13. <http://www.stj.nasa.gov/tto/spinoff1998/and10.htm>
14. <http://sec353.jpl.nasa.gov/>
15. <http://is.arc.nasa.gov/AR/tasks/IntPh.html>
16. <http://www.incose-la.rog/mini-conf/miniconf2003AgendaOSL1b.pdf>
17. <http://rsd.gsfc.nasa.gov/rsd/research-seng/>
18. <http://www.sun.com/aboutsn/media/features/mars.html>
19. <http://www.raytheon.com/pmdata/eclipse/ref-docs/eclipse.pdf>
20. <http://www.dscper.net/~1e328/mcct-apl-en.html>
21. [http://honeywellaerospace.com/search\\_local.asp](http://honeywellaerospace.com/search_local.asp)
22. <http://content.honeywell.com/dses/>
23. <http://content.honeywell.com/dses/space/default.asp>
24. <http://www.ssloral.com/html/products/programscomm.html>
25. <http://www.msss.com/venus>
26. <http://www.appsig.com/prods/engineering.html>
27. <http://cfa-www.harvard.edu/~scranmer/SURF/#Images>
28. <http://www.bristol.ca/Products.html>
29. <http://www.corba.org/vendors/pages/altair.html>
30. <http://www.visage.com/>
31. <http://gmsec.gsfc.nasa.gov/demoLab.htm>
32. [http://discovery.larc.nasa.gov/explorer/GSFC\\_Services\\_final\\_030115.pdf](http://discovery.larc.nasa.gov/explorer/GSFC_Services_final_030115.pdf)
33. <http://www.spaceref.ca/news/viewpr.html?pid=1192>

**2004**

**NASA FACULTY FELLOWSHIP PROGRAM**

**MARSHALL SPACE FLIGHT CENTER**

**THE UNIVERSITY OF ALABAMA  
THE UNIVERSITY OF ALABAMA IN HUNTSVILLE  
ALABAMA A&M UNIVERSITY**

**RELIABILITY ASSESSMENT OF CONCEPTUAL  
LAUNCH VEHICLES**

Prepared By:	Lisa A. Bloomer
Academic Rank:	Assistant Professor
Institution and Department:	Middle Tennessee State University Department of Mathematical Sciences
NASA/MSFC Directorate:	Safety and Mission Assurance
MSFC Colleague:	Vyga Kulpa

## **Introduction**

Planning is underway for new NASA missions to the moon and to MARS. These missions carry a great deal of risk, as the Challenger and Columbia accidents demonstrate. In order to minimize the risks to the crew and the mission, risk reduction must be done at every stage, not only in quality manufacturing, but also in design. It is necessary, therefore, to be able to compare the risks posed in different launch vehicle designs. Further, these designs have not yet been implemented, so it is necessary to compare these risks without being able to test the vehicles themselves.

This paper will discuss some of the issues involved in this type of comparison. It will start with a general discussion of reliability estimation. It will continue with a short look at some software designed to make this estimation easier and faster. It will conclude with a few recommendations for future tools.

## **Risk and Reliability**

Risk and reliability are very closely related. Risk is defined as the probability that a system will fail, and reliability is the probability that it will perform as designed. So, risk is a number that is hopefully close to zero, reliability is a number close to one, and they are related in that reliability is one minus risk.

Because the reliability of a system is unknown, it is necessary to estimate it. If the system has already been designed and built in large numbers, it is a straightforward statistical exercise to estimate the reliability. Simply test the system many times, and estimate the reliability as the number of times the systems performed as designed, divided by the total number of trials. This number is referred to as *demonstrated reliability*.

Point estimates of reliability can be misleading. For example, if a system is tested 1000 times with no failures, the point estimate is that the system is 100% reliable. But this estimate does not match reality – no system is 100% reliable. It is useful to provide an interval estimate instead. So, if a system is tested 1000 times with no failures, we can say with 95% confidence that the reliability is somewhere between 0.997 and 1. A more common statement is that the reliability is 0.997 with 95% confidence. This is just an abbreviation. One way to interpret the confidence level is that the probability that the reliability is in the specified interval is 0.95 – that is, that there is a 5% chance of an error. The confidence level, paired with the width of the interval, is an indication of uncertainty. A system that has been tested ten thousand times will have a shorter confidence interval at the same confidence level than one that was tested one thousand times.

A goal articulated by the Astronaut Office is that the reliability for crewed vehicles should be 0.999 with 95% confidence. That is, the risk of a member of the crew dying should be less than 1 in 1000, with a less than 5% chance that the risk is greater. To verify that level of reliability, the launch vehicle would have to be tested 2995 times with no failures. This level of testing is highly unlikely for a system so complex and expensive. The Space Shuttle, for example, has flown 113 missions. Furthermore, the

system was modified several times, so combining those missions into one demonstrated reliability number is statistically suspect.

Estimating reliability in another way – by testing at a component level and calculating system reliability as a function of the component reliabilities – yields a number called *predicted reliability*. For example, if a system consists of two components, both of which must function for the system to function, and the components each have a reliability of 0.99, then the system reliability is  $0.99 \times 0.99 = 0.9801$ . Finding the predicted reliability of a more complex system requires detailed knowledge about how the system works. This knowledge can be summarized in fault trees or other diagrams which can then be used to make the calculation of predicted reliability easier.

As with demonstrated reliability, predicted reliability is more useful if it is reported in terms of confidence intervals rather than point estimates. Tracking how the confidence level is affected by the combination of estimates is difficult. For example, if a system has two components whose reliability are estimated at a 95% level, and the components are manufactured independently of each other, the system's confidence level is greater than  $0.95 \times 0.95 = 0.9025$ , and less than  $1 - 0.05 \times 0.05 = 0.9975$ . But this range is quite large, and different assumptions about the components and their interrelation in the system yield different values for the confidence level of the system. Because this problem is complicated, it is common to use simulation to estimate the predicted reliability. This will be discussed further in the next section.

Demonstrated and predicted reliability numbers are both estimates of an underlying reliability which is unknown. In fact, however, they measure different quantities. Demonstrated reliability gives the reliability of a system as built and tested. That is, it is affected not only by the design of the system, but also by the quality of the manufacturing process, any issues in storage and transport, and the variables (such as temperature and human factors) introduced during testing. The uncertainty of demonstrated reliability number is mainly affected by the number of tests run. Predicted reliability, on the other hand, is based on the design of the system and any assumptions about other factors affecting reliability. For example, guidelines for the reporting of figures of merit during a conceptual study of launch vehicles allow the assumption that the software running the system is 100% reliable. Also, predicted reliability numbers will, by the nature of the calculations, not include unanticipated risks. Therefore, there are more sources of uncertainty in a predicted reliability number. However, in a system that has only been tested a few times, the demonstrated reliability will be highly uncertain and the predicted reliability may be more certain. This may lead to the two numbers being combined in a weighted average that takes into account the relative uncertainties.

### **Reliability Software**

The predicted reliability of systems is often estimated using simulation. Usually, the risk of a failure in a particular component is calculated, taking into account variables such as the age of the component, temperature, etc. Then, using this risk, a randomized decision is made as to whether that component failed. The consequences of such a failure are

tracked using event sequence diagrams, and a notation is made if the failure of the component resulted in the failure of the system. This process is repeating a large number of times, and the proportion of times the system failed is reported. By varying the values of the input variables according to probability distributions that reflect uncertainty, many different estimates for system reliability can be made. Then a 95% confidence interval for system reliability can be estimated by, for example, making the upper endpoint 1 and the lower endpoint the 5<sup>th</sup> percentile of the simulated reliabilities.

The Flight-oriented Integrated Reliability and Safety Tool (FIRST) was developed by Science Applications International Corp (SAIC) to predict the reliability of launch vehicles through several figures of merit: the probability of Loss of Vehicle (LOV), Loss of Payload (LOP), and Loss of Mission (LOM). Loss of Crew (LOC) is also included, but the definition of this figure of merit has not yet been agreed upon by all the stakeholders, so it may have to be changed. FIRST started as an Excel and Crystal Ball model. A user interface has been added and capabilities increased. FIRST also contains reliability information about many components of launch vehicles. The current version is FIRST 2.7.3, with version 2.8 to be released shortly.

The main strength of FIRST is that it speeds up the analysis of launch vehicles, which allows several conceptual configurations to be compared. FIRST has also been used to determine the effects of design decisions. For example, the decision to add an engine to allow for recovery if one engine fails (an “engine-out capability”) involves the tradeoff of increased weight, possibly increasing the number of flights needed to accomplish a mission, versus the ability to recover from an engine failure. Quantifying what happens to the LOM figure with and without engine-out capability helps with these decisions.

FIRST was designed to be used by SAIC analysts who understand the estimation process as well as the inner workings of the software. It should therefore be run by someone with a lot of reliability experience and training in the software. It should also be mentioned that the reliability information that FIRST contains for the various engines and other components each come from different NASA sources and have not been vetted as a group. Some components – types of engines, for example – are not included, and there is no simple way to add in a conceptual component. FIRST 2.7.3 does not easily allow for multistage craft, but this should be added in FIRST 2.8.

There are other software packages available for reliability analysis. Failure Environment Analysis System – MSFC (FEAS-M) is a physics based system that allows the user to create trees describing the relationships between different variables and then simulate. FEAS-M was developed at Marshall Space Flight Center. Quantitative Risk Assessment System (QRAS) was developed at NASA and is currently being maintained by the University of Maryland. It was used to perform a probabilistic risk assessment of the Space Shuttle Program a few years ago. Defect Detection and Prevention (DDP) is a software package designed by the Jet Propulsion Laboratory to manage implementation of a reliability system from design through manufacturing.

Commercial software is also available. The spreadsheet Excel and the simulation add-in Crystal Ball are powerful for their flexibility. The company Reliasoft has several reliability packages available for different types of analysis. And Relex also has several software packages that do reliability analysis.

FIRST fills a specific niche in the analysis of launch vehicles. The other software packages are general and can implement this type of analysis, but are not already set up to do so. Also, the data about component reliability that are stored within FIRST would have to be easily accessed to use these packages. It should be emphasized that predicted reliability estimates from one package should not be closely compared to those from another package. This is because it is highly unlikely that the two models used the same assumptions. If it becomes necessary to do such a comparison, effort should be made to identify differing assumptions.

### **Conclusion**

The estimation of the risk and reliability of launch vehicles is an important task, especially coming when the vehicles are still at a conceptual stage. This allows designs to compete not only on a basis of cost and feasibility, but also on risks posed to the crew and the mission. There are two types of estimated reliability, demonstrated and predicted reliability. If the system has not yet been built, it is impossible to calculate demonstrated reliability and it becomes necessary to predict reliability based on that of the components of the system.

Various software packages are available for this estimation process. FIRST is designed for the analysis of launch vehicles, while other software packages are available for more general tasks. All of the software requires the user to be knowledgeable about reliability analysis as well as the system being analyzed.

An important component of the process of estimating reliability for a system based on the reliability of the components is to have a database of components available. These data should contain the best available information on each component as well as estimates for the certainty of the information stored.

### **References**

[1] “Astronaut Office Position on Future Launch System Safety,” LMA Correspondence Control # 04-AST-00013, May 4, 2004.

[2] Birolini, A. Reliability Engineering: Theory and Practice, 3<sup>rd</sup> edition. Springer, NY 1999.

[3] Rausand, M. and Høyland, A. System Reliability Theory: Models, Statistical Methods, and Applications, 2<sup>nd</sup> edition. Wiley, NJ 2004.

**2004**

**NASA FACULTY FELLOWSHIP PROGRAM**

**MARSHALL SPACE FLIGHT CENTER**

**THE UNIVERSITY OF ALABAMA  
THE UNIVERSITY OF ALABAMA IN HUNTSVILLE  
ALABAMA A&M UNIVERSITY**

**FIBER REINFORCED COMPOSITES FOR  
INSULATION AND STRUCTURES**

Prepared By:	Roy M. Broughton, Jr.
Academic Rank:	Professor
Institution and Department:	Auburn University Department of Textile Engineering
NASA/MSFC Directorate:	Engineering
MSFC Colleagues:	Gweneth Smithers Tom Delay

## **Introduction**

The work involves two areas:

Composites – optimum fiber placement with initial construction of a pressure vessel, and  
The general subject of insulation, a continual concern in harsh thermal environments.

## **Insulation**

During a first meeting about insulating materials, a question was asked about fibers for a resilient insulating blanket. As we (at Auburn) have more than 10 years experience in the development of high temperature, resilient, insulating batting (Figure 1), I prepared and presented a lecture on fibrous insulation and the technology of its production. I also had some crimped carbonaceous fiber at Auburn University, and provided a quantity of this fiber for use by NASA. That collaboration is continuing.

Since the temperature requirements for materials used by NASA are often substantially more severe than the testing previously done on the carbonaceous fiber batting (Figure 1), a test was performed on this batting in a plasma torch located at MSFC. That test burned through the sample in about 4 seconds (1000 seconds is considered acceptable for the more severe applications). Even a carbon-carbon composite does not survive the plasma torch test unless it is coated with a temperature/oxidation resistant coating.

Figure 1. Demonstration of temperature/flame resistant carbonaceous batting –

Dr. David Hall, Professor Emeritus, Textile Engineering, Auburn University.



A temperature/oxidation resistant material, suitable for use as an adhesive and coating in the carbonaceous batting was sought. The primary material selected was an alumina/silicate based binder/coating (Pyropaint 634 AL-L from Aremco Products Inc). A phenol-formaldehyde resol used in the fabrication of carbon/carbon composites was also obtained for trial as an adhesive/coating,

The alumina paint is a two component mixture – Part A is reported by the manufacturer to be a low viscosity suspension of colloidal silica (sol) in water. Part B is an alumina powder. Mixing instructions suggest three parts powder to one part silica suspension in

water. According to the manufacturer, a small amount of the liquid can be added as a thinner if needed. The major concern with thinning (having too little of the powder) is the tendency of the silica binder to shrink and crack as it dries. When applying to a porous material like a batting, there is also a concern that the liquid will be pulled into the porous batting leaving a pigment rich (alumina) coating on the surface that will flake off easily. The manufacturer has experience with application of their refractory paint to porous ceramics and metals, but does not seem to have experience using the materials as a binder in nonwoven fibrous felts where the paint can penetrate very well and the pigment may be filtered out to various degrees with the penetration.

Some initial trials were made to see how the coating would perform. First a moderate density carbonaceous batting was simply painted with the paint, mixed to the manufacturers specifications. Subsequently attempts were made to saturate the batting with the paint thinned with water. This approach allows sufficient liquid to saturate the batting without loading it with excessive binder or pigment, and also without changing the binder/pigment ratio. As the battings were allowed to dry, some of the binder and pigment migrated under the influence of gravity to the bottom of the samples. This appeared to give a coating more on the individual fibers rather than producing a solid painted surface on the batting. The samples were allowed to dry at room conditions for 25 hours before putting them in an oven at ~300 F for ~ 1 hour. The weight add-on of the samples was measured and is shown in Table 1. Further experimentation will be necessary to select the best process and conditions for optimum performance. Samples of the coated and the saturated felt were tested in the plasma torch to see what if any improvement in performance is observed.

Samples of the carbonaceous felt were saturated with a phenol formaldehyde resol dissolved in methanol. The resol was diluted with methanol to allow an easy distribution of the fluid in the felt. The methanol readily soaks into the felt which essentially behaves as a sponge for the solution, and could be wrung out just like a sponge or wash cloth soaked in liquid. The amount of liquid added was limited therefore and the felt simply dipped in the solution on one side. All the liquid was readily absorbed into the felt. Subsequently the felt was inverted and squeezed to distribute the liquid binder. The solids content of the resol solution was not known and initially was not measured. The weight gain of the sample was measured and results shown in Table 1 – samples 1-5.

Samples 6 – 10 consist of felt treated with an alumina/silicate binder. Samples 2 and 3 (saturated with phenolic resin) were subsequently treated by painting the alumina/silicate on the surface. Samples 2 and 10 were tested in the plasma torch.

Both samples failed at about 100 seconds, more than an order of magnitude better than the untreated sample, but still well short of the desired time to failure. The sample bonded with phenolic and subsequently painted with alumina/silicate on the surface seemed to perform better over the longer time period, indicating the desirability of an impervious high temperature coating over the whole surface. Some additional tests will be run to try to improve the thermal resistance.

**Table 1: Glue/resin added to carbonaceous batting**

Sample number	Resin/Coating	Resin on weight of carbon fiber (%)	~ Density (lb/ft <sup>3</sup> )	Comments
1	Phenolic	21	6.3	
2	Phenolic	35	7.0	Coated*
3	Phenolic	37	7.1	Coated*
4	Phenolic	75	8.6	
5	Phenolic	165	13.8	Squeezed out excess
6	Alumina/silicate	147	12.8	Painted on surface
7	Alumina/silicate	145	12.7	Saturated
8	Alumina/silicate	98	10.3	Saturated
9	Alumina/silicate	218	16.6	Saturated + painted
10	Alumina/silicate	132	19.0	Saturated

\* Subsequently coated with alumina-silica composition

### **Fiber Placement and Composite Tank**

We continued a project begun by Dr. David Beale, to cover an aluminum tank liner/pressure vessel with braided Kevlar. Dr. Beale had suggested a braid angle approaching 50degrees; however, it became obvious that the braided structure would not lie close to the tank surface in the neck region if that braid angle was maintained.

The initial work undertaken was to learn how to set the machine controls. The two primary controls are the mandrel speed and the rotational speed of the yarn carriers. The results of this effort are shown in Figures 2 and 3.

A simple geometric model of the braided structure was developed assuming a circular yarn cross section and a 65 % packing factor for fibers in the yarn bundles. Using 18 axial yarns of 1000 denier Kevlar and 18 yarns spiraling in each direction, a model was developed for the size of the braid as a function of braid angle (Figure 4). This model combined with the graphs below allowed the selection of the machine settings, and the

settings appeared to be approximately correct – until we began to vary the yarn tensions on the machine. At that point, the assumptions about yarn shape became obviously untrue (Figure 5).

**Figure 2. Machine setting vs rotational speed**

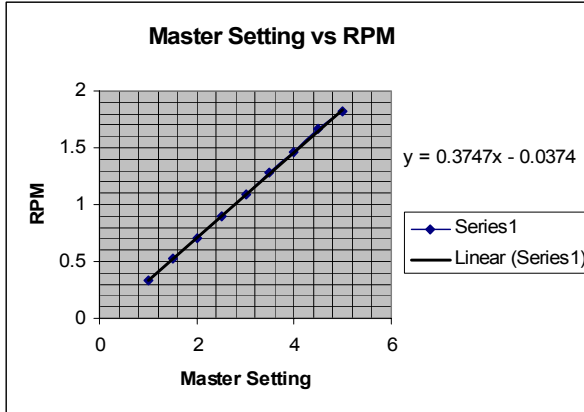


**Figure 3 Machine setting vs mandrel speed**

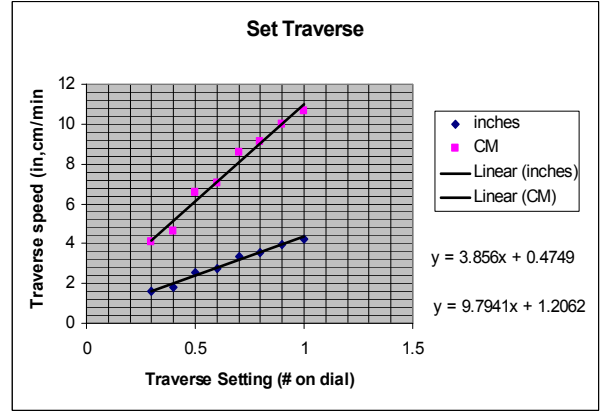


**Figure 4: Braid diameter as a function of braid angle – with minimum yarn spacing**

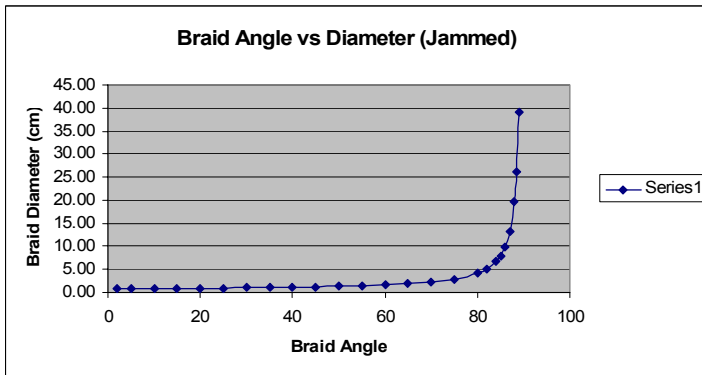
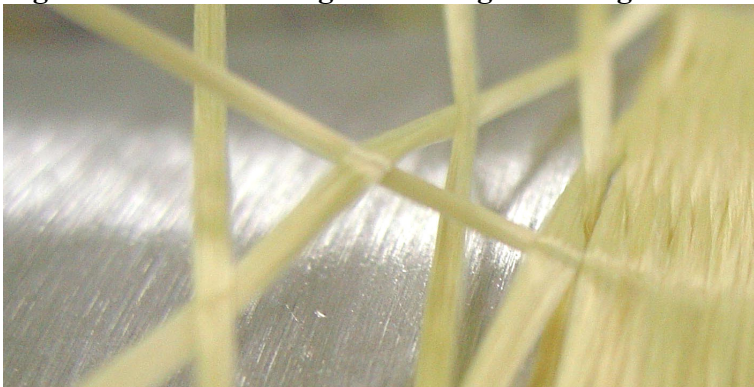


**Figure 5. Yarn crossing illustrating flattening of the lower tensioned yarn**



At this point we discarded the model and adjusted the machine by intuition about the desired result and the adjustments that would achieve it. The most satisfactory result was produced by using 18 axial yarns until the tank neck begins to flare outward, then another 18 axials were added. The axial yarn tensions were significantly higher than the spiral yarns. A nonwoven Kevlar felt was placed under the braid and an epoxy wetted carbon fiber layer was placed over the braid (see Figures 6 and 7). The tanks will be tested by overpressure until failure and with a rifle shot while under pressure. Results from these tests are not yet available.

**Figure 6 Braid and felt covered tank on the braiding machine**

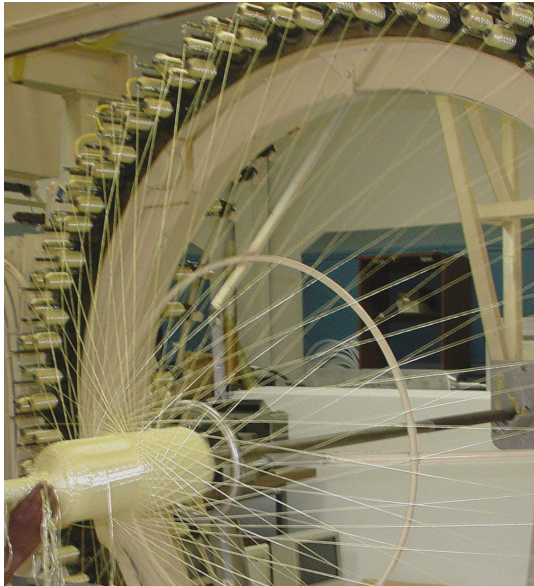


**Figure 7 Covering the braid with epoxy coated carbon fiber**



### **Acknowledgements**

Appreciation is expressed to Christy Cunningham, a senior in Fiber Engineering at Auburn University who worked on the project this summer, and to Tom Delay and Gweneth Smithers who were the MSFC sponsors for the Summer Faculty Fellow and the Accompanying Student. Appreciation is also expressed to all the personnel of ED 34 who provided advice, directions and instructions as the author learned his way around MSFC.

**2004**

**NASA FACULTY FELLOWSHIP PROGRAM**

**MARSHALL SPACE FLIGHT CENTER**

**THE UNIVERSITY OF ALABAMA  
THE UNIVERSITY OF ALABAMA IN HUNTSVILLE  
ALABAMA A&M UNIVERSITY**

**SUB-GRID MODELING OF ELECTROKINETIC  
EFFECTS IN MICRO FLOWS**

Prepared By:	C. P. Chen
Academic Rank:	Professor
Institution and Department:	University of Alabama in Huntsville Chemical and Materials Engineering
NASA/MSFC Directorate:	Science
MSFC Colleague:	Dr. Helen Cole

## **Introduction**

Advances in micro-fabrication processes have generated tremendous interests in miniaturizing chemical and biomedical analyses into integrated microsystems (Lab-on-Chip devices). To successfully design and operate the micro fluidics system, it is essential to understand the fundamental fluid flow phenomena when channel sizes are shrink to micron or even nano dimensions. One important phenomenon is the electro kinetic effect in micro/nano channels due to the existence of the electrical double layer (EDL) near a solid-liquid interface. Not only EDL is responsible for electro-osmosis pumping when an electric field parallel to the surface is imposed, EDL also causes extra flow resistance (the electro-viscous effect) and flow anomaly (such as early transition from laminar to turbulent flow) observed in pressure-driven microchannel flows.

Modeling and simulation of electro-kinetic effects on micro flows poses significant numerical challenge due to the fact that the sizes of the double layer (10 nm up to microns) are very thin compared to channel width (can be up to 100's of  $\mu\text{m}$ ). Since the typical thickness of the double layer is extremely small compared to the channel width, it would be computationally very costly to capture the velocity profile inside the double layer by placing sufficient number of grid cells in the layer to resolve the velocity changes, especially in complex, 3-d geometries. Existing approaches using “slip” wall velocity and augmented double layer are difficult to use when the flow geometry is complicated, e.g. flow in a T-junction, X-junction, etc. In order to overcome the difficulties arising from those two approaches, we have developed a sub-grid integration method to properly account for the physics of the double layer. The integration approach can be used on simple or complicated flow geometries. Resolution of the double layer is not needed in this approach, and the effects of the double layer can be accounted for at the same time. With this approach, the numeric grid size can be much larger than the thickness of double layer. Presented in this report are a description of the approach, methodology for implementation and several validation simulations for micro flows.

## **Description of the Sub-Grid Modeling**

To enable simulations without resolving the double layer, its effects on the flow can be modeled using the concept of a  $\zeta$  potential near the wall. A body force term, resulting from the interaction of the  $\zeta$  potential and the applied pressure drop, is added to the fluid momentum equations, written as:

$$\frac{\partial \rho u_i}{\partial t} + \frac{\partial}{\partial x_j} \rho u_j u_i = -\frac{\partial p}{\partial x_i} + \frac{\partial \tau_{i,j}}{\partial x_j} + \rho_e E_i \quad (1)$$

The last term of equation (1) represents the electrokinetic effect. For streaming potential

induced by the applied pressure,

$$\lambda_0 E_i = -u_i \rho_e, \quad (2)$$

and the local electric charge density,  $\rho_e$ , is governed by the Poisson equation

$$\nabla^2 \zeta = -\frac{\rho_e}{\varepsilon \varepsilon_0}. \quad (3)$$

In the above equations,  $\rho$  is the fluid density,  $u_i$  the Cartesian velocity components,  $p$  the pressure,  $\tau_{ij}$  the stress tensor,  $\varepsilon$  the fluid permittivity,  $\delta=1/\kappa$  the Debye thickness of the double layer, and  $\lambda_0$  the bulk fluid conductivity. Under equilibrium situation, the ion distribution can be described by the exponential function, then equation (3) becomes the well-known Poisson-Boltzmann equation. For small surface charge situation investigated in this study, the linearized form of the Poisson-Boltzmann equation can be used. Equation (3) thus becomes:

$$\nabla^2 \zeta = \kappa^2 \zeta \quad (4)$$

with BCs?: 
$$\begin{cases} \zeta = \zeta_0, & y = 0 \\ \zeta = 0, & y = \infty \end{cases}$$

$\zeta$  is the potential field inside the electrical double layer and  $\zeta_0$  is the zeta potential.

Equations (3) and (4) will be used to substituted into the last term of equation (1) for the electrokinetic effect. (We would combine  $\varepsilon$  and  $\varepsilon_0$  into one single symbol  $\varepsilon$  in the following formulation.) Considering the nature of  $\zeta$  potential, we analytically integrate the equation (4) combining with the boundary conditions, along a local wall normal direction to obtain the distribution:

$$\zeta = \zeta_0 e^{-\kappa y} \quad (5)$$

Where,  $y$  is normal distance to the wall, and  $\zeta_0$  is the value of  $\zeta$  potential at the wall. The electrokinetic source term defined in equation (1) is only applied in a very narrow region near the wall. We analytically integrate it while neglecting the impact of  $\zeta$  potential outside the double layer, with assumption that the velocity profile within the double layer to be linear, and the application of Grahame equation [1] relating surface potential to surface charge density,  $\sigma$ , the source term becomes

$$\vec{S} = \frac{1}{\lambda_0} \sigma^2 \kappa \frac{1}{4} (1 - 3e^{-2}) A u_c \quad (6)$$

Where,  $V$  is grid volume near the wall,  $A$  is the area of the wall face (see figure 1). The vector  $S$  denotes the momentum source contributions due to the streaming potential effect in different directions. The shear stress on the wall is calculated as:

$$\vec{\tau}_w = -\frac{1}{\lambda_0} \frac{1}{4} \frac{\sigma^2}{\frac{e^2}{e^2 - 3} \delta} u_c \quad (7)$$

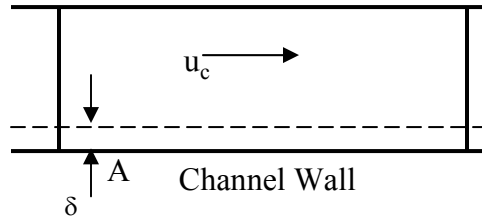


Figure 1. Integration Grid Volume.

In deriving equation (7) we used the relation  $\delta = \frac{1}{\kappa} \cdot u_c$ .  $u_c$  is cell center velocity of grid near the wall and  $u_w$  is the wall velocity. The wall velocity is zero for a stationary wall. This definition of the effective distance essentially reduces the apparent wall shear stress, calculated based on the available information during calculations (i.e.  $u_c$ ,  $u_w$  and  $\delta$ ).

The above equations were implemented into ESI-Group's CFD-ACE+ v2004 "Electro" module. Due to the sub-grid model nature, the grid system near the wall should be carefully constructed such that the first cell away from wall should cover the EDL thickness.

## Results and Discussion

The model was first compared to the benchmark test case of rectangular microchannel flow of Ren at al. [2]. Detailed channel dimensions and testing conditions were described in [2]. The model prediction and the experimental data are shown in Table 1. As discussed in [1], the electro-viscous effect would be significant when the ionic concentration of the solution is smaller the  $5 \times 10^{-3}$  M. As stated in [2], the data for KCl aqueous solution of  $10^{-2}$  M was taken to be the case without EDL effect. As can be seen from Table 1. The model predictions compared well (within 5%) with the experimental data.

	No EDL	No EDL	With EDL DIUF H2O	With EDL DIUF H2O
$dP/dx$ ( $10^6$ Pa/m)	Re, pred.	Re, exp.	Re, pred.	Re, exp.
2	1.01	~1.05	0.79	~0.82
3	1.50	~1.45	1.20	~1.25
4	1.98	~1.90	1.58	~1.62

Table 1. Prediction and experimental data [2] comparison.

The second test case involved a T-junction micro flow on the Caliper N145 chip. The present model predicts up to about 40% deduction in flow rate when EDL effect is accounted for, as seen in Figure 2. Due to the uncertainties introduced by the dye in the experimental procedure for obtaining velocity data [3], the comparison is qualitative and the model shows correct trend for this complex micro fluidics system.

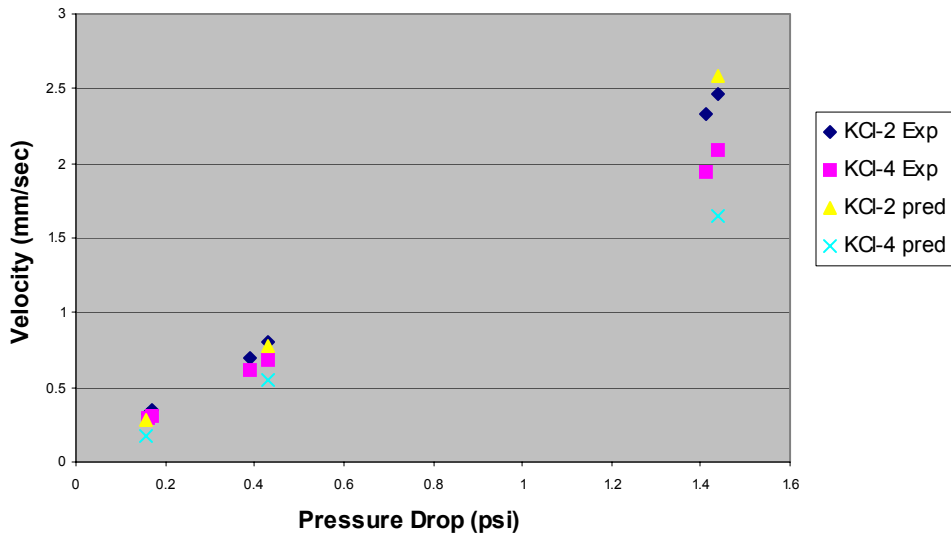


Figure 2. Prediction and data comparison for Caliper N145 chip.

## **Conclusion**

A sub-grid model was developed to account for electro-viscous effect in lab-on-chip microfluidics system. The model was successfully implemented into CFR-ACE+, and validation study was performed. The present model predicts straight micro channel flow well and qualitatively predicts T-junction flow correctly. The electro-viscous effects were found to be quite significant and reduce flow rate (up to 40% in T-junction flows), when compared to the classical laminar theory. Further refinement of the model to account for realistic velocity profile and non-linear Boltzmann distributions within EDL are desirable. Further validations with carefully designed complex micro flow experiments are also recommended.

## **Acknowledgements**

The author would like to thank the entire LOCAD (Lab-on-Chip Application Development) team of engineers and scientists in Marshall Space Flight Center. Mr. Kartik Shah in ESI-Group and Dr. Z. J. Chen's help in model implementation are acknowledged.

## **References**

- [1] Hunter, R. J. (2001), *Foundation of Colloidal*, 2<sup>nd</sup> ed., Oxford University Press.
- [2] Ren, L, Qu, W. and Li, D. (1996), "Interfacial Electrokinetic Effects on Liquid Flow in Microchannels," *Int. J. Heat and Mass Transfer*, vol. 44, pp. 3125-3134.
- [3] Hunterhower, H. (2004), "Study to Aid Computer Modeling of Lab-on-Chip Technologies," Presentation at NASA-Marshall Space Flight Center, USRP Summer Program, July, 21.

**2004**

**NASA FACULTY FELLOWSHIP PROGRAM**

**MARSHALL SPACE FLIGHT CENTER**

**THE UNIVERSITY OF ALABAMA  
THE UNIVERSITY OF ALABAMA IN HUNTSVILLE  
ALABAMA A&M UNIVERSITY**

**INCORPORATION OF A CHEMICAL EQUILIBRIUM  
EQUATION OF STATE INTO LOCI-CHEM**

Prepared By:	Carey F. Cox, Ph.D.
Academic Rank:	Assistant Professor
Institution and Department:	Louisiana Tech University Mechanical Engineering Program
NASA/MSFC Directorate:	Space Transportation
MSFC Colleague:	Dr. Jeff West

## Introduction

Renewed interest in development of advanced high-speed transport, reentry vehicles and propulsion systems has led to a resurgence of research into high speed aerodynamics. As this flow regime is typically dominated by hot reacting gaseous flow, efficient models for the characteristic chemical activity are necessary for accurate and cost effective analysis and design of aerodynamic vehicles that transit this regime. The LOCI-Chem code recently developed by Ed Luke at Mississippi State University for NASA/MSFC and used by NASA/MSFC and SSC represents an important step in providing an accurate, efficient computational tool for the simulation of reacting flows through the use of finite-rate kinetics [3]. Finite rate chemistry however, requires the solution of an additional N-1 species mass conservation equations with source terms involving reaction kinetics that are not fully understood. In the equilibrium limit, where the reaction rates approach infinity, these equations become very stiff. Through the use of the assumption of local chemical equilibrium the set of governing equations is reduced back to the usual gas dynamic equations, and thus requires less computation, while still allowing for the inclusion of reacting flow phenomenology.

The incorporation of a chemical equilibrium equation of state module into the LOCI-Chem code was the primary objective of the current research. The major goals of the project were: (1) the development of a chemical equilibrium composition solver, and (2) the incorporation of chemical equilibrium solver into LOCI-Chem. Due to time and resource constraints, code optimization was not considered unless it was important to the proper functioning of the code.

## Procedure for the Determination of Equilibrium Properties

The primary objective was accomplished through the modification and incorporation of a "black box" chemical equilibrium solver for the determination of the equilibrium composition and thus thermodynamic properties of the reacting flow. This "black box" solver was written in a generic fashion to solve any arbitrary mixture of thermally perfect gases. Unlike curvefits of equilibrium properties which are limited to the specific mixture the empirical data was collected for, the methodologies can be applied to any reacting flow given a few reference thermodynamic properties [3]. The equilibrium composition solver solves a set of nonlinear governing equations comprising NS-NE laws of mass action,

$$w_i(\rho_j, T) = \sum_{r=1}^{NR} (v_{i,r}'' - v_{i,r}') \left[ K_{c,r} \prod_{s=1}^{NS} \left( \frac{\rho_s}{M_s} \right)^{v_{s,r}'} - \prod_{s=1}^{NS} \left( \frac{\rho_s}{M_s} \right)^{v_{s,r}''} \right], i = 1, NS - NE$$

NE elemental mass constraints,

$$w_{NS-NE+i}(\rho_j) = \sum_{s=1}^{NS} \frac{\alpha_{i,j}}{M_j} \frac{\rho_j}{\rho} - \left[ \sum_{s=1}^{NS} \frac{\alpha_{i,j}}{M_j} \frac{\rho_j}{\rho} \right]_{t=0}, i = 1, NE$$

and either the caloric equation of state

$$d(\rho_j, T) = (\rho e)_{t=0} - \sum_{j=1}^{NS} \rho_j \left[ \int_{T_{ref}}^T c_{v_j}(\tau) d\tau + e_{f_j} \right]$$

or the thermal equation of state

$$d(\rho_j, T) = (p)_{t=0} - \sum_{j=1}^{NS} \rho_j R_j T$$

for NS species mass fractions and an additional dependent variable, where NR, NE and NS represent the number of reactions, elements and species, respectively. The assumption of local chemical equilibrium means that the complete thermodynamic state can be determined through the specification of two state variables, specifically for the purposes of the current work as either a function of density and internal energy, pressure and density, or pressure and temperature. The caloric equation of state is used for the first situation, and the thermal equation of state for the latter two. The additional dependent variable is temperature for the first two cases and global density for the state as a function of pressure and temperature. Newton's method is employed to linearize the governing equations which are then iterated upon until convergence is achieved.

Upon convergence, the complete equilibrium composition is known via the species densities as well as the temperature. Through application of the standard mixture rules, various thermodynamic properties can be obtained: internal energy, enthalpy, gas constant, pressure, etc. Further by reusing the Jacobians utilized during the solution process, partial derivatives of species mass fractions with respect to density and temperature can be obtained. These can then be used to determine other properties of interest, such as the equilibrium isentropic index and hence equilibrium speed of sound. Full details of these procedures can be found in [1].

Coupling to the flow solver, simply requires the incorporation of the equilibrium equation of state module into LOCI-Chem. Whenever thermodynamic properties are required, the flow solver simply calls for the state defined as a function of either internal energy and density, pressure and density, or pressure temperature. The complete thermodynamic state is provided as a c++ object and can be queried for the desired properties. In addition to the thermodynamic properties, special derivatives of pressure and specific energy per unit volume with respect to density and pressure are provided for the flux computation.

### **Results for the Composition Solver**

In order to access the accuracy of the techniques used for the determination of the equilibrium properties, comparisons were made of results to theoretical and empirical data. Specifically, the validation study involved the determination of properties for a 17-species air model, with comparisons of both equilibrium composition and thermodynamic properties for a number of densities ranging from 1/10000<sup>th</sup> to 100 atmospheres, where atmospheric density would be 1.293 kg/m<sup>3</sup>. A composition plot for the case at approximately 100 atmospheres is presented in Figure 1(a) as seen on the next page. As can be seen there is excellent agreement with the theoretical results up to a temperature of about 8000K. This is the point at which the mixture is beginning to ionize. The particular thermodynamic model employed for the species internal energy is a simple vibrational model whereby ionization energy is not accounted for and hence the discrepancy. Figure 1(b) shows pressure profiles at constant density as functions of temperature. Comparisons are made to values obtained from the empirical curve fits of Tannehill, et al [5]. Again there is excellent agreement up to the point at which ionization

becomes important. Similar results were obtained for other densities and thermodynamic properties. The capability of the equilibrium solver to handle arbitrary mixtures was demonstrated by obtaining solutions of equilibrium composition and thermodynamic properties using a 6-species hydrogen-oxygen combustion model, the results of which are not shown.

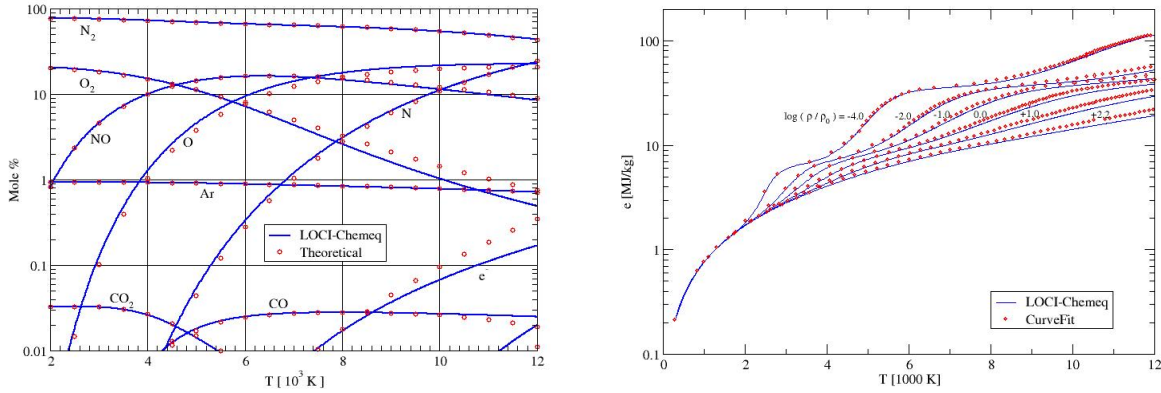


Figure 1: 17-Species Air Results (a) Composition for 100 Atmospheres, and (b) Internal Energy vs. Temperature

### Shocktube Solution

After incorporating the chemical equilibrium equation of state module into LOCI-Chem a demonstration of its effectiveness and utility was desired. This was accomplished by investigating a simple shocktube problem where the left state was defined with a pressure of 1 MPa and density of 1.00 kg/m<sup>3</sup> and the right state was defined with a pressure of 100 kPa and 1.00 kg/m<sup>3</sup>. Results of the shocktube problem are represented with the evolution of temperature as presented in Figure 2. Looking at the shock wave propagating to the right, it is easy to

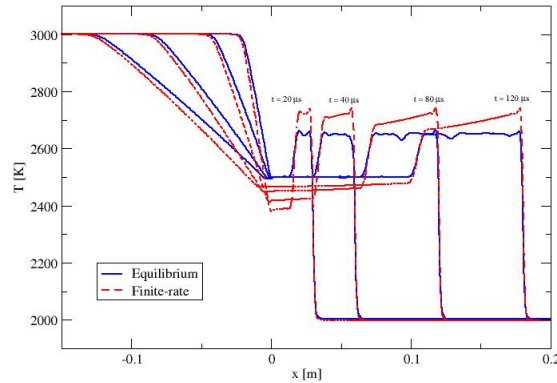


Figure 2: Evolution of Temperature for the Shocktube Problem

recognize the finite-rate values jumping up to the frozen limit and as time progresses, the shock propagates, the temperature relaxes to the equilibrium solution. This is a well known physical phenomenon representing the fact that the kinetic energy created across the shock is first converted to thermal energy and then relaxes through chemical energy to the equilibrium limit.

## **Further Work**

Results obtained using the chemical equilibrium solver were promising and there was good agreement with theoretical and empirical data. However, there were some problems that were noticed. While the finite-rate solution for the shocktube problem required only minutes, the equilibrium solution required hours. This can be attributed to the lack of good initial guesses passed to the equilibrium composition solver caused by the lack of a mechanism to save mass fractions and temperature values from previous iterations in LOCI-Chem. This problem needs to be addressed in future work. Particular remedies include retaining previous composition information or even hints towards a good initial starting point based upon ranges of values.

## **Conclusions**

A chemical equilibrium equation of state module has been added to LOCI-Chem. This module provides a less computationally expensive alternative to finite-rate chemistry while still providing the capability of modeling reacting flows. This solution methodology has proven to be accurate, though not necessarily efficient at this point.

## **Acknowledgements**

The author expresses his gratitude and appreciation to the members of the Space Transportation Directorate, Fluid Dynamics Analysis Group (TD-64), in particular, Jeff West, Dan Dorney, and Robert Garcia, whose assistance and guidance made this a profitable and enjoyable experience for all. Thank you all. Special thanks is accorded Ed Luke of Mississippi State University, who bore the brunt of numerous discussions about and debug sessions with the LOCI-Chem code.

## **References**

- [1] Cox, C., *An Efficient Solver for Flows in Local Chemical Equilibrium*, PhD thesis, Mississippi State University, December 1992.
- [2] Cox, C. and Cinnella P., "A General Solution Procedure for Flows in Local Chemical Equilibrium," *AIAA Journal*, Vol. 32, No. 3, pp. 519-527, March 1994.
- [3] Luke, E., *A Rule-Based Specification System for Computational Fluid Dynamics*, PhD thesis, Mississippi State University, December 1999.
- [4] Hilsenrath, J. and Klein, M., "Tables of Thermodynamic Properties of Air in Chemical Equilibrium Including Second Virial Corrections from 1500° K to 15,000° K," AEDC-TR-65-58, 1965.
- [5] Srinivasan, S., Tannehill, J.C., and Weilmuenster, K.J., "Simplified Curve Fits for the Thermodynamic Properties of Equilibrium Air," NASA RP-1181, 1987.

**2004**

**NASA FACULTY FELLOWSHIP PROGRAM**

**MARSHALL SPACE FLIGHT CENTER**

**THE UNIVERSITY OF ALABAMA  
THE UNIVERSITY OF ALABAMA IN HUNTSVILLE  
ALABAMA A&M UNIVERSITY**

**Fiber Reinforced Composite Materials Used for Tankage**

Prepared By:	Christy Cunningham
Academic Rank:	Undergraduate Senior
Institution and Department:	Auburn University Department of Textile Engineering
NASA/MSFC Directorate:	Engineering
MSFC Colleague:	Gweneth Smithers

## **Introduction**

The Nonmetallic Materials and Processes Group is presently working on several projects to optimize cost while providing effect materials for the space program. One factor that must be considered is that these materials must meet certain weight requirements. Composites contribute greatly to this effort. Through the use of composites the cost of launching payloads into orbit will be reduced to one-tenth of the current cost. This research project involved composites used for aluminum pressure vessels. These tanks are used to store cryogenic liquids during flight. The tanks need some type of reinforcement. Steel was considered, but added too much weight. As a result, fiber was chosen. Presently, only carbon fibers with epoxy resin are wrapped around the vessels as a primary source of reinforcement. Carbon fibers are lightweight, yet high strength. The carbon fibers are wet wound onto the pressure vessels. This was done using the ENTEC Filament Winding Machine. It was thought that an additional layer of fiber would aid in reinforcement as well as containment and impact reduction. Kevlar was selected because it is light weight, but five times stronger than steel. This is the same fiber that is used to make bulletproof vests trampolines, and tennis rackets.

A braided structure was chosen because it is conformable to a variety (but not all) of shapes. The braided structure was manufactured by using the Wardwell Maypole Braider. This piece of equipment produces a braid by using the same principle as the popular children's game, "Braid the Maypole"; hence the name Maypole Braider. In this game children grab ribbons which hang from the top of a pole. They then move in a circular motion, some to the left and some to the right. As they meet, they go over the first person and under the second. This creates a braid. The Maypole Braiding machine has several carriers, which hold the yarn packages, on its front and the rear. They contain springs, which keep the yarns in constant tension. The carriers (like the children) on the front of this circular machine rotate. The carriers on the rear do not move. These rear carriers hold the yarns called axials. The axial yarns are pulled through the front side of the machine. They are held in a constant position. The carriers on the front of the machine are called wrapping yarns. They wrap around the axial yarns, thereby creating a braid. All of the yarns are pulled through a ring to a central location where they interlace, called the braiding point. This is the point where the mandrel or object being braided on is pushed through. This machine has a control box with the following controls: start/stop, emergency stop, stop motion on/off, run/jog, forward/reverse, auto/manual, braider/feeder/braider & feeder, traverse ratio, and master speed. The forward/reverse button controls the direction that the traverse moves. The traverse is the top part of the machine which moves in a horizontal direction. The traverse has a lower part that holds the mandrel after it is pushed through the braid point. The auto/manual button allows continuous operation of the machine when on auto, but non-continuous when on manual. The braider/feeder/braider & feeder button controls operation of the braider and feeder simultaneously as well and non-simultaneously.

The traverse ratio controls the speed that the traverse moves. The master speed controls the speed at which the machine braids. Both are unitless.

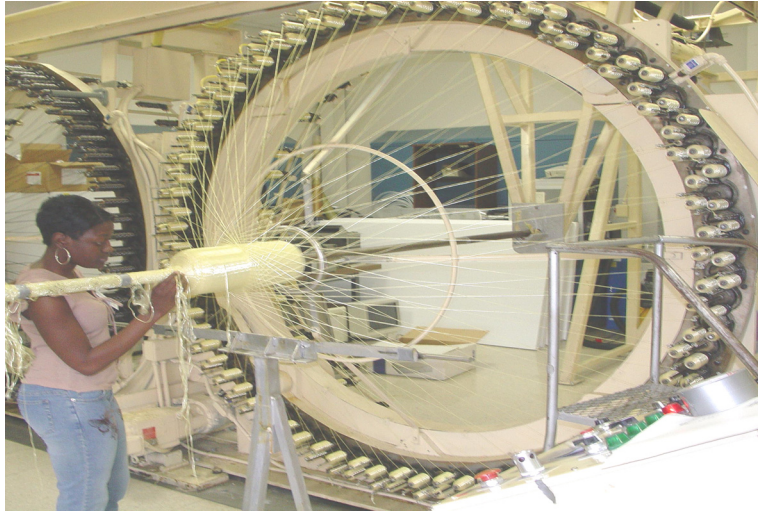


Figure 1: Wardwell Maypole Braider

### **Fiber Reinforcements Used for Tankage**

Rubber bands were placed on the empty carriers. This was done to disable the stop motion and allow the machine to run continuously. Some of the rear carriers had to be replaced so that all eighteen operated by the same roller mechanism. Since the machine had been sitting idle for months, it was run to remove old surface yarns. Shafts were screwed into the ends of the pressure vessels and it was pushed through the braiding point onto the traverse. Several trials were done, but a useable structure was not produced. Some modifications had to be made to the braiding machine in order to produce a suitable structure. New springs were added to the carriers to provide better tensioning. Lubricants were applied to the machine so that the carriers released the yarns properly. The second ring was removed to prevent filaments from forming. After these adjustments were made the research was divided into three projects. Each project used a different technique of combining materials for the composite.

In the first project, Kevlar was braided over a bare pressure vessel. This was done to see if it was best to start the braid on the tank and move down toward the shaft or vice versa. It was also done to see if any additional adjustments had to be made. Several runs using a different number of axial and wrapping yarns were done. It was determined that the tightest structure was formed by using eighteen wrapping yarns in each direction. Eighteen axial yarns were used up until the point where the tank flares out into a disk shape.

This is the section just after the bottleneck of the tank. At this point an additional eighteen axials were pulled through. This increased the tension in the structure, which resulted in tighter braiding.

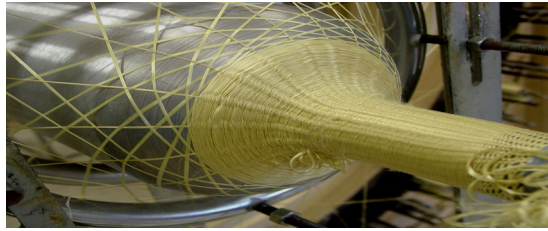


Figure 2: Braiding Over Bare Pressure Vessel

In the second project the vessel was wrapped with felt. The felt was also made from Kevlar. The felt was applied dry with double-sided tape. Rubber bands were placed on the end of the bottlenecks to hold the felt ends in place. The structure (also applied dry) was braided over the felt. Carbon fibers were then wet wound over the structure. The epoxy resin was allowed to cure.



Figure 3: Braiding Over Felt



Figure 4: Wet Filament Winding Over Structure

In the third project, the carbon fibers were wet wound onto the tank first. The epoxy resin was allowed to cure. A layer of felt was wrapped over the cured carbon fibers of one tank. This was done so that one impact test could be performed with the felt and one without it. This will determine if the felt aids in impact reduction. The braided structure was applied over this layer of felt. The braided structure was applied directly on top of the cured carbon fiber for the other tank. A second layer of carbon fibers was wet wound on top of the braided structure for both tanks. The epoxy resin was allowed to cure.



Figure 5: Wet winding of carbon fibers

## **Testing and Results**

Two tests are performed on the pressure vessels to see if they are more efficient with the addition of the structure. One test they undergo is an impact test. In this test the pressure vessels are shot with fifty caliber rifles. Observations will be made to see if the Kevlar structure and felt reduces the impact of the bullet. This test will also determine if the braided structure is useful for containment of metal fragments when the tank fails. The second test that is performed on these pressure vessels is a burst test. In this test, the tanks are filled with water. They are then placed inside of a machine where the pressure is increased to several thousand pounds per square inch until the tank fails. This test will also determine if the structure is useful for containment. The bare tanks burst at 1300 psi. The tank with carbon fibers and epoxy resin burst at 7800 psi. With the addition of the braided structure, the tanks should be able to withstand well over 8000 psi. (These tests have not been performed yet on the tanks with the braided structure and felt. Some of them have to be shipped to Utah, so there are no results to report.) The braided structure and felt material only add 800 grams to the tanks.



Figure 7: Bare tanks fail at 1300 psi



Figure 8: Tank w/ carbon and resin fails at 7800 psi

## **Future Applications for the Braided Structure**

The structure can be used in future space exploration missions and possibly the return to flight mission. It can be used to reinforce larger pressure vessels and other tankage. In the case of meteors or any other debris hitting the tank, it will reduce the impact. If by chance the tanks fail, it will serve as a safety and protective material by containing the metal fragments from tank. Possible future applications may include cryogenic research. Any lightweight high strength material can always aid in furthering the space exploration program. It may also be useful to the military and Department of Homeland Security to protect tanks containing explosive liquid from terrorist attacks.

## **Resources**

This project required the use of a braiding machine and Kevlar fibers, which were provided by the United States Army. Aluminum pressure vessels, carbon fibers with epoxy resin, and a machine for filament winding were provided by Marshall Space Flight Center. A machine to perform the burst test was provided by the east testing area employees. The impact test will be done by engineers in Utah. A digital camera was used to take photographs of the different

structures. These pictures were used to make observations, an analysis, and to determine the most proficient structure for this application.

### **Conclusion**

This form of composite material is useful to Marshall Space Flight Center because it provides a very cost efficient mean of reinforcing aluminum pressure vessels. The material adds very little weight, but high strength. Therefore, the vessels are more durable and less susceptible to damage. If anything hits the tank, the structure will reduce the impact. Not only does the structure serve as a reinforcement and impact reducer, it can be used as a safety and protective material as well.

### **Acknowledgements**

The author would like to thank God for the ability and opportunity to perform this research; and her parents, Frank and Rosie Cunningham, for all of their support. Special thanks to the materials engineers and scientists in the nonmetallic materials research area of the Marshall Space Flight Center's Engineering Directorate. Special thanks to United States Army for the use of their equipment and supplies, Dr Roy Broughton, Gweneth Smithers, Charles Henderson, and the NFFC Program for the opportunity to work with such a prestigious group of engineers and researchers.

### **References**

- [1] <http://www.fhwa.dot.gov/bridge/frp/frp197.htm>
- [2] <http://www.science.org.au/nova/059/059key.htm>

**2004**

**NASA FACULTY FELLOWSHIP PROGRAM**

**MARSHALL SPACE FLIGHT CENTER  
THE UNIVERSITY OF ALABAMA  
THE UNIVERSITY OF ALABAMA IN HUNTSVILLE  
ALABAMA A&M UNIVERSITY**

**INTEGRATION OF LAUNCH VEHICLE SIMULATION/ANALYSIS  
TOOLS AND LUNAR CARGO LANDER DESIGN (PART2/2)**

Prepared By:	George Brian DeJean, Accompanying Student Yeu-Sheng Paul Shiue, Professor Jeffrey King, USRP student
Academic Rank:	Undergraduate Senior
Institution and Department:	Christian Brothers University Mechanical Engineering Department
NASA/MSFC Directorate:	Engineering
MSFC Colleague:	Mr. Bill Pannell

## **Introduction**

The Graphical User Interface (GUI) design using Matlab for Maveric II's inputs and outputs and the Maveric II conversion from UNIX to PC is discussed in part 1 of this project (Page XL-1).

Part 2, which will be discussed in this report, will discuss the development of a Lunar Cargo Lander (unmanned launch vehicle) that will transport usable payload from Trans-Lunar Injection to the moon. The Delta IV-Heavy was originally used to transport the Lunar Cargo Lander to TLI, but other launch vehicles have been studied. In order to uncover how much payload is possible to land on the moon, research was needed in order to design the sub-systems of the spacecraft. The report will discuss and compare the use of a hypergolic and cryogenic system for its main propulsion system. The guidance, navigation, control, telecommunications, thermal, propulsion, structure, mechanisms, landing gear, command, data handling, and electrical power sub-systems were designed by scaling off other flown orbiters and moon landers. Once all data was collected, an excel spreadsheet was created to accurately calculate the usable payload that will land on the moon along with detailed mass and volume estimating relations. As designed, The Lunar Cargo Lander can plant 5,400 lbm of usable payload on the moon using a hypergolic system and 7,400 lbm of usable payload on the moon using a cryogenic system.

## **Problem Statement**

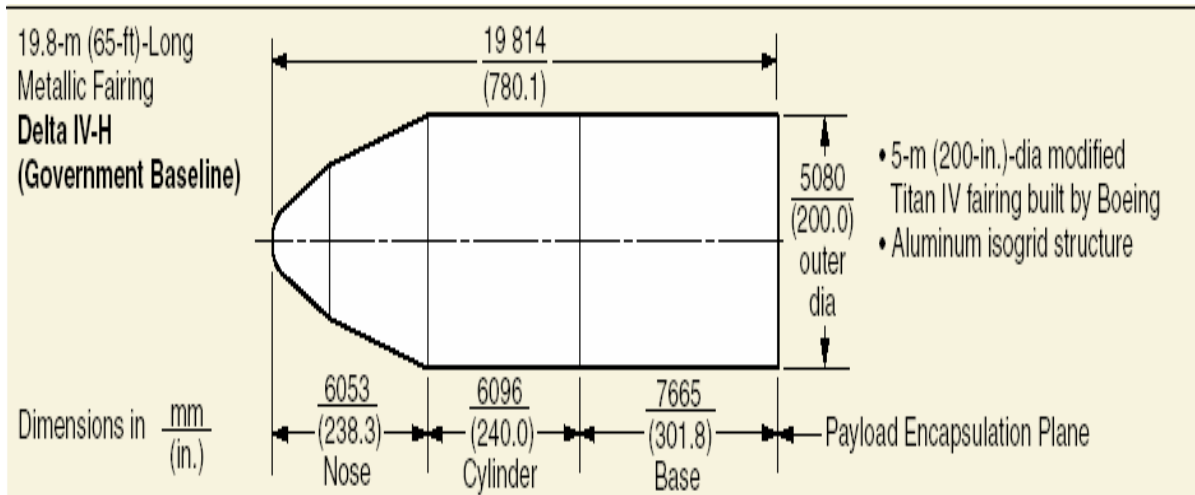
Develop a vehicle capable of being launched on a Delta-IV Heavy Launch Vehicle which can land on the moon with the goal of pre-implanting cargo for a new lunar mission. Consider other launch vehicles capable of inserting a payload into Trans-Lunar Injection (TLI).

## **Lunar Cargo Lander Travel**

The Delta-IV Heavy Launch Vehicle will transport the Lunar Cargo Lander (LCL) from earth to TLI. After reaching TLI, the LCL will be released. The LCL will then start its propulsion system in order to make the first burn from TLI to Lunar Orbit Insertion (LOI). The LCL will then make its second burn, which is from LOI to landing on the moon.

## **Research**

Initial research consisted of accumulated data from many sources, including Boeing engineers, Johnson Space Center, websites, software, and vehicle weight statements from other flown vehicles. The Delta IV values used for the LOI burn and the Landing burn were 3609 ft/sec and 6562 ft/sec. The LCL constraints, which is decided by what can fit in the payload of the Delta-IV Heavy, for the mass was 21,197 lbm and for the size was based upon the dimensions shown in the figure below:



The research then continued on into the type of engines that would be used for the propulsion system. For the Main Propulsion System (MPS), the cryogenic engine and the hypergolic engine were designed for the LCL in order to compare the results of the two types of engines. For the other main components of the spacecraft sub-system, which includes the Reaction Control System (RCS), Legs, Guidance, Navigation and Control (GNC), Telecommunications (Comm), Command and Data Handling (CDH), Thermal (Th), Electrical Power (EP), and Structure and Mechanisms (SM), the mass, volume, and surface area were scaled off of the Apollo Lunar Module, Clementine, Lunar Schooner, Surveyor, Orbital Maneuvering Vehicle, and Prospector.

### **Engine Alternatives**

The cryogenic system uses an engine that is fed liquid oxygen (LO<sub>2</sub>) as its oxidizer and liquid hydrogen (LH<sub>2</sub>) as its fuel. This system produces a higher performance, but oxidizer and fuel must be kept at cryogenic temperatures of -270°F and -430°F. Two specific engines were chosen for the cryogenic system. The first engine is a Pratt&Whitney RL 10B-2, which supplies a thrust of 24,750 lbf, an Isp of 465.5 sec, a mass of 610 lbm, and an oxidizer fuel ratio of 5.88. The second engine is a Pratt&Whitney RL 10A3-3A, which supplies a thrust of 16,500 lbf, and an Isp of 444.4 sec, a mass of 310 lbm, and an oxidizer fuel ratio of 5.88. The RL 10A3-3A was given consideration since the vehicle weight when it is approaching the moon will be around 9,000 lbm, which does not need the amount of thrust that is supplied by the RL 10B-2. The RL 10A3-3A is also 300 lbm less than the RL 10B-2. Therefore, both engines were considered even though the RL 10B-2 has a higher Isp.

The hypergolic system uses an engine that is fed dinitrogen tetroxide (N<sub>2</sub>O<sub>4</sub>) as its oxidizer and monomethylhydrazine (MMH) as its fuel. The system produces a lower performance, but the fuel and oxidizer are storable and reliable. One engine was chosen for the hypergolic system, which is the Rocketdyne RS-72. The RS-72 supplies a thrust of 12,500 lbf, an Isp of 338 sec, a mass of 340 lbm, and an oxidizer fuel ration of 2.08.

## **Lunar Cargo Lander Excel Sheets**

After all of the data was found, two excel sheets were created to estimate the amount of usable payload that the Lunar Cargo Lander (LCL) could put on the moon. One excel sheet controls the hypergolic system while the other is set up for the cryogenic system. Both sheets have the same format, but the cryogenic sheet is set up to have a bigger thermal sub-system because of the cryogenic temperatures. The input needed to run the sheet is mass before LOI burn (mass initial), delta V for the LOI and Landing burn, Engine specifications (Isp, Oxidizer/Fuel Ratio, and Thrust), and Tank specifications (for fuel, oxidizer, and pressure chemical: ullage, density, tank diameter). The excel sheet then outputs the following general information: mass after LOI burn, MPS propellant used for LOI burn, mass before Landing burn, MPS propellant used for Landing burn, mass flow rate, LOI burn time, Landing burn time, Propellant total for MPS and RCS, Landing weight, weight of Spacecraft sub-systems, usable Payload landed on the moon. The input also feeds the calculation of all components of the propulsion system by derived equations to give its mass, volume, surface area, and height. The components of the propulsion system that are listed are the tanks for MPS and RCS and the tank's insulation, anti-vortex, slosh add-in, and engine insulation. The input also feeds the calculation of the propellant used for the MPS and RCS system. The mass estimation for the landing gear is scaled off of the Lunar Module and Surveyor. The mass for GNC, Comm, CDH, EP are scaled off of Clementine and Prospector. The mass estimation for the Thermal sub-system is scaled off of the Orbital Maneuvering Vehicle. The mass estimation for the Structure and Mechanism sub-system used several vehicles to scale from including the Lunar Module, OMV, Surveyor, and Clementine. The figure below shows a part of the mass estimating relation page:

<b>Spacecraft Sub-system</b>	<b>2937.44</b>				
<b>Propulsion</b>	<b>794.18</b>				
<b>MPS</b>		730.18			
-Engine			349.84		
--Boeing RS 72 (1)			340.00	website	
--insulation			9.84	intros	
-Tanks (cylinder) (contains MPS & RCS fuel)		288.24			
--MMH tank			102.70	calculated and intros	
--MMH insulation			11.62	calculated and intros	
--MMH antivortex			1.65	calculated and intros	
--N2O4 tank			122.96	calculated and intros	
--N2O4 insulation			13.38	calculated and intros	
--N2O4 antivortex			3.18	calculated and intros	
--N2O4 slosh			0.79	calculated and intros	
--Helium tank			23.32	calculated	
--Helium insulation			3.65	calculated	
--metal bladders for MMH&N2O4 tank			5.00	Clementine	
-Valves,pipes,plumbing,fitting			92.10	OMV	
<b>RCS</b>		64.00			
-Thrusters (16)			64.00	Clementine	
<b>Landing Gear</b>	<b>162.00</b>				
-Leg (4)		162.00		LM	
<b>CNC</b>	<b>12.12</b>				

### Lunar Cargo Lander Excel Sheet – Future Work

Future work will include adding the same features that the Propulsion sub-system has to all of the other spacecraft sub-systems, which includes deriving formulas to estimate the mass, volume, and dimensions for all sub-components featured in the spacecraft sub-system. Future work will also include the flexibility to have list boxes to choose if it is a hypergolic system or cryogenic system, lists of engines, and lists for choosing fuels, oxidizers, and substance used for pressure-fed system. The ability to choose different sub-components for each sub-system will also be looked into. Power consumption and Cost estimating relations will also be added. The goal is to have a program that can have the ability to create an initial design for any launch vehicle needed to go from TLI to the moon.

### Cryogenic and Hypergolic Mass Comparison

The Lunar Cargo Lander Excel Sheet was used to compare the cryogenic system with two different engines and the hypergolic system. The main emphasis of the sheet is to find out how much actual payload can be put on the moon based on the delta IV-Heavy transporting the LCL to TLI. The results were as follows:

	<b>Cryogenic</b>		<b>Hypergolic</b>
<b>Engine</b>	<b>RL10 B2</b>	<b>RL10 A3-3A</b>	<b>RS-72</b>
<b>Propulsion</b>	1422.15	1131.27	804.05
<b>LG</b>	196.94	179.68	165.23
<b>GNC</b>	44.1	44.1	42.42
<b>Comm</b>	52	52	50.14
<b>CDH</b>	52.7	52.7	50.69
<b>Thermal</b>	266.6	266.6	238.42
<b>EP</b>	165.7	165.7	158.67
<b>S&amp;M</b>	1316.55	1316.55	1440.93
<b>Total Sub-system</b>	3516.73	3208.6	2950.54
<b>Propellant</b>	11081.95	11437.11	13611.56
<b>Payload</b>	<b>7401.35</b>	<b>7354.28</b>	<b>5437.9</b>

The comparison shows that the cryogenic system will put approximately 2,000 pounds more usable payload on the moon; however, the hypergolic system is more reliable. When the cost estimation relation is added on, the best system will be chosen. As for now, the best system is obviously the cryogenic model, which also gives the ability to use the liquid hydrogen and liquid oxygen residuals as water if needed.

### **Analysis of 10% changes to the initial mass and delta V for LOI and Landing**

For this analysis, the excel sheet gives the min and max for the following:

	<b>min</b>	<b>max</b>
<b>LOI burn time</b>	138.18	189.52
<b>Landing burn time</b>	161.32	228.63
<b>Sub-system Weight</b>	2906.17	2963.67
<b>Propellant</b>	11049.22	14385.13
<b>Payload on moon</b>	3620.65	6301.86

These values give a range of min and max for the burn times, sub-system weight, propellant used, and usable payload that will be landed on the moon. This analysis shows the range that the possible payload could put on the moon for a hypergolic system if major adjustments are needed during actual creation of the vehicle.

### **Historical Comparison**

A comparison between the sub-systems of the Lunar Cargo Lander and other flown vehicles was also studied. The Surveyor and Apollo Lunar Module were studied closely

since they were both lunar landers. The LCL's sub-systems for propulsion, landing gear, thermal, and structure and mechanics have nearly the same overall percentage of dry weight for each of those sub-systems as the LM and the Surveyor; therefore, it shows that the scaling for those sub-systems can be verified at an initial design level. The LCL's sub-systems for guidance, navigation, and control, electrical power, telecommunications, and command and data handling have a smaller overall percentage of dry weight for each of the sub-systems as compared to the Clementine, Prospector, and Lunar Schooner; however, the percentage is less than those vehicles because the electronics has a step increase thus allowing a larger vehicle like the Lunar Cargo Lander to have the same weight for the electronics as the smaller vehicles of Clementine and Prospector.

### **Using other Launch Vehicles**

Other launch vehicles were looked at to see if there is a better option to carry the LCL to TLI than the Delta-IV Heavy. The Titan III was discovered to not be a possibility due to its inability to have a large enough payload bay to carry the LCL. The Ariane 5 and the Atlas V (500 series) was discovered to allow the LCL to land around 3,900 lbm on the moon for a scaled down model of the LCL. The Delta IV-Heavy enables a larger payload to be put on the moon, but cost estimation is needed in order to accurately say which one of the three is the best option.

### **CAD Designs**

Three Cad models were developed. Two models were created for the cryogenic system. One design has the payload on top of the sub-systems with a ladder to it for the astronauts to climb up to get what is in there. The other design has the payload folding down on the side of the Lunar Cargo Lander so that access to the payload will be much easier. Entry doors will be on the sides allowing the astronauts to have walk-in access. The hypergolic system has the payload contained on the sides sitting next to the sub-systems allowing the same walk-in access. Detailed cad designs are one of the areas future work will focus on.

### **Conclusions**

The Delta IV-Heavy will transport the Lunar Cargo Lander to TLI where the LCL will transport 5,400 lbm of usable payload using a hypergolic system and 7,400 lbm of usable payload using a cryogenic system from TLI to the moon.

### **Acknowledgements**

The authors would like to thank Mr. Bill Pannell, Mr. Bert Dolerhie, Mr. Geoffrey Beech, and all personnel in Engineering Directorate for providing a quiet but stimulating work environment and support.

## References

1. George P. Sutton. Rocket Propulsion Elements: Sixth Edition. John Wiley & Sons, Inc. 1992.
2. James R. Wertz and Wiley J. Larson. Space Mission Analysis and Design. Microcosm Press and Kluwer Academic Publishers. 1999.
3. Delta IV Payload Planner's Guide Version Nov 2002.

2004

NASA FACULTY FELLOWSHIP PROGRAM

MARSHALL SPACE FLIGHT CENTER

THE UNIVERSITY OF ALABAMA  
THE UNIVERSITY OF ALABAMA IN HUNTSVILLE  
ALABAMA A&M UNIVERSITY

**COUPLED ELECTROMAGNETIC RESONATORS FOR  
ENHANCED COMMUNICATIONS AND TELEMETRY**

Prepared By:	Dr. John O. Dimmock
Academic Rank:	Professor
Institution and Department:	The University of Alabama in Huntsville Department of Physics
NASA/MSFC Directorate:	Science
MSFC Colleague:	Dr. David D. Smith

## 1. Introduction

Future NASA missions will require the collection of an increasing quantity and quality of data which, in turn, will place increasing demands on advanced sensors and advanced high bandwidth telemetry and communications systems. The capabilities of communication and telemetry systems depend, among other factors, on the stability, controllability and spectral purity of the carrier wave. These, in turn, depend on the quality of the oscillator, or resonator, or the Q of the system. Recent work on high Q optical resonators has indicated that the Q, or quality factor, of optical microsphere resonators can be substantially enhanced by coupling several such resonators together.<sup>1-3</sup> In addition to the possibility of enhanced Q and increased energy storage capacity, the coupled optical resonators indicate that a wide variety of interesting and potentially useful phenomena such as induced transparency and interactive mode splitting can be observed depending critically on the morphology and configuration of the microresonators. The purpose of this SFFP has been to examine several different coupled electromagnetic oscillator configurations in order to evaluate their potential for enhanced electromagnetic communications.

## 2. Coupled LRC circuits

The first such configuration examined was that of three capacitively coupled LRC circuits as shown in Figure 1.

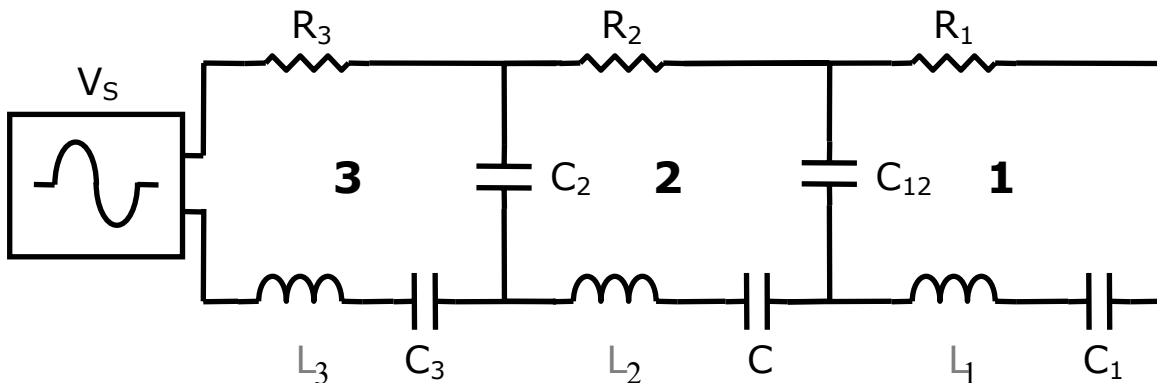


Figure1 Circuit diagram for three capacitively coupled LRC circuits

In this configuration a driving oscillator, connected to circuit 3, produces a voltage input designated as  $V_S$ . A general analysis of the voltages and currents in the three circuits was derived for arbitrary values of the inductances  $L_1$ ,  $L_2$ , and  $L_3$ , resistances,  $R_1$ ,  $R_2$ , and  $R_3$ , circuit capacitances,  $C_1$ ,  $C_2$ , and  $C_3$ , and circuit-to-circuit coupling capacitances  $C_{12}$ , and  $C_{23}$ . It was determined that when the inductances and capacitances are adjusted so that the resonant frequencies of the three individual circuits are the same the coupled circuit displays three separate resonances, one at the common resonant frequency and one higher and one lower frequency split-off resonance. Figure 2 shows the stored energy in each of the three circuits as a function of oscillator frequency for a given selection of circuit parameter values.

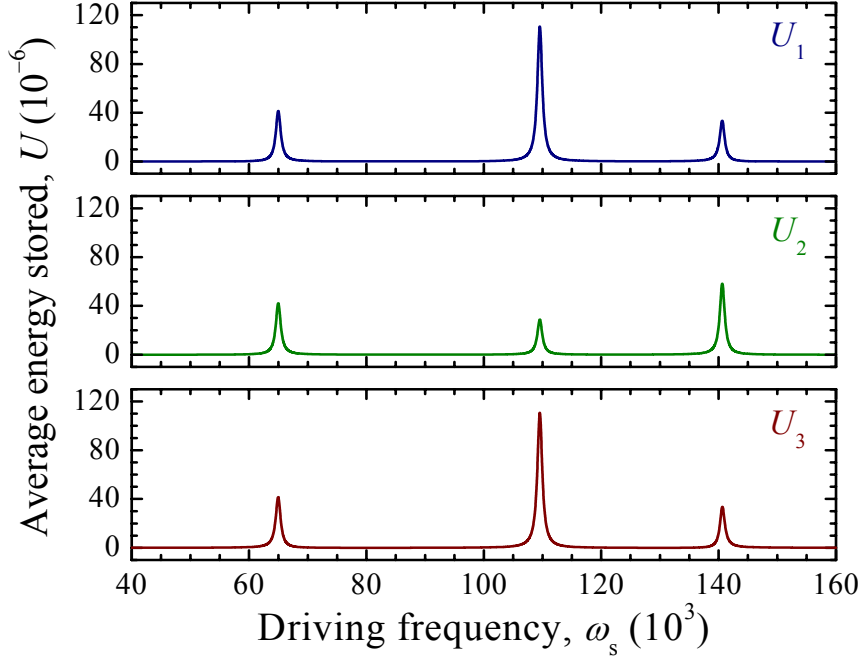


Figure 2 Energy, in micro-Joules, stored in each of the three coupled LRC circuits as a function of the oscillator frequency,  $\omega_s$ , in Hz, for the following values of the circuit parameters:  $L_1 = L_2 = L_3 = 1$  mH,  $R_1 = R_2 = R_3 = 1$   $\Omega$ ,  $C_1 = 1/6.5$   $\mu$ F,  $C_2 = 1$   $\mu$ F,  $C_3 = 1/6.5$   $\mu$ F,  $C_{12} = 1/5.5$   $\mu$ F, and  $C_{23} = 1/5.5$   $\mu$ F and a driving voltage of 1 V RMS.

Figure 2 clearly shows this resonance splitting. The upper, middle and lower figures show respectively the average energy stored in circuits 1, 2, and 3 as a function of frequency. The central resonance is at the common circuit frequency which for the chosen circuit parameters is 109.54 kHz. For the same values of L and R a single LRC circuit tuned to any of the three frequencies shown, driven with 1 V RMS would store 500  $\mu$ J of energy, considerably larger than that of any of the three circuits at any resonance. A single circuit would have a Q of  $\omega L/R$  which at the center frequency is 109.45. In the present case where we have chosen  $L_1 = L_2 = L_3$  and  $R_1 = R_2 = R_3$  the Q of all three resonances of the three coupled circuits will also be given by  $\omega L/R$  and will thus be the same as that of a single circuit at each of those frequencies. If the L/R ratios for the three circuits are different, the Q values for the coupled circuit resonances will always be smaller than that of a single circuit with the largest value of L/R. If  $\omega_{11}$ ,  $\omega_{22}$ , and  $\omega_{33}$  are the resonant frequencies of the individual circuits given by

$$\omega_{11}^2 = \frac{1}{L_1} \left( \frac{1}{C_1} + \frac{1}{C_{12}} \right), \quad \omega_{22}^2 = \frac{1}{L_2} \left( \frac{1}{C_2} + \frac{1}{C_{12}} + \frac{1}{C_{23}} \right), \quad \omega_{33}^2 = \frac{1}{L_3} \left( \frac{1}{C_3} + \frac{1}{C_{23}} \right) \quad (1)$$

and

$$\omega_{12}^4 = \frac{1}{L_1 L_2 C_{12}^2}, \quad \text{and} \quad \omega_{23}^4 = \frac{1}{L_2 L_3 C_{23}^2} \quad (2)$$

are the resonant frequencies associated with the coupling capacitors, the resonant frequencies of the three coupled circuits are given by

$$(\omega_{11}^2 - \omega^2)(\omega_{22}^2 - \omega^2)(\omega_{33}^2 - \omega^2) = (\omega_{11}^2 - \omega^2)\omega_{23}^4 + (\omega_{33}^2 - \omega^2)\omega_{12}^4. \quad (3)$$

The sum of the three solutions to equation 3 are related to the three individual resonant frequencies by

$$\sum_i \omega_i^2 = \omega_{11}^2 + \omega_{22}^2 + \omega_{33}^2. \quad (4)$$

Similarly, if we designate the loss factors for the three separate circuits by  $\gamma_{11}$ ,  $\gamma_{22}$ , and  $\gamma_{33}$ , then the loss factors for the three resonances are related to those of the individual circuits by

$$\sum_i \gamma_i = \gamma_{11} + \gamma_{22} + \gamma_{33}, \quad (5)$$

where  $\gamma_{ii} = R_i/L_i$ .

It can also be readily shown that the three loss factors,  $\gamma_i$ , all lie between the minimum and maximum values of the  $\gamma_{ii}$ . Therefore none of the resonances of the three coupled LRC circuits will have a loss factor less than that of the value for the least lossy of the individual circuits, and thus the coupled circuits will not have a Q larger than that of the highest Q individual circuit. In addition, it can be shown that the sum of the total energy that can be stored in all three circuits together at all three resonant frequencies is equal to the energy that can be stored in a single circuit with the same values of L and R. Figure 3 is a plot of the stored energy in each of the three coupled circuits as a function of the coupling capacitance keeping the center frequency constant.

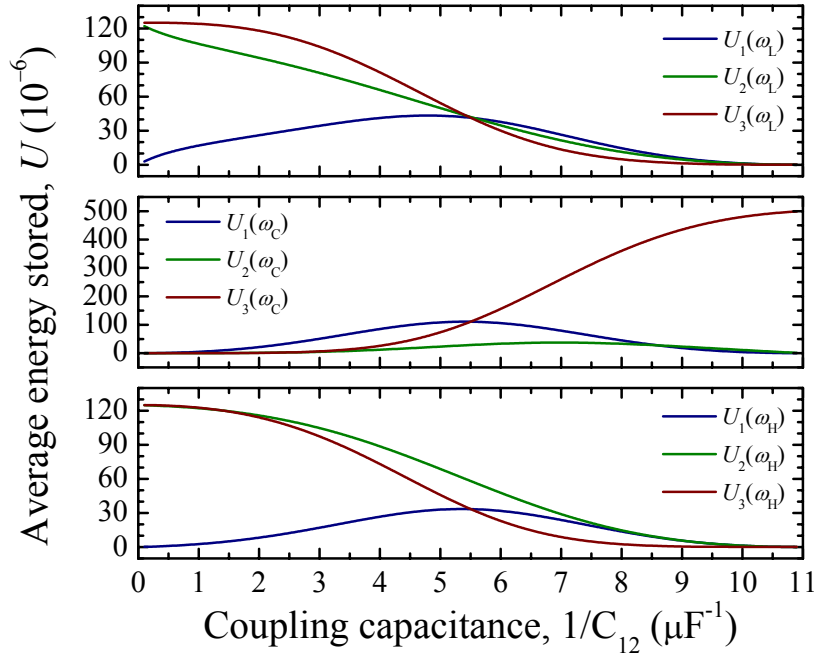


Figure 3 Plot of the energy stored in each of the three coupled circuits as a function of the coupling capacitance with the center frequency held constant. The parameters are the same as in Figure 2 except that  $1/C_{12}$  is allowed to vary keeping  $(1/C_{12} + 1/C_{23})$  constant at the value of Figure 2.

The upper, middle and lower plots in Figure 3 show the stored energy in each of the three circuits at the lowest, center and highest resonant frequencies respectively. (The plot shown in Figure 2 corresponds to a coupling capacitance in the middle of Figure 3.) Figure 3 shows that for small values of  $1/C_{12}$ , which correspond to large values of  $1/C_{23}$ ,

more energy is stored in circuits 2 and 3 than in circuit 1. This can be understood if one considers that the strength of the coupling between the circuits is proportional to the inverse of the respective coupling capacitances. Thus the left hand side of Figure 3 corresponds to strong coupling between circuits 3 and 2 but weak coupling between circuits 2 and 1. Thus one would expect that the bulk of the energy would be concentrated in circuits 3 and 2 as seen in Figure 3. Furthermore it is seen that there is virtually no energy in the central resonance at low values of  $1/C_{12}$ . In this region of the plot the tri-circuit configuration is behaving as though there were only two circuits connected and circuit 1 is effectively isolated. When two circuits are coupled the resonance splits into two, one at higher and one at lower frequency than that of the original circuits. This is exactly what is happening here. Similarly the right hand side of Figure 3 corresponds to weak coupling between circuits 3 and 2 but strong coupling between circuits 2 and 1. Thus on the right hand side of Figure 3 all of the energy is stored in circuit 3, which is behaving like a single circuit with a resonance at the center frequency. Very little is coupled to circuits 2, and 1 and all of the energy is in the center frequency resonance.

Figure 4 is a plot of the total energy stored in all three coupled circuits as a function of the coupling capacitance. Figure 4 shows that the total energy that can be stored in all of the coupled circuits together at all frequencies together is independent of the coupling capacitances and equal to 500  $\mu\text{J}$ , which is that of a single circuit with the same loss factor as the individual coupled circuits.

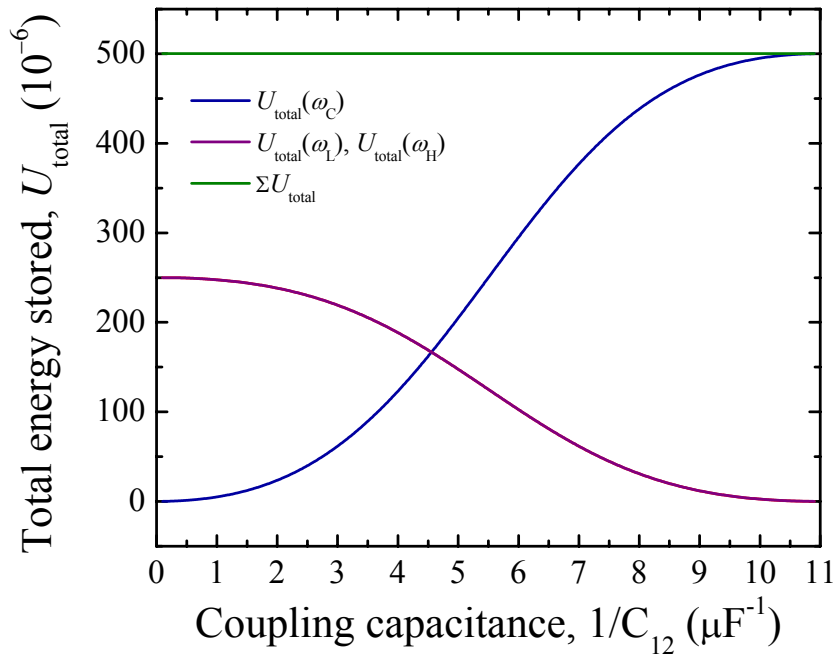


Figure 4 Total energy stored in all three coupled circuits as a function of the coupling capacitance and the sum of these for the three resonant frequencies.

Again Figure 4 shows that when the coupling between circuits 1 and 2 is weak, and the coupling between circuits 2 and 3 is strong, left hand side of Figure 4, virtually all of the energy, which is concentrated in circuits 2, and 3, is in the higher and lower split-off resonances with very little in the center frequency. Likewise at the right hand

side of Figure 4 where the coupling between circuit 3 and circuit 2 is weak, all of the energy is in circuit 3 and at the center frequency appropriate for a single circuit.

The conclusion of this section of the work is that although coupled LRC RF circuits evidence a splitting of the resonant frequency into as many branches as there are coupled circuits no enhancement in energy storage capacity or improvement in Q occurs. We have already seen that such enhancements and improvements do occur in the case of coupled ring resonators<sup>1-3</sup>.

### 3. Coupled optical resonators

The next investigation undertaken was that of coupled optical Fabry-Perot cavities and optical ring resonators. The mathematical analysis of the Fabry-Perot and optical ring resonator situations is essentially identical. In the following we will refer to these generically as coupled optical resonators, dropping the distinction. The principal difference between coupled optical resonators and coupled LRC circuits is that the wavelength of the oscillation can not be ignored in the case of the optical resonators while it can be, and is, ignored in the case of the RLC circuits. All dimensions in the LRC circuit are considered to be small compared to the wavelength of the resonant frequency. In the above case that wavelength is approximately 3 km. So long as this is very large compared to dimensions of the circuits the analysis should be valid. In the case of the optical resonators the element dimensions are comparable to the wavelength of the oscillation and the resonator dimensions as well as the other resonator parameters will control the behavior of the coupled elements. Figure 5 is a representation of three coupled Fabry-Perot structures.

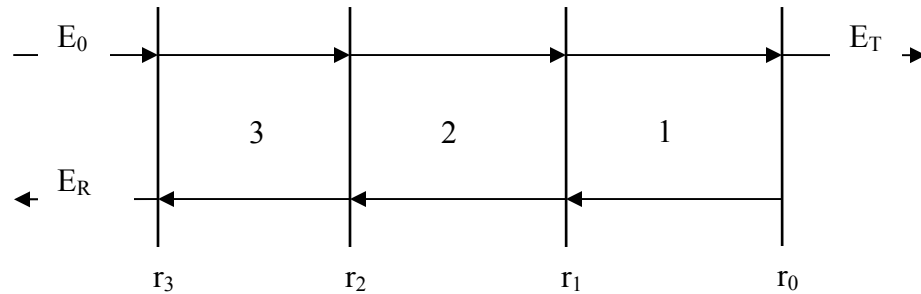


Figure 5 Diagram of triply coupled Fabry-Perot cavities

In Figure 5 electromagnetic energy is incident from the left as  $E_0$ . A portion of that energy is reflected from mirror 3, with reflectance  $r_3$ , as  $E_R$  and a portion transmitted to mirror 2 and so forth. If none of the mirrors are perfectly reflecting there will be transmitted energy represented as  $E_T$ . The analysis of coupled Fabry-Perot structures, as the one shown in Figure 5, must take into account not only the magnitude and phase of the reflected and transmitted energy at each mirror but also the optical path length of each cavity. The analysis proceeds virtually identically to that in reference 1 for the ring resonators. The following analysis applies to coupled optical ring resonators as well as to coupled Fabry-Perot resonators and we will adopt the language of the optical resonators.

The analysis pertains to the Fabry-Perot coupled resonators as well. In the following we will emphasize the differences between this work and that of reference 1 as well as our conclusions.

The first difference between this work and that of reference 1 is that the optical reflection coefficients are allowed here to be complex whereas in reference 1 they are considered to be real. In general one can write the complex reflection and transmission coefficients as  $r = r_0 e^{i\phi_r}$  and  $t = t_0 e^{i\phi_t}$ . An analysis of the reflection determines that  $r$  and  $t$  can be written as

$$r = r_0^2 \pm ir_0 \cdot t_0 \quad \text{and} \quad t = t_0^2 \mp it_0 r_0 \quad (6)$$

where  $r_0$  and  $t_0$  are real and positive. It is easy to show from this that

$$\phi_t = \phi_r \pm \pi/2. \quad (7)$$

In reference 1,  $\phi_r$  is set equal to 0, and  $\phi_t = \pi/2$  so equation 7 is preserved but  $r$  is considered to be real. Fortunately one can absorb the phase shift of the reflections in the phase related to the cavity optical path length so that none of the results in reference 1 are negated so long as one remembers that these phase shifts are included in the path lengths. In the remainder of this report we will follow the notation in reference 1 in which  $r$  and  $t$  are real and the relationship expressed in equation 7 is incorporated directly in the equations.

The second difference is that reference 1 considered primarily optical cavities of the same size and thus the same phase shift. This results in a large splitting of the optical cavity modes, similar to the case of the coupled LRC circuits, which is a major conclusion of reference 1. Reference 1 also examined the amplification, or magnification, of the optical energy which can occur when multiple cavities are appropriately coupled. This result represents a significant difference between coupled optical cavities and coupled LRC circuits where no such magnification is observed. However, because only coupled cavities with the same phase shift were considered, reference 1 observes somewhat limited enhancement in the cavity resonance  $Q$  and energy storage capacity particularly for even numbers of coupled cavities. It was determined in this work that higher  $Q$  and larger energy storage can be achieved by introducing a  $\pi$  phase shift between the cavities. Nevertheless it was also determined that  $Q$  and energy storage is still largest for a single optical cavity provided that optimum cavity size and coupling reflectivity can be achieved. However, in the case where these optimum factors can not be achieved it may be possible to achieve larger energy storage in coupled cavities and a larger  $Q$  than can be achieved in a single cavity. This is another, and quite significant, difference between the results of the analysis on coupled optical resonators and LRC circuits.

We will start with the analysis of a single optical resonator. Consider in Figure 5 that the configuration consists of a single cavity, sections 3 and 2 don't exist, and that  $r_0=1$  so no energy is transmitted. The ratio of the optical power stored in cavity 1 to the incident power is given by

$$M_{11} = \frac{t_1^2 a_1^2}{(1 - r_1 a_1)^2 + 4r_1 a_1 \sin^2\left(\frac{\phi_1}{2}\right)} \quad (8)$$

where  $t_1$  is the transmission and  $r_1$  is the reflectance of the first mirror,  $a_1$  represents the possible loss in the first cavity,  $a_1 = 1$  for a lossless cavity, and  $\phi_1$  is the round-trip phase change in the cavity. The maximum energy stored occurs at the maximum value of  $M_{11}$  which occurs at  $\phi_1 = \pi n$ . In this case

$$M_{11\max} = \frac{(1-r_1^2)a_1^2}{(1-r_1a_1)^2} \quad (9)$$

and

$$Q_{11} = \frac{\sqrt{r_1a_1}}{(1-r_1a_1)} \quad (10)$$

where  $t_1^2 = 1-r_1^2$ . If the value of  $r_1$  can be adjusted, the optimum values of  $M_{11}$  and  $Q_{11}$  are obtained when  $r_1 = a_1$ . In this case

$$M_{11\text{opt}} = \frac{a_1^2}{(1-a_1^2)} \quad (11)$$

and

$$Q_{11\text{opt}} = \frac{a_1}{(1-a_1^2)}. \quad (12)$$

It turns out that this is the best that can be done when the magnification and  $Q$  factors are limited purely by the cavity losses. If, however, the limitation is due in part to a limited reflectivity then enhanced magnification and improved  $Q$  can be obtained through the use of multiple cavities. This is shown quite convincingly in reference 1. Reference 1 shows that greatly enhanced values of magnification can be achieved particularly for odd numbers of coupled resonators. This is due to the fact that reference 1 considers zero phase difference in the optical path lengths of the coupled cavities.

In the present work we will consider two coupled cavities as basically most of the effects can be seen in this configuration. In this case simply consider that cavity 3 in Figure 5 is missing and again that  $r_0 = 1$ . For two cavities equation 8 becomes rather more complicated. Considering the magnification achieved in cavity 1 of a two-cavity coupled system one obtains, instead of equation 8

$$M_{21} = \frac{t_2^2 t_1^2 a_2 a_1^2}{A + B \sin^2\left(\frac{\phi_1}{2}\right) + C \sin^2\left(\frac{\phi_2}{2}\right) + D \sin^2\left(\frac{\phi_1 + \phi_2}{2}\right) + E \sin^2\left(\frac{\phi_1 - \phi_2}{2}\right)} \quad (13)$$

where

$$\begin{aligned} A &= [(1-r_1a_1) + r_2a_2(a_1-r_1)]^2 \\ B &= 4r_1a_1(1+r_2^2a_2^2) \\ C &= 4r_1r_2a_2(1+a_1^2) \\ D &= -4r_2a_2a_1 \\ E &= -4r_1^2r_2a_1a_2 \end{aligned} \quad (14)$$

For the magnification achieved in cavity 2 of a two-cavity coupled system we obtain

$$M_{22} = \frac{t_2^2 a_2^2 \left[ (a_1 - r_1)^2 + 4r_1 a_1 \sin^2\left(\frac{\phi_1}{2}\right) \right]}{A + B \sin^2\left(\frac{\phi_1}{2}\right) + C \sin^2\left(\frac{\phi_2}{2}\right) + D \sin^2\left(\frac{\phi_1 + \phi_2}{2}\right) + E \sin^2\left(\frac{\phi_1 - \phi_2}{2}\right)} \quad (15)$$

For  $\phi_2 = \phi_1$  equations 13 and 15 simplify somewhat. Figures 6 and 7 are plots of the values of  $M_{21}$  and  $M_{22}$  as functions of  $\phi_1$ , where  $\phi_2 = \phi_1$ , showing the expected resonance splitting. The magnitude of this splitting is a function of the various cavity parameters.

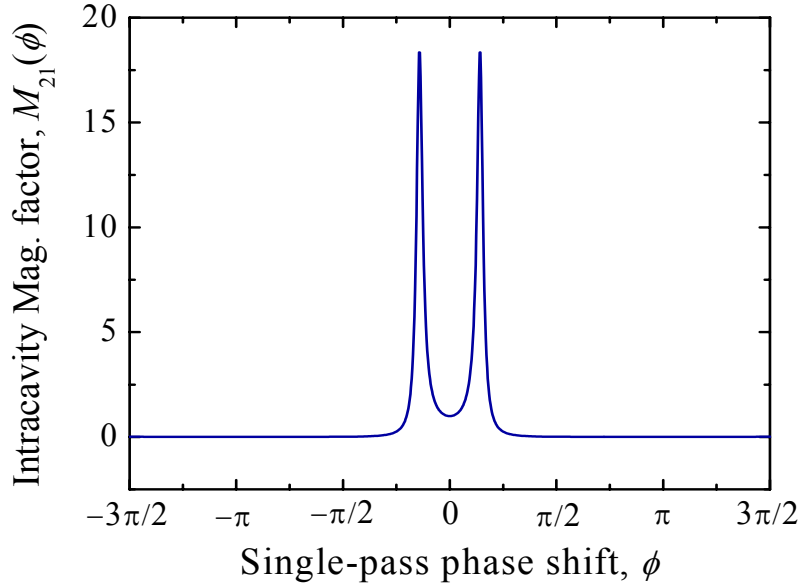


Figure 6 Value of  $M_{21}$  versus  $\phi_1$  for  $\phi_2 = \phi_1$ . In this plot we have used  $r_1 = r_2 = 0.9$ , and  $a_1 = a_2 = 0.999$ .

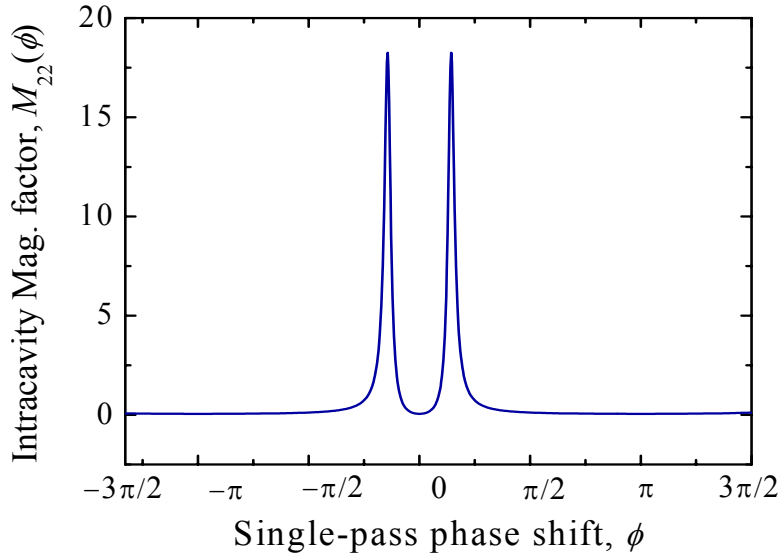


Figure 7 Value of  $M_{22}$  versus  $\phi_1$  for  $\phi_2 = \phi_1$  and the same parameters as in Figure 6

The magnitude of the phase shift is given by

$$\cos\phi = \frac{r_1(a_1 + r_2 a_2)(1 + r_2 a_2 a_1)}{4r_2 a_1 a_2} \quad (16)$$

As the right hand side of equation 16 approaches 1 with increasing values of reflectance, the two resonances merge into one at  $\phi = 2\pi n$ . For larger values the resonance remains at  $\phi = 2\pi n$ . In this situation  $M_{21}$  becomes

$$M_{21\max} = \frac{t_1^2 t_2^2 a_1^2 a_2}{[(1 - a_1 r_1) + a_2 r_2 (a_1 - r_1)]^2} \quad (\text{for } \phi_2 = \phi_1). \quad (17)$$

Again we can examine the optimum value of  $M_{21}$  by maximizing with respect to  $r_2$  and  $r_1$ . This results in  $r_1 = a_1$  and  $r_2 = 0$  in which case

$$M_{21\text{opt}} = \frac{a_2 a_1^2}{(1 - a_1^2)} = M_{11\text{opt}} \cdot a_2. \quad (18)$$

Since  $a_2 \leq 1$   $M_{21\text{opt}} \leq M_{11\text{opt}}$ . Furthermore if we ignore cavity losses by setting  $a_1$  and  $a_2$  equal to one, equation 17 becomes

$$M_{21\max} = \frac{(1 + r_1)}{(1 - r_1)} \cdot \frac{(1 - r_2)}{(1 + r_2)} \quad (\text{for } \phi_2 = \phi_1) \quad (19)$$

whereas for the single circuit, under the same circumstances we would have

$$M_{11\max} = \frac{(1 + r_1)}{(1 - r_1)}. \quad (20)$$

This is the same result as that obtained in reference 1 where the ratios continue to invert from cavity to cavity so that, for example

$$M_{31\max} = \frac{(1 + r_1)}{(1 - r_1)} \cdot \frac{(1 - r_2)}{(1 + r_2)} \cdot \frac{(1 + r_3)}{(1 - r_3)} \quad (\text{for } \phi_2 = \phi_1) \quad (21)$$

etc. It should be noted, however, from equations 11 and 18, that the optimized magnification for the lossless case is infinite.

If we do not set  $\phi_1 = \phi_2$  we get different results. For example, if we set  $\phi_2 = \phi_1 + \pi$  and plot equations 13 and 15 versus  $\phi_1$ , we get the results shown in Figures 8 and 9 using otherwise the same cavity parameters as in Figures 6 and 7. In this case we see that for  $M_{21}$  and  $M_{22}$  there is no splitting of the resonance and that the magnitude of the  $\phi_1 = 0$  resonance for  $M_{21}$  in Figure 8 is considerably larger than that of the split resonances in Figure 6. For  $\phi_2 = \phi_1 + \pi$  the expression for  $M_{21\max}$  in equation 17 is changed to

$$M_{21\max} = \frac{t_1^2 t_2^2 a_1^2 a_2}{[(1 - a_1 r_1) - a_2 r_2 (a_1 - r_1)]^2} \quad (\text{for } \phi_2 = \phi_1 + \pi) \quad (22)$$

and the expression for  $M_{22\max}$  in equation 19 is changed to

$$M_{22\max} = \frac{t_2^2 a_2^2 (a_1 - r_1)^2}{[(1 - a_1 r_1) - a_2 r_2 (a_1 - r_1)]^2} \quad (\text{for } \phi_2 = \phi_1 + \pi) \quad (23)$$

Note that the only change is in the sign of  $a_2 r_2$  which, however, as we will see, makes a big difference. Nevertheless, if we again optimize  $M_{21\max}$  by maximizing with respect to  $r_1$  and  $r_2$  we get the same results as we did for equation 17, namely equation 18 and a

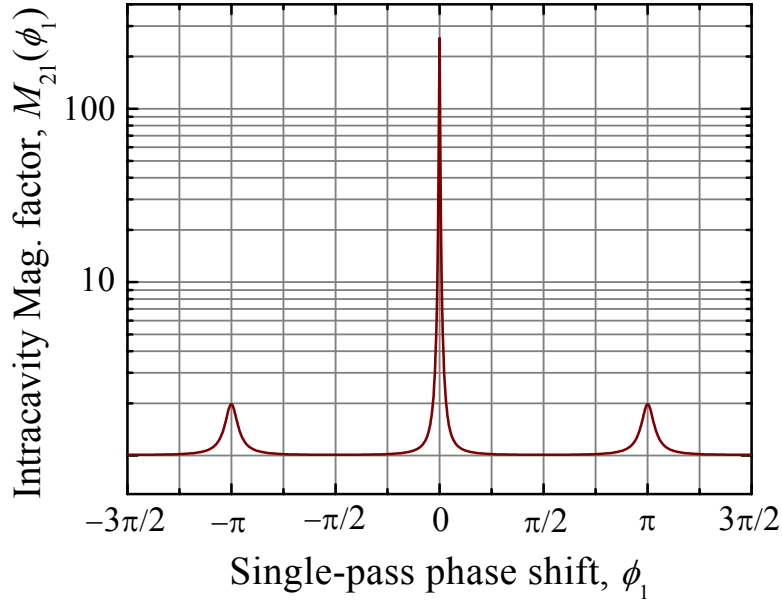


Figure 8. Value of  $M_{21}$  versus  $\phi_1$  for  $\phi_2 = \phi_1 + \pi$  using otherwise the same cavity parameters as in Figure 6 Note that Figure 8 is plotted on a log scale with 1 added so as to avoid the  $-\infty$  for  $M_{21\max} = 0$ .

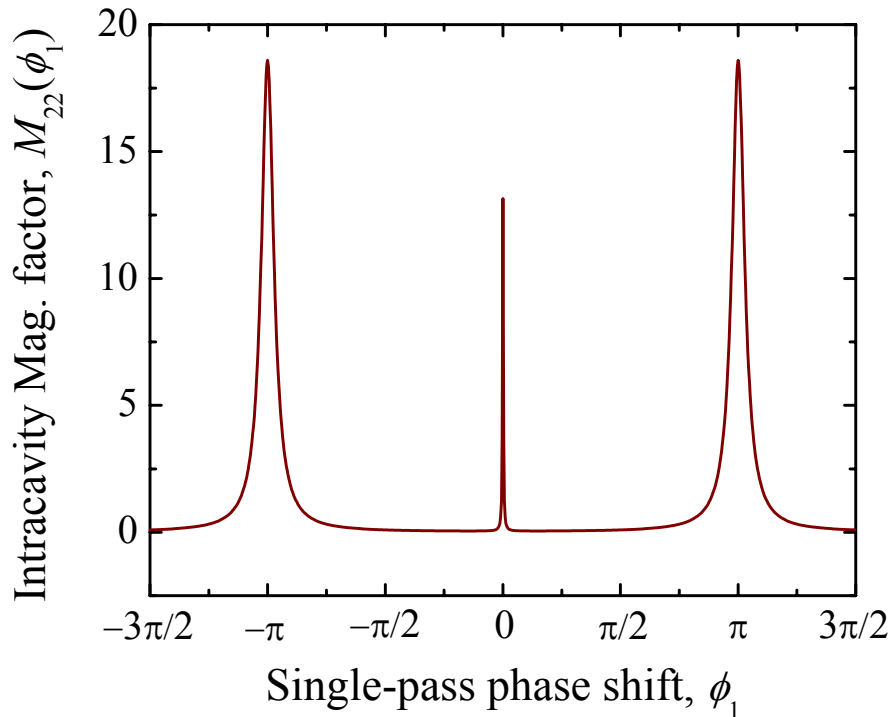


Figure 9. Value of  $M_{22}$  versus  $\phi_1$  for  $\phi_2 = \phi_1 + \pi$  using otherwise the same cavity parameters as in Figure 6

single circuit is still superior. However, the results for the lossless case with limited  $r_1$  and  $r_2$  are significantly different. Equation 22 becomes

$$M_{21\max} = \frac{(1+r_1)}{(1-r_1)} \cdot \frac{(1+r_2)}{(1-r_2)} \quad (\text{for } \phi_2 = \phi_1 + \pi) \quad (24)$$

and equation 23 becomes

$$M_{22\max} = \frac{1+r_2}{1-r_2}. \quad (\text{for } \phi_2 = \phi_1 + \pi) \quad (25)$$

Each additional cavity adds to the magnification of  $M_{21\max}$  if this relative phase relation is continued.

We can use equations 22 and 23 to calculate the values of  $M_{21\max}$  and  $M_{22\max}$ . This results in  $M_{21\max} = 254.63$  and  $M_{22\max} = 13.13$  in good agreement with Figures 8 and 9. These can be compared to  $M_{11\max} = 18.64$  given by equation 9 and the same parameters. If instead we were to use the lossless equations 24 and 25 we would obtain  $M_{21\max} = 361$  and  $M_{22\max} = 19$  and equation 11 gives  $M_{11\max} = 19$ .

As can be seen, the magnification is greatly enhanced by the addition of a second resonant cavity so long as the parameters are not optimized. It is also useful to determine the effect the addition of a second cavity has on the quality factor,  $Q$ . Examination of Figures 8 and 9 indicate that  $Q$  can be quite large. The value of  $Q$  corresponding to  $M_{21\max}$  is given by

$$Q_{21} = \frac{\sqrt{r_1(a_1(1+a_2^2r_2^2) - a_2r_2(1+a_1^2)) + 4r_2a_1a_2}}{((1-a_1r_1) - a_2r_2(a_1 - r_1))} \quad (\text{for } \phi_2 = \phi_1 + \pi). \quad (26)$$

With  $a_1 = a_2 = 0.999$  and  $r_1 = r_2 = 0.9$  as above, equation 26 gives  $Q_{21} = 143.7$  compared to a value of  $Q_{11}$  from equation 10 of  $Q_{11} = 9.40$ . For the same values of reflectivity, the lossless cases give  $Q_{21} = 171.0$  and  $Q_{11} = 9.49$ . And, as for the magnifications, the quality factors,  $Q$ , can be greatly enhanced for the two-cavity structure over that of a single cavity. However they remain below those of the optimum values for a single cavity with a loss factor of 0.999. For this case we would obtain  $M_{11\text{opt}} = 499.25$ ,  $Q_{11\text{opt}} = 499.75$ , given by equations 11 and 12 respectively, and  $M_{21\text{opt}} = 498.75$ , and  $Q_{21\text{opt}} = 499.75$  given by equations 22 and 26 respectively. Values are collected in Table I. (for  $\phi_2 = \phi_1 + \pi$ )

	$M_{21}$	$Q_{21}$	$M_{11}$	$Q_{11}$
Given Values	254.63	159.63	18.64	9.40
Lossless	361.00	174.28	19.00	9.49
Optimum	498.75	499.75	499.25	499.75

Table I

It is useful to attempt to get some insight into these results. First, for the case where we consider that  $\phi_2 = \phi_1$ , we see that the single-cavity resonance is split into two. This is similar to what one experiences in the case of two coupled LRC circuits. In the case of two identical coupled LRC circuits the higher and lower frequency resonances correspond respectively to in-phase and out-of-phase coupling through the coupling capacitor. When the coupling is out of phase, which occurs for the lower frequency resonance, currents in the two circuits flow in opposite directions through the coupling capacitor, and no total current flows through this capacitor. In this case no voltage appears across the capacitor and this capacitance is effectively eliminated from the circuit. As the capacitors are in series, the elimination of one increases the overall

effective capacitance lowering the resonant frequency. The opposite is the case for the higher resonance where the coupling is in phase, the coupling capacitor is effectively included twice in series so the overall capacitance is lowered and the resonance frequency is raised.

In the case of the coupled optical cavities there is an effective  $\pi/2$  phase shift in transmission through the cavity-to-cavity coupling as indicated in equation 7. Cavity-to-cavity transmission in the in-phase resonance essentially goes through this coupling interface twice increasing the effective overall optical path length and reducing the resonant frequency. The out-of-phase resonance essentially does not go through the coupling interface at all reducing the effective overall optical path length and increasing the resonant frequency. Let us re-examine equation 16 for the line splitting. Equation 16 indicates that the line splitting vanishes as the reflectances become large, and consequently as the transmission through the coupling interfaces becomes very small. In this case the resonators are only weakly coupled and very little of the energy goes through the coupling interface. Little of the energy suffers the phase shift due to transmission and the splitting vanishes. In the opposite extreme as the reflectances become very small virtually all of the energy goes through the coupling interface and the splitting becomes very large and can approach  $\pi$ . In this case the difference in phase shift between the in-phase resonance and the out-of-phase resonance cases is twice  $\pi/2$  or  $\pi$  as given by equation 16. The interference between the waves results in a limitation on the magnification such that the resonant magnifications for two coupled resonant circuits are about the same as for a single resonant cavity with the same parameters.

In the case where  $\phi_2 = \phi_1 + \pi$  the waves are shifted by  $\pi/2$  during each half-circuit so the waves are effectively out of phase with each other by  $\pi/2$  and do not constructively or destructively interfere resulting in no splitting. This lack of interference and splitting allows for the greatly improved magnification and cavity  $Q$ .

#### 4. Conclusions

In this work we showed for the LRC case that coupling two or more resonant circuits together can result in resonant line splitting and that electromagnetic energy can be stored in any of the coupled circuits, depending on the circuit parameters, but that no enhancement in the magnitude of either the stored energy or the  $Q$  of the resonance can be achieved over that of a single resonant circuit. In this case the circuit resonance frequencies only depend on the circuit parameters namely the values of the circuit inductances and capacitances. In the case of the coupled optical cavities we can also observe resonant line splitting and that electromagnetic energy can be stored in any of the coupled cavities. In contrast to the LRC case, we can also get a substantial enhancement of the magnitude of the stored energy and the effective cavity  $Q$  over that of a single resonator provided these factors are limited by the coupling between the cavities. However, when this coupling can be optimized we see that the energy storage and  $Q$  of a single cavity is superior to that of the coupled cavities. The advantages of the coupled resonators come in their ability to show line splitting, enhanced energy storage, and high  $Q$  even when the cavity-to-cavity coupling is limited. Under these circumstances one should also be able to obtain reduced laser thresholds through the use of coupled optical cavities wherein at least one of them displays gain.

## ACKNOWLEDGMENTS

I would like to sincerely acknowledge and thank NASA for the support of the SFFP program. I would also like to sincerely thank the Marshall Space Flight Center and Dr. David D. Smith for the opportunity of working on this very interesting research program. The time has been far too short and has passed far too quickly. Moreover my special thanks go to Mr. Hongrok Chang without whose support and help far less would have been accomplished. Mr. Chang has been a constant companion in this work checking my calculations, making those of his own, and providing excellent advice as to how to proceed; and, not the least, creating all of the figures in this report.

## REFERENCES

1. Smith, David D., Chang, Hongrok, and Fuller, Kirk A., *Whispering-gallery mode splitting in coupled microresonators*, J. Opt. Soc. Am. B 10887 (2003)
2. Smith, David D., Witherow, William K., and Fuller, Kirk A., *Coupled-Resonator-Enhanced Sensor Technologies*, NASA MSFC Center Director's Discretionary Fund – FY 2003, Project Number: 03-17.
3. Rosenberger, A. T., and Naweed, Ahmer, *Induced Transparency and Related Effects in Coupled Whispering-Gallery Microresonators*, to be published.

**2004**

**NASA FACULTY FELLOWSHIP PROGRAM**

**MARSHALL SPACE FLIGHT CENTER**

**THE UNIVERSITY OF ALABAMA  
THE UNIVERSITY OF ALABAMA IN HUNTSVILLE  
ALABAMA A&M UNIVERSITY**

**ENHANCEMENT AND ANALYSIS OF  
REAL-TIME RADIOGRAPHY IMAGES**

Prepared By:	Dr. Edward R. Doering
Academic Rank:	Associate Professor
Institution and Department:	Rose-Hulman Institute of Technology Electrical and Computer Engineering
NASA/MSFC Directorate:	Engineering (ED32)
MSFC Colleague:	Dr. Sam Russell

## Introduction

Shuttle Redesigned Solid Rocket Motor (RSRM) nozzle interiors fabricated from carbon phenolic composite exhibit “ply lift” when hot fired. The composite surface is smooth when fabricated, but the individual plies separate and lift away from the surface when exposed to high-temperature and high-pressure exhaust gas. Figure 1 shows a cross section of a post-fired composite in which ply lift is evident as dark fissures. Surface charring is also visible as a darker band about 0.2 inches thick. Charring is normal, but ply lift is not desirable since the fissures could possibly initiate an abnormal exhaust path from the RSRM. The underlying mechanisms of ply lift are under investigation as part of the Shuttle Return-To-Flight Program.

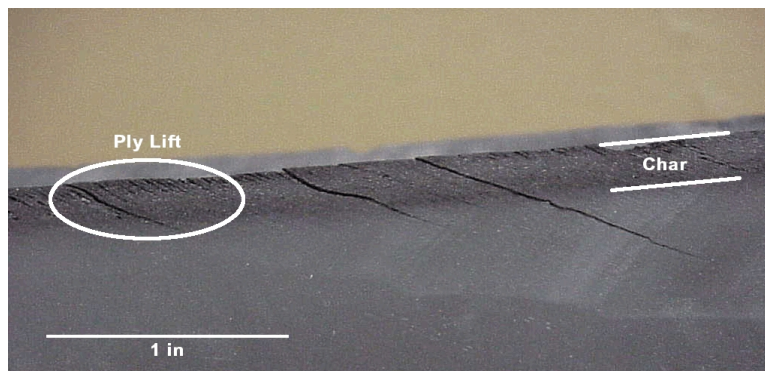


Figure 1: Cross section of post-fired carbon phenolic composite.

Subscale solid rocket motors are used as a cost-effective way to simulate actual hot firing of the RSRM. The Solid Fuel Torch (SFT) subscale motor is specifically designed to evaluate RSRM materials. The output of the SFT is channeled through a convergent cone fabricated from carbon phenolic composite. Real-time radiography (RTR) of the cone interior during hot firing permits direct observation of ply lift dynamics over time, thereby providing information to validate analytical models of the ply lift process. Key information to extract from the image sequence includes:

1. time when ply lift is first detectable,
2. minimum detectable length of the ply lift crack,
3. charring depth over time,
4. charring depth as a function of position along the cone, and
5. lift height over time.

The RTR setup was optimized to minimize geometric unsharpness and to maximize contrast. The ply lift and charring processes are visible to experienced radiographers, but photon counting noise and low contrast obscure the ply lift indications for the casual observer. Moreover, quantitative measurement of phenomena such as charring depth versus time would be tedious if done manually, since the typical RTR image sequence is 300 to 400 frames long. Thus, the goals of this project are two-fold:

1. Enhance the RTR image sequence to facilitate human interpretation, and

2. Analyze the RTR image sequence to extract quantitative information such as ply lift height as a function of time.

### **Enhancement of RTR Image Sequence**

A Pantak X-ray source and a Varian 2520 flat panel amorphous silicon detector image the cone's interior. The source operates at 160 kVp and 4 mA. Frames are captured at approximately 8 frames per second, with a total sequence length of 30 to 40 seconds. Figure 2 shows a frame from the post-fire image, where crack-like lines indicate ply lift and the band of lighter intensity indicates charring and ply lift. Pressure and temperature sensors and associated wiring are visible in the center of the cone.

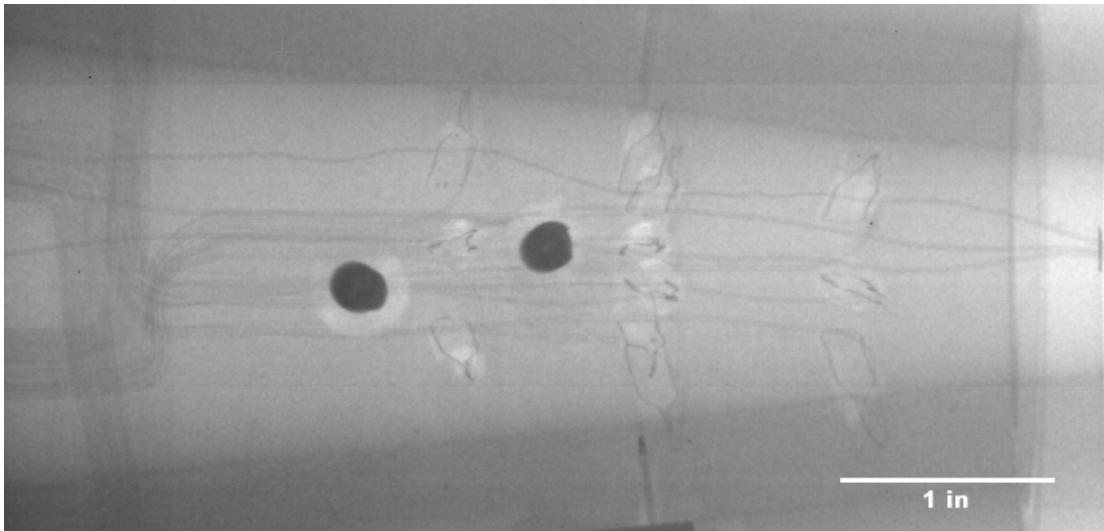


Figure 2: RTR image of cone interior.

The X-ray source intensity fluctuates somewhat, causing a global variation in the mean value of each frame. A region of interest (ROI) was selected at the edge of the image away from the ply lift and charring region. The mean value of the ROI was found and subtracted on a frame-by-frame basis. Removing this fluctuation reduces visual flicker in the final contrast-enhance image, and also improves reliability of intensity thresholding-based feature detection.

Frames are captured in “raw mode” to maximize the frame rate flat panel detector, so darkfield correction must be applied as a post-processing step. Frames acquired after the X-ray source was shut off are averaged to estimate the fixed-pattern noise of the detector. This “darkfield” image is subtracted from all frames before further processing.

Photon counting noise is reduced using a running average of four frames, equivalent to a time window of 0.5 seconds duration. Image signal-to-noise ratio increases by  $\sqrt{N}$ , where  $N$  is the number of frames, but temporal blurring also increases with increased frames. Four frames were selected to balance noise reduction against temporal blurring.

Image subtraction is used to highlight any differences that appear after hot firing begins. Frames captured just before firing were averaged to minimize noise and used as the reference

background image, which is subtracted from each frame in the sequence. Figure 3 shows the resulting difference image after contrast stretching, with the plylift cracks and charring region now clearly evident.

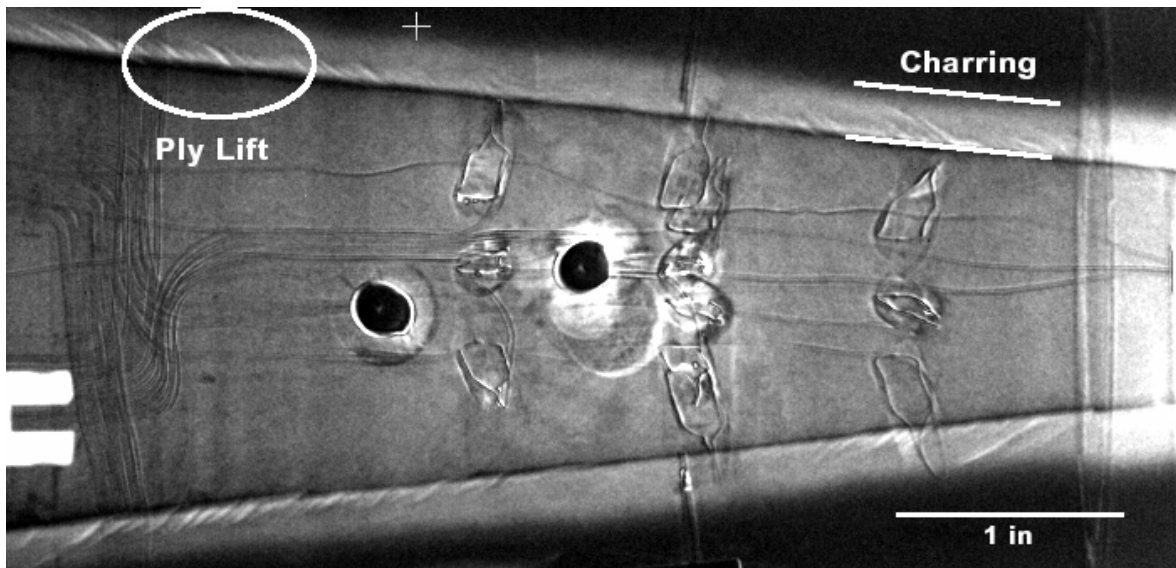


Figure 3: Enhanced RTR image showing ply lift and charring

### **Analysis of RTR Image Sequence**

The first frame of the difference sequence is a zero-mean Gaussian noise field with standard deviation of  $\sigma$  intensity levels. Thresholding the image at  $+9\sigma$  clearly delineates the plylift cracks, while thresholding at  $+2\sigma$  shows the charring. The interior edge of the convergent cone becomes detectable at two seconds.

The charring region was isolated by rotating to correct for the angle of the interior cone boundary, cropping the image, and thresholding to create a binary image. The thickness of the charring region can then be observed as a function of position in the cone and as a function of time. Figure 4(a) plots the boundary position as a function of time.

The intensity of the cone interior gradually increases with time which indicates a reduction in the mass attenuation coefficient of the material. Figure 4(b) plots the intensity normalized to the starting value. The plots in Figure 4 show a similar trend, indicating that perhaps either measurement technique could be used to estimate char depth.

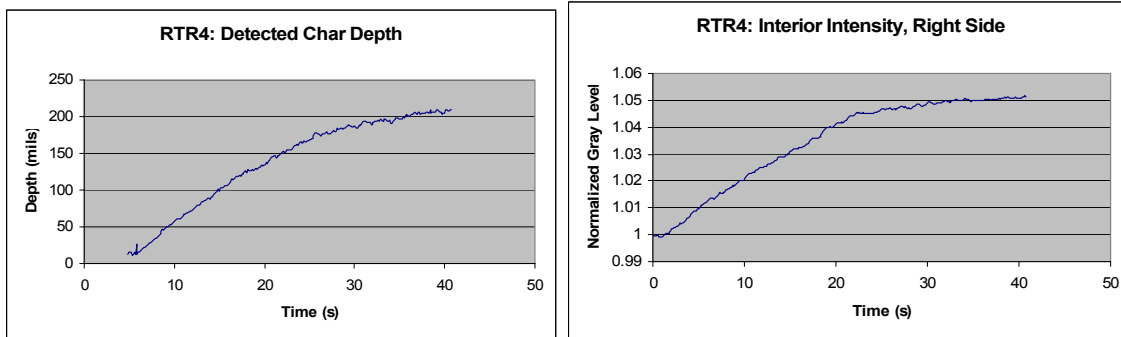


Figure 4: Char depth versus time for (a) edge tracking and (b) intensity increase.

The ply lift boundaries on the cone interior wall were isolated by an edge tracking algorithm, and the total reduction of the cone's inner diameter over time was measured. Dividing by two yield the average ply lift height as plotted in Figure 5. The reduction begins at 2 seconds, and then increases quickly to a plateau at 15 seconds. The ply lift process is noticeably more abrupt in comparison to the charring depth plots of Figure 4.

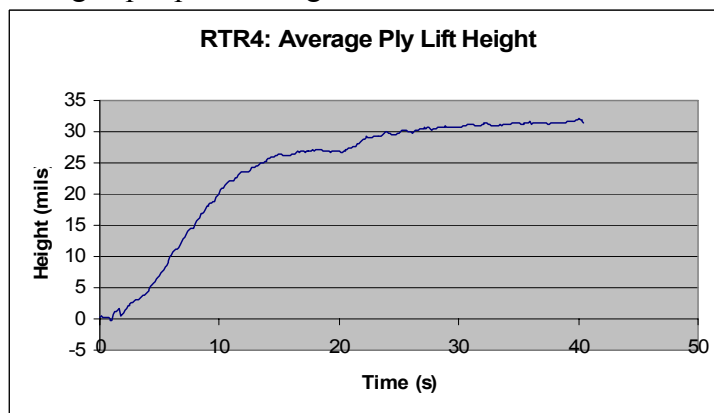


Figure 5: Average ply lift height versus time.

## **Conclusion**

Real-time radiography has been demonstrated as an effective way to observe ply lift dynamics during hot firing. A series of corrective techniques for X-ray tube intensity fluctuation, detector fixed-pattern noise, and photon counting noise followed by background subtraction and contrast enhancement yield an image sequence that is enhanced for human interpretation. Automated analysis by edge tracking allows ply lift dynamics such as lift height and charring depth to be quantified over time.

## **Acknowledgements**

The author would like to thank Ron Beshears and Sam Russell for their on-going support, as well as the entire team of engineers and technicians in the Nondestructive Evaluation and Tribology Group of the Marshall Space Flight Center's Engineering Directorate.

2004

**NASA FACULTY FELLOWSHIP PROGRAM**

**MARSHALL SPACE FLIGHT CENTER  
THE UNIVERSITY OF ALABAMA**

**CONTROLS FOR REUSABLE LAUNCH VEHICLES  
DURING TERMINAL AREA ENERGY MANAGEMENT**

Prepared By:	Brian J. Driessen
Academic Rank:	Assistant Professor
Institution and Department:	University of Alabama in Huntsville Department of Mechanical and Aerospace Engineering
NASA/MSFC Directorate:	Space Transportation
MSFC Colleague:	Charles E. Hall

## Notation

$R$	.....	rotation matrix from a frame fixed to the vehicle and a global inertial reference frame. Or, if $w$ is a vector expressed in the vehicle's coordinate frame, then $Rw$ is the same vector expressed in the global frame.
$\bar{i}_G, \bar{j}_G, \bar{k}_G$	.....	global x-axis (North), global y-axis (East), global z-axis (Down)
$\bar{i}_A, \bar{j}_A, \bar{k}_A$	.....	vehicle x-axis (forward), vehicle y-axis (right), vehicle z-axis (down)
$J$	.....	inertia matrix of RLV vehicle, $J \in R^{3 \times 3}$ , $J = J^T > 0$
$m$	.....	vehicle mass
$g$	.....	scalar, acceleration due to gravity
$q$	.....	Euler angles of RLV orientation, $q \in R^3$ (roll, pitch, and yaw), representing the orientation of the vehicle relative to a global inertial reference frame. $q \equiv (q_{roll}, q_{pitch}, q_{yaw})^T$ .
$\omega$	.....	angular velocity of RLV expressed in vehicle coordinates, $\omega \in R^3$
$\bar{a}$	.....	$\in R^3$ , acceleration of vehicle mass center, expressed in vehicle coordinates, i.e., $a = R^T \ddot{p}$ .
$a_n$	.....	projection of $a$ onto the global negative z unit axis $-\bar{k}_A$ , i.e., the component of $a$ , also called the "normal acceleration" of the vehicle
$v_m$	.....	vehicle Mach number (at center of mass)
$\delta$	.....	$\delta \in R^8$ is the vector of control surface positions, for left and right flaps, left and right rudders, two inboard elevons, and two outboard elevons.
$\delta_{min}, \delta_{max}$	.....	$\delta_{min} \in R^8$ , $\delta_{min} < 0$ , $\delta_{max} \in R^8$ , $\delta_{max} > 0$ , denote the lower and upper limits of the control surface positions $\delta$ .
$\dot{\delta}_{max}$	.....	$\dot{\delta}_{max} \in R^8$ denotes an upper limit on $ \dot{\delta} $ , about 30 degrees per second for each control surface, except for the flaps with a limit of $10^\circ s^{-1}$ .
$\tau_a$	.....	$\tau_a \in R^3$ , net aerodynamic torque exerted on the vehicle, expressed in the vehicle frame.
$F_a$	.....	$F_a \in R^3$ , net aerodynamic force exerted on the vehicle, expressed in the vehicle frame.
$S_\tau$	.....	$\partial \tau_a / \partial \delta$ , called the "torque sensitivity matrix."
$A(q)$	.....	$A \in R^{3 \times 3}$ . known partial derivative of $\omega$ with respect $\dot{q}$ . $A$ is nonsingular along any guidance commanded trajectory. $A$ is a (known) function of $q$ . $\omega = A(q)\dot{q}$ .

$M$	.....	$JA$
<i>subscript g</i>	.....	denotes a guidance-commanded quantity.
		For example, $q_{roll}g$ is the guidance-commanded value of $q_{roll}$ .
$sk(v)$	.....	the 3 by 3 matrix that when post-multiplied by a vector $w$ gives the cross product of $v$ and $w$ . Or, $sk(v)w = v \times w$ .
$\dot{p}$	.....	the vehicle's linear velocity in global coordinates.
$Q$	.....	dynamic pressure, $\frac{1}{2}\rho\ \dot{p}\ _2^2$ , where $\rho$ is the air density.
$\alpha$	.....	angle of attack
$\beta$	.....	sideslip angle

### **The Problem**

During the terminal energy management phase of flight (last of three phases) for a reusable launch vehicle, it is common for the controller to receive guidance commands specifying desired values for (i) the roll angle  $q_{roll}$ , (ii) the acceleration  $a_n$  in the body negative z direction,  $-\bar{k}_A$ , and (iii)  $\omega_3$ , the projection of  $\omega$  onto the body-fixed axis  $\bar{k}_A$ , is always indicated by guidance to be zero. The objective of the controller is to regulate the actual values of these three quantities, i.e make them close to the commanded values, while maintaining system stability.

The equations of motion are given by:

$$\begin{aligned}
 JA\ddot{q} &= -J\dot{A}\dot{q} - sk(A\dot{q})JA\dot{q} + \tau_a & f &\equiv -sk(A\dot{q})JA\dot{q} - J\dot{A}\dot{q} \\
 M\ddot{q} &= f + \tau_a & M &\equiv JA \\
 \ddot{q} &= F + M^{-1}\tau_a & F &\equiv M^{-1}f \\
 ma &= F_a + mgR^T e_3 & e_3 &\equiv (0, 0, 1)^T
 \end{aligned}
 , \quad \text{where} \tag{1}$$

The following are measured and available to the controller:  $\delta$ ,  $q$ ,  $\omega$ ,  $a$ ,  $\alpha$ ,  $\beta$ ,  $v_M$ , and  $Q$ . In the next section, we present a controller for this problem, including simulation results.

### **Proposed Controller**

Denote the commanded orientation of the vehicle as  $q_c$ , whose value will be designed shortly. The commanded torque,  $\tau_{ac}$ , is output by the orientation controller and is chosen so as to make the model-based value of  $\ddot{q}$  satisfy:

$$\ddot{q} + [\Lambda_1]\dot{q} + [\Lambda_2](q - q_c) + [\Lambda_3]\int_0^t (q - q_c)dt = 0 \tag{2}$$

where the  $[\Lambda_i]$  are diagonal gain matrices producing stability within the last equation. The values used in our simulation were:

$$\Lambda_1 = \text{diag}(2\mu, 3\mu, 3\mu), \quad \Lambda_2 = \text{diag}(\mu^2, 3\mu^2, 3\mu^2), \quad \Lambda_3 = \text{diag}(0, \mu^3, \mu^3), \quad \mu = 4 \tag{3}$$

giving two-percent settling times of 1 second. First,  $q_{c1}$  is already given as the guidance-command for the roll-angle. Then, the yaw-command  $q_{c3}$  is chosen as  $q_{c3} = \text{atan2}(\dot{p}_2, \dot{p}_1)$ , which

would be associated with zero side-slip if  $\dot{p}_3$  were zero. Finally, the commanded pitch angle,  $q_{c2}$ , is chosen as:

$$q_{c2} \equiv \theta_c, \quad (4)$$

where  $\theta_c$  is purely model-based and approximates the value of  $q_{c2}$  that would produce  $a_n$  as:

$$a_n = a_{nc} \equiv a_{ng} - k_i \int_0^t (a_n - a_{ng}) dt \quad (5)$$

at the current mach, dynamic pressure, zero-sideslip, while  $q_1 = q_{c1}$  and  $q_3 = q_{c3}$ . The value of  $\theta_c$  is constructed as follows. Off-line, before flight, a table is constructed which inputs angle of attack, mach, and dynamic pressure, and outputs the corresponding  $a_n$ . At the current time,  $t$ , a *simple one-dimensional search within this table* produces the value of  $\theta_c$ , at virtually no computational cost. The second term in the expression for  $a_{nc}$  in (5) helps to correct for modeling errors. The integral gain  $k_i$  was chosen as  $k_i = 4/5$ , making (5) slower than (2).

The surface deflections  $\delta$  are driven by actuators with 3<sup>rd</sup> order (flaps) or 4<sup>th</sup> order (rudders/elevons) actuator models. These actuators have either a 0.15-second 2% time-constant {flaps} or a 0.05-second 2% time-constant {rudders/elevons}. The commanded deflections,  $\delta_c$ , are chosen as follows. Since the aerodynamic torque,  $\tau_a$ , is not a perfectly linear function of  $\delta$ , using a delayed value of the Jacobean,  $S(t-\Delta)$ ,  $\Delta = 0.006s$  as for one controller sample period, we perform a truncated {fixed number} set of damped {half-step} Newton-Raphson iterations, with the single *fixed* Jacobean, i.e., fixed for that time instant (or sample period). In particular,

$$\hat{\delta}_{k+1} = sat \left[ \left\{ \hat{\delta}_k + \frac{1}{2} G^+ \begin{pmatrix} -\hat{\delta}_k \\ -(\tau_a - \tau_{ac}) \end{pmatrix} \right\}_{1:8}, 0.75\delta_{\min}, 0.75\delta_{\max} \right], \quad (k=1, \dots, 20) \quad (6)$$

where the subscript 1:8 denotes the first eight entries of the vector and where we are saturating at 75% of the true actuator bounds to help avoid hitting the true actuator limits. The same percentage is used for rate-limit avoidance. The iteration is initialized at  $\delta(t-\Delta)$ . The simulations used 20 iterations, thus involving 20 evaluations of the look-up table for the aerodynamic torque (at the current  $v_M$ ,  $Q$ ,  $\alpha$ , and  $\beta = 0$ ), 20 back substitutions, and one matrix factorization. The matrix  $G$  is the one associated with the stationarity condition for minimizing the sum of the squares of the  $\delta_i$  subject to achieving the specified torque:

$$G \equiv \begin{bmatrix} I & S(t-\Delta)^T \\ S(t-\Delta) & 0 \end{bmatrix} \quad (7)$$

The output of these Newton iterations is fed into a direct rate-limiter, with the rate-limits set at 75% of  $\dot{\delta}_{\max}$ . This result is in turn fed into a filter  $\frac{100^2}{s^2 + 200s + 100^2}$ , the output of which is

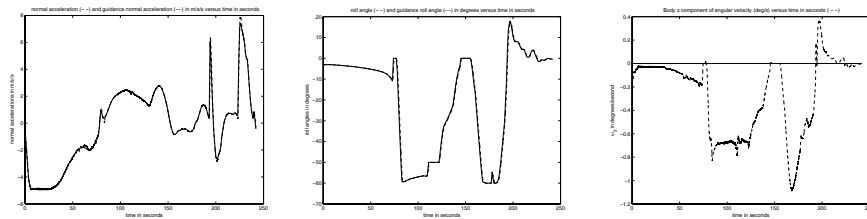
declared our commanded actuator deflection,  $\delta_c$ . In all simulations, this choice of  $\delta_c$  produced absolutely no saturation of the actuators' *actual* bounds nor any saturation of the actuators' *actual* rate-limits; thus, the 3<sup>rd</sup> order (flaps) and 4<sup>th</sup> order (rudders/elevons) dynamic actuator models were fully satisfied within all simulations, the results of which we now present in the next section. For possible reference,

$$\begin{aligned} \delta_{\min} &= [-15; -15; -60; -30; -30; -30; -30; -30] \text{ degrees} \\ \delta_{\max} &= [26; 26; 30; 60; 25; 30; 25; 30] \text{ degrees} \end{aligned} \quad (8)$$

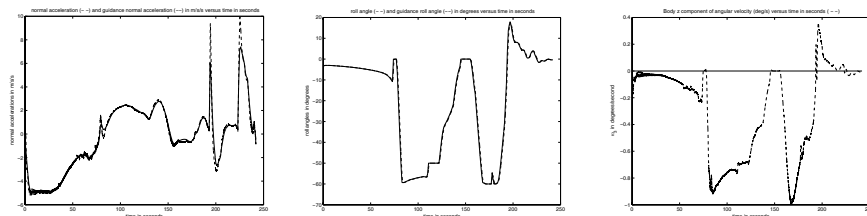
In the next section, we present numerical simulation results for a set of typical guidance commands. In these simulations, the guidance-commands are *open-loop* [which is not typical of the actual guidance but gives a practical test of the controller].

## Results

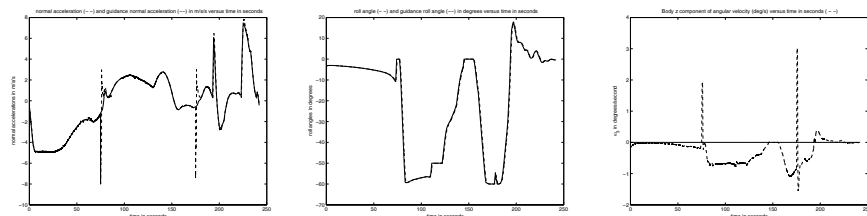
A set of typical guidance commands  $(a_{nd}, q_{roll})_d$  were used to test the proposed controller. The nominal case's result is shown in Figures 1-3 below. In the second case, the actual body-z air force is *two times larger* than that of the model – see Fig's 4-6. In the third case, 1.2g {where 1g is 9.81 m/s/s} *windgusts*, each of duration 1 second, occur at times  $t = 75s$  and  $t = 175s$  -- Fig's 7-9. In these plots, the axes-ranges are  $[0s, 243s]$ ,  $[-70^\circ, 20^\circ]$ ,  $[-6m/s^2, 8m/s^2]$ , or  $[-1.2^\circ/s, 0.4^\circ/s]$ , except for Fig's 4, 7 and 9 with ranges  $[-6m/s^2, 10m/s^2]$ ,  $[-10m/s^2, 8m/s^2]$  and  $[-2^\circ/s, 4^\circ/s]$ .



Figures 1-3.  $a_n$  (m/s/s), roll (deg),  $\omega_3$  (deg/s). dashed = actual, solid = guidance



Figures 4-6.  $a_n$  (m/s/s), roll (deg),  $\omega_3$  (deg/s). dashed = actual, solid = guidance



Figures 7-9.  $a_n$  (m/s/s), roll (deg),  $\omega_3$  (deg/s). dashed = actual, solid = guidance

## Acknowledgements

The author would like to thank the entire team of engineers and scientists in the guidance and control research area of the Marshall Space Flight Center's Transportation Directorate. Special thanks goes to my NASA colleague Charlie Hall and the NFFP program managers Gerry Karr and Jeanelle Bland.

**2004**

**NASA FACULTY FELLOWSHIP PROGRAM  
Accompanying Student**

**MARSHALL SPACE FLIGHT CENTER**

**THE UNIVERSITY OF ALABAMA  
THE UNIVERSITY OF ALABAMA IN HUNTSVILLE  
ALABAMA A&M UNIVERSITY**

**Optical Cryogenic Tank Level Sensor**

Prepared By:	Amanda Duffell
Academic Rank:	Graduate Student
Institution and Department:	University of Alabama in Huntsville, Department of Physics
Professor Accompanied:	Prof. Don A. Gregory
NASA/MSFC Directorate:	Transportation
MSFC Colleague:	John Wiley

## Introduction

Cryogenic fluids play an important role in space transportation. Liquid oxygen and hydrogen are vital fuel components for liquid rocket engines. It is also difficult to accurately measure the liquid level in the cryogenic tanks containing the liquids. The current methods use thermocouple rakes, floats, or sonic meters to measure tank level. Thermocouples have problems examining the boundary between the boiling liquid and the gas inside the tanks. They are also slow to respond to temperature changes. Sonic meters need to be mounted inside the tank, but still above the liquid level. This causes problems for full tanks, or tanks that are being rotated to lie on their side.

The Transportation Directorate is currently working on an optical probe to measure tank level. It would offer a fast, cheap and reliable alternative to the present measuring methods. Two designs are being developed. One is based on evanescent light wave coupling from a solid quartz rod or optical fiber to the surrounding liquid. The second is based on losses in a series of engineered air/glass interfaces in a segmented quartz rod or notched optical fiber.

## Theory

The propagation of light through a waveguide is controlled by the refractive indices of the guide and its surrounding medium. Snell's Law is the basic equation to explain refraction phenomenon, Eqn. 1, Fig. 1.

$$\text{Equation 1} \quad n_1 \sin \theta_1 = n_2 \sin \theta_2$$

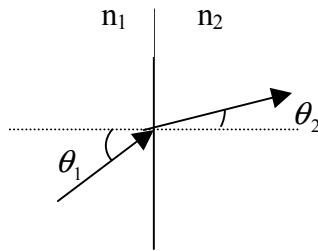


Figure 1 Illustration of Snell's Law with  $n_2 > n_1$

Total Internal Reflection (TIR) is the effect of light reflecting predominantly inside the medium of high refractive index, instead of refracting and passing through a boundary to a medium with lower refractive index. TIR occurs when  $\theta_2 \geq \theta_c$ . The critical angle,  $\theta_c$ , is when  $\theta_1 = 90^\circ$ . At that point, all light at the  $n_2:n_1$  boundary reflects back into material  $n_2$ .<sup>1</sup> TIR is critical to transmitting light through a waveguide, such as an optical fiber or a piece of quartz tubing, Fig 2.

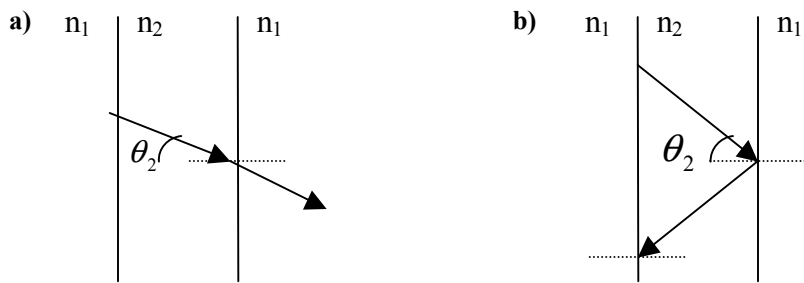


Figure 2 Case a)  $\theta_2 \leq \theta_c$ , no TIR occurs

Case b)  $\theta_2 \geq \theta_c$ , TIR occurs

TIR is most efficient when  $n_2 \cdot n_1$  is large because a greater range of angles can propagate through the medium  $n_2$ . For example, light will propagate with less loss through glass surrounded by air than water, Table 1.

Material	Index of Refraction
Glass	1.46
Water	1.3
Air	1
Plastic Fiber	1.33

Table 1 Indices of Refraction

Evanescent coupling occurs when light propagates through surface modes on a material. The surface modes allow transfer of light from the propagation medium to its surrounding. Evanescent coupling is most efficient when the two materials have similar refractive indices.<sup>2</sup>

The main source of loss in an optical system is material interfaces. These losses can be estimated by the Fresnel reflectance, R, and transmittance, T, Eqn. 2 and 3, for normal incidence.

Equation 2 
$$r = \left( \frac{n_1 - n_2}{n_1 + n_2} \right)^2$$

Equation 3 
$$t = 1 - r$$

From these equations, it can be seen that transmission losses from one material to another can be minimized when the refractive indices are more similar.<sup>3</sup>

## Experimental

Two different methods were used in designing the optical tank level probes. One depends on evanescent coupling effects and the other is based on Fresnel reflection losses.

### Evanescent Coupling

The evanescent coupling probes used optical fiber for the waveguide and air, water, or liquid nitrogen as the coupling medium. The basic concept for this design is that the fiber would transmit more effectively in air than in liquid because of the refractive index difference. Because evanescent modes couple through the surface of the fiber, it was important to remove the fibers' cladding, or to choose fibers that were not clad.

When the cladding is removed from glass fibers they become very brittle and difficult to work with, especially in large lengths. Large path lengths are necessary because evanescent coupling is a weak effect and needs to occur over a long section of fiber for the effects to be measurable. The handling problems made glass fibers a poor probe choice.

An alternative to glass fiber is plastic fiber. The plastic fiber is pliable and not brittle, so it does not require cladding to be handled routinely. Another benefit of plastic fiber is that its refractive index closely matches that of water, which enhances the coupling effect. The evanescent coupling effect can also be increased by increasing the surface roughness of the fiber, by creating more places for loss (scatter) to occur, while still preserving the fiber's transmission properties. The disadvantage of the plastic fiber is the lack of standard coupling devices to input the laser and feed the output into a data system. This problem could be fixed with appropriate hardware.

### Fresnel Reflection Losses

Two probes were built using the principle of Fresnel reflection losses. The first probe used segments of quartz rods, arranged with a small air gap between each rod, Fig. 3.

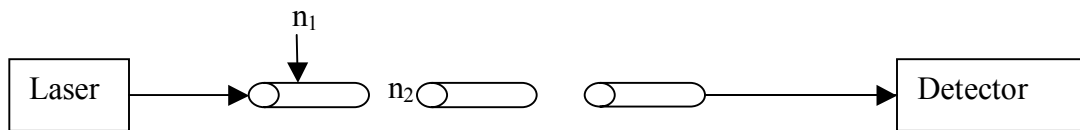


**Figure 3** Losses occur at each  $n_1$  to  $n_2$  interface

The idea is, as the tank fills, the transition region between the rods switches from being filled with air to being filled with liquid. There is then a corresponding increase in transmission. At a glass/air interface the transmission loss is 4%. At each glass/water interface the transmission loss is only .5%. These losses are predicted by the Fresnel equations. This probe is easy to assemble and it can withstand moderately rough

handling. The main problem with this design is that it is very difficult to get adequate power through the array of rods and through to the detector. This problem could be solved with better optical components.

The second design based on Fresnel losses used the plastic fiber again. This time small notches were cut into the fiber. The notches played the same role as the air gap in the segmented quartz rod probe.

### Test Setup

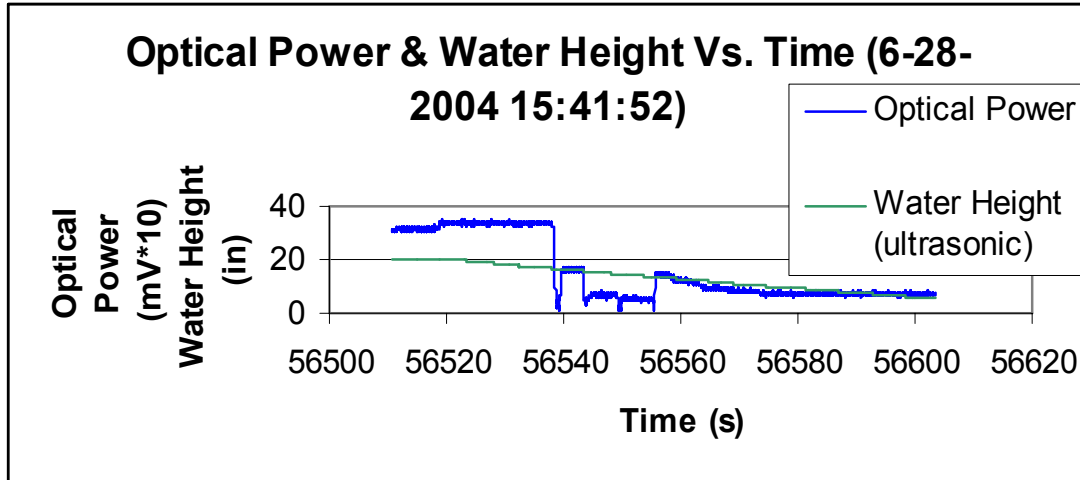
All of the probes were tested in water before they were tested in liquid nitrogen. A 3 feet tall water tank was provided that was equipped with a drainage device to allow tank level measurements as the tank was emptied and filled. The optical tank level measurements were verified by a sonic level meter, pressure sensor and flow meter. The LN2 was tested in a static configuration where the probes were placed in a full liquid nitrogen dewar.

### Results

There were mixed results from all probes tested. Problems occurred with low transmission, wetting of the probe's surface, and overall system construction. The results are summarized below.

The roughened plastic fiber showed approximately 10% decrease in transmission when submerged in liquid nitrogen, (LN2). Transmission increased back to pre-test levels when the fiber was first removed from the LN2. However, as the fiber returned to room temperature condensation and frost covered it. The condensation effectively resubmerged the fiber and transmission decreased again, making the sensor unreliable with repeated use. This would not present a large problem once the sensor is deployed in an enclosed LN2 tank, where temperature does not change so rapidly and water vapor is not available for condensation.

The data from the segmented quartz rod probe produces a step output, with a noisy section between each step that represents the turbulence as the gap is partially filled with liquid.



The notched plastic fiber also showed a step response in the data. Unfortunately it had the same condensation problems in LN2 as the roughened plastic fiber.

### **Conclusion and Recommendations**

It appears that more work should be done with the plastic fibers. If a more stable probe and coupling setup were built, more accurate results could be obtained, especially in a more controlled temperature environment.

The segmented rod probed could be significantly improved by using better optics. The current quartz pieces are not polished on the faces, resulting in substantial loss at each interface. Gradient Index (GRIN) lens are available in the general cylindrical shape required and they would relay collimated light through the linear array with low scattering losses at the interfaces. The improved optics should reduce the overall signal to noise ratio of the probe.

### **Acknowledgments**

I would like to thank everyone in TD72 for being helpful and supportive of this project. I give special thanks to: NASA Faculty Fellowship Program (NFFP), my NASA colleague, John Wiley, for being a great listener and encourager, Val Korman, Madison Research Corporation, for his daily guidance and ideas, Edwin Sutton, LB&B, for his fast and courteous technical support, and finally, to my UAH faculty advisor, Prof. Don Gregory, for the opportunity to participate in this program.

### **References**

1. Hecht, Eugene, Optics, 2<sup>nd</sup> Edition, Addison-Wesley Massachusetts, 1990, p.170.
2. *ibid* p.107.
3. *ibid* p.99.

2004  
NASA FACULTY FELLOWSHIP PROGRAM

MARSHALL SPACE FLIGHT CENTER

THE UNIVERSITY OF ALABAMA  
THE UNIVERSITY OF ALABAMA IN HUNTSVILLE  
ALABAMA A&M UNIVERSITY

**CONTROL OF COMBUSTION-INSTABILITIES THROUGH  
VARIOUS PASSIVE DEVICES**

Prepared By:	Kader Frendi
Academic Rank:	Associate Professor
Institution and Department:	The University of Alabama in Huntsville Department of Mechanical and Aerospace Engineering
NASA/MSFC Directorate:	Transportation
MSFC Colleague:	Tom Nesman

## **Introduction**

It is well known that under some operating conditions, rocket engines (using solid or liquid fuels) exhibit unstable modes of operation that can lead to engine malfunction and shutdown. The sources of these instabilities are diverse and are dependent on fuel, chamber geometry and various upstream sources such as pumps, valves and injection mechanism. It is believed that combustion-acoustic instabilities occur when the acoustic energy increase due to the unsteady heat release of the flame is greater than the losses of acoustic energy from the system [1, 2].

Giammar and Putnam [3] performed a comprehensive study of noise generated by gas-fired industrial burners and made several key observations; flow noise was sometimes more intense than combustion roar, which tended to have a characteristic frequency spectrum. Turbulence was amplified by the flame. The noise power varied directly with combustion intensity and also with the product of pressure drop and heat release rate. Karchmer [4] correlated the noise emitted from a turbofan jet engine with that in the combustion chamber. This is important, since it quantified how much of the noise from an engine originates in the combustor.

A physical interpretation of the interchange of energy between sound waves and unsteady heat release rates was given by Rayleigh [5] for inviscid, linear perturbations. Bloxidge et al [6] extended Rayleigh's criterion to describe the interaction of unsteady combustion with one-dimensional acoustic waves in a duct. Solutions to the mass, momentum and energy conservation equations in the pre- and post-flame zones were matched by making several assumptions about the combustion process. They concluded that changes in boundary conditions affect the energy balance of acoustic waves in the combustor. Abouseif et al [7] also solved the one-dimensional flow equations, but they used a one-step reaction to evaluate the unsteady heat release rate by relating it to temperature and velocity perturbations. Their analysis showed that oscillations arise from coupling between entropy waves produced at the flame and pressure waves originating from the nozzle. Yang and Culick [8] assumed a thin flame sheet, which is distorted by velocity and pressure oscillations. Conservation equations were expressed in integral form and solutions for the acoustic wave equations and complex frequencies were obtained. The imaginary part of the frequency indicated stability regions of the flame.

Activation energy asymptotics together with a one-step reaction were used by McIntosh [9] to study the effects of acoustic forcing and feedback on unsteady, one-dimensional flames. He found that the flame stability was altered by the upstream acoustic feedback. Shyy et al [10] used a high-accuracy TVD scheme to simulate unsteady, one-dimensional longitudinal, combustion instabilities. However, numerical diffusion was not completely eliminated. Recently, Prasad [11] investigated numerically the interactions of pressure perturbations with premixed flames. He used complex chemistry to study responses of pressure perturbations in one-dimensional combustors. His results indicated that reflected and transmitted waves differed significantly from incident waves.

In the present paper, an extension of the work performed by Frendi [12] is carried-out. In particular, an attempt is made at understanding the onset of combustion instabilities as well as the use of passive devices to control them. Following the systematic experimental investigation of Laudien *et al.* [13], who studied the design of acoustic cavities, a numerical investigation is performed. The remainder of the paper is organized as follows; a brief description of the mathematical model is given in the next section followed by the numerical techniques used to solve it. Details of the results are then discussed followed by the concluding remarks.

### **Mathematical Model**

The model used to describe this problem is based on the nonlinear Euler equations, which can be written as

$$\frac{\partial \mathbf{U}}{\partial t} + \frac{\partial \mathbf{F}_i}{\partial x_i} = \mathbf{B} \quad (1)$$

where

$$\mathbf{U} = \begin{bmatrix} \rho \\ \rho v_j \\ \rho E \end{bmatrix} \text{ and } \mathbf{F}_i = \begin{bmatrix} \rho v_i \\ \rho v_i v_j + p \delta_{ij} \\ \rho v_i (E + p / \rho) \end{bmatrix} \quad (2)$$

and  $E = c_v T + \mathcal{Y}_2 v_i v_i$ . The closure is obtained through the equation of state for an ideal gas,  $p = \rho R T$ . For a two-dimensional axi-symmetric model the definition of the vector  $\mathbf{B}$  results from the transformation to cylindrical coordinates. If  $x_1$  is the axis of symmetry, the vector  $\mathbf{B}$  can be written as

$$\mathbf{B} = -\frac{1}{x_2} \begin{bmatrix} \rho v_2 \\ \rho v_2 v_1 \\ \rho v_2 v_2 \\ \rho v_2 (E + p / \rho) \end{bmatrix}. \quad (3)$$

### **Method of Solution**

The numerical methodology employed to solve Equation (1) can be described as a combination of a temporal discretization scheme, a spatial discretization scheme and, a discontinuity-capturing scheme. In the time discretization scheme the value of  $\mathbf{U}$  is sought given its value at a previous time by means of a Taylor series expansion. The spatial discretization is done using the Galerkin finite element method in which the integrated weighted-residual is minimized. To resolve discontinuities in the flow field, a convective flux correction term is devised. A second order accuracy is achieved in time while a second order or higher accuracy is achieved in space. Details of the numerical scheme can be found in [14, 15]. The boundary conditions used are rigid slip wall along the chamber walls and characteristic boundaries at the inlet (upstream boundary) and exit (downstream boundary). When acoustic disturbances are introduced in the chamber, the inlet pressure is specified as

$$p = p_0(1 + \varepsilon \sin(\omega t)) \quad \text{or} \quad p = p_0(1 + \varepsilon R(t)) \quad (4)$$

with  $\varepsilon$  being the excitation amplitude,  $\omega = 2\pi f$  the frequency and  $R(t)$  a random number. In Equation (4),  $p_0$  is the chamber pressure. The other inlet quantities are specified using the method of characteristics.

### **Results and Discussions**

The numerical investigation carried-out in this paper follows the detailed experimental investigation performed by Laudien et al. [13]. In particular, acoustic tests are performed in an axi-symmetric combustion chamber having the shape shown on Figure 1. A loudspeaker is placed at the center of the inlet boundary and emits plane harmonic or random acoustic waves. As described in section III, a finite element technique is used. Figure 1 also shows a typical grid used. A denser grid is used near the acoustic source. The conditions in the chamber are those of air at  $T = 300$  K and  $P = 1$  atm.

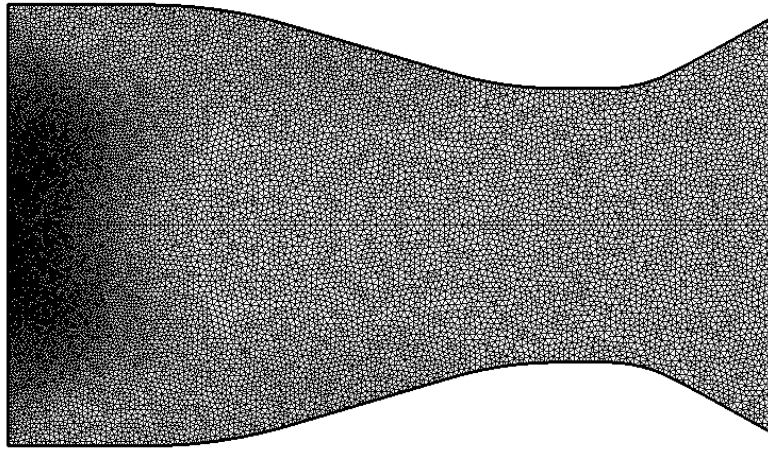


**Figure 1:** Typical unstructured grid used.

At first, the natural frequencies of the chamber are determined. To this end a random acoustic disturbance is introduced by the loudspeaker and the pressure fluctuations are monitored at several points in the chamber. Figure 2 shows the sound pressure level (SPL) as a function of the frequency at a point along the top chamber wall. Several peaks corresponding to the various chamber modes are obtained. In order to determine the mode shapes, one can excite the individual modes by introducing a plane, harmonic

acoustic wave at the given frequency. Following the determination of the natural frequencies of the chamber, a frequency of 1880 Hz, corresponding to a chamber mode, is selected for extensive tests. The first such test is to obtain the chamber response to a high (i.e. nonlinear) and low (i.e. linear) excitation amplitude. Figures 3(a)-(b) show the time histories of the pressure at an observation point along the top wall.

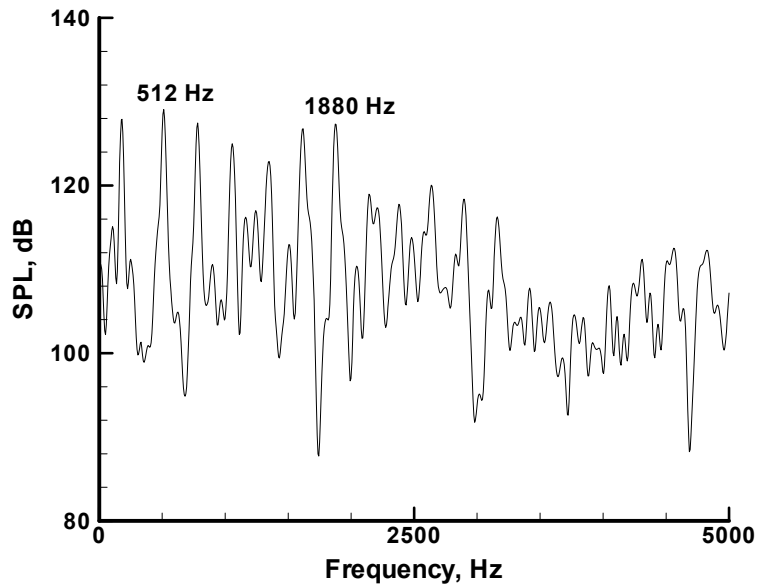


**Figure 2:** Frequency response of the combustion chamber to a random excitation.

Figure 3(a) shows rapid growth of the pressure oscillations and a slowly varying mean pressure, whereas Figure 3(b) shows a slow growth of the oscillations around a zero mean pressure. The corresponding power spectra are shown on Figs. 4(a)-(b). For the high excitation amplitude case,  $\varepsilon = 0.5$ , strong harmonics are shown to exist along with the fundamental frequency. It is believed that the nonlinear interaction between the fundamental and its harmonics is responsible in part for the rapid growth of the fluctuations. This point is confirmed by Fig. 4(b) which shows weak harmonics and therefore a quasi-linear behavior and weaker growth as shown by Fig. 3(a).

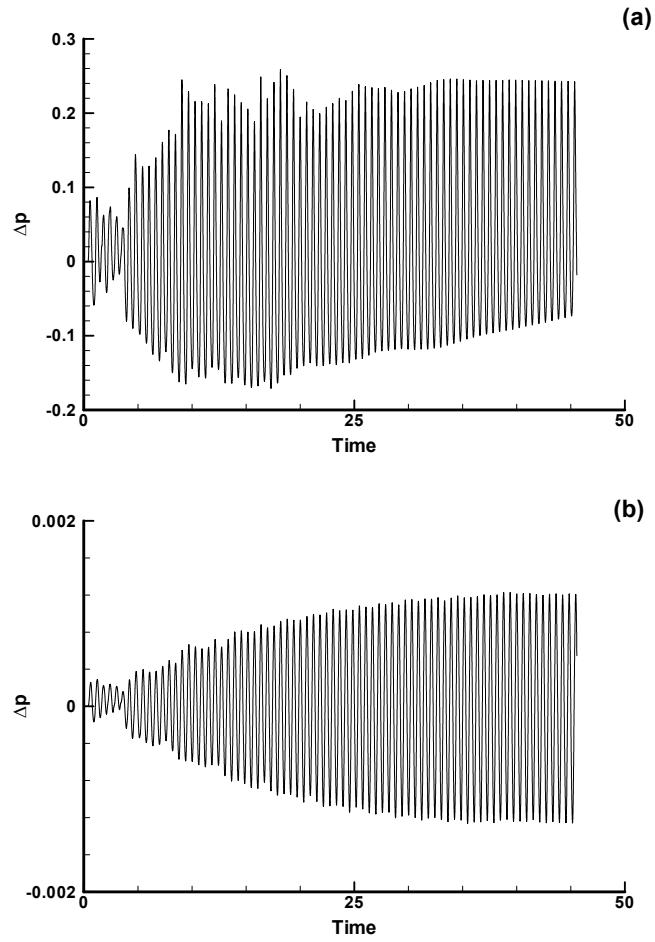


**Figure 3:** Time history of the pressure at a point along the top wall (a)  $\varepsilon = 0.5$ , (b)  $\varepsilon = 0.001$

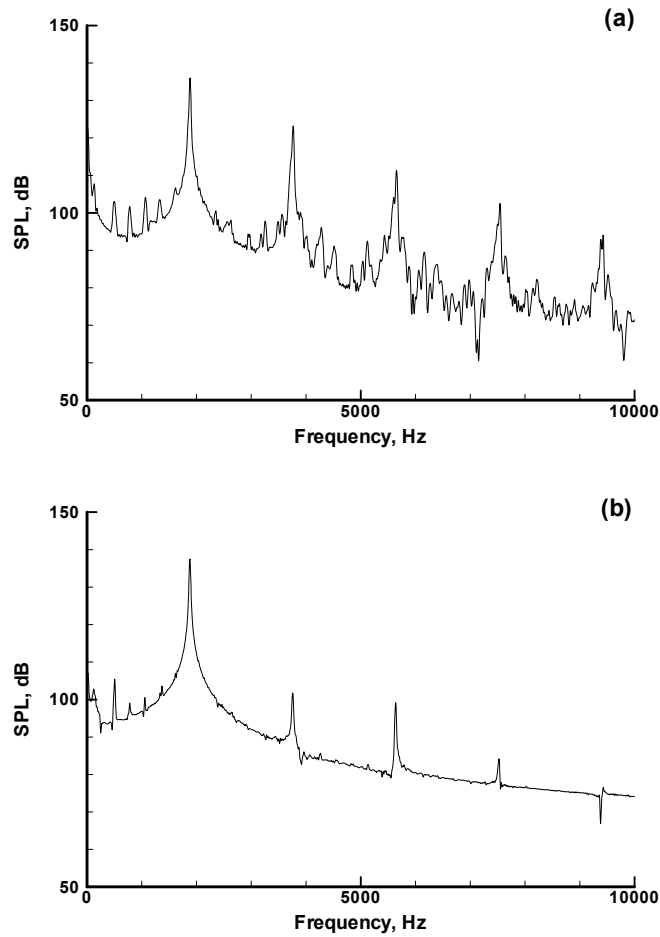


**Figure 4:** Sound pressure level at a point along the top wall (a)  $\varepsilon = 0.5$ , (b)  $\varepsilon = 0.001$ .

In order to assess the level of damping of a given mode by the chamber, the loudspeaker is turned on and then off and the pressure oscillations in the chamber are monitored at a given point. Figure 6 shows the damping level for two different modes 1880 Hz (Fig. 5(a)) and 512 Hz (Fig. 5(b)). In addition to the pressure oscillations, a decay curve described by  $Xe^{-\eta\omega t}$  is also shown, where  $\eta$  is the decay factor. The Figure shows that the mode corresponding to 1880 Hz decays faster than the mode corresponding to 512 Hz.

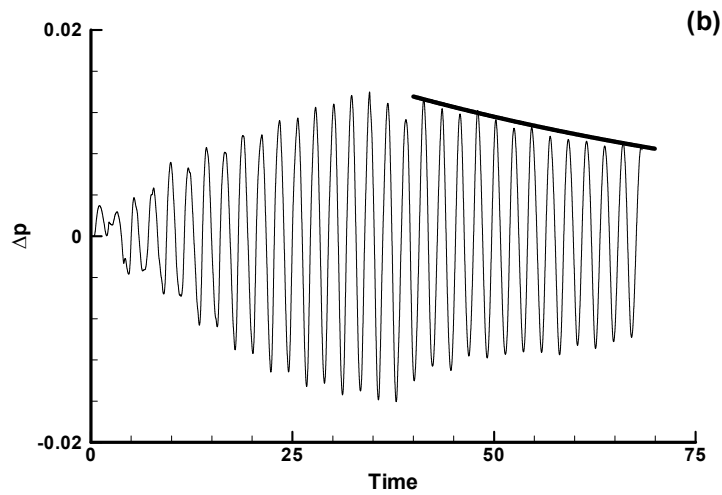
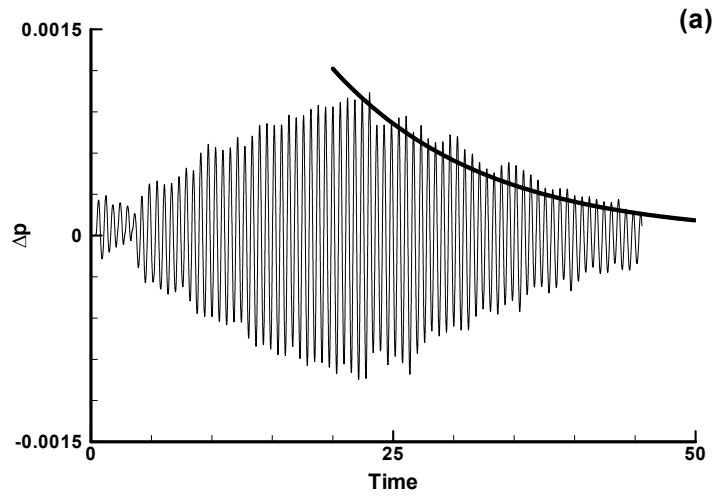


**Figure 5:** Decay rate of the pressure oscillations for two different chamber modes corresponding to (a) 1880 Hz (b) 512 Hz.

### Baffles

Following the preliminary studies presented above, the effect of adding a baffle in the radial direction of the inlet boundary, Figure 6, on the pressure oscillations in the chamber, is investigated. Figure 7 shows the pressure oscillations at the observation point along the top wall obtained with and without the baffle. The Figure shows a significant reduction of the oscillation amplitude of the pressure. The excitation amplitude used is  $\varepsilon = 0.1$ .

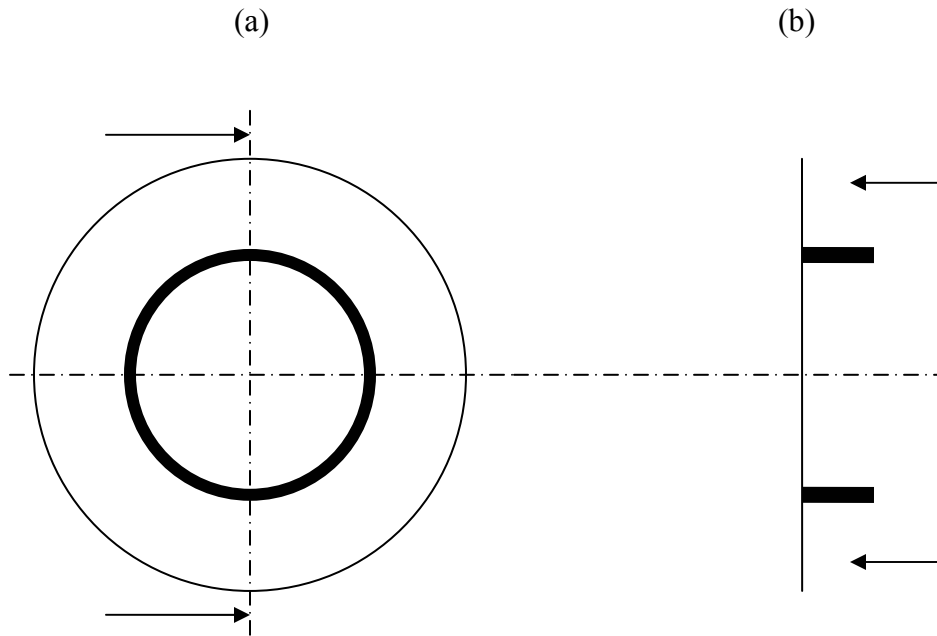


**Figure 6:** Sketch of the inlet boundary with a circular baffle; (a) front view, (b) side view

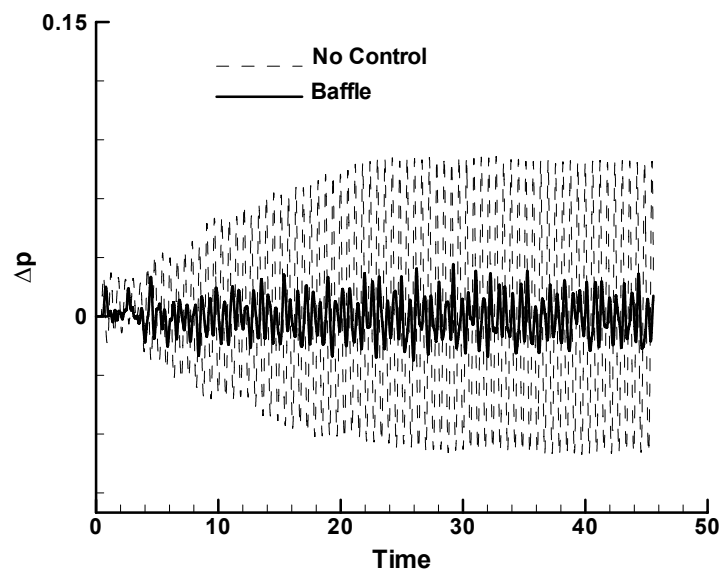


**Figure 7:** Effect of a radial baffle on the pressure oscillations in the chamber.

Figure 8 shows the corresponding power spectra. This figure answers a critical question that can be asked based on Figure 7, which is: where did the excitation energy go? The answer based on Figure 8 is: the energy is redistributed on a broader frequency spectrum. The reason

for this redistribution is that the excitation frequency, 1880 Hz, is no-longer a fundamental mode of the chamber, therefore there is no resonance.

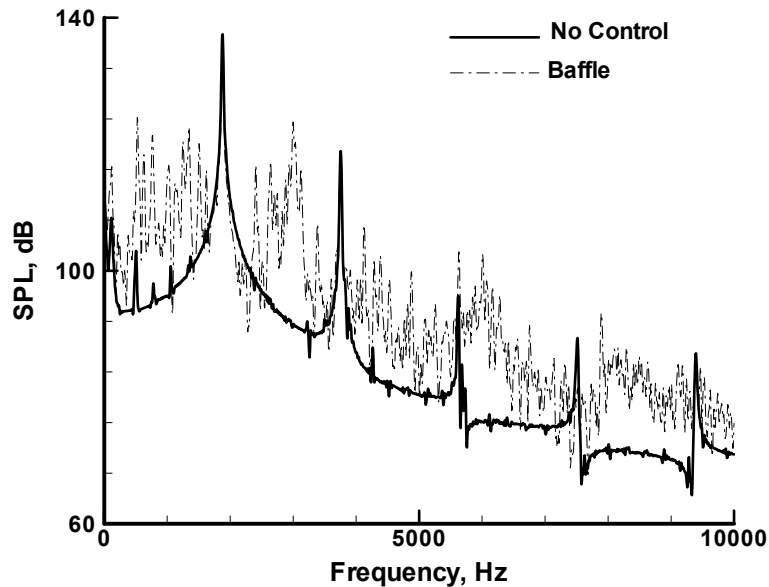


**Figure 8:** Power spectra of the pressure oscillations in the chamber with and without a baffle.

The effect of the baffle on the mode corresponding to the 512 Hz frequency is shown on Figs. 9(a)-(b). Figure 9(a) shows that after the excitation source is turned-off, Time > 30, a weak decay of the pressure oscillations is obtained without using the baffle. When a baffle is used, Fig. 9(b), the decay rate is larger as indicated by the steeper exponential curve. Therefore, one can conclude that even though the mode corresponding to the 512 Hz frequency is not suppressed by the baffle, its damping is increased. This results is in agreement with the experimental measurements of Laudien et al. [13]. The overall sound pressure level in the chamber based on the root-mean-square (rms) pressure has also dropped from 170 dB to 156.5 dB.

### **Helmholtz Resonators**

Helmholtz resonators, known also as acoustic cavities, are very popular passive control devices. Their use is wide spread; from controlling instability waves to noise reduction devices such as liners. A Helmholtz resonator is composed of an inlet of area  $S$  and length  $\ell$

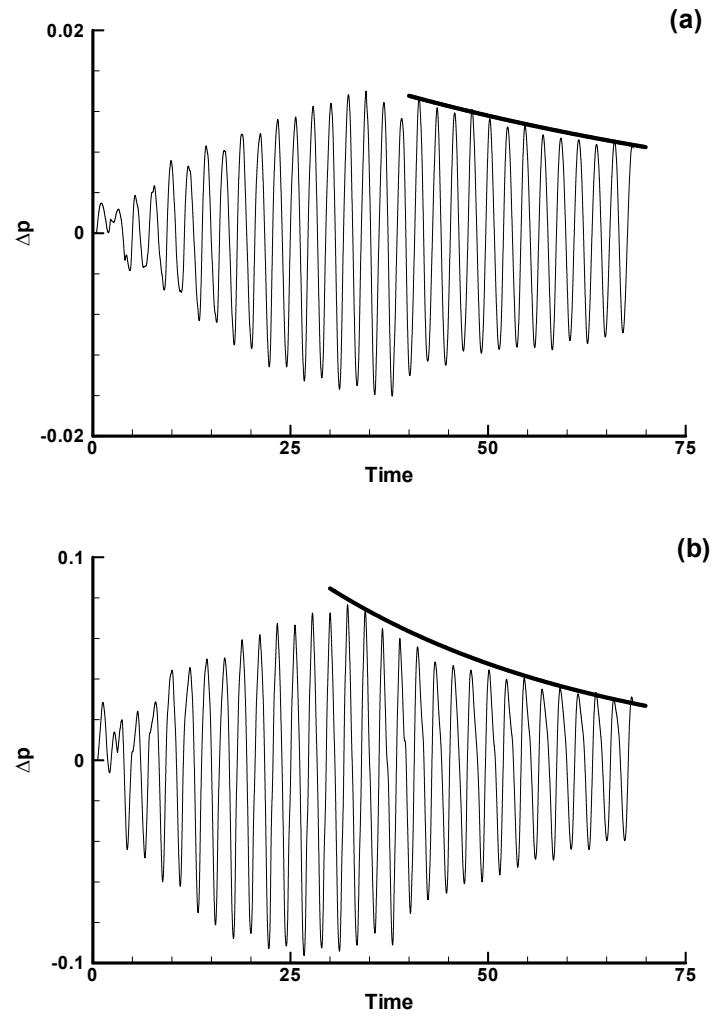


**Figure 9:** Time history of the chamber pressure along the top wall with the excitation source turned-on and then off (Time > 30), (a) without a baffle, (b) with a baffle.

followed by a cavity of volume  $\mathbf{V}$ , as shown in Fig. 10. For such a resonator, the resonant frequency is given by

$$f_0 = \frac{c}{2\pi} \sqrt{\frac{S}{V(l + \Delta l)}} \quad (5)$$

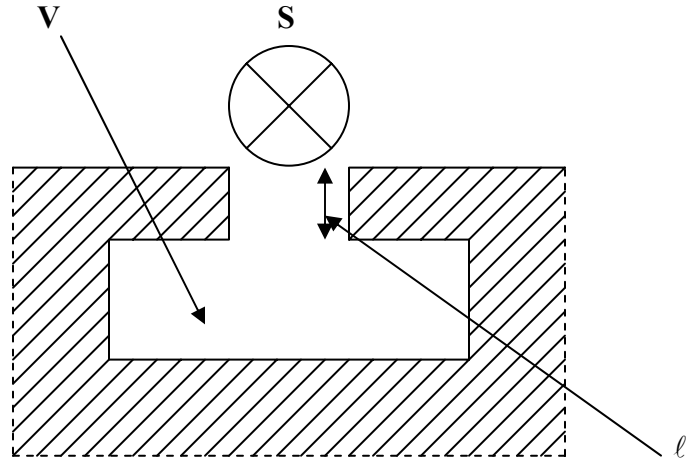


**Figure 10:** Typical geometry of a Helmholtz resonator.

where  $c$  is the speed of sound in the chamber and  $\Delta l \approx 0.85d$  with  $d$  being the inlet diameter. The Helmholtz resonator used is tuned to a resonant frequency of 1880 Hz, which corresponds to a chamber mode. When all the corners are sharp, Figure 11 shows that the presence of the resonator has reduced the pressure fluctuations in the chamber significantly. Similar to the baffle case, the power spectra show the presence of more frequencies when the resonator is used, supporting the argument that energy has been diverted from the fundamental to other frequencies. The overall sound pressure level in the chamber based on the rms-pressure has also dropped from 170 dB to 154 dB (2.5 dBs better than the baffle).

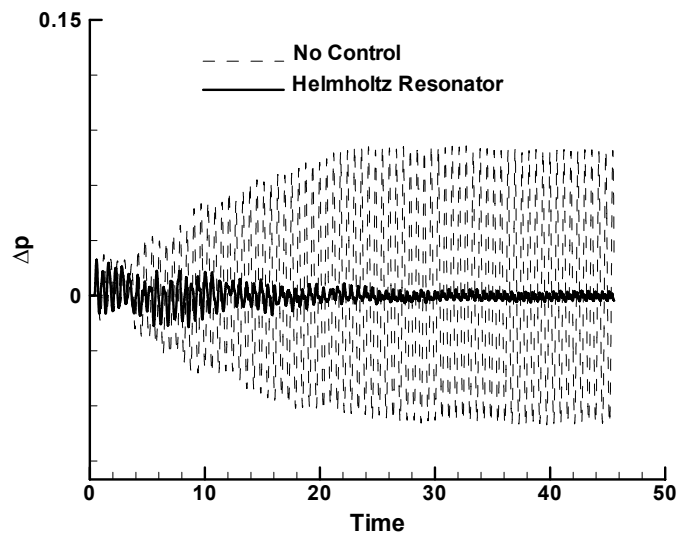


**Figure 11:** Effect of a Helmholtz resonator on the pressure oscillations in the combustion chamber.

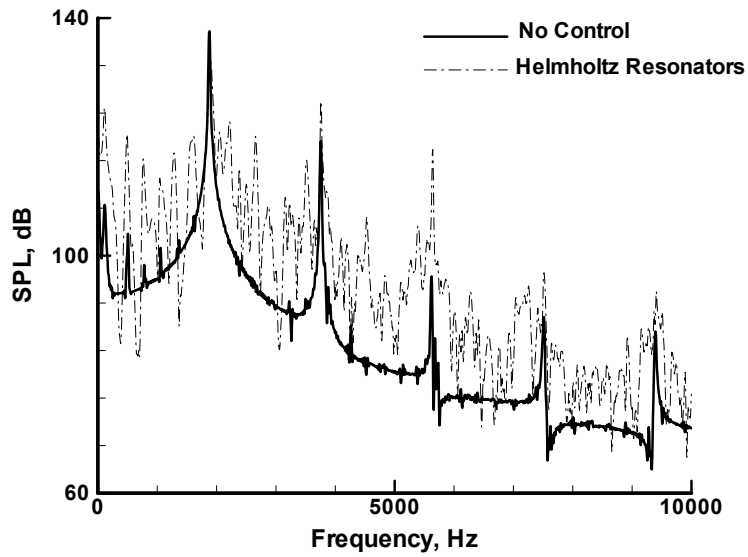


**Figure 12:** Power spectra of the pressure oscillations in the chamber with and without a resonator.

The effect of smoothing the various corners of the resonator on the overall sound pressure level in the chamber is shown on Figure 13. The figure shows that the best result is obtained when both inlet corners (referred to as throat corners on the Figure) are smoothed. Smoothing the other interior resonators corners did not achieve any additional improvement, as shown by the figure. Notice that “inlet corner” on the figure refers to the corner facing the combustion chamber.

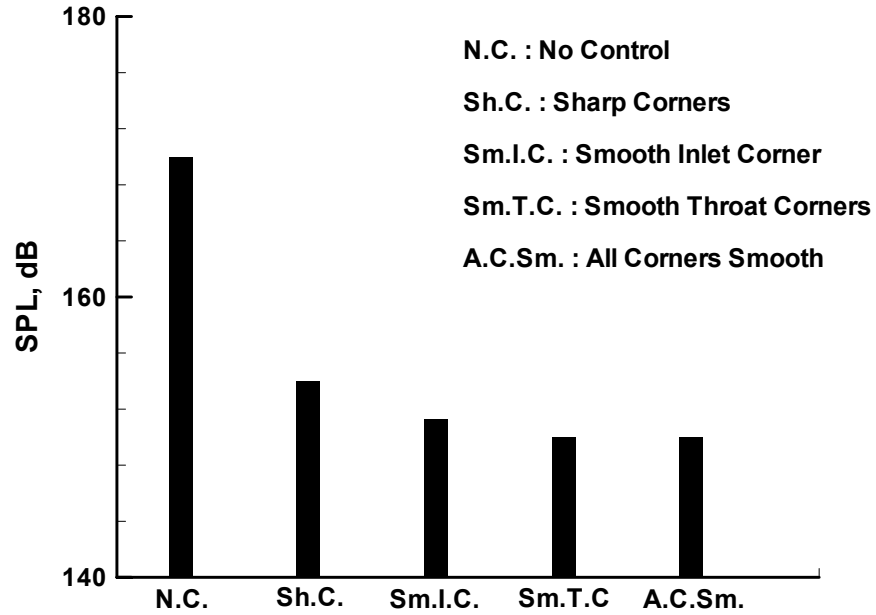


**Figure 13:** Effect of smoothing the resonator corners on the overall sound pressure level.

According to the experimental results of Laudien et al. [13], the resonator becomes less effective at higher noise levels in the chamber. This result is confirmed by our computations, which show less-drop in dB-level, Figure 14, even with the best configuration of Fig. 13.

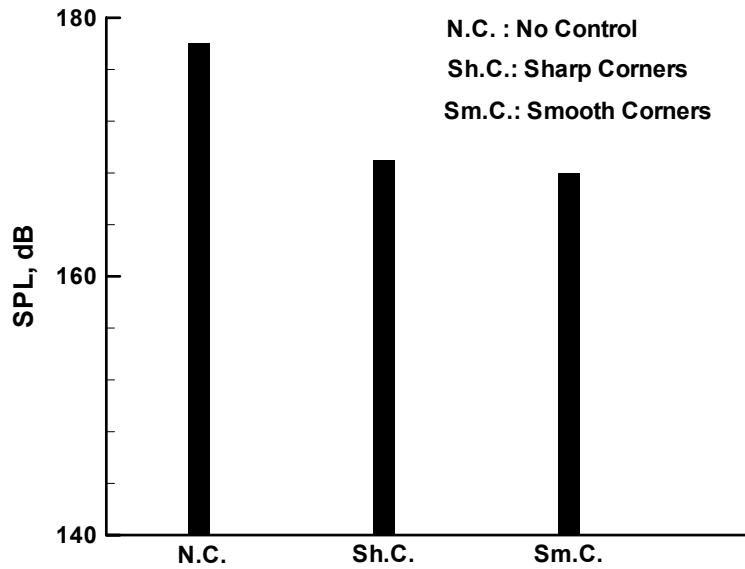


**Figure 14:** Effect of a Helmholtz resonator on the overall sound pressure level of a combustion chamber at high noise levels.

The problem in designing a Helmholtz resonator is the required knowledge of the tuning or resonant frequency. Therefore, one question we needed to answer is how effective a resonator is when the design frequency is slightly off? This is of practical importance since in an actual combustion experiment the frequency to be controlled is not known accurately. To answer this question, a resonator tuned to a frequency of 1800 Hz was used to control a mode of frequency 1880 Hz. Figure 15 shows the overall sound pressure level in the chamber with an “On-Design” and an “Off-Design” resonator. The “Off-Design” resonator achieves 13.5 dB less reduction than the “On-Design” one. This is significant since the “Off-Design” frequency is only 80 Hz off the design value.

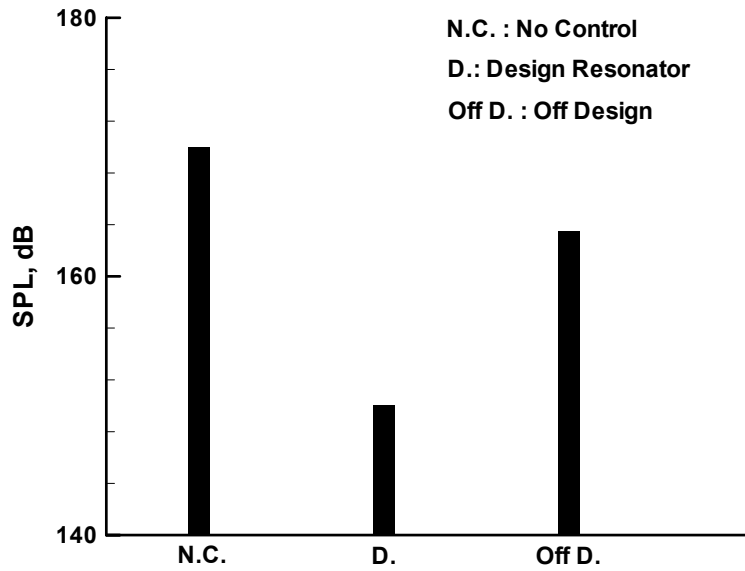


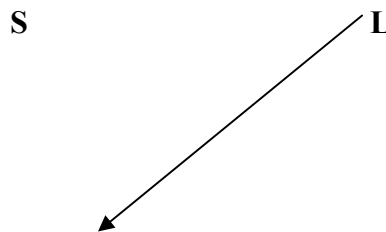
**Figure 15:** Effect of resonator design frequency on the overall sound pressure level in the combustion chamber.

### Quarter-Waves

Another passive control device commonly used is a quarter-wave. It is somewhat similar to a Helmholtz resonator except for the absence of the cavity part, Figure 16. The resonant frequency of a quarter-wave is given by

$$f_0 = \frac{c}{4(L + \Delta\ell)} \quad (6)$$

with  $c$  being the speed of sound and  $\Delta\ell \approx 0.85d$  with  $d$  the quarter-wave diameter.



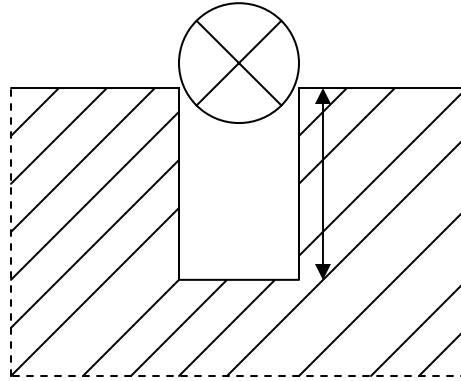


**Figure 16:** Typical geometry of a quarter-wave.

In practice, several shapes of quarter-waves are used. In this study two of these shapes will be investigated; an L-shaped quarter-wave and a straight quarter-wave. In addition, the effect of smoothing the corners will be analyzed. Figure 17 shows the time history of the chamber pressure with and without a tuned quarter-wave. A significant reduction in pressure oscillations is achieved when using a quarter-wave. Figure 18 shows the corresponding power spectra. Similar to the baffle and resonator, the quarter-wave effect is to detune the

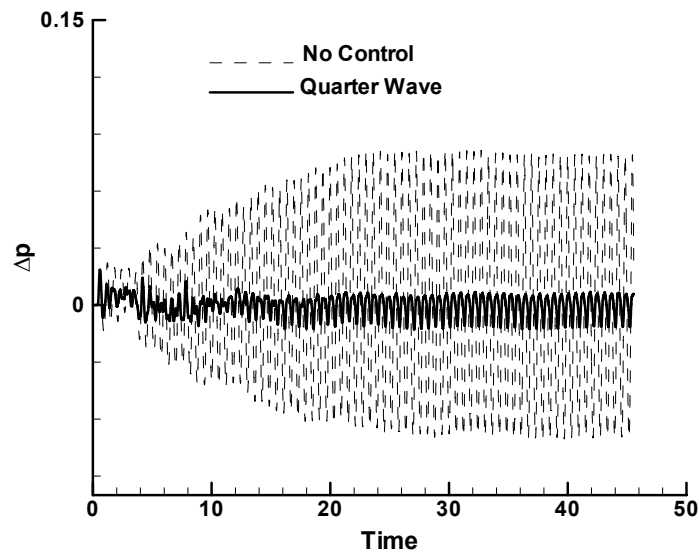


**Figure 17:** Effect of a quarter-wave on the pressure oscillations in the combustion chamber.

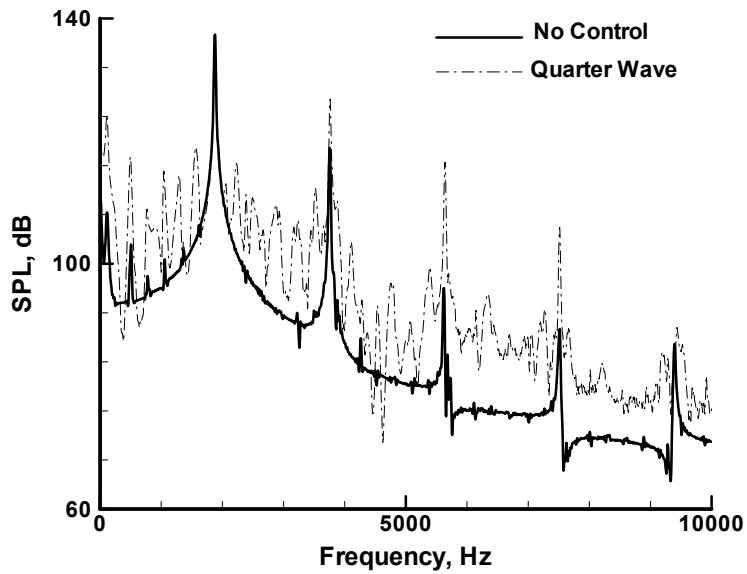


**Figure 18:** Power spectra of the pressure oscillations in the chamber with and without a quarter-wave.

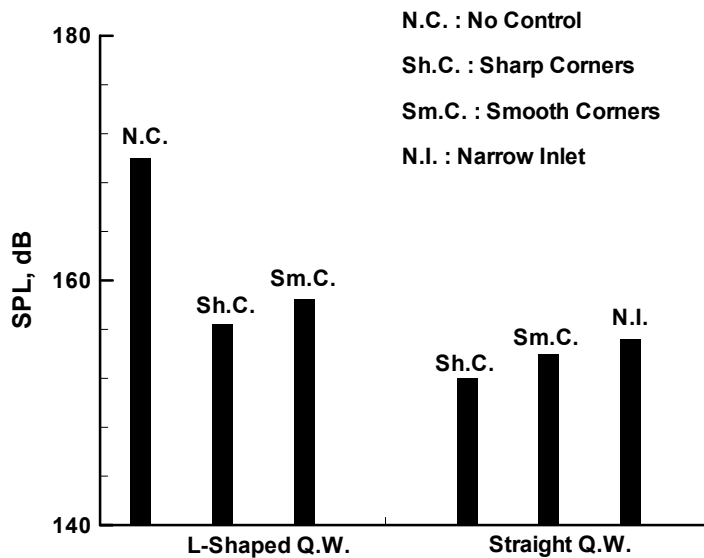
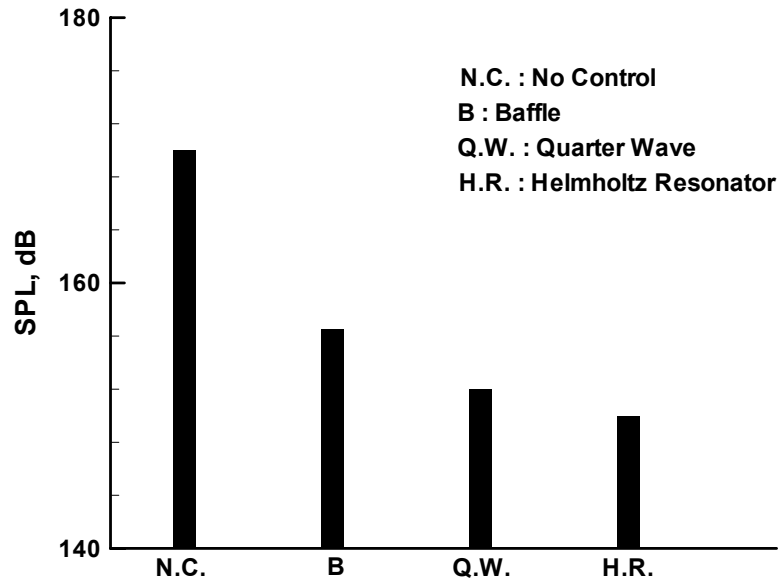


**Figure 19:** Effect of L-shaped and Straight quarter-waves with different corner geometries on the overall sound pressure level in the chamber.

chamber and spread the energy to other frequencies. A comparison of an L-shaped quarter-wave to a straight one with various corner geometries is shown on Figure 19. For all corner geometries, the straight quarter-wave achieves more reduction in SPL than the L-shaped one. The figure also shows that smoothing the inlet corners has an adverse effect on the overall

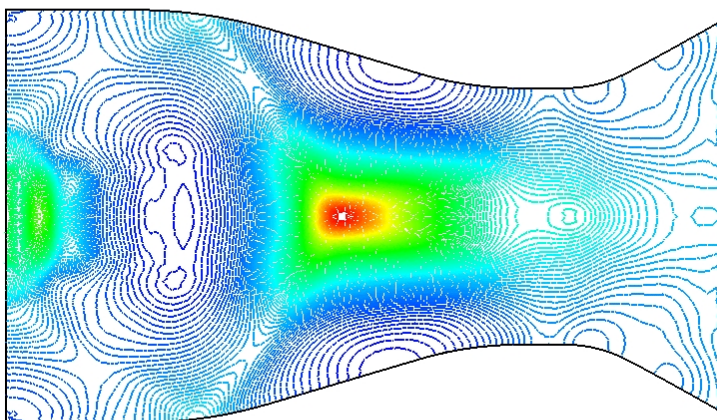
SPL in the chamber for both quarter-wave geometries. For the straight quarter-wave, a narrow inlet resulted in a higher SPL, as expected.

Figure 20 shows a comparison of overall SPL in the combustion chamber for all the passive devices tested in this study. The figure shows that the Helmholtz resonator with a smooth inlet gives the best results.



**Figure 20:** Comparison of overall sound pressure level in the chamber obtained with the various passive devices.

Figures 21-24 show the instantaneous pressure contours in the chamber obtained with the various passive devices. A different pattern can be observed for each device.



**Figure 21:** Instantaneous pressure contours in the combustion chamber obtained without a passive device.

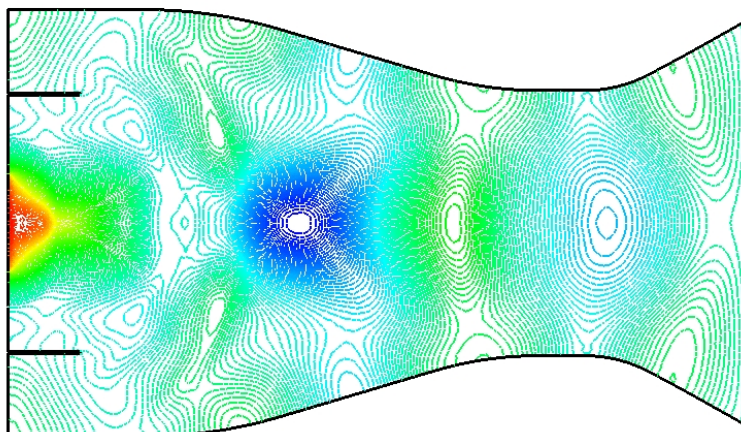


**Figure 22:** Instantaneous pressure contours in the combustion chamber obtained with a baffle.

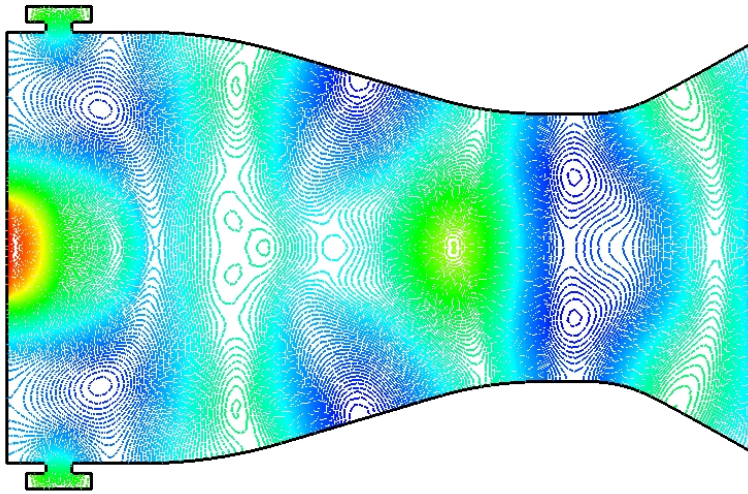


**Figure 23:** Instantaneous pressure contours in the combustion chamber obtained with a Helmholtz resonator.

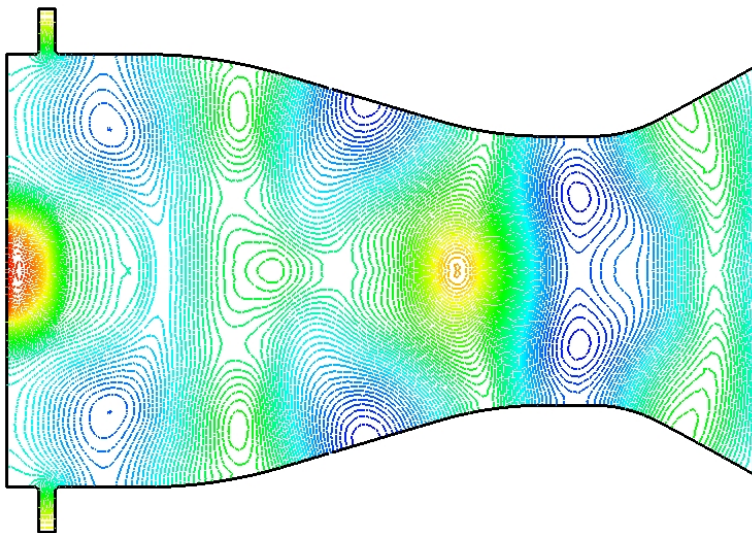


**Figure 24:** Instantaneous pressure contours in the combustion chamber obtained with a quarter-wave.

### **Concluding Remarks**

Numerical experiments have been carried-out to study the effectiveness of various passive devices to control combustion instabilities. The results show that, for the given mode studied, a Helmholtz resonator with a smooth inlet achieves the best control results. However, at high sound pressure levels in the chamber, the resonator becomes less effective. For the case of a quarter-wave, it is found that a straight shape performs better than an L-shaped quarter-wave. In addition, smoothing the corners of a quarter-wave inlet may have an adverse effect on the overall sound pressure level in the chamber. The computational results presented here are in good qualitative agreement with the experimental measurements of Laudien *et al.* [13].

### **Acknowledgements**

This work was supported by a summer faculty fellowship from NASA Marshall Space Flight Center with Tom Nesman as the technical monitor.

### **References**

- [1] Yang, V., and Anderson, W.E., "Liquid Rocket Engine Combustion Instability", *Progress in Aeronautics and Astronautics*, Vol. 169, Editor-in-Chief Paul Zarchan, 1995.
- [2] "Liquid Propellant Rocket Combustion Instability", NASA SP-194, Edited by David T. Harrje, 1972.
- [3] Giammar, R.D., and Putnam, A.A., "Combustion Roar of Premix Burners, Singly and in Pairs," *Combustion and Flame*, Vol. 18, 1972, pp. 435-438.
- [4] Karchmer, A.M., "Identification and Measurement of Combustion Noise from a Turbofan Engine Using Correlation and Coherence Techniques," NASA TM-73747, 1977.
- [5] Rayleigh, J.W.S., "The Explanation of Certain Acoustical Phenomena," *Nature*, Vol. 18, 1878, p. 319.
- [6] Bloxidge, G.J., Dowling, A.P., Hooper, N., and Langhorne, P.J., "Active Control of Reheat Buzz," *AIAA Journal*, Vol. 26, 1988, pp. 783-790.
- [7] Abouseif, G.E., Keklak, J.A., and Toong, T.Y., "Ramjet Rumble: The Low Frequency Instability Mechanism in Coaxial Dump Combustors," *Combustion Science and Technology*, Vol. 36, 1984, pp. 83-108.
- [8] Yang, V. and Culick, F.E.C., "Linear Theory of Pressure Oscillations in Liquid-Fueled Ramjet Engines," *AIAA Paper 83-0574*, 1983.
- [9] McIntosh, A.C., "The Effect of Upstream Acoustic Forcing and Feedback on the Stability and Resonance of Anchored Flames," *Combustion Science and Technology*, Vol. 49, 1986, pp. 143-167.
- [10] Shyy, W., Thakur, S., Udaykumar, H.S., "A High Accuracy Sequential Solver for Simulation and Active Control of Longitudinal Combustion Instability," *Computing Systems in Engineering*, Vol. 4, No. 1, 1993, pp. 27-41.
- [11] Prasad, K., "Interaction of Pressure Perturbations with Premixed Flames", *Combustion and Flames*, Vol. 97, pp. 713-200, 1994.
- [12] Frendi, A., "On the Role of Acoustic Coupling on Combustion Instabilities", *AIAA-2002-3181*, Hilton Head, South Carolina, 2003.
- [13] Laudien, E., Pongratz, R., Pierro, R., and Preklik, D., "Experimental Procedure Aiding the Design of Acoustic Cavities", *Liquid Rocket Engine Combustion Instability*, edited by Vigor Yang and William Anderson, *Progress in Aeronautics and Astronautics*, Vol. 169, pp.377-399, 1995.
- [14] Canabal, F., and Frendi, A., "A Finite Element Based Flux Correction Scheme for the Euler Equations", *AIAA-2003-3121*.

- [15] Canabal, F., “Prediction and Suppression of Ignition Overpressure”, PhD Thesis, University of Alabama in Huntsville, 2004.

2004

**NASA FACULTY FELLOWSHIP PROGRAM**

**MARSHALL SPACE FLIGHT CENTER**

**THE UNIVERSITY OF ALABAMA  
THE UNIVERSITY OF ALABAMA IN HUNTSVILLE  
ALABAMA A&M UNIVERSITY**

**LOCAL INTENSITY ENHANCEMENTS IN SPHERICAL  
MICROCAVITIES: IMPLICATIONS FOR PHOTONIC  
CHEMICAL AND BIOLOGICAL SENSORS**

## Introduction

In this report, we summarize recent findings regarding the use spherical microcavities in the amplification of light that is inelastically scattered by either fluorescent or Raman-active molecules. This discussion will focus on Raman scattering, with the understanding that analogous processes apply to fluorescence.

Raman spectra can be generated through the use of a very strong light source that stimulates inelastic light scattering by molecules, with the scattering occurring at wavelengths shifted from that of the source and being most prominent at shifts associated with the molecules' natural vibrational frequencies. The Raman signal can be greatly enhanced by exposing a molecule to the intense electric fields that arise near surfaces (typically of gold or silver) exhibiting nanoscale roughness. This is known as surface-enhanced Raman scattering (SERS). SERS typically produces gain factors of  $10^3 - 10^6$ , but under special conditions, factors of  $10^{10} - 10^{14}$  have been achieved (Felidj, 2003).

An intriguing mechanism for near-field enhancement arises from microcavity whispering gallery modes (WGMs). Also known as morphology-dependent resonances (MDRs), these modes appear at sharply defined spectral positions for any sufficiently large and lossless spherical particle. (MDRs also appear in cylindrical and spheroidal microstructures.) A key feature of a resonator is its quality factor  $Q$ , which is the ratio of stored energy to the energy lost per cycle through the cavity. Microspheres can sustain  $Q$ s approaching  $10^{10}$  (cf. Vernooy et al., 1998). The dramatic increases in photon densities within these microcavities have been shown to produce low-threshold nonlinear optical effects such as stimulated Raman scattering, lasing, spectral hole burning, and cavity quantum electrodynamic effects. In addition to very high photon densities in the mode volumes of microcavities, very strong evanescent fields reside on and near their outer surfaces. Vigorous research has begun into ways to use these strong surface fields to detect and analyze minute amounts of molecular species adsorbed onto the resonator. Optical shifts in MDRs have been used to detect adsorption of proteins onto glass spheroids and resonant enhanced evanescent wave fluorescence has been proposed for photonic biosensing, as have integrated optical microcavities.

Calculations presented below indicate that the absorption cross sections of metal nanoparticles immobilized onto dielectric microspheres can be greatly enhanced by cavity resonances in the microspheres. Molecules attached to the immobilized nanoparticles would thus experience cascaded surface-photoenhancements (CSPs), leading to increased gains in Raman scattering of several orders of magnitude over conventional SERS effects. Gain factors of  $10^3 - 10^4$  are predicted for realistic, though challenging, experimental conditions using homogenous microspheres. Our calculations further indicate that carefully structured cladded microspheres, acting as coupled microcavities, could produce a further gain of 3 or 4 orders of magnitude. Cascaded surface photoenhancement thus has the potential of pushing sensitivities of chemical and biological detectors to dramatically lower thresholds.

## Enhanced absorption by nanoparticles on a microcavity

The electric field at any point may be expanded in vector spherical harmonics  $\mathbf{N}_{np}$ . The vector spherical harmonics may be written as  $\mathbf{N}_{np} = Rg\mathbf{N}_{np} + iIg\mathbf{N}_{np}$ , where Rg and Ig stand for ‘regular’ (finite at the origin) and irregular. The expansion for the incident field (here, an infinite plane wave) is

$$\mathbf{E}^{\text{inc}} = \sum_{np} q_{np} Rg\mathbf{N}_{np}, \quad (1)$$

and for the external and internal fields of a homogeneous sphere, respectively,

$$\mathbf{E}^{\text{Sca}} = \sum_{np} q_{np} a_{np} \mathbf{N}_{np}, \quad (2)$$

$$\mathbf{E}^{\text{Cor}} = \sum_{np} q_{np} c_{np} Rg\mathbf{N}_{np} \quad (3)$$

where the expansion coefficients  $a_{np}$  and  $c_{np}$  are functions of the sphere’s refractive index  $m$ , radius  $a$ , and the wavelength  $\lambda$ . These coefficients and the  $q_{np}$  are well-known (cf. Fuller and Mackowski, 2000), and are also used in calculating the cross sections for scattering and absorption,  $C_{sca}$  and  $C_{abs}$ , respectively.

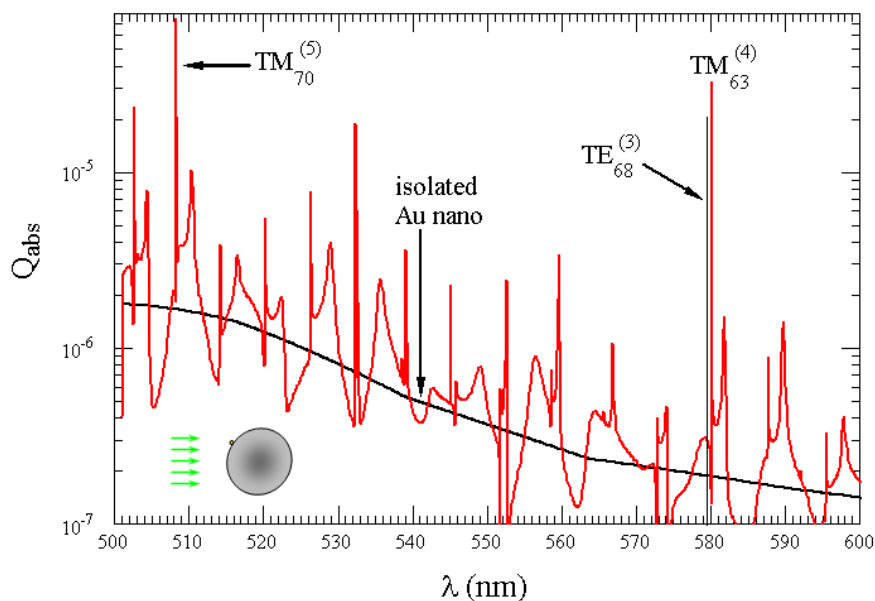


Figure 1: Absorption efficiency spectrum of a 10 nm Au sphere on a 5  $\mu\text{m}$  latex microbead. The position of the nanoparticle (not drawn to scale) relative to the incident beam is shown in the inset in the lower left corner of the graph. The absorption efficiency of the nanoparticle in the absence of the sphere is given by the black curve. The calculations are based on an exact formulation for compounded sphere systems (Fuller and Mackowski, 2000).

Figure 1 shows how the absorption efficiency  $Q_{abs}$  ( $= C_{abs}$  divided by, in this case, the microsphere’s geometric cross section) of a Au nanoparticle may be enhanced near the surface of a microcavity as the wavelength of the incident beam is tuned through a series of microsphere WGMs. There is no absorption in the microsphere itself, and so this graph shows that the Au nanoparticle is being exposed to greatly enhanced local intensities.

For illustrative purposes, latex beads were chosen as the microcavities for this calculation. In practice, one must choose microcavities that are made from materials, such as silica, that will not themselves produce a strong Raman background signal. The  $Q_{abs}$  spectra and local energy densities will be similar for equivalent modes, regardless of the dielectric chosen.

The electromagnetic ‘terrain’ responsible for this resonance-enhanced absorption is shown in Fig. 2, which is a plot of the ratio of the energy density near or in the microcavity to that of the incident field. This calculation was made with an existing version of the author’s computer program for scattering and absorption by a sphere. That this is a 3rd-order resonance may be inferred from the presence of three concentric rings in the mode volume of the cavity.

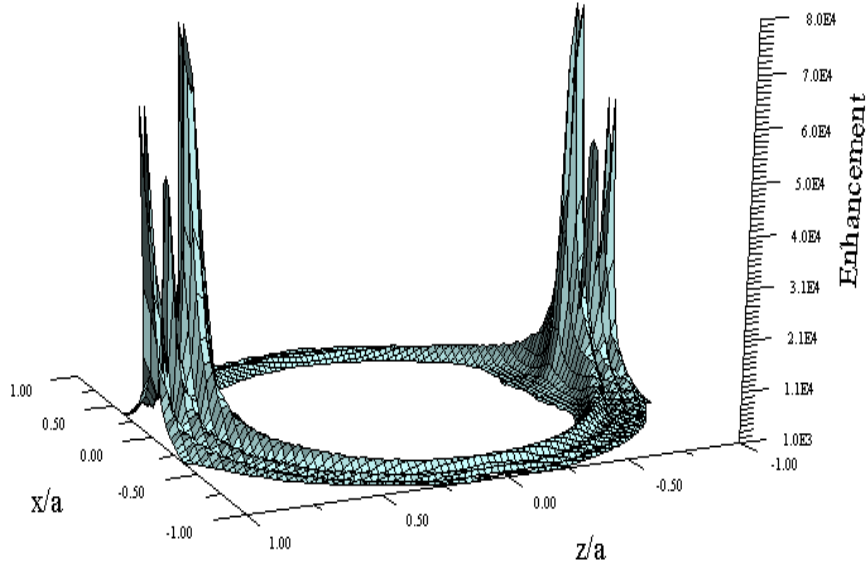


Figure 2: Electromagnetic energy density in the equatorial plain of a microsphere tuned to a 3rd-order  $TE_{69}$  resonance. The incident field propagates parallel to the  $z$ -axis. In order to better illustrate the structure of the mode volume of the resonance, only enhancements of greater than  $10^3$  are shown.

### Internal and near fields of homogeneous and core-shell microspheres on resonance

The geometry of the problem is illustrated in Figure 3 for the case of a sphere with a concentric spherical inclusion. The field associated with a particular  $n$  may be written as a sum of partial waves multiply reflected between the surface of the core and the outer (concave) surface of the shell. Defining

$$f_{np} = \frac{c_{np}}{1 - 2a_{np}\check{a}_{np}} \quad (4)$$

we have shown (Fuller and Smith, 2003) that the fields in the core and shell may be written, respectively, as

$$\mathbf{E}^{\text{shl}} = \sum_{np} q_{np} f_{np} (Rg\mathbf{N}_{np} + 2a_{np}\mathbf{N}_{np}) \quad \text{and} \quad \mathbf{E}^{\text{cor}} = \sum_{np} q_{np} f_{np} 2c_{np} Rg\mathbf{N}_{np}. \quad (5)$$

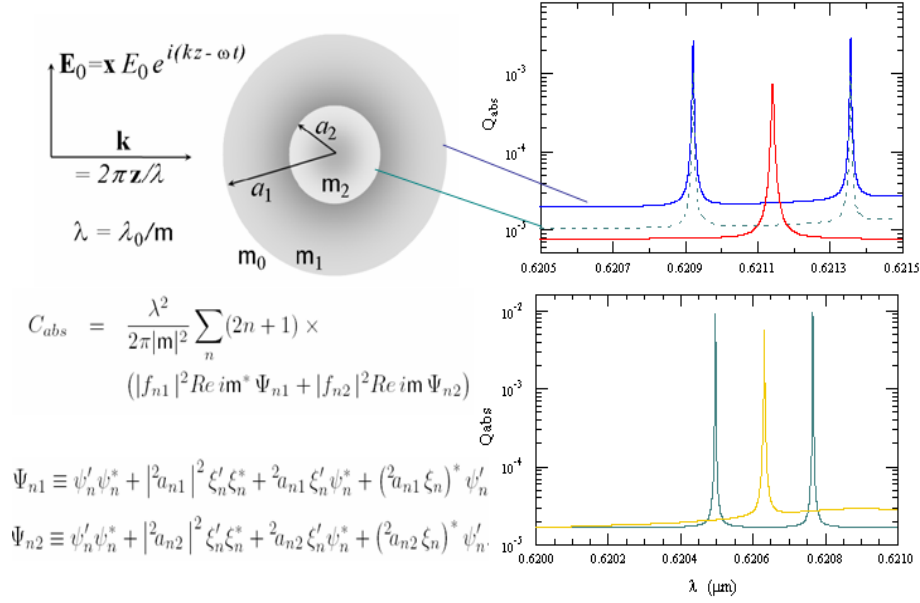


Figure 3: Geometry of the core-shell problem along with two illustrations of mode splitting by coupled concentric microcavities that have been tuned to co-resonance. The equation for the absorption cross section at a particular distance from the center of the microcavity is also provided, and was developed by Fuller and Smith (2003). Evaluation of the equation at the outer surface of the shell and at the surface of the core then gives the total absorption cross section of the layered sphere and of the core, respectively. The difference of these two cross sections then gives the absorption cross section of the shell.

Also shown in Fig. 3 is the spectrum of slightly absorbing microcavities. The mode splitting displayed Fig. 3 is potentially of great consequence to the future development of Raman-based detection and analysis: The enhancement of the intensity of Raman scattering by metal nanoparticles is expressed in terms of incident and scattered local electric field amplitudes  $E_{loc}$  as

$$I_{SERS} \propto G_{SERS} \propto \frac{|E_{loc}(\omega_{exc})|^2 |E_{loc}(\omega_{RS})|^2}{|E_0(\omega_{exc})|^2 |E_0(\omega_{RS})|^2}, \quad (6)$$

where  $\omega_{exc}$  and  $\omega_{RS}$  are the circular frequencies of the incident (excitation) and Raman scattered light, respectively. Excitation of the nanoparticle-microsphere systems discussed above results in a gain of

$$|E_{loc}(\omega_{exc})|^2 / |E_0(\omega_{exc})|^2 \approx 10^2 - 10^4. \quad (7)$$

If, however, one were able to tune coupled cavity resonators to co-resonance, such that the excitation frequency coincided with the left peak in Fig. 3 and the right peak were centered on a Raman-active band, then that spectral feature would be amplified by a factor of  $10^4 - 10^8$  beyond the gain already realized from SERS alone.

Fig. 4 provides a view of the local intensity enhancement for both homogeneous and co-resonant concentric microcavities. For this part of the work, the author's computer program for calculating scattering and absorption by a homogeneous sphere was modified to allow calculation of the internal and near fields of core-shell systems. The modifications were made in a way that should allow for easy extension of the program to the case of multilayered structures.

Figs. 3 and 4 as well as Figs. 1 and 2 indicate that an order-of-magnitude jump in absorption efficiency relates roughly to an order-of-magnitude increase in  $|\mathbf{E}|^2$  near the surface of the cavity and so the absorption spectrum of a nanoparticle on the surface of the microsphere may be used to predict SERS gain factors. Calculations also indicated that coupling between the nanoparticle and the resonator will spoil the cavity  $Q$  if the diameter of the Au particle exceeds  $\approx 150$  nm. Also from Figs. 2 and 4 it should be noted that considerably larger (by yet another order of magnitude) gain factors are present near the poles of the microcavities.

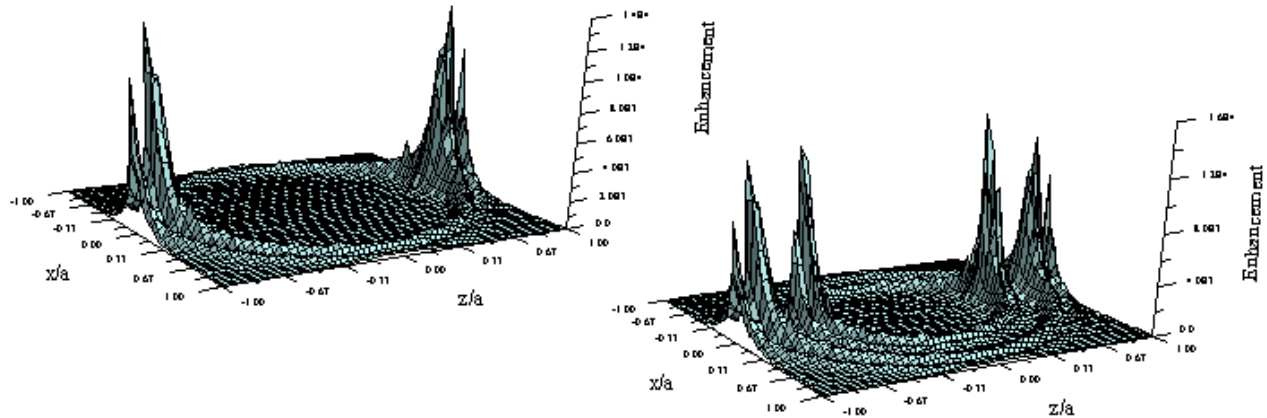


Figure 4: Enhancement factors in resonant homogeneous sphere and in co-resonant core-shell microcavity

## Acknowledgments

The author wishes to express his great appreciation for the many valuable discussions with Dr. David D. Smith, and for the productive environment provided by MSFC for the performance of this research.

## References

Félidj, N., J. Aubard, G. Lévi, J. R. Krenn, A. Hohenau, G. Schider, A. Leitner, and F. R. Aussenegg, Optimized surface-enhanced Raman on gold nanoparticle arrays, *Appl. Phys. Lett.* **82** 3095–3097(2003).

Fuller, K. A. and D. W. Mackowski, “Electromagnetic Scattering by Compounded Spherical Particles,” in *Light Scattering by Nonspherical Particles*, M. I. Mishchenko, J. W. Hovenier, and L. D. Travis, Eds., Academic Press, NY 2000.

Fuller, K. A. and D. D. Smith, ‘Partial wave analysis of coupled photonic structures,’ in *The 2002 NASA Faculty Fellowship Program Research Reports*, J. Bland Ed., Marshall Space Flight Center, 2003.

Smith, D. D. and K. A. Fuller, Photonic bandgaps in Mie scattering by concentrically stratified spheres, accepted for publication, *J. Opt. Soc. Am. B*, **19** No. 10. (2002).

Vernooy, D. W., V. S. Ilchenko, H. Mabuchi, E. W. Streed, and H. J. Kimble, High- $Q$  measurements of fused-silica microspheres in the infrared, *Opt. Lett.* **23**, 247–249( 1998)

2004

**NASA FACULTY FELLOWSHIP PROGRAM**

**MARSHALL SPACE FLIGHT CENTER**

**THE UNIVERSITY OF ALABAMA  
THE UNIVERSITY OF ALABAMA IN HUNTSVILLE  
ALABAMA A&M UNIVERSITY**

**ANALYSIS OF UPPER AIR, GROUND AND REMOTE  
SENSING DATA FOR THE ATLAS FIELD CAMPAIGN  
IN SAN JUAN, PUERTO RICO**

Prepared By:	Jorge E. González-Cruz
Academic Rank:	Professor
Institution and Department:	Santa Clara University Mechanical Engineering Department
NASA/MSFC Directorate:	Global Hydrology and Climate Center
MSFC Colleague:	Dr. Jeff Luvall Dr. Doug Rickman

## **Introduction**

The general climate of the island of Puerto Rico is dominated by the easterly trade winds from the Atlantic Ocean, and during synoptically calm days by the topographic and local land surface characteristics [1]. The urban canopy of the metropolitan area of San Juan, capital city of the Island, may introduce a new microclimate that changes the characteristics of the low atmosphere and interacts with the other microclimates already present in the island. The primitive land cover and land use (LCLU) of the metropolitan area of San Juan was composed by broadleaf trees, moist soils, and very dense vegetation in general.

The urban LCLU changes the balance for the mass, momentum and energy between the bottom boundary and the lower atmosphere, creating different climate conditions over urban and rural regions. Some of these differences are low relative humidity and high temperatures observed in urban areas when compared to rural areas. These in turn produces a convective circulation over the urban areas, a phenomenon compared to the sea and land breezes, commonly known as heat islands (UHI). Factors that contribute to the formation of the UHI are anthropogenic heat sources, aerosols from pollutants, fast water canalization due to the presence of buildings and streets, among others. The comparison between urban and rural climates is the most common approach to analyze the UHI. These contrasts are larger in clear and calm conditions and tend to disappear in cloudy and windy weather. The UHI was recognized in the early 1950's as closed isotherms that separates the city from the general temperature field [2].

The impact of the urban LCLU in San Juan, Puerto Rico, was quantified calculating the difference between historical data sets for the air temperature over an identified urban area and a rural area  $dT(U-R)$ . The analysis of the climatological data revealed that a UHI exists in the metropolitan area of San Juan, Puerto Rico. The data reveals a permanent urban heat island effect present in the SJMA during the year, which is increasing at a rate of  $0.41^{\circ}\text{C}/\text{decade}$ . These findings encouraged the planning and execution of an intense field campaign in February 2004 referred as the ATLAS San Juan mission. The focus of the remaining of this report is the analysis of the data for this field campaign.

## **Description of the Atlas Mission**

The Airborne Thermal and Land Applications Sensor (ATLAS) from NASA/Stennis operates in the visual and IR bands. ATLAS is able to sense 15 multispectral radiation channels across the thermal - near infrared - visible spectrums and is capable of approximately 2.0 meter resolution per pixel when flown in NASA's Learjet. An ATLAS mission flight was conducted in San Juan, Puerto Rico during February 2004 to further investigate the impact of urban growth in the regional climate of this tropical city. The flight plan for the mission is shown in Figure 1 below. The central area of San Juan was covered at 5 meters resolution in day and night flights. The remaining areas were covered at 10 meters resolution. The flights were conducted between February 11<sup>th</sup> and February 16<sup>th</sup>. In order to analyze the existence of an urban heat island in San Juan, and to support the Atlas sensor data, several experimental campaigns for data collection were designed and conducted by different teams. The focus of the next sections is in the analysis of the supporting measurements during the San Juan ATLAS field campaign, specifically for upper air and ground weather stations.

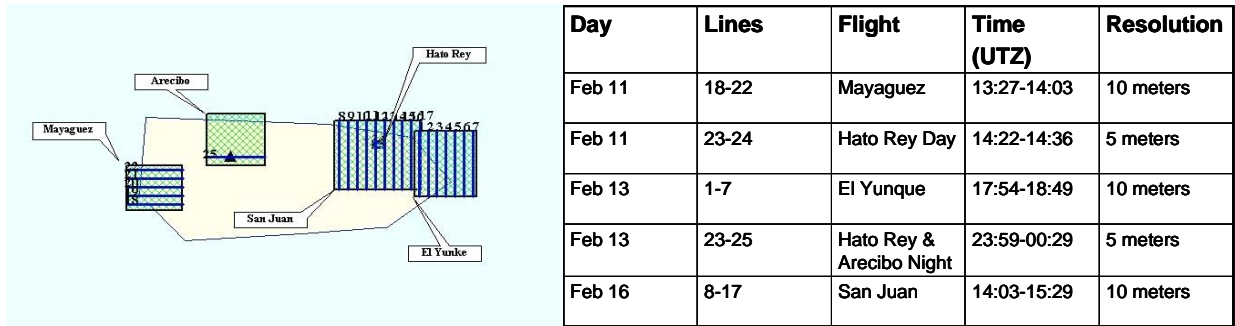


Figure 1: San Juan ATLAS Mission flight plan and execution

### Upper Air Data

The upper air information consisted of sounding launches and synoptic information provided by the NCAR Reanalysis group. These data were complemented by a regional modeling exercise to verify consistency. The San Juan office of the National Weather Service (NWS) increased the frequency of the standard soundings during the mission days, and these were complemented by launches from Mayagüez in the west coast, San Juan, and Dorado, about 25 miles east of San Juan. A total of 29 soundings were launched during the mission.

The upper air data clearly shows that the atmosphere was unusually stable and dry during the days of the mission. February 11, for example, when lines 18-24 were collected, presented a highly stable and dry atmosphere as shown in Figure 2(a) below. The differences between the dew point and the temperature of the sound indicate a dry atmosphere. To evidence the dry conditions and stability of the atmosphere, NCAR reanalysis was used to verify the upper air synoptic conditions. This data set represents the most comprehensive combined upper air analysis at a resolution of 2.5 degrees [3]. The surface surface Lifted Index (LI) for 12 UTZ February 11, 2004 is shown in Figure 2(b) below. The LI is found by comparing the temperature of a parcel of air raised from the surface to the 500 mb level to that of the actual temperature at 500 mb. When the LI is the troposphere is unstable relative to surface based convection. Fortunately, a prevailing positive LI was present in the Caribbean region during the days of the mission. The exception for these conditions occurred in February 14<sup>th</sup> when low, cold clouds were present until late in the morning leading to local instability and precipitation in the San Juan area.

The density and frequency of the sounding launches provided the unique opportunity of observing the temporal and spatial variation of the atmospheric boundary layer across the Island of Puerto Rico. Combined sounding data for San Juan (SJ) and Mayagüez (MZ) are presented in Figure 2(a) below. It can be noted that the atmosphere is relatively humid at 00 UTZ and becomes dry as the local heating pushes upward the moist clouds leaving a drier lower atmosphere. It can also be noted that differences in the local boundary layers are present for San Juan and Mayagüez for levels below 900 mb only, may be due to the topography of Puerto Rico which presents peaks as high as 1,300 meters between the two locations. A comparison of the upper air data for San Juan(SJU) and Dorado (DOR), about 25 miles west of San Juan, reflects minimum differences in the lower thermal boundary layer for 00UTZ in February 14, 2004 and increasing humidity by 06 UTZ as shown in Figure 2(c). The differences in the thermal or mechanical boundary layers between these two points will be a direct effect of the urban landscape in San Juan. When the atmosphere is dry and stable, minimum differences are

observed, however, the humidity will increase faster in the rural area than in San Juan as the night progresses.

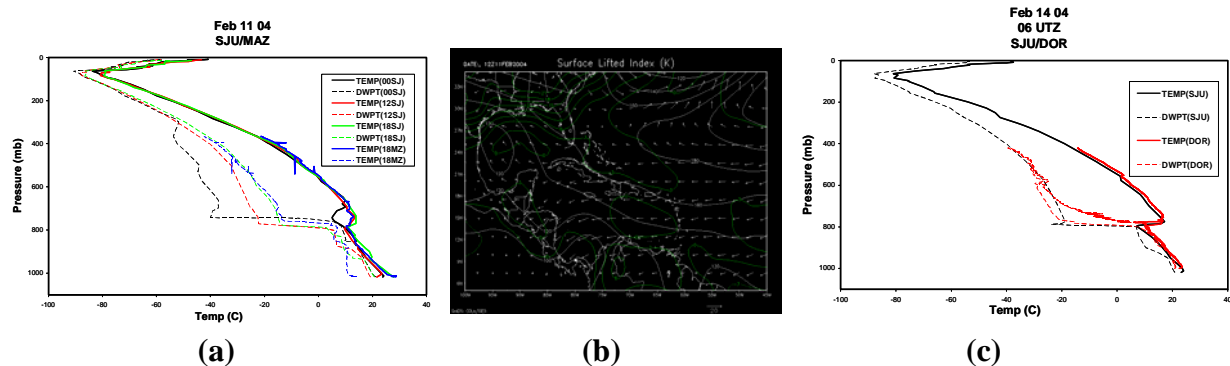


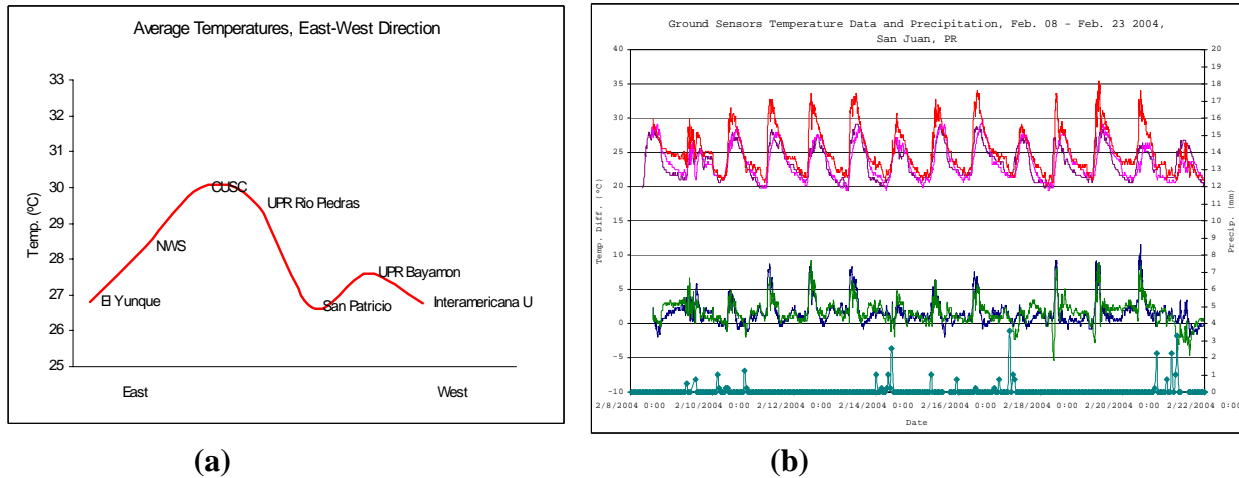
**Figure 2: (a) Combined upper air data for San Juan(SJ) and Mayagüez(MZ), and (b) Surface lifted index for February 11 (c) Combined upper air data for San Juan(SJU) and Dorado(DOR) for February 14, 2004 for 00UTZ**

### Ground Stations Analysis

Weather stations and temperature sensors were placed at along lines following the prevailing northeasterly winds in order to analyze possible temperature differences between the commercial area, residential areas, and rural areas. The logging frequency of all the data loggers, stations and sensors alike, was set to 5 minutes. The UHI effect is defined as the dome of elevated air temperatures that presides over cities in contrast to their cooler rural surroundings. The weather station and temperature sensor data show some indications of an UHI in the metropolitan area of San Juan, P.R. and its surroundings as shown in Figure 3(a). It is clearly seen that the average noon temperatures during the time period of the Atlas Mission evidence the existence of a pronounced Urban Heat Island, with the peak of the high temperature dome exactly over the commercial area of downtown San Juan, represented by the stations in the Sagrado Corazón University and the UPR-Río Piedras Campus.

An analysis of the data gathered by the different stations shows that there were significant temperature differences between urban and rural areas during the Atlas mission. Peak true temperatures occurred at mid afternoon, and ranged from 33 to 35°C in urban areas, and between 26-28°C in sub-urban and rural areas. Low temperatures consistently reached 20-22 degrees in the late evening (around 10:00 pm). Maximum temperatures in rural areas were substantially lower than those in urban areas in the mid to late morning hours, more specifically between 9:00 am and noon with average temperature differences of 4.5°C in such time frame, a temporal pattern not observed in previous Urban Heat Island studies of large continental cities, more notably the Atlanta, GA UHI measured by NASA in the early nineties [4]. It is also observed the nonappearance of a Cool Island, a dip of negative  $dT(U-R)$  opposite to the Heat Island caused by thermal heat storage. This might be due to the high density of low rising buildings in the metropolitan area of San Juan, despite having a large concrete density within the city. The high concrete density, and the importance of the soil moisture content and vegetation evapotranspiration in controlling the urban tropical climate, is evidenced by the variability of the UHI pattern with respect to rainfall. Even for relatively small and short precipitation events, in the order of only 8.4 mm during the entire mission, the temperatures in the commercial core of San Juan and the surrounding residential and rural areas become very similar, showing a low

dT(U-R). These results are summarized in Figure 3(b), which shows the true temperature, temperature difference, and accumulated surface precipitation for selected stations.



**(a)**  
**Figure 3(a) East-West cross-section of average noon temperature at selected locations in the San Juan Metropolitan Area and rural adjoining areas.**

**(b)**  
**Figure 3(b). True temperature at a urban-commercial, urban-residential, and rural areas (top three series); temperature differences between the commercial area and the residential and rural areas (middle two series); precipitation total recorded every 5 minutes by the San Juan National Weather Service (bottom series).**

## Conclusions

- The upper air analysis for the days of the San Juan ATLAS Mission in San Juan, Puerto Rico, clearly shows that the lower and upper atmosphere of the Caribbean remained unusually dry and stable during the mission days, conditions favorably for UHI. A comparison of upper air data for San Juan, Mayagüez, and Dorado reflects that differences in the thermal boundary layers are due to the topography of the Island and to the differences between rural and urban landscapes.
- The weather station and temperature sensor data clearly show indications of the existence of an UHI in the metropolitan area of San Juan, P.R. Temperatures were on average 4.5°C higher in the urban areas when compared to the observation of rural areas during the time period of 10:00 am to noon. The precipitation pattern and cloud coverage significantly affected the UHI of San Juan, PR.

## References

1. Landsberg, H. E., 1981, *The Urban Climate*, Academic Press, Maryland.
2. Kalnay, E.; Kanamitsu, M.; Kistler, R.; Collins, W.; Deaven, D.; Gandin, L.; Iredell, M.; Saha, S.; White, G.; Woollen, J.; Zhu, Y.; Leetmaa, A.; Reynolds, R.; Chelliah, M.; Ebisuzaki, W.; Higgins, W.; Janowiak, J.; Mo, K. C.; Ropelewski, C.; Wang, J.; Jenne, R., and Joseph, D., 1996, "The NCEP/NCAR 40-Year Reanalysis Project," *Bulletin of the American Meteorological Society*.
3. Daly, C., E. H. Helmer and M. Quiñones, 2003: Mapping the climate of Puerto Rico, Vieques and Culebra. *Int. J. Climatology*, 23, 1359-1381.
4. <http://www.ghcc.msfc.nasa.gov/atlanta/>

2004

**NASA FACULTY FELLOWSHIP PROGRAM**

**MARSHALL SPACE FLIGHT CENTER**

**THE UNIVERSITY OF ALABAMA  
THE UNIVERSITY OF ALABAMA IN HUNTSVILLE  
ALABAMA A&M UNIVERSITY**

**SPECIFIC IMPULSE AND MASS FLOW RATE ERROR**

Prepared By:	Don A. Gregory
Academic Rank:	Professor
Institution and Department:	University of Alabama in Huntsville, Department of Physics
NASA/MSFC Directorate:	Transportation
MSFC Colleague:	Mr. John Wiley

## INTRODUCTION

Specific impulse is defined in words in many ways. Very early in any text on rocket propulsion a phrase similar to “specific impulse is the thrust force per unit propellant weight flow per second” will be found. **(2)** It is only after seeing the mathematics written down does the definition mean something physically to scientists and engineers responsible for either measuring it or using someone’s value for it. A very typical mathematical definition is: **(3)**

$$I_{sp} = \frac{\int_0^T F_t dt}{g \int_0^T \dot{m}_e dt} \quad (1)$$

where  $F_t$  is the thrust and  $\dot{m}_e$  is the mass flow rate. The dot indicates a time derivative as usual and  $g$  is the acceleration due to gravity. If the numerator and denominator of (1) are multiplied by the inverse of the time period, the two integrals take on a new meaning:

$$I_{sp} = \frac{\frac{1}{T} \int_0^T F_t dt}{g \frac{1}{T} \int_0^T \dot{m}_e dt} \quad (2)$$

Now the integrals are averages and the specific impulse can be more correctly defined as the average thrust produced by the rocket engine divided by ( $g$  times) the average mass flow rate. The units of specific impulse are seconds. This definition is much more amenable to both scientists and engineers. The procedure followed in most textbooks will be reviewed here for completeness and to act as an introduction to the modifications to come later.

The usual freshman physics development of the rocket flight equations begins with the conservation of momentum equation: **(4)**

$$\sum p = 0 \quad (3)$$

$$m_R v_R - m_e v_e = 0 \quad (4)$$

where  $m_R$  is the mass of the rocket,  $m_e$  is the mass of the exhausted propellant, and  $v_R$  and  $v_e$  are the velocities of the rocket and the exhausted propellant respectively. Taking the time derivative of momentum gives the force:

$$\frac{dp}{dt} = F \quad (5)$$

and applying this to the momentum equation gives:

$$\frac{d}{dt}(m_R v_R - m_e v_e) = 0 \quad (6)$$

$$\frac{d}{dt}(m_R v_R) - \frac{d}{dt}(m_e v_e) = 0 \quad (7)$$

The last term is the rocket thrust:

$$F_t = \frac{d}{dt}(m_e v_e) \quad (8)$$

Performing the derivative correctly, knowing that the mass of the rocket is time dependent gives:

$$F_t = m_e \dot{v}_e + v_e \dot{m}_e \quad (9)$$

Now if  $v_e$  is a constant, then of course  $\dot{v}_e = 0$  so that:

$$F_t = v_e \dot{m}_e \quad (10)$$

Substituting this into the  $I_{sp}$  equation (1) gives:

$$I_{sp} = \frac{\int_0^T v_e \dot{m}_e}{g \int_0^T \dot{m}_e dt} \quad (11)$$

and again, assuming  $v_e$  is a constant and if it is further assumed that  $\dot{m}_e$  is also a constant, then:

$$I_{sp} = \frac{v_e \dot{m}_e \int_0^T dt}{g \dot{m}_e \int_0^T dt} \quad (12)$$

then:

$$I_{sp} = \frac{v_e}{g} \quad (13)$$

which is the normally encountered result, which is perfectly acceptable if both the mass flow rate and the exhaust velocity are constants. (5) This is indeed often the case, or is at least assumed to be the case, for most rocket propulsion measurements. In this investigation however the interest is in determining how an error in the mass flow rate measurement affects the specific impulse, so these simplifications cannot be used.

### THE INSTANTANEOUS SPECIFIC IMPULSE

The very use of the word impulse implies an integration over time so perhaps it is not appropriate to use the term as it will be used in the following argument but for historical reasons it will be used anyway. An instantaneous specific impulse (which of course literally doesn't make much sense) is defined to be:

$$I_{sp}^* \equiv \frac{1}{2} \frac{F_t}{g \dot{m}_e} \quad (14)$$

where the asterisk indicates that the term is related to the classical definition but not identical to it. The particular interest in this investigation is in how the specific impulse varies with mass flow rate so it is logical to try to determine the derivative of the specific impulse with respect to the mass flow rate:

$$\frac{dI_{sp}^*}{d\dot{m}_e} = \frac{1}{2g} \frac{d}{d\dot{m}_e} \left( \frac{F_t}{\dot{m}_e} \right) \quad (15)$$

$$= \frac{1}{2g} \left[ \frac{-F_t}{(\dot{m}_e)^2} + \frac{1}{\dot{m}_e} \frac{dF_t}{d\dot{m}_e} \right] \quad (16)$$

Now equation (9) gives the correct form for  $F_t$ , so substituting this into (16) gives:

$$\frac{dF_t}{d\dot{m}_e} = \frac{d}{d\dot{m}_e} [m_e \dot{v}_e + v_e \dot{m}_e] \quad (17)$$

$$= m_e \frac{d\dot{v}_e}{d\dot{m}_e} + \dot{v}_e \frac{dm_e}{d\dot{m}_e} + v_e + \dot{m}_e \frac{dv_e}{d\dot{m}_e} \quad (18)$$

where all the terms have units of velocity as they should. Substituting (18) into (16) and rearranging gives:

$$\frac{dI_{sp}^*}{d\dot{m}_e} = \frac{1}{2g} \left\{ \frac{m_e}{\dot{m}_e} \frac{d\dot{v}_e}{d\dot{m}_e} + \frac{\dot{v}_e}{\dot{m}_e} \frac{dm_e}{d\dot{m}_e} + \frac{dv_e}{d\dot{m}_e} - \frac{m_e \dot{v}_e}{(\dot{m}_e)^2} \right\} \quad (19)$$

At this point it is tempting to write an equation relating the mass of the exhausted propellant to the mass flow rate and the elapsed time. Such an equation would look like:

$$m_e = \dot{m}_e t \quad (20)$$

and this would greatly simplify (19) thereby leading to a quick solution but there is a problem with this if thought goes beyond freshman physics. Assume that (20) is true for a moment, then:

$$\dot{m}_e = \frac{d}{dt} (\dot{m}_e t) \quad (21)$$

$$= \dot{m}_e + t \ddot{m}_e \quad (22)$$

which implies

$$\ddot{m}_e = 0 \quad (23)$$

and this certainly is not physical for the problem at hand since the principle interest here is in determining how a change in  $\dot{m}_e$  affects  $I_{sp}^*$ , so  $\ddot{m}_e$  must exist. It is then tempting to assume that perhaps  $\ddot{m}_e$  is a constant, which would also help in simplifying (19). This implies that:

$$\dot{m}_e = At \quad (24)$$

where A is a constant. This requires  $\dot{m}_e$  to be a linear function of time which might be correct for some applications but is too restrictive for the general problem at hand, so it is important to stay with equation (19) as the fundamental result. This is somewhat

analogous to a classical mechanics problem with non-constant acceleration. Such a problem does not come up often but it is nevertheless quite physical.

Examine one term of equation (19):

$$\frac{\dot{v}_e}{\dot{m}_e} \frac{dm_e}{dm_e} \quad (25)$$

This can be rewritten as:

$$\frac{dv_e}{dt} \frac{dt}{dm_e} \frac{dm_e}{dm_e} = \frac{dv_e}{dm_e} \quad (26)$$

which does simplify equation (19):

$$\frac{dI_{sp}^*}{dm_e} = \frac{1}{2g} \left\{ \frac{m_e}{\dot{m}_e} \frac{d\dot{v}_e}{dm_e} + 2 \frac{dv_e}{dm_e} - \frac{m_e \dot{v}_e}{(\dot{m}_e)^2} \right\} \quad (27)$$

The last term in (19) can also be simplified:

$$\dot{v}_e \frac{m_e}{(\dot{m}_e)^2} = \frac{m_e}{\dot{m}_e} \left( \frac{\dot{v}_e}{\dot{m}_e} \right) = \frac{m_e}{\dot{m}_e} \frac{dv_e}{dm_e} \quad (28)$$

so that equation (19) now becomes:

$$\frac{dI_{sp}^*}{dm_e} = \frac{1}{2g} \left\{ \frac{m_e}{\dot{m}_e} \frac{d\dot{v}_e}{dm_e} + 2 \frac{dv_e}{dm_e} - \frac{m_e}{\dot{m}_e} \frac{dv_e}{dm_e} \right\} \quad (29)$$

which is the fundamental result of this investigation.

Rewriting equation (29) slightly:

$$\frac{dI_{sp}^*}{dm_e} = \frac{1}{g} \frac{dv_e}{dm_e} + \frac{1}{2g} \frac{m_e}{\dot{m}_e} \left( \frac{d\dot{v}_e}{dm_e} - \frac{dv_e}{dm_e} \right) \quad (30)$$

Now if the last term was not present, then:

$$\frac{dI_{sp}^*}{dm_e} = \frac{1}{g} \frac{dv_e}{dm_e} \quad (31)$$

Integrating:

$$\int dI_{sp}^* = \frac{1}{g} \int dv_e \quad (32)$$

gives:

$$I_{sp}^* = \frac{v_e}{g} \quad (33)$$

which is the classical textbook result (equation 13) obtained if the exhaust velocity and mass flow rate are assumed to be constants.

The last term in equation (30):

$$\frac{1}{2g} \frac{m_e}{\dot{m}_e} \left( \frac{d\dot{v}_e}{d\dot{m}_e} - \frac{dv_e}{dm_e} \right) \quad (34)$$

can be thought of as a “correction” to  $\frac{dI_{sp}^*}{d\dot{m}_e}$  for the case of  $v_e$  and  $\dot{m}_e$  being non-constant. So the classical specific impulse can be written in terms of the instantaneous specific impulse as:

$$I_{sp}^* = I_{sp} + \frac{1}{2g} \int \frac{m_e}{\dot{m}_e} \left( \frac{d\dot{v}_e}{d\dot{m}_e} - \frac{dv_e}{dm_e} \right) d\dot{m}_e \quad (35)$$

This is the final result.

## DISCUSSION

As an exercise and example, it is possible to construct plausible functions for the derivatives in the last term of equation (30) to get an idea of how the specific impulse error depends on the error in the mass flow rate. It seems reasonable to assume that the mass of the expelled propellant increases in time, but that dependence is usually not known, so as a guess, assume that:

$$m_e(t) = At^n \quad (36)$$

where A is a constant and n represents a collection of random numbers whose average is 1. For n = 1 the dependence is linear which might make sense for some applications. If equation (36) is assumed to be true then:

$$\dot{m}_e(t) = nAt^{n-1} \quad (37)$$

Now the dependence of the exhaust velocity on the mass flow rate is required. It seems that there shouldn't be much of a dependence here so it is assumed that:

$$v_e = Bm_e^q \quad (38)$$

where B is a constant and q is defined similar to n except the average is 0. This says that the exhaust velocity does not vary much with the mass flow rate. This leads to:

$$\frac{dv_e}{dm_e} = qBm_e^{q-1} \quad (39)$$

For the dependence of the time derivative of the exhaust velocity on the mass flow rate, a dependence similar to equation (36) is assumed:

$$\dot{v}_e = C\dot{m}_e^j \quad (40)$$

where C is a constant and j is defined like n and q and it has an average of 1. This then leads to:

$$\frac{d\dot{v}_e}{d\dot{m}_e} = jC\dot{m}_e^{j-1} \quad (41)$$

As a reality check, notice that the time derivative of the mass flow rate is:

$$\ddot{m}_e(t) = n(n-1)At^{n-2} \quad (42)$$

which is not a constant in time, and that was required from the outset. However, if n is allowed to take its average value then the derivative is zero, which might be reasonable as a steady state condition. The final functional form needed is the dependence of the exhaust velocity on the mass flow rate. This is assumed to be simply linear:

$$v_e = D\dot{m}_e \quad (43)$$

so that the derivative is a constant:

$$\frac{dv_e}{d\dot{m}_e} = D \quad (44)$$

The functional assumptions made thus far allow the basic result (equation 30) to be written in terms of a time variable only:

$$\frac{dl_{sp}^*}{dm_e} = \frac{D}{g} + \frac{1}{2gn} \left[ jC(nA)^{j-1} t^{(n-1)(j-1)+1} - qBA^{q-1} t^{n(q-1)+1} \right] \quad (45)$$

## RESULTS

The result of fundamental interest is that of equations (30) and (35). The traditional specific impulse can be written in terms of a new instantaneous specific impulse. This new term is useful in that the parameters are more readily measurable and applicable in experiments where high speed data can be obtained. The assumptions made in the discussion may not be very physical but do allow a visualization of how the error in the specific impulse due to an error in the mass flow rate might change in time. To plot the results of equation (45) a range of values was chosen for  $n, j$ , and  $q$  which met the basic criteria for the averages:

$$n = 0, 1, 2 \qquad q = -1, 0, 1 \qquad j = 0, 1, 2$$

A curve was generated for each of the 27 possible combinations of the indices and then the curves were averaged. The result is shown in Figure 1. A general increase in the derivative of the instantaneous specific impulse with respect to the mass flow rate is an indication of an increase in the error expected in the instantaneous specific impulse when an error in the mass flow rate is present. If the derivative was zero it would mean that the instantaneous specific impulse does not depend on the mass flow rate, which is non-physical. If the derivative was a constant then that would mean that the instantaneous specific impulse changes linearly with mass flow rate, which is the textbook result. The results in Figure 1 indicate that the derivative depends on the chosen variable (time) in a nonlinear way, which is a more physical result given the initial assumptions taken at the beginning of this research.

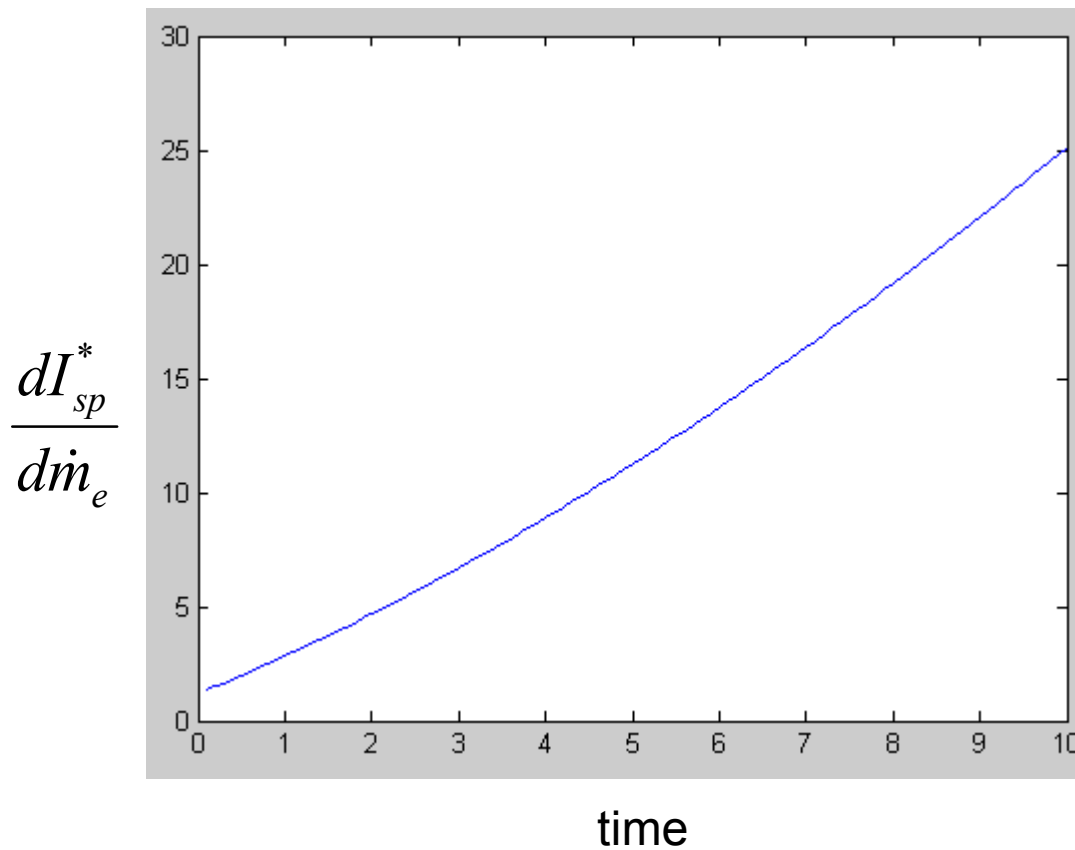


**Figure 1: A plot of equation (45) showing the dependence of the derivative of the instantaneous specific impulse with respect to the mass flow rate versus time.**

## CONCLUSIONS

The initial goal of this research was to determine how an error in the measure of the mass flow rate in a rocket engine would affect the specific impulse. This well defined problem developed into an examination of the specific impulse itself and why it is used and what the limitations are when it is measured. In order to describe the physics of the problem, a new term had to be defined that was related to the specific impulse and it was called the instantaneous specific impulse for lack of a better term. The definition proved to be useful in that the parameters could be measured more readily than the integral required in the usual definition and the new term could be written in terms of the old one with the addition of a correction which took care of the non-constant behavior of the exhaust velocity and the mass flow rate, which was assumed from the beginning. A simple, perhaps nonrealistic set of dependencies on time were later assumed for the various parameters so that a visual representation of the results could be derived.

## REFERENCES

1. Tsiolkovsky. *Investigating Space with Rocket Devices*, Nauchnoye Obozreniye (Science Review), Russia, 1898.
2. Sutton, George P., *Rocket Propulsion Elements*, John Wiley and Sons, 5<sup>th</sup> Edition, 1986, p. 3
3. *ibid* p.21
4. *University Physics*, F. Sears and M. Zemanski, Addison-Wesley, 4<sup>th</sup> Edition, 1970, p. 201
5. Benson, Tom, NASA Glenn Learning Tech., <http://www.grc.nasa.gov/WWW/K-12>

2004

**NASA FACULTY FELLOWSHIP PROGRAM**

**MARSHALL SPACE FLIGHT CENTER**

**THE UNIVERSITY OF ALABAMA  
THE UNIVERSITY OF ALABAMA IN HUNTSVILLE  
ALABAMA A&M UNIVERSITY**

**A THEORETICAL INVESTIGATION OF OXIDATION  
EFFICIENCY OF A VOLATILE REMOVAL ASSEMBLY  
REACTOR UNDER MICROGRAVITY CONDITIONS**

Prepared By:

Dr. Boyun Guo

Academic Rank:

Associate Professor

Institution and Department:

University of Louisiana at Lafayette  
Department of Petroleum Engineering

NASA/MSFC Directorate:

Flight Projects

MSFC Colleague:

Robert M. Bagdigian

## **Introduction**

Volatile Removal Assembly (VRA) is a subsystem of the Closed Environment Life Support System (CELSS) installed in the International Space Station. It is used for removing contaminants (volatile organics) in the wastewater produced by the space station crews. The major contaminants are formic acid, ethanol, and propylene glycol. The VRA contains a slim packbed reactor (3.5 cm diameter and four 28 cm long tubes in series) to perform catalyst oxidation of wastewater at elevated pressure and temperature under microgravity conditions. In the reactor, the contaminants are burned with oxygen gas ( $O_2$ ) to form water and carbon dioxide ( $CO_2$ ) that dissolves in the water stream. Optimal design of the reactor requires a thorough understanding about how the reactor performs under microgravity conditions. The objective of this study was to develop a mathematical model to interpret experimental data obtained from normal and microgravity conditions, and to predict the performance of VRA reactor under microgravity conditions.

Catalyst oxidation kinetics and the total oxygen-water contact area control the efficiency of catalyst oxidation for mass transfer, which depends on oxygen gas holdup and distribution in the reactor. The process involves bubbly flow in porous media with chemical reactions in microgravity environment. This presents a unique problem in fluid dynamics that has not been studied. Guo *et al.* (2004) developed a mathematical model that predicts oxygen holdup in the VRA reactor. No mathematical model has been found in the literature that can be used to predict the efficiency of catalyst oxidation under microgravity conditions.

## **Mathematical Model**

A mathematical model has been developed in this study to simulate the oxidation efficiency of the VRA reactor. The longitudinal distribution of the oxygen mass flow rate in the reactor can be expressed as follows (derivation of the model is available from the author):

$$\dot{M}_{O_2} = \dot{M}_{O_2-0} e^{-\frac{3r_{O_2}\Psi_b x}{r_b\rho_{O_2}v_b}} \quad (1)$$

where  $\dot{M}_{O_2}$  is oxygen mass flow rate at the point  $x$ -distance from the reactor inlet,  $\dot{M}_{O_2-0}$  is oxygen mass flow rate at the reactor inlet,  $r_{O_2}$  is rate of oxidation per unit contact area between oxygen and water,  $\Psi_b$  is the average sphericity of oxygen bubbles (the ratio of bubble's shortest diameter to longest diameter),  $r_b$  is the average radius of bubbles,  $\rho_{O_2}$  is the density of oxygen gas, and  $v_b$  is the average velocity of bubbles.

It is customary to use the term oxygen utilization ( $U_{O_2}$ ) in evaluation of VRA reactor performance. The expression for  $U_{O_2}$  can be theoretically derived based on Eq. (1):

$$U_{O_2} = 1 - R_{O_2-L} = 1 - e^{-\frac{3r_{O_2}\Psi_b L}{r_b\rho_{O_2}v_b}} \quad (2)$$

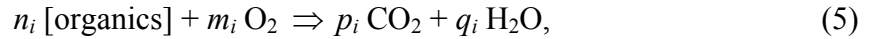
where  $L$  is the length of the reactor and  $R_{O_2-L}$  is the remaining oxygen at the outlet of the reactor. The oxygen mass consumption potential in the reaction is then expressed as:

$$\Delta M_{O_2} = U_{O_2} \dot{M}_{O_2-0} t_w \quad (3)$$

where  $t_w$  is the residence time of water in the reactor. The water residence time can be calculated based water injection rate, reactor size, packbed porosity, and oxygen holdup in the reactor. Based on the molar equivalency in the oxidation, the amount of organics  $i$  removed in the reaction can be expressed as:

$$\Delta M_i = \frac{\Delta M_{O_2} W_{mi}}{32 N_i} \quad (4)$$

where  $W_{mi}$  is the molecular weight of organics  $i$ , and  $N_i$  is molar number of oxygen utilization for each mole of organics  $i$  defined in the following oxidation reaction:



i.e.,  $N_i = m_i/n_i$ . Typical values of  $N_i$  are shown in Table 1.

The oxygen mass flow rate at the reactor inlet  $\dot{M}_{O_2-0}$  is a design parameter. The density of oxygen gas ( $\rho_{O_2}$ ) can be calculated with gas law for ideal gas under given pressure and temperature. The sphericity of bubble ( $\Psi_b$ ) may be affected by reactor geometry and gas holdup in the reactor. Due to lack of means of estimating its value, we used 0.5 throughout this study. The average flow velocity of oxygen bubbles ( $v_b$ ) can be estimated based on oxygen injection rate, reactor cross-sectional area, packbed porosity, and oxygen holdup. The oxygen holdup can be estimated with the mathematical model described by Guo *et al.* (2004).

The rate of oxidation per unit water-oxygen contact area ( $r_{O_2}$ ) depends on the total flux rate ( $J$ ) at which volatile organics disperse (Taylor, 1953):

$$J_i = - \left( \frac{D_{oi}}{F} + \frac{v_y^2 r_p^2}{48 D_{oi}} \right) \frac{dC_i}{dy} \quad (6)$$

where  $D_{oi}$  is the molecular diffusivity of organics  $i$ ,  $F$  is called formation factor which is defined as tortuosity divided by porosity of packbed,  $\frac{dC_i}{dy}$  is the concentration gradient of organics  $i$  in the direction perpendicular to the bubble surface,  $v_y$  is the average convection velocity, and  $r_p$  is the average pore radius.

A mathematical model was developed in this study to estimate the size of gas bubbles in a flowing liquid (derivation of the model is available from the author):

$$N_{WeC} = \frac{\rho_L d_m}{g \sigma} \left[ 1.1548 \sqrt{\frac{g d_m (\rho_L - \rho_g)}{\rho_L C_d}} - v_L \right]^2 \quad (7)$$

where  $N_{WeC}$  is the critical Weber number,  $\rho_L$  and  $\rho_g$  are densities of liquid and gas, respectively,

$v_L$  is liquid velocity, and  $C_d$  is drag coefficient. If all other parameter values are known, the maximum bubble diameter  $d_m$  can be solved numerically from Eq. (7). The critical Weber number was determined to be 979 based on matching the calculated bubble diameter to the data (air bubble size in water). By matching the calculated oxygen bubble diameter to the observed oxygen bubble length (4 to 6 inches) under 1-G conditions, we estimated that the drag coefficient in the VRA reactor to be about  $C_d = 3.9$ .

### **Model Calibration**

The VRA reactor performance data obtained from ethanol oxidation an experimental test conducted in ground surface conditions were used to calibrate the model. The reactor influent contained 144 mg/L of ethanol. The reactor effluent contained 91 mg/L of acetic acid and no ethanol. Material balance calculations show that the oxygen utilization is 87%. This value was obtained from the model by assuming that the organics concentrations drop from the initial concentrations in the pore space to zero at the catalyst surface within a distance of a half pore radius, and adjusting convection velocity to 0.2957 times the longitudinal water velocity.

### **Results**

Figure 1 presents calculated oxygen mass flow rate under 1-G and 0.01-G conditions. In this case, the oxygen utilizations under 1-G and 0.01-G conditions are 63.42% and 60.11%, respectively. The calculated oxygen utilization drops by 5.23% under micro gravity conditions.

### **Conclusions**

A mathematical model has been developed in this study to estimate oxidation efficiency in the VRA reactor under microgravity conditions. The following conclusions are drawn.

1. The remaining oxygen gas in the VRA reactor should decline exponentially with reactor length. The decline rate is directly proportional to rate of oxidation per unit area and bubble sphericity, and inversely proportional to bubble size, oxygen density and bubble velocity.
2. Gravity affects oxygen utilization through changing several parameters including oxygen bubble size. More research efforts are required to further investigate the effects of microgravity on VRA reactor performance.
3. The currently VRA design is very conservative. The oxygen utilization is about 60%.

### **Acknowledgements**

The author would like to thank Robert Bagdigian, Donald Holder, and Layne Carter for collaborating this research in the ECLSS Group of the MSFC's Flight Projects Directorate.

### **References**

- [1] Guo, B., Holder, D.W., and Layne, C.: "Distribution of Flowing Fluids in a Confined Porous Medium under Microgravity Conditions," *Physics of Fluids* (August 2004), **16**, No. 8, 1-6.
- [2] Taylor, G.I.: "Dispersion of Soluble Matter in Solvent Flowing Slowly through a Tube," *Proc., Roy. Soc.*, **219** (1953), 186-194.

Table 1 – Baseline Concentration of Volatile Organics in the Waste Water

Organics Name	Molecular Weight	Liquid Molecular Diffusivity (cm <sup>2</sup> /s)	Molar Number of Oxygen Utilization	Influent Concentration (mg/L)
Acetaldehyde	44.05	0.00006953	2.5	2.74
Acetone	58.08	0.00005924	4	4.41
1-butanol	74.1	0.00005924	6	1.5
Ethanol	46.07	0.00006953	3	39.2
Ethylene glycol	62.07	0.00005924	2.5	5.51
Formaldehyde	30.03	0.00006953	1	5.89
Formic Acid	46.03	0.00006953	0.5	49.9
Methanol	32.04	0.00006953	1.5	7.94
Propylene glycol	76.1	0.00005924	4	35.4
1-propanol	60.1	0.00005924	4.5	0.45
2-propanol	60.1	0.00005924	4.5	1.6
Urea	60.06	0.00005924	1.5	3.55

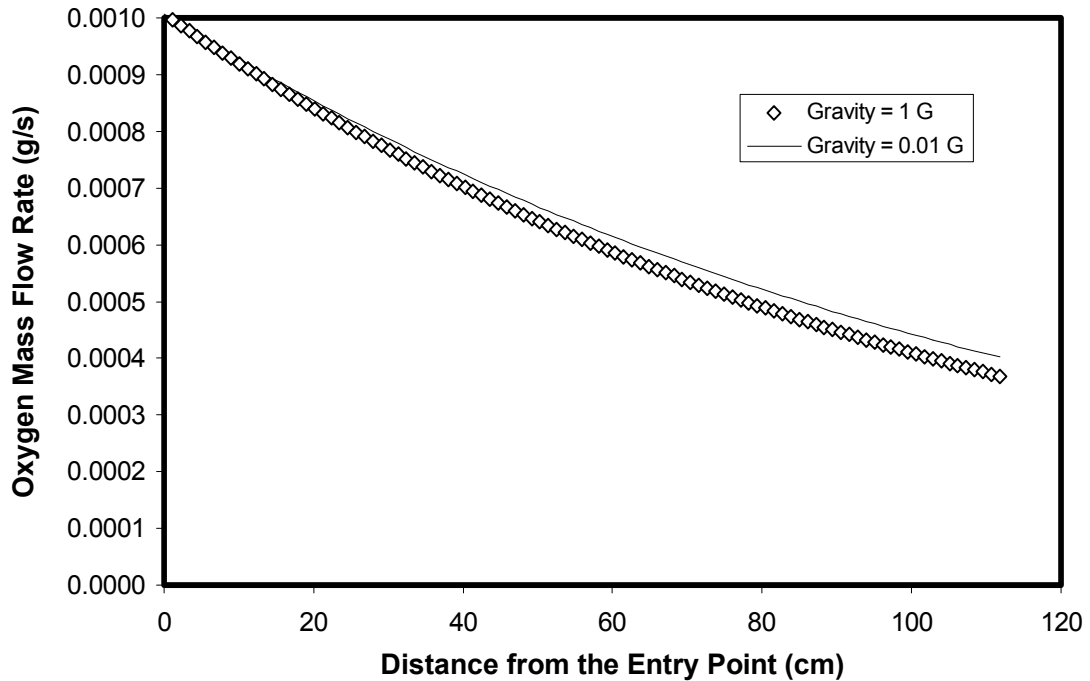


Figure 1 – Model-Calculated oxygen mass flow rate under 1-G and 0.01-G conditions

2004

**NASA FACULTY FELLOWSHIP PROGRAM**

**MARSHALL SPACE FLIGHT CENTER**

**THE UNIVERSITY OF ALABAMA  
THE UNIVERSITY OF ALABAMA IN HUNTSVILLE  
ALABAMA A&M UNIVERSITY**

**Optimal Configuration of  
Human Motion Tracking Systems:  
A Systems Engineering Approach**

Prepared By:	Captain Steve Henderson
Academic Rank:	Instructor
Institution and Department:	United States Military Academy Department of Systems Engineering
NASA/MSFC Directorate:	Engineering
MSFC Colleague:	George S. Hamilton, PE

## **Introduction**

Human motion tracking systems represent a crucial technology in the area of modeling and simulation. These systems, which allow engineers to capture human motion for study or replication in virtual environments, have broad applications in several research disciplines including human engineering, robotics, and psychology.

These systems are based on several sensing paradigms, including electro-magnetic, infrared, and visual recognition. Each of these paradigms requires specialized environments and hardware configurations to optimize performance of the human motion tracking system. Ideally, these systems are used in a laboratory or other facility that was designed to accommodate the particular sensing technology. For example, electromagnetic systems are highly vulnerable to interference from metallic objects, and should be used in a specialized lab free of metal components [1].

In practice, specialized “tracker friendly” environments are not always available. A particular research project or simulation might force adding a human motion tracking system to a facility that does not possess the optimal sensor environment. This situation describes the setting at Marshall Space Flight Center’s Collaborative Engineering Center Army-NASA Virtual Innovation Laboratory (MSFC CEC-ANVIL). The CEC-ANVIL is a collaborative environment that evolved over time and features a variety of engineering tools and technologies configured in a standard 20 meter X 20 meter modified office. This room, which features heavy metal induced interference, features a partial CAVE Automatic Virtual Environment (CAVE) that is used for modeling, analysis, and decision making. The Human Engineering component of the MSFC Systems Engineering Support Group desires to add a human motion tracking capability to this setting.

## **The Systems Engineering and Management Process**

We will apply the Systems Engineering and Management Process (SEMP) in order to address this problem. This process, developed at the United States Military Academy, helps engineers systematically design large-scale, complex systems to address problems [2]. We will first introduce this process before applying it to the MSFC CEC-ANVIL Human Motion Tracking problem.

The SEMP, shown in Figure 1, is a four phase iterative process involving nine unique steps. A descriptive scenario specifies the current state of a given system or situation. A normative scenario describes the desired state of the system or situation. The difference between these two scenarios is the problem. In the case of the CEC-ANVIL, the descriptive scenario is a uninstalled MotionStar tracking system operating in a sub-optimal environment. The normative scenario is an optimal system that meets the human tracking needs of the CEC-ANVIL.

The engineering process on the inside of the diagram is an iterative process we execute to arrive at the normative scenario. The first phase of the process, the problem definition phase, involves two steps – needs analysis and value system design. The needs analysis step entails understanding, redefining, and formalizing the problem definition. The value system design step involves constructing an upfront value system that fits within the context of the problem definition and can later help ideate and evaluate potential alternatives.

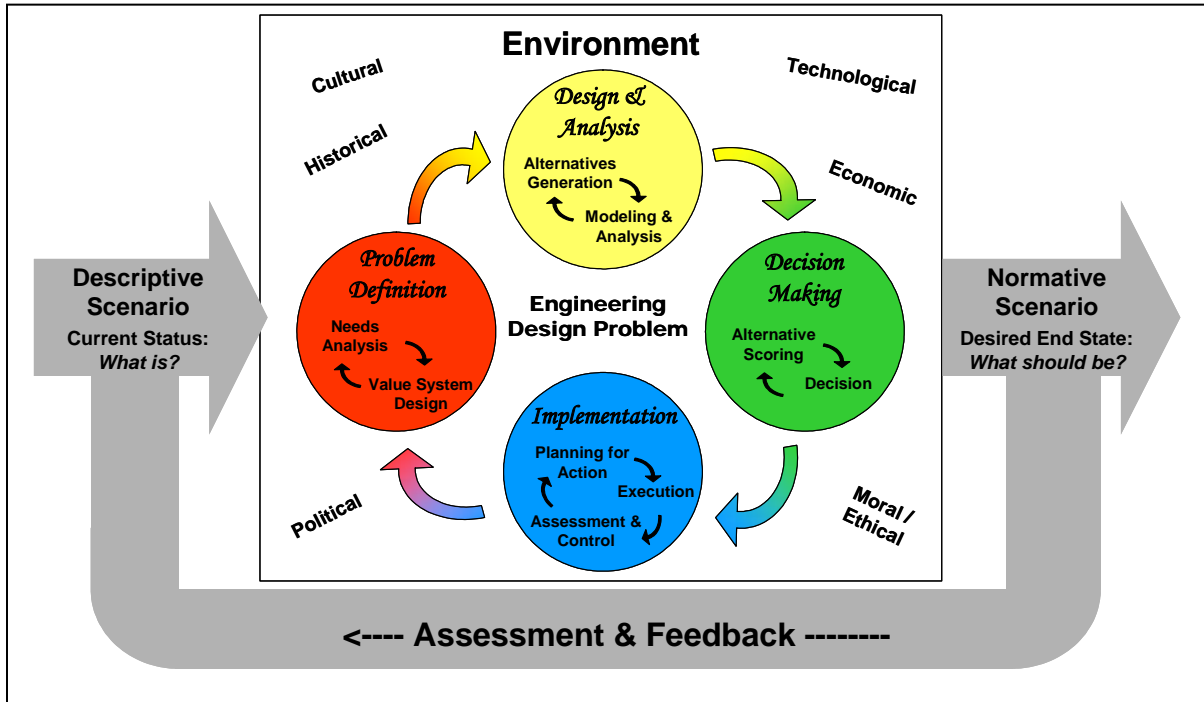


Figure 1 – The Systems Engineering and Management Process

The second phase of the SEMP is the design and analysis phase which is broken down into alternatives generation and modeling and analysis steps. Alternatives generation involves creating potential alternatives to address the needs defined in the needs analysis step. The modeling and analysis step is concerned with identifying the feasibility of alternatives, as well as optimizing and measuring each alternative.

The third phase of the SEMP is the decision making phase which is broken down into the alternative scoring and decision steps. In the alternative scoring step, we use the value system from the problem definition phase to calculate a “total value score” for each alternative. In the decision step, we use these value scores to recommend one alternative to the decision maker. This decision includes a detailed sensitive and cost-value analysis.

The final phase, implementation, involves the three remaining steps of the process – plan of action, execution, and assessment and control. The plan of action represents the project plan detailing how we will implement our winning alternative. Execution involves actually employing hardware, software, and other resources to create the alternative. Assessment and control involves observing and controlling the system over its lifetime.

It is important to note the iterative nature of the SEMP and its four major phases. The iteration at each phase represents the continual processing and prototyping that is conducted at each phase until certain conditions are set to commence the next phase. The iterative nature of the SEMP prompts us to re-execute when the descriptive scenario no longer matches the normative scenario.

### **Problem Definition**

We begin the application of the SEMP to the MSFC CEC-ANVIL motion tracking problem at the problem definition phase. The problem definition phase begins with the needs analysis step.

### **Needs Analysis**

Needs analysis begins with receipt of the Initial Problem Statement (IPS). This is a rough description of the problem provided by the chief decision maker. In the case of MSFC's CEC-ANVIL Motion Tracking problem, the Human Engineering Team Lead provided the following initial problem statement:

*“We have a Flock of Birds we want to get working, and mounted into a position, either in the ceiling or on the floor, where we can use it for human factors research and engineering. We'd like the audience to be able to sit at the table and watch as the puppeteer demonstrates the work in front of the workbench [3]*

The next step of the problem definition process involves a detailed study of this initial problem statement and all involved systems. To accomplish this, we will identify facts and constraints and perform a complete system decomposition.

The following represent salient facts involving the MSFC CEC-ANVIL Human Motion Tracking System:

- The primary motion tracking system consists of an Ascension MotionStar system. This system features a CPU, 10 magnetic sensors, an extended range controller, a transmitter, and cabling. This system captures the location and attitude of each sensor and transmits this information to the CPU then onto a LAN/WAN via Ethernet.
- The motion tracking system also consists of an Immersion CyberGlove/CyberTouch system that features a sensor glove, controller, and cabling. This system captures positioning and orientation of the five fingers on one hand. This information is gathered by the controller then sent via serial cable to a subscribing CPU.
- The primary modeling and simulation program used by the stakeholders is EDS Jack. This program allows a puppeteer to control virtual humanoids with the human motion tracking system. The stakeholders are also interested in using the human motion tracking system with the Delmia Ergo modeling package.

- MSFC CEC-ANVIL will use the human motion tracking for briefings to decision makers and for detailed human engineering analysis.

To further define our problem, we identify the following constraints:

- The Human Motion Tracking system is confined to MSFC CEC-ANVIL. We cannot relocate the system to a more suitable facility.
- The published usable range of the MotionStar transmitter is 10 ft. This was later refined to 8 feet through analysis.
- The length of the required cabling connecting the MotionStar sensors and transmitter to the MotionStar CPU is approximately 10 meters. Therefore, the entire human motion tracking system (human, MotionStar, CyberGlove) is confined to a 10 meter radius.
- Observers must have an unobstructed view of the CAVE wall from a centrally located conference table. The conference table cannot move.
- The system should also allow the puppeteer to directly view the CAVE wall when observers are not present.
- The system must interface with EDS Jack software.
- Any structural components for mounting the transmitter, CPU, or sensors cannot be made of metal.

In order to gain further insight into what actually comprises the human motion system, we will conduct a detailed system decomposition. First, this will help us identify the key functions of the system, which we will use to build a value hierarchy later in the process. Second, the decomposition will aid us in better understanding what components are part of the system, which will help define potential alternatives.

The decomposition for the human motion tracking system, shown in Figure 2, consists of functional decomposition, component decomposition, and structural decomposition. The functional decomposition examines the key functions of the motion tracking system, and was conducted after observing how the human motion tracking system fits with the organization's processes. The main functions of the system are: display a virtual environment to the operator (person wearing the tracker), display the virtual environment to the observers (decision makers and VIPs), mimic the operator, facilitate interaction, facilitate maintenance, and provide a safe environment.

The component decomposition looks at all the physical components in the system, and consists of structural, operational, and flow components. Structural components are those that provide some sort of physical structure to the system - hardware mounts, consoles, harness, wires. Operational components are components that actually transform other components - sensors,

CPU, software, transmitter. Flow components are components that are transformed – in this case the digital and analog signals that make up the human motion tracking information.

The hierarchical decomposition looks at the human motion tracking system within the context of higher, lower, and adjacent systems. The parent system for the human motion tracking system is the CEC-ANVIL. Lateral systems include other notable systems within the CEC-ANVIL that might impact the motion tracking system – namely the CAVE, a video teleconferencing system (VTS), and numerous CAD workstations.

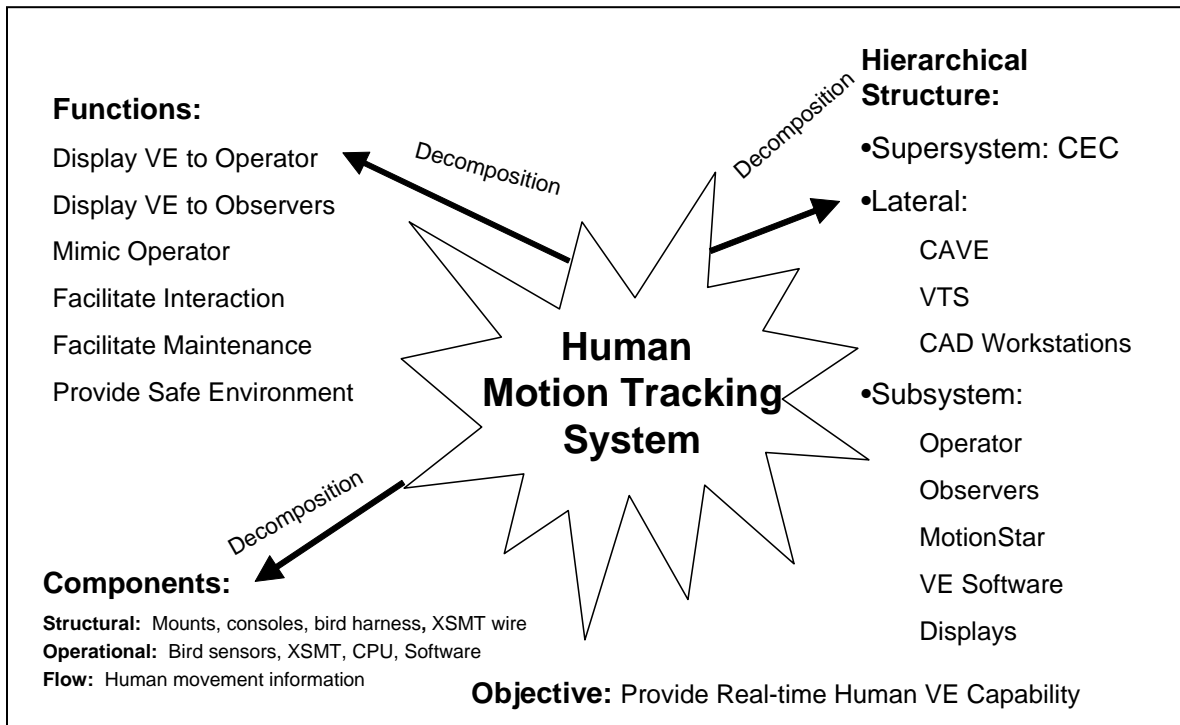


Figure 2 – System Decomposition of the HMCS

To augment our component and structural decomposition, we construct a context diagram of the system. This diagram, shown in Figure 3, provides another view of the component and hierarchical decomposition. The outer circle of the diagram represents the system boundary. This boundary represents everything we can control in the system, and is based off the decision maker’s designated level of authority. The circles inside the boundary represent components of the human motion tracking system, with the MotionStar component represented with its own sub-system boundary and sub-components. The circles outside the system boundary represent objects in our environment (the CEC) that might impact the human motion tracker but over which the system has no control.

The decomposition process described above helps us scope the system. Identifying the system’s boundary, functions, and components enables us to conduct an appropriate and meaningful stakeholder analysis. The goal of the stakeholder analysis is to identify stakeholder needs, wants, and desires. In this scenario, we will consider three stakeholders – the decision maker,

the sponsor, and the users. After many discussions and interviews, we arrive at the following needs, wants, and desires.

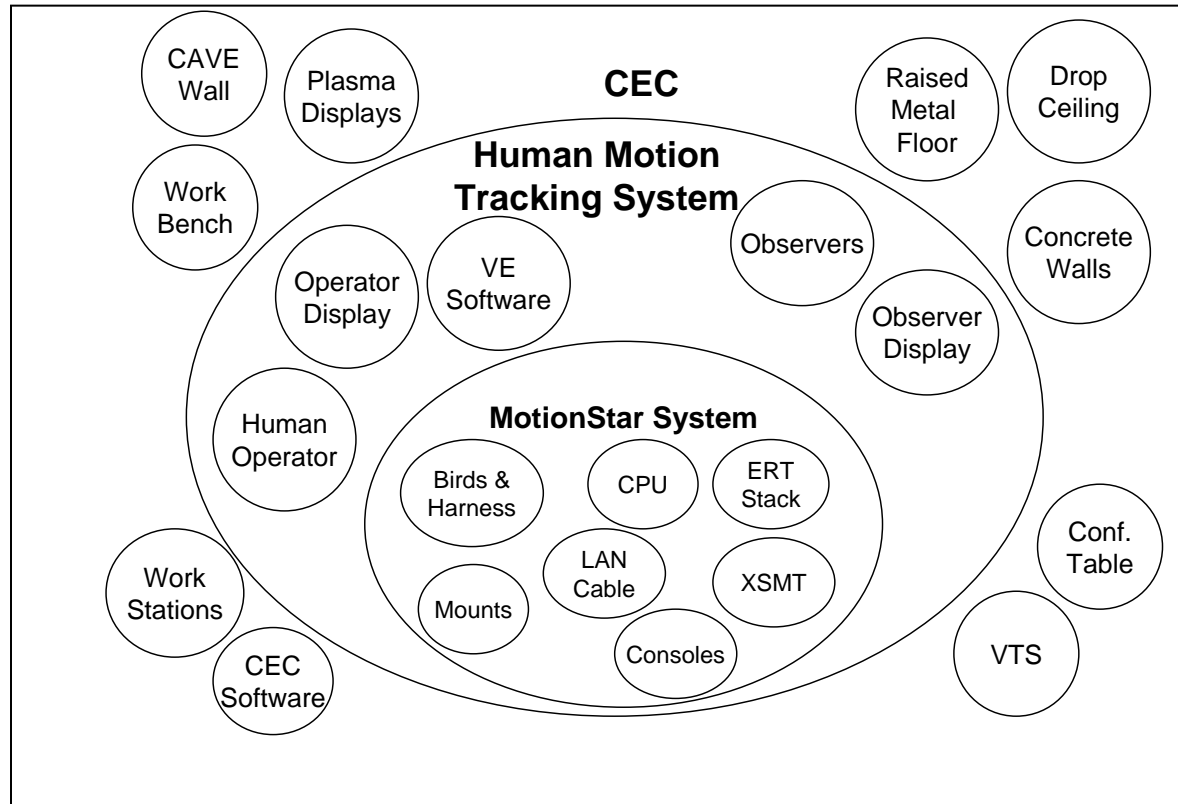


Figure 3 – HMTS Context Diagram

The decision maker, the Human Engineering Team Lead, desires a system configuration that allows engineers to easily and quickly incorporate human motion tracking into an overall engineering process. He desires a system that will enhance the human engineering research capabilities of the CEC and one that employs an aesthetically pleasing, organized hardware configuration. The system must offer accurate and reliable system performance and allow an audience of higher decision makers to observe use of the system. The system must also incorporate both the CyberGlove and MotionStar sub systems.

The sponsor, the MSFC Systems Engineering Support Group (ED42) Manager, is the person who actually owns the equipment and the CEC-ANVIL. He desires to fill a need to integrate human factors early on to drive the overall design process. He also wants to increase the CEC-ANVIL role in providing training to users of designed systems. He also wants to research how motion tracking can enhance the various engineering processes within the entire Systems Engineering Support Group. He sees the system developing into a unique capability that ED42 can “sell” to MSFC and NASA.

The users represent the last group of concerned stakeholders. These individuals, contract technicians who staff the CEC-ANVIL, want an easy to use system they can employ when assigned a human motion tracking mission. The system should also be easy to maintain and not interfere with other lab equipment and capabilities.

The last act in the needs analysis step is to use the facts/constraints, detailed system decomposition, and stake holder analysis to construct a revised problem statement. This statement represents what we think the decision maker needs, which may or may not reflect what they initially provided in the initial problem statement. The revised problem statement considers all the facts and stakeholders desires within the designated scope of the system. For our problem, we arrive at the following revised problem statement:

*ED42 (CEC) desires to implement a functional human motion tracking system to enhance their human engineering and analysis capability. This system will acquire real-time human position data for controlling human models inside virtual and CAD environments. This system will augment their engineering processes by bringing humans into the design process early on, and enhance their ability to communicate analysis to decision makers and customers. Specific tasks include:*

- (a) Configuring visualization software packages to read the location of motion sensors transmitted by the MotionStar “Flock” and CyberGlove and translate this into controllable human models*
- (b) Developing techniques and procedures for integrating these controlled human models with other virtual environments and CAD models*
- (c) Designating a place to permanently mount the MotionStar system*
- (d) Developing an easy to use suit for wear of the MotionStar sensors*

### Value System Design

The next step in the SEMP is value system design. The value system design step creates a value model that reflects the stakeholder needs, want, and desires. This value model will later serve to evaluate how well potential design alternatives meet the needs of the stakeholders.

Figure 4 shows a value hierarchy (tree) that reflects the value model for this system. The top of the tree lists the overall operational need for the human motion tracking system – provide human motion tracking capability. The next layer of the tree represents the main system functions discovered in functional decomposition conducted during the needs analysis step. For each of these functions, we created an objective that is used to gauge how well each function is being performed. Below each objective is an evaluation measure that represents a measurable metric that corresponds to each objective. These are briefly described below.

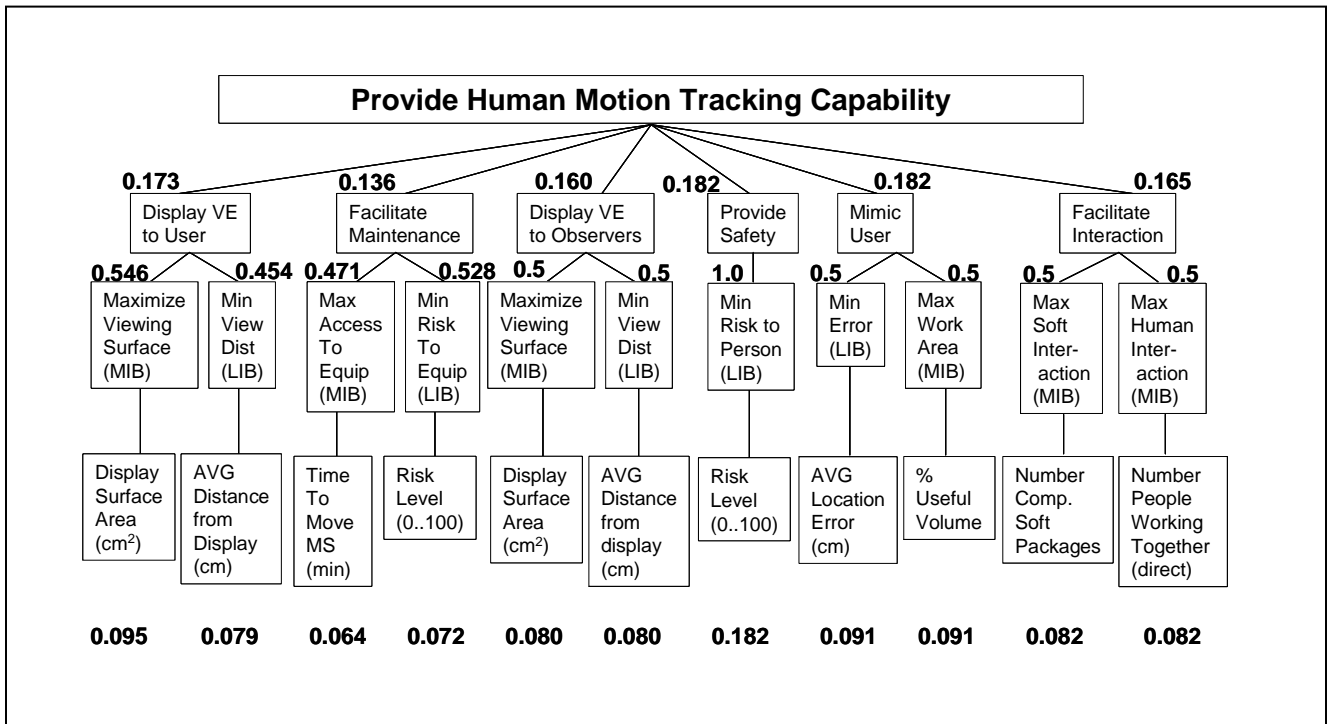


Figure 4 – HMTS Value Hierarchy

Function: Display Virtual Environment (VE) to User

Objective: Maximize Viewing Surface. Here we assume a bigger screen is better for the user to view the VE. More screen is better (MIB).

Evaluation Measure: Primary user display surface in cm<sup>2</sup>.

Function: Display Virtual Environment (VE) to User

Objective: Minimize Viewing Distance. Here we assume that a closer screen (in general) is better for a user to view the VE. Less distance if better (LIB).

Evaluation Measure: Average user distance from display surface in cm.

Function: Facilitate Maintenance.

Objective: Maximize Access to Equipment. Here we assume technicians want quick access if they need to move or maintain the equipment. More access is better.

Evaluation Measure: Average time to move entire system in minutes.

Function: Facilitate Maintenance.

Objective: Minimize Risk to Equipment. Here we assume we want to minimize the risk of damage to the equipment. Less risk is better.

Evaluation Measure: Risk level on scale of 0 (no risk) to 100 (extremely high risk).

Function: Display Virtual Environment (VE) to Observer.

Objective: Maximize Viewing Surface. Here we assume that the system that a bigger screen is better for the *observer* to view the VE. More screen is better (MIB).

Evaluation Measure: Primary *observer* display surface in cm<sup>2</sup>.

Function: Display Virtual Environment (VE) to Observer.

Objective: Minimize Viewing Distance. Here we assume that a closer screen (in general) is better for an *observer* to view the VE. Less distance is better (LIB).

Evaluation Measure: Average *observer* distance from display surface in cm.

Function: Provide Safety.

Objective: Minimize Risk to Persons. Less risk is better.

Evaluation Measure: Risk level on scale of 0 (no risk) to 100 (extremely high risk).

Function: Mimic User.

Objective: Minimize Error. Here we want to minimize the discrepancy between a sensor's reported location and a sensor's actual location. Less error is better.

Evaluation Measure: Average location error in cm.

Function: Mimic User.

Objective: Maximize Work Area. Here we want to maximize the area a user has to operate the system. More area is better.

Evaluation Measure: Percent Useful Volume. This metric is calculated by measuring what percentage of the user's body falls within 170 cm of the transmitter. This distance was determined as the useful work area based on experiments described in the modeling and analysis phase.

Function : Facilitate Interaction.

Objective : Maximize Software Interaction. Ideally, we want our tracking system to work with many various software packages. More is better.

Evaluation Measure : Number of compatible software packages.

Function : Facilitate Interaction.

Objective : Maximize Human Interaction. Here, we want our system to allow as many people as possible to simultaneously interact on a problem. More is better.

Evaluation Measure : Number of people who can directly interact while using the system.

The numbers at each node of the value model represent global and local weights. Global weights accompany the evaluation measures, while local weights correspond to the functions and objectives. These weights were calculated after interviewing each stakeholder about the relative importance of each function. Various stakeholder preferences were weighted based off the relative importance of the stakeholder. The results were then normalized to arrive at the values shown in Figure 4.

### **Design and Analysis**

After defining our problem and value model, we now turn to the design and analysis Phase of the SEMP. This phase is broken down into two steps – alternatives generation and modeling and analysis.

#### **Alternatives Generation**

Based on two key constraints – must use the MotionStar/CyberGlove and must use EDS Jack software – our alternatives are limited to variations in hardware configuration. This includes where and how to mount the MotionStar CPU, transmitter, and sensors. Because this paper is focused on mitigating the effects of interference on the MotionStar system, we will confine our alternatives to the location of the MotionStar transmitter.

Based on the configuration of the CEC-ANVIL, we explored several reasonable potential alternatives for transmitter location:

- Above Ceiling Tile Site
- Below Ceiling Tile Site A
- Below Ceiling Tile Site B
- Below Ceiling Tile Site C
- Below Ceiling Tile Site D
- Below Raised Floor Site
- Mobile Unit (32 in)
- Mobile Unit (14 in)

These are shown in Figures 5a-5d. We also “considered” another clearly infeasible option – placing the system outdoors in a parking lot free of any metal – as a baseline.

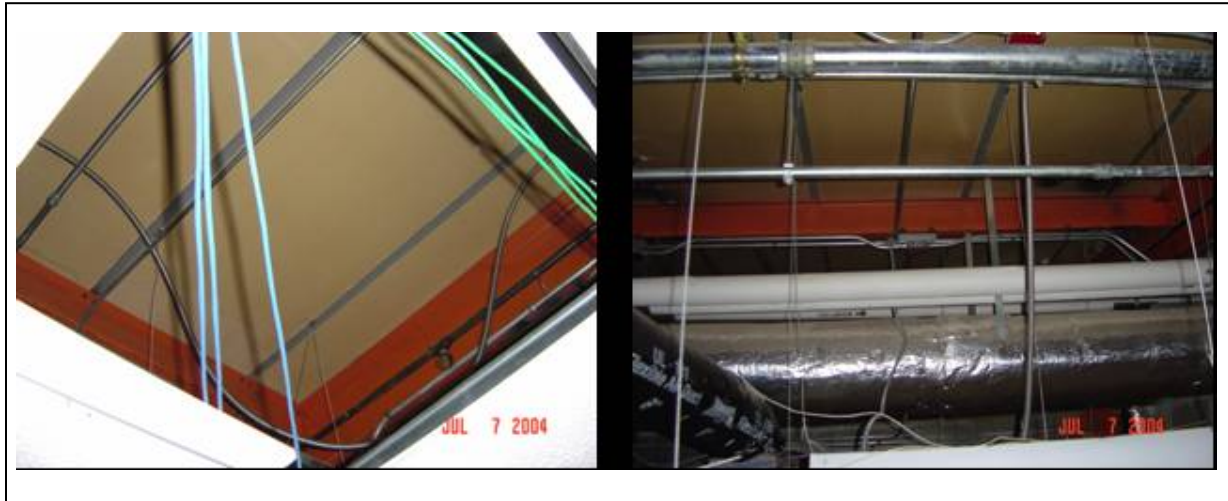


Figure 5a – Above Ceiling Tile Site



Figure 5b – Below Raised Floor Site

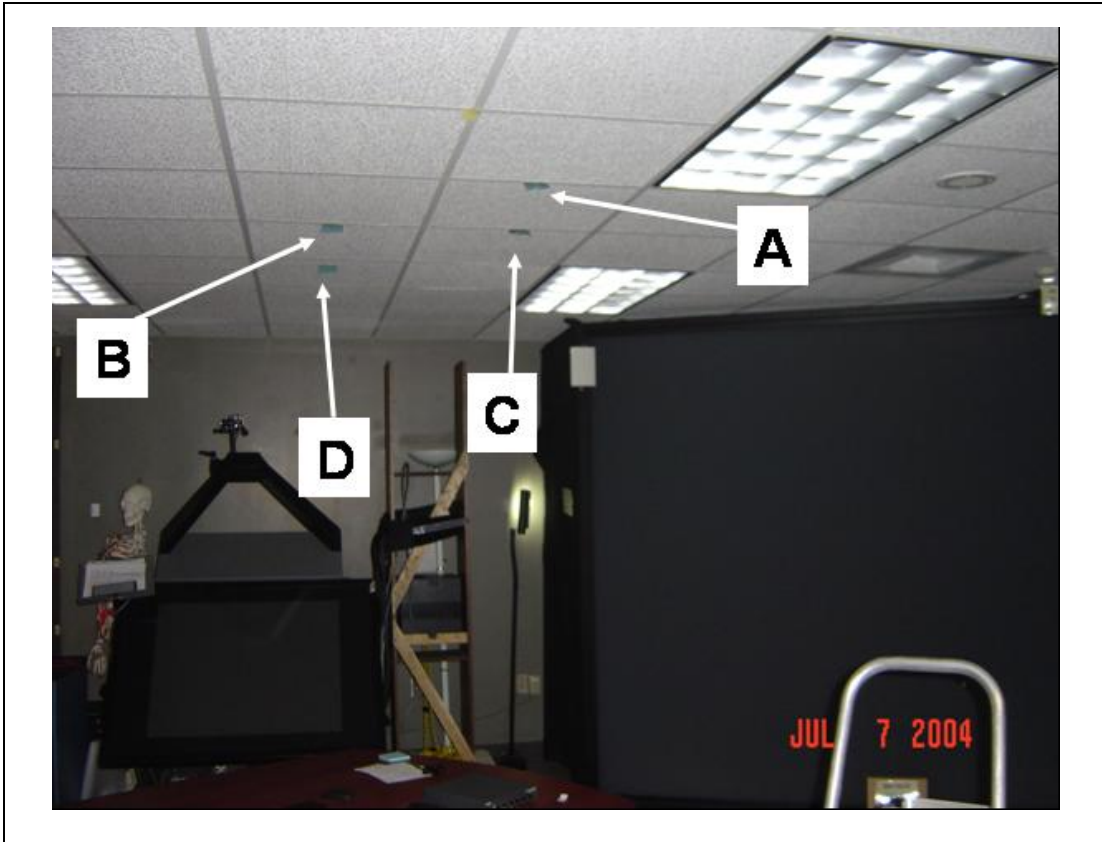


Figure 5c –Below Ceiling Sites A-D



Figure 5d – Mobile 32 and 14 inch sites

Our next step is to reduce these potential alternatives to a set of feasible alternatives. Figure 6 lists a matrix that summarizes the constraints uncovered during the Problem Definition Phase. Figure 7 shows a feasibility screen matrix that applies the constraints to each potential alternative.

CONSTRAINT TITLE	PHYSICAL CONSTRAINT	WHO PROVIDED	TYPE	NOTES
Confined to CEC	Inside CEC	Analyst	HARD	
MotionStar XSMT Limit	<= 8ft	Analyst	SOFT	Bird length from Transmitter (XSMT)
Bird Harness Length	<= 30ft	Designers	HARD	Location within 30ft of CPU
Unobstructed CAVE View (Observers)	N/A	Decision Maker	SOFT	
Usuable CAVE View (User)	N/A	Analyst	SOFT	
System must interface with JACK	N/A	Decision Maker	SOFT	
Static Conference Table	N/A	Decision Maker	HARD	
Acceptable Position Errors	< 40% error	Analyst	HARD	No excessive jumping or Major position errors

Figure 6 – Constraint Matrix

ALTERNATIVE	Confined to CEC	MotionStar XSMT Limit	Bird Harness Length	Unobstructed CAVE View (Observers)	Usuable CAVE View (User)	System must interface with JACK	Static Conference Table	Acceptable Position Errors	OVERALL
Above Ceiling	YES (GO)	10ft (NO GO)	15ft (GO)	YES (GO)	YES (GO)	YES (GO)	YES (GO)	NO (NO GO)	NO GO
Below Floor	YES (GO)	4 ft (GO)	15ft (GO)	YES (GO)	YES (GO)	YES (GO)	YES (GO)	NO (NO GO)	NO GO
Baseline (Parking Lot)	NO (NO GO)	6 ft (GO)	15ft (GO)	YES (GO)	YES (GO)	YES (GO)	YES (GO)	YES (GO)	NO GO
SITE A	YES (GO)	8 ft (GO)	15ft (GO)	YES (GO)	YES (GO)	YES (GO)	YES (GO)	YES (GO)	GO
SITE B	YES (GO)	8 ft (GO)	15ft (GO)	YES (GO)	YES (GO)	YES (GO)	YES (GO)	YES (GO)	GO
SITE C	YES (GO)	8 ft (GO)	15ft (GO)	YES (GO)	YES (GO)	YES (GO)	YES (GO)	YES (GO)	GO
SITE D	YES (GO)	6ft (GO)	15ft (GO)	YES (GO)	NO (NO GO)	YES (GO)	YES (GO)	NO (NO GO)	NO GO
MOBILE 14 inch	YES (GO)	6 ft (GO)	15ft (GO)	YES (GO)	YES (GO)	YES (GO)	YES (GO)	YES (GO)	GO
MOBILE 32 inch	YES (GO)	6 ft (GO)	15ft (GO)	YES (GO)	YES (GO)	YES (GO)	YES (GO)	YES (GO)	GO

Figure 7 – Feasibility Screening Matrix

From the feasibility screening matrix, we see that only five potential alternatives are feasible alternatives: below ceiling sites A-C, and the 14 and 32 inch mobile sites.

### Modeling and Analysis

We next look at modeling and analyzing each alternative. This process consisted of measuring displacement errors at each site by comparing a sensor's actual location versus virtual location. For the virtual location, we used the Jack software's ruler function to measure the distance between the virtual transmitter and virtual sensor (bird). For the actual location, we attached the actual sensor to a wooden pole at the end of a 10 foot plastic chain attached to the MotionStar transmitter. The chain was marked at 2 foot increments. At each alternative site, we first moved the sensor (bird) to the 4ft mark on the chain. We then attached the chain (at point of sensor intercept) to the pole at a height of 80 inches. At this height, we took measurements at 90 degrees left of center transmitter, 45 degrees left of center, 0 degrees center, 45 degrees right of center, and 90 degrees right of center. We then moved the sensor to the 40 inch point on the pole, repeated the process, then moved the sensor to the 3 inch point on the pole and repeated the process again. Finally, we repeated this entire sequence at the 6 and 8 foot marks on the chain. Figure 8 shows an augmented photograph of this process.

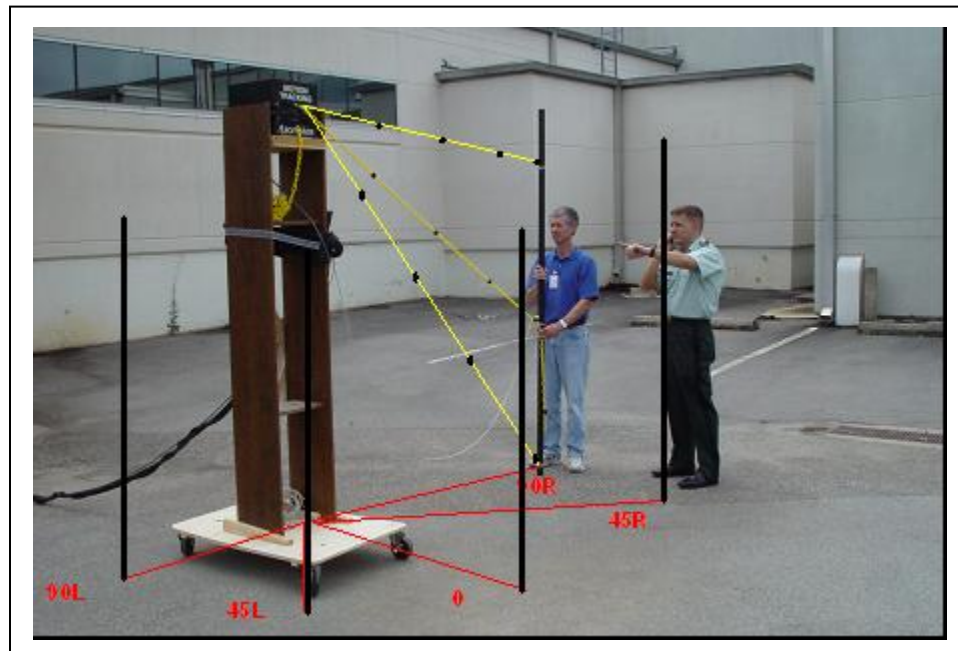


Figure 8 – Displacement Error Measurements

These measurements resulted in 45 displacement error calculations per site. Using these samples, we calculated error envelopes and an average error per site. Figure 9a and 9b show sample error envelopes, while Table 1 shows the average error calculations for each alternative.

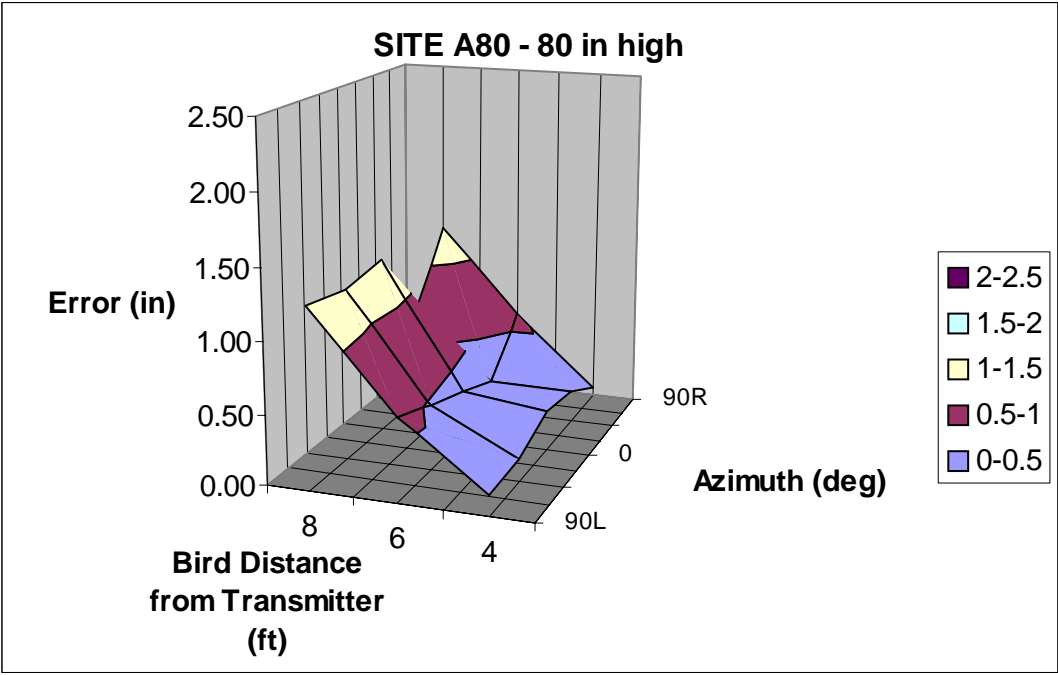


Figure 9a – Average Error for Site A (Sensor at 80 inches)

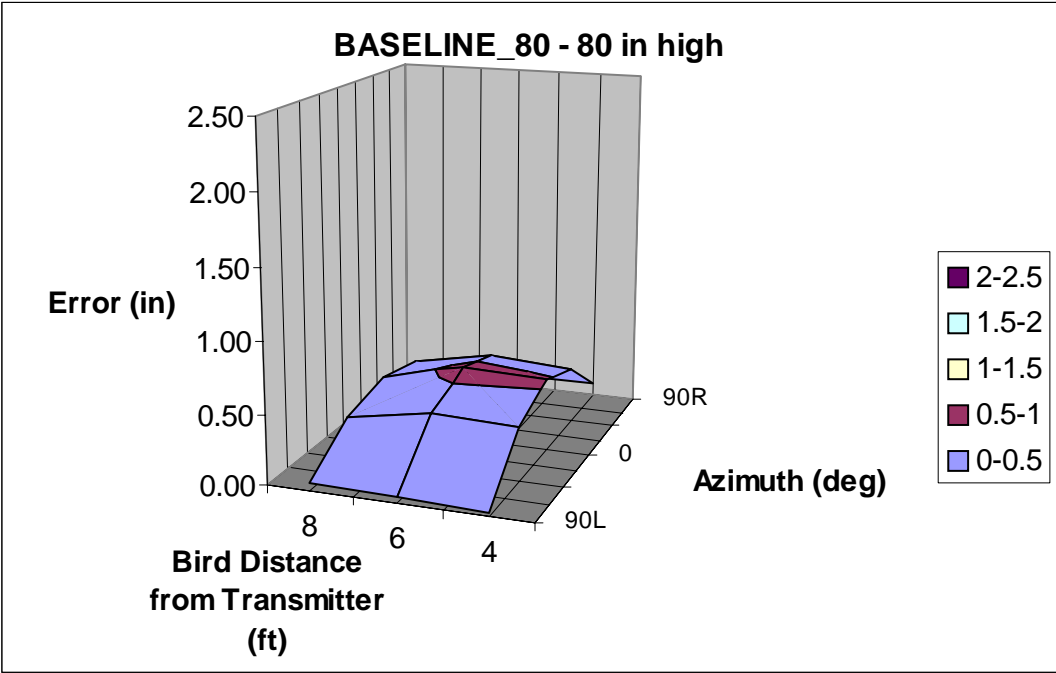


Figure 9b – Average Error for Baseline (Sensor at 80 inches)

ALTERNATIVE	AVG ERROR
ALTERNATIVE 1 (SITE A80)	0.615714286
ALTERNATIVE 2 (SITE B80)	0.652666667
ALTERNATIVE 3 (SITE C80)	0.670322581
ALTERNATIVE 4 (MOBILE 14)	0.59338022
ALTERNATIVE 5 (MOBILE 32)	0.510118355

Table 1 – Average Error for Each Alternative

This modeling and analysis served several key purposes. First, it provided raw data we will later use to compare alternatives. Second, by comparing the sites to a baseline (Figure 10), we were able to confirm that measurement errors were a result of a “noisy” lab environment, not hardware or software malfunction. This led to several important discoveries about the laboratory, such as the fact that metal lined floor tiles caused serious degradation of sensors near the floor.

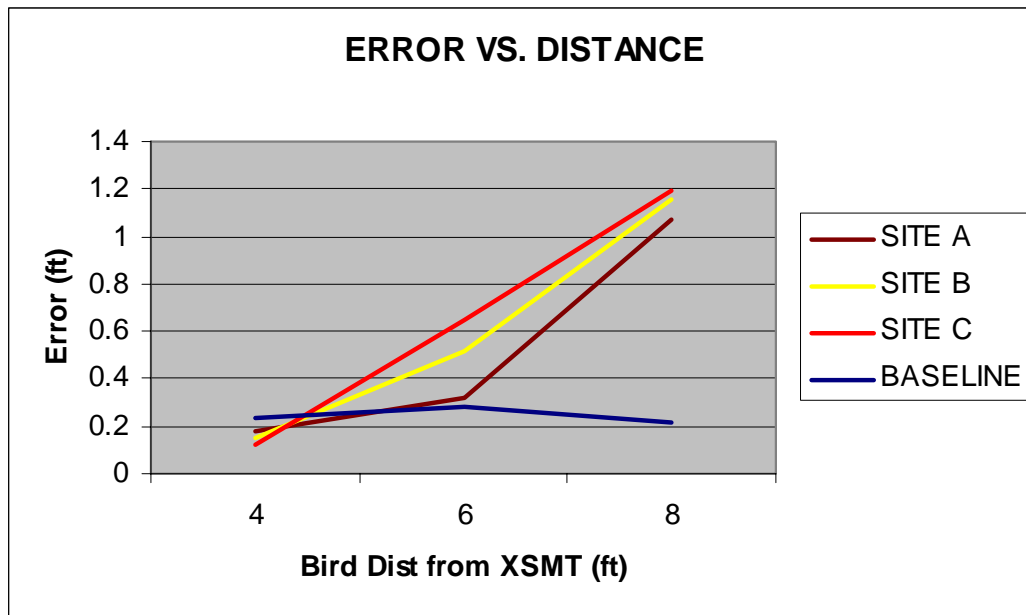


Figure 10 – Displacement Error versus Sensor Distance

### Decision Making

The first step of decision making is alternative scoring. In this step, we first gather raw data for each of the evaluation measures in our value hierarchy. This data is gathered by direct measurement, and shown in the following raw data matrix (Figure 11):

Evaluation Criteria	SITE A	SITE B	SITE C	M_14	M_32
User Display Surface Area (cm <sup>2</sup> )	69000	6020	69000	69000	69000
User - AVG Distance From Display (cm)	150	78	150	120	120
Estimated time to move MotionStar (min)	10	10	10	0	0
Risk Level To Equipment	MED	MED	MED	LOW	LOW
Observer Display Surface Area (cm <sup>2</sup> )	69000	69000	69000	69000	69000
Observer AVG Distance From Display (cm)	400	400	400	400	400
Risk Level to Personnel	MED	MED	MED	LOW	LOW
Average Location Error (cm)	18.76697	19.8933	20.4314	18.086229	15.54841
% Useful Volume	75.00%	75.00%	75.00%	100.00%	100.00%

Figure 11 – Raw Data Matrix

Our next systems engineering task is to translate the raw data into comparable value scores. This allows us to combine evaluation measures with dissimilar units (e.g. cm<sup>2</sup> and risk level) into an overall value score for each alternative. We accomplish this with value curves. Each value curve shows value or utility (y-axis) as a function of a particular raw data value (Figure 12a-g). For example, in the case of Average Location Error (Figure 12a) we notice that a 12 inch error yields approximately 60% of total possible value to the stakeholder. We developed these curves by asking the stakeholders to describe how they value each evaluation measure.

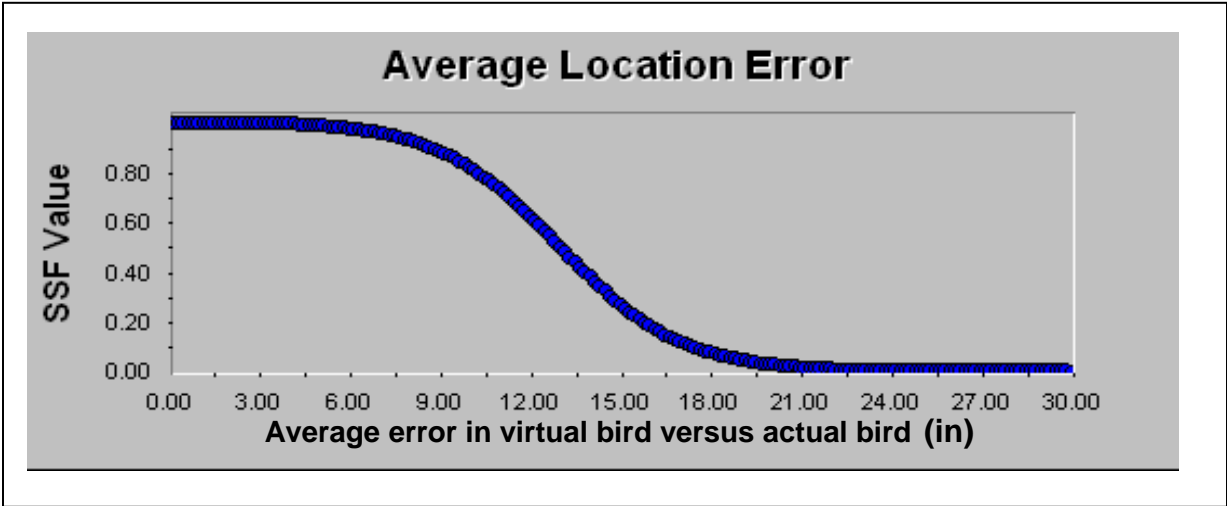


Figure 12a – Value Curve for Average Location Error

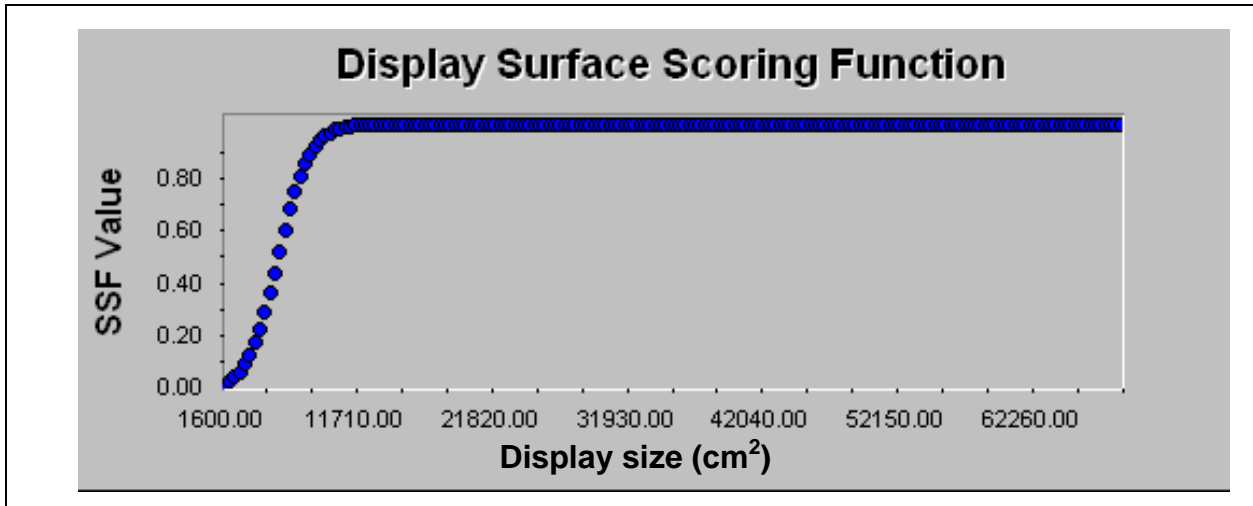


Figure 12b – Display Surface (User and Observer) Value Score

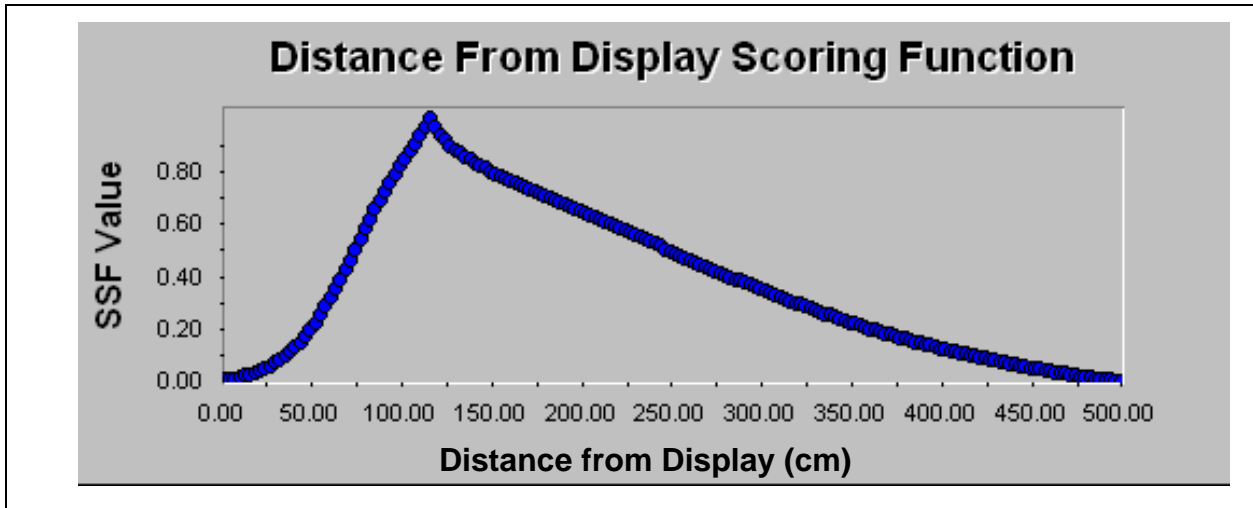


Figure 12c – Distance from Display (User and Observer) Value Curve

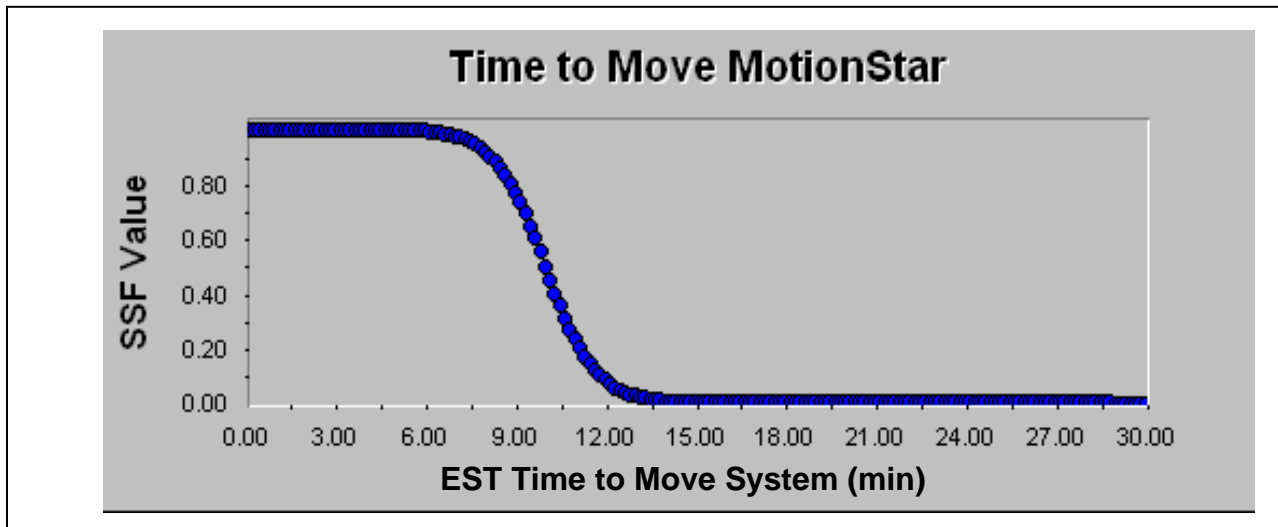


Figure 12d – Time to Move Motion Star Value Curve

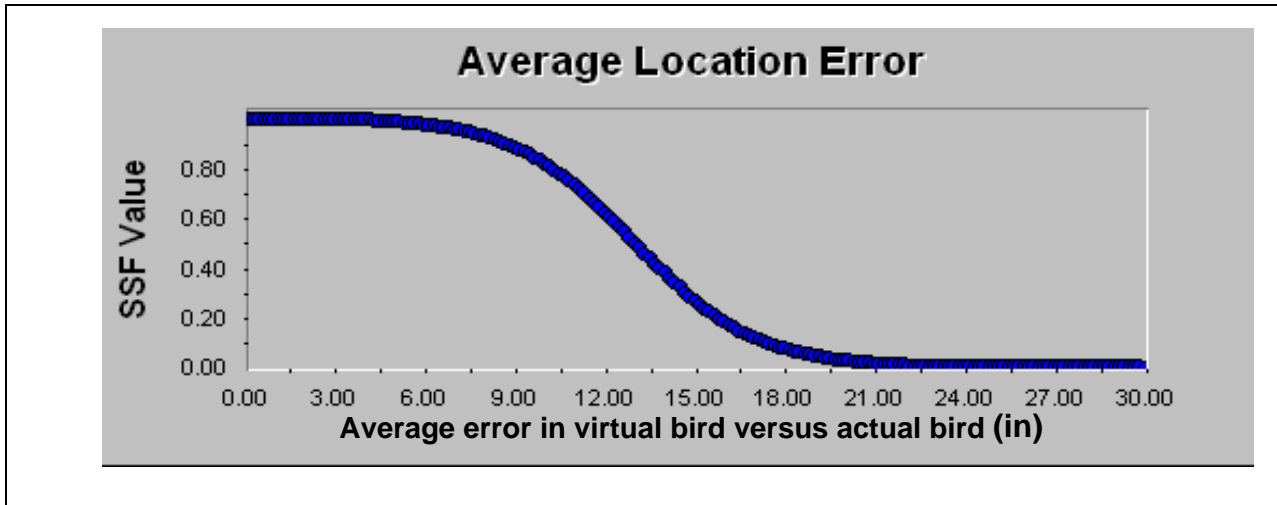


Figure 12e – Average Location Error Value Curve

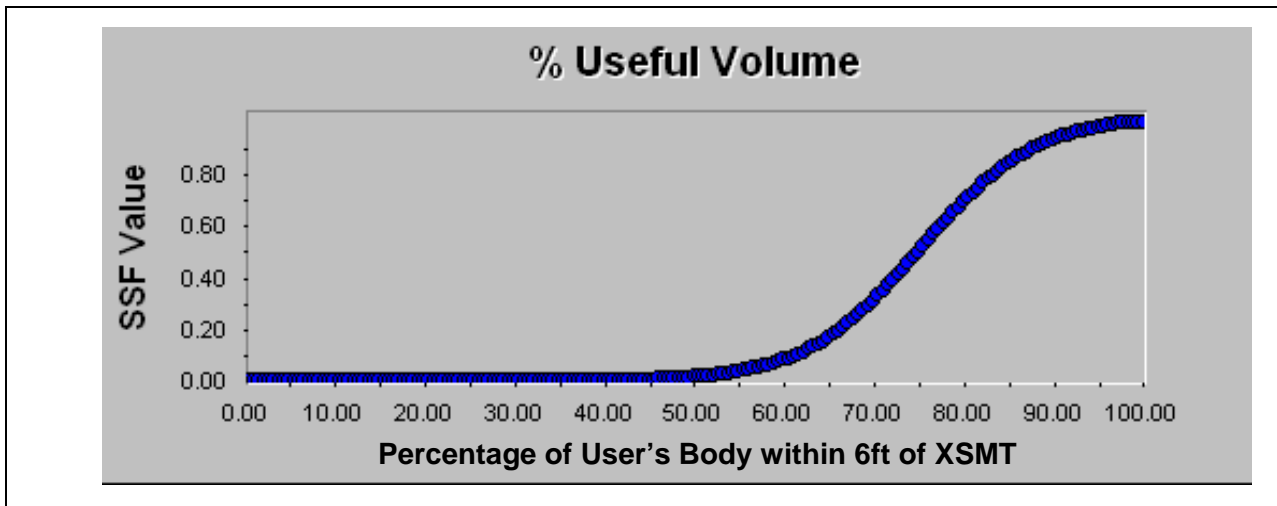


Figure 12f – Percent Useful Volume Value Curve

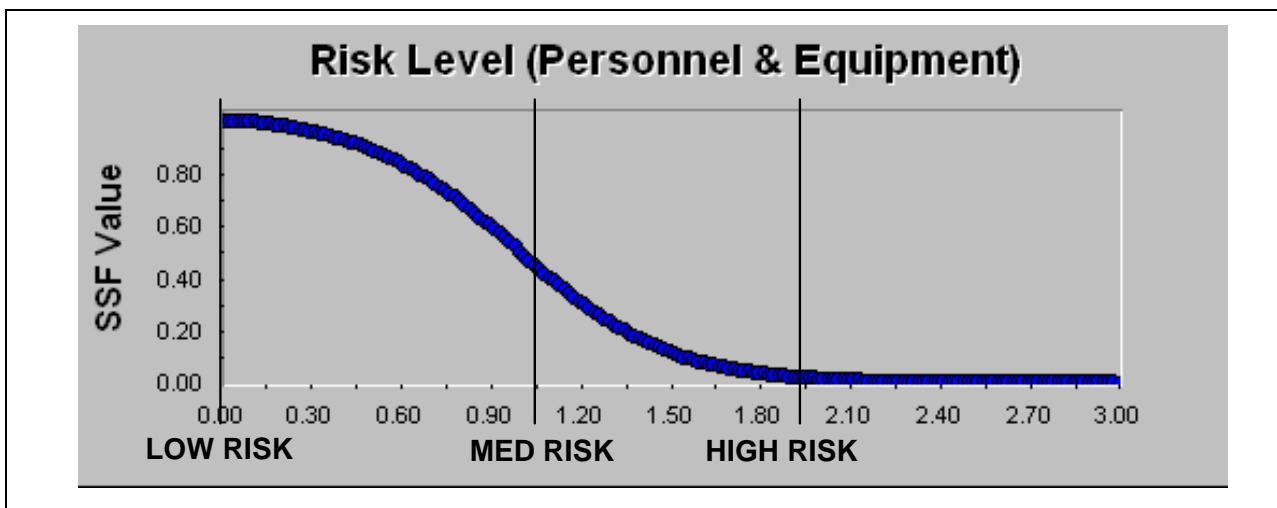


Figure 12g – Risk Level (Personnel and Equipment) Value Curve

The next step of the decision making phase is to recommend a decision. To accomplish this, we take the raw data matrix and use the value curves to construct a decision matrix (Figure 13). This shows the translated evaluation measure value scores for each alternative. These value scores are multiplied by the local weights for each evaluation measure as determined in our value model from the problem definition phase. These products are then added to obtain a total value score for each alternative.

<b>Evaluation Criteria</b>	<b>Weight</b>	<b>SITE A</b>	<b>SITE B</b>	<b>SITE C</b>	<b>M_14</b>	<b>M_32</b>
<b>User Display Surface Area (cm<sup>2</sup>)</b>	<b>0.095</b>	100.00	50.00	100.00	100.00	100.00
<b>User - AVG Distance From Display (cm)</b>	<b>0.077</b>	80.30	50.00	80.30	100.00	100.00
<b>Estimated time to move MotionStar (min)</b>	<b>0.064</b>	50.00	50.00	50.00	100.00	100.00
<b>Risk Level To Equipment</b>	<b>0.072</b>	50.00	50.00	50.00	100.00	100.00
<b>Observer Display Surface Area (cm<sup>2</sup>)</b>	<b>0.08</b>	100.00	100.00	100.00	100.00	100.00
<b>Observer AVG Distance From Display (cm)</b>	<b>0.08</b>	12.70	12.70	12.70	12.70	12.70
<b>Risk Level to Personnel</b>	<b>0.182</b>	50.00	50.00	50.00	100.00	100.00
<b>Average Location Error (cm)</b>	<b>0.092</b>	18.02	12.11	9.89	22.48	44.62
<b>% Useful Volume</b>	<b>0.092</b>	50.00	50.00	50.00	100.00	100.00
<b>TOTAL SCORE</b>		<b>46.86</b>	<b>39.23</b>	<b>46.11</b>	<b>69.28</b>	<b>71.32</b>

Figure 13 – Decision Matrix

From these results we notice that the 32 inch mobile configuration, with total value of 71.32, is the best choice. To bolster our confidence in this recommendation we also conducted a sensitivity analysis of the decision. In the sensitivity analysis, we individually varied the importance of each evaluation measure to see if our recommendation would change if an evaluation becomes more or less important. We found no such sensitivity.

### **Implementation**

The last phase of the SEMP is the implementation phase. This phase is characterized by three steps - plan of action, execution, and assessment & control. Our plan of action entailed developing a CAD drawing (Figure 14) for an all plastic mobile cart made of PVC piping. We then executed this initial plan and built a to-scale prototype. We then conducted testing with the actual transmitter, and discovered the PVC pipe exhibited structural fatigue. This assessment and control step prompted us to execute another iteration of the implementation phase to modify our implementation plan and incorporate more supporting PVC components (Figure 15).

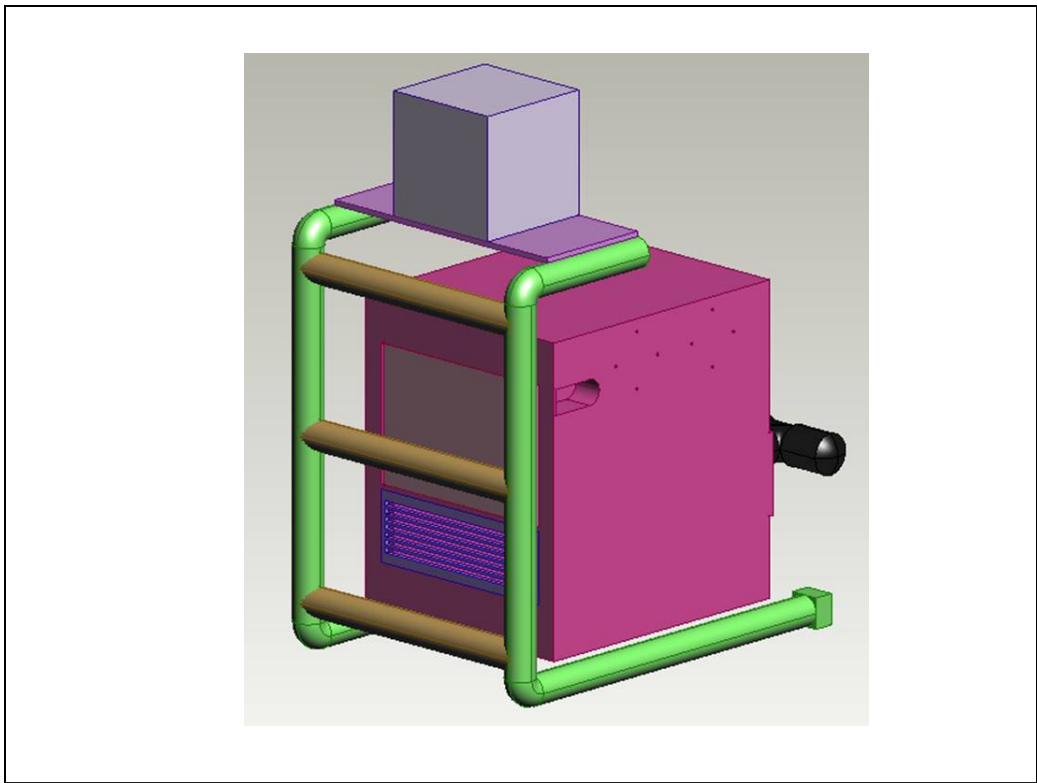


Figure 14 – Initial CAD for Implementation



Figure 15 – Second Implementation Iteration

The implementation also included constructing a sensor harness, which also involved several iterations of the implementation phase (Figure 16).

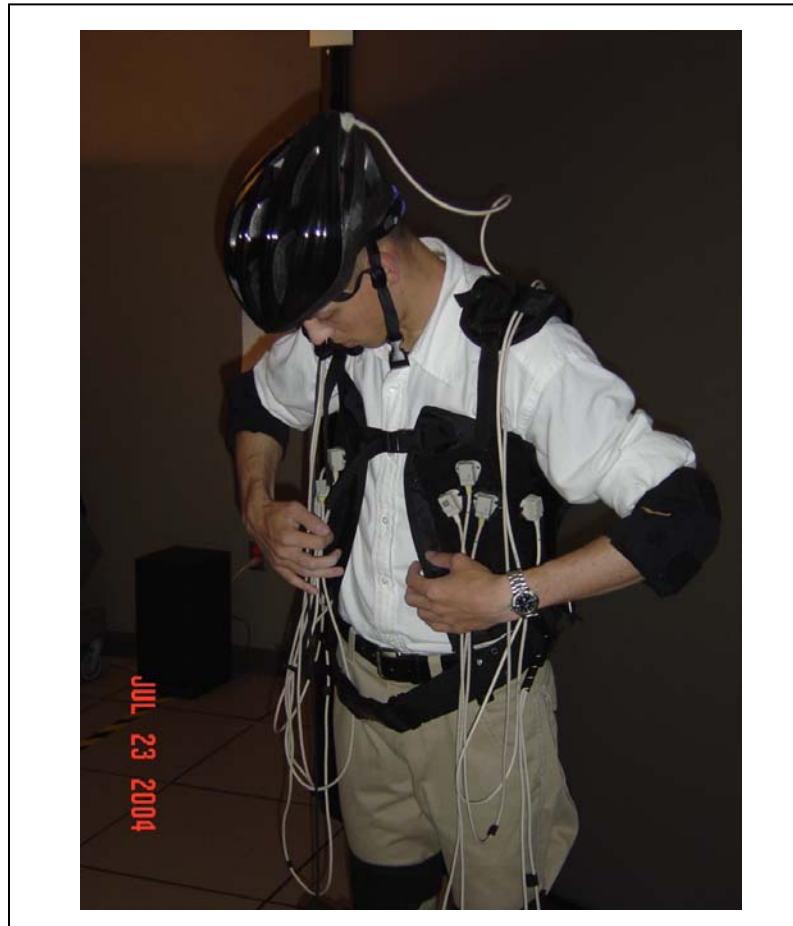


Figure 16 –Implementation of Sensor Harness

### **Conclusion**

The net result of this systems engineering approach is a functional human motion tracking system that best meets the needs of the stakeholders in ED42 given the sub-optimal environment of the CEC-ANVIL. The SEMP's robust and thorough approach to the problem helped us grasp the essential need for the system and helped uncover design possibilities (a mobile unit) not previously obvious to the decision maker.

### **Acknowledgements**

The author would like to thank the entire team of NASA engineers and contractors at the Marshall Space Flight Center's System Engineering Support Group (ED42). Special thanks to George Hamilton for his mentorship and this opportunity, Mark Blasingame for his invaluable support in the CEC-ANVIL, and to Glen Jones for broadening my intellectual and leadership horizons. Also, special thanks to Cadet Matt Labo for his help during the implementation phase.

## **References**

- [1] Installation and Operation Guide. Ascension Technology Corporation. October 1999. pg 7.
- [2] *Introduction to the Systems Engineering and Management Process*. United States Military Academy Department of Systems Engineering Whitepaper. January 2001. pg 1.
- [3] Hamilton, G. Personal Interview. June 2004.

**2004**

**NASA Faculty Fellowship Program**

**Marshall Space Flight Center**

**The University of Alabama  
The University of Alabama in Huntsville  
Alabama A&M University**

**Learning Effectiveness of the NASA Digital Learning  
Network**

Prepared By:	Billy Hix
Academic Rank:	Professor
Institution and Department:	Motlow College Department of Information Systems and Education
MSFC Directorate:	CD 60
MSFC Colleague:	Mr. Jim Pruitt

## **Introduction**

Student participation in actual investigations which develop inquiry and intellectual skills has long been regarded as an essential component of science instructions (Schwab, 1962; White, 1999). Such investigations give students an opportunity to appreciate the spirit of science and promote an understanding of the nature of science. However, classroom research conducted over the past 20 years describes science teaching as primarily teacher centered. Typical instruction consists of whole class, noninteractive activities in which individual seatwork has constituted the bulk of classroom interactions (Tobin and Gallagher, 1997). Students typically learn science from textbooks and lectures. Their main motivation is to do reasonably well on tests and examinations (Layman, 1999).

During the past five years, infrastructure constraints have reduced to the point that many schools systems can now afford low cost, high quality video conferencing equipment (International Society for Technology in Education, 2003). This study investigates the use of interactive video conferencing vs. face to face interaction with hands-on, inquiry based activities. Some basic questions to be addressed are:

- How does the delivery method impact the students understanding of the goals of the experiment?
- Are students' explanation of the strategies of experimentation different based on the method of instruction that was provided.
- Do students engaged in a workshop with the instructor in the room vs. an instructor over video conferencing have different perception of the understanding of the subject materials?

The following study took place during a four week period in the spring of 2004. The two control groups were rural 5<sup>th</sup> and 6<sup>th</sup> grade school classrooms, one that I was able to visit once each week to conduct a hands-on projects called "Return to the Moon" and the other I taught the same lessons by use of video conferencing.

The teacher in each school was involved in the teaching experiment. They sat with the students and participated as a student during each of the four lessons. Both teachers had over 10 years of experience in the classroom. However, they did not present any of the materials presented outside the class time allotted for either a face to face presentation or video conference. Each teacher did allow for one hour per week to be used in Internet based research by the students. Also, the teacher that participated with the video conference portion of the program had to act in the role as facilitator, due to the fact that these were hands-on activities and someone had to manage the classroom materials needed.

Participants in the study were 19 fifth and sixth grade students from Lincoln County and a class of 20 fifth and sixth graders from Moore County Tennessee. Both classes were provided with the same classroom materials and Internet resources.

## **Curriculum**

The class used a series of hands-on, standards based curriculum materials generated from the TeachSpace Program conducted in Tennessee. The series of four meetings used the following curriculum units:

- How far away are the moon and the planets?
- What would you leave on the moon?
- History of moon exploration
- Introduction to Rocketry
- How do rockets fly?
- Build your own powered rockets.

For the investigative activity, students constructed paper model rockets and launched them on an air powered launcher which was provided to the students. Using an inquiry based curriculum each student built a series of rockets that lead to discussions basic on failure analysis of their current design. Each design by the students incorporated more facts about the physics of rocketry. Using air powered, paper based rockets made for quick turnaround of design and rocket testing. Each rocket had to be the same length (12 inches) and use the same weight of paper in construction. However, there was no requirement based on weight, thickness, number of fins, location of fins, type of nosecone, and weight of nosecone, of the rocket.

### **Tracking Device**

By building an altitude tracker provided in the NASA Educational Product titled “Rockets – An Educator’s Guide with Activities in Science, Mathematics, and Technology”, students were able to track the altitude of their rocket in flight. Each flight was recorded in an Excel spreadsheet to be able to do analysis of their launches, as well as the launches of the entire class.

### **Data Corpus**

The data corpus consisted of the following:

- Classroom Lessons: Four, 1.5 hour lessons, one lesson per week over a month time frame.
- Pre-test of objectives
- Observations by the classroom teachers: The goal of this data collection was to observe the patterns and shifts of interaction that occurred during classroom lessons.
- Informal interviewing of the children
- Field observation notes
- Teacher Interviews
- Post test of students

Due to the abbreviated nature of this document, no example will be provided of the student’s data recording sheet. However, they did record the number of the test, launch

site conditions, data about their rocket (weight, design review and notes), altitude, and performance notes.

### **Results of the students understanding of the experimentation**

For the purpose of this document, I will focus on the student's understanding of the rocket building experiment. After the four lessons, 5 students from each group were selected at random for a personal interview. Each interview lasted approximately 20 minutes. In addition, the entire class was interviewed twice during the course of the program, once at the midway point in the course and once at the end.

Upon the first interview, students were unclear as to what the model rocket activity was about. For the most part, students in both groups were not yet thinking in terms of building a rocket and going to the moon unit and connecting it to the rest of the curriculum activities. 62% of the video conferencing students and 54% of the face to face students felt that the reason for building a rocket was just "something to do" and had not made the connection to returning to the moon.

Upon the 2<sup>nd</sup> interview, 88% of the student responses of the face to face group knew that the building the rocket exercise was to determine which type of rocket would go the highest. Many students articulated the various design features of their models. The students were also able to answer questions outlining the steps needed to build a rocket and also explanation of why some rocket designs work and others do not. In addition, they spoke of the problems in going to the moon and then on to Mars without prompting.

Only 69% of the video conference group could outline in detail the steps to construct the rocket or answer questions regarding different design features and their effect on the flight of the rocket. To reduce this difference (88% vs. 69%), it is thought that the video based group needed more follow up and also needed another class in which more discussions could take place in the discussion of design. As they built their rockets and launch them outside, the video based group did not get the instant feedback that that face to face group received. Even though they recorded notes and data regarding their flight, maybe small details were left uncovered.

### **Student Perceptions of the Classroom Environment**

A classroom survey was created for the students to complete at the end of the program. The survey was made up of 25 items encompassing five constructs: Participation, Autonomy, Relevance, Commitment to Learning, and Disruptions to Learning. Again, due to the abbreviated form of this document, I will highlight just a few of the findings.

Given the nature of the hands on activities conducted in the program, students gave very high marks in the participation category. However, the difference of knowledge gained between the pre and post test with the video conference class was lower than expected. While mean scores did improve in the area of understanding content, the increase was not significant when compared to the face to face group.

Both groups scored very similar in all categories with the exception being in the understanding of the curriculum. Commitments to Learning and Disruptions to Learning were almost identical.

It is apparent that the face to face group had more opportunities to experience reflection and examination of each activities. Sometimes the reflection might be nothing more than a question that is posed as the rocket is flying in the air. However, from these combined observations, students gained a wealth of knowledge. Both programs were interactive and with the exception of live feedback at the launch site, were the same. However, the nature of TV is to sit and listen, which was noted by the lack of questions during each presentation, where as the face to face group was much more active in the lecture and hands on portion of the program.

### **Findings**

The present study had a number of limitations due to variables between the two groups. Also, the short time period involved provided for a shallow baseline. However, the results produced a marked difference in results between the two groups.

Students involved in video conferencing activities such as the NASA Digital Learning Network, will need a great number of interactive lessons to balance the increase in gains as provided by the face to face interaction. Teachers cannot be responsible for providing the needed information before the video conference. Not only do the video lessons need to be in greater number, they need to be in shorter duration. Students enjoyed the hands on nature of the class, however, for greater gains with the video conference group, students needed more time with the conferencing mentor to be able to provide more in depth interaction. The students that were involved with the video conference often felt that they were just “doing” an experiment, where as the face to face group seem to look at the broader picture and were excited to do multiple experiments on rocket design. This desired goal will require more research to be able to provide the same level of teaching excitement in a video conference.

Student involved in video conferencing learning activities will need lessons that encourage maximum interaction to keep their interest. There should be no “talking heads”, but programs that require the student to become an active part of the lesson. The Digital Learning Network should never be used to just review the students findings. Students should feel the technology is empowering them to become active participants in the exercise. One could think of a make believe mission into space as a good example of this level of activity. The mission control would be located with the person conducting the lesson and the students would be given a set of problems to solve during the activity. Then mission control could add at random times problems or changes for the students to solve in real time. The students would be divided into teams and each team would be solving problems and reporting their findings to mission control. If students and teachers are just given a set of problems to solve or research prior to the video conference and

then students just report their findings or reports over the video conference, students will not be very impressed or inspired.

Finally, the reflective learning aspects of this study provide a beginning to an increased understanding of what students can do in a hands on, reflective classroom environment. For any video based series of lessons, students must have follow up lessons that engage the classroom teachers and students.

### **List of Recommendations**

- Interactive lessons should be interactive, not to just review the findings of a class work project with an authoritative figure. This will place much great pressure of creating good lessons for the DLN that are interactive and not just a lesson that the students and their teacher conduct and then there is a wrap-up and review of the lesson over the DLN.
- To reach the same impact level as face to face, more lessons of shorter duration are needed.
- Teachers need to be mentored prior to conducting the lesson with regards to inquiry based learning. Often the teacher needed more help in changing teaching styles than the students needed in conducting the lesson. This mentoring could take place with a pre-recorded interview with the people that will conduct the video conference that will highlight the best practices of the process.
- Students need more assistance in seeing the big picture when conducting a class by video conferencing.
- Lessons have to be much more detailed when using the Digital Learning Network due to the fact that it is harder to recover from any mistakes made.
- A pre-recorded lesson needs to be made available to the students to provide instructions on how to interact with the video conference so that the “newness” of the medium does not detract from the learning experience.

**2004**

**NASA FACULTY FELLOWSHIP PROGRAM**

**MARSHALL SPACE FLIGHT CENTER  
THE UNIVERSITY OF ALABAMA  
THE UNIVERSITY OF ALABAMA IN HUNTSVILLE  
ALABAMA A&M UNIVERSITY**

**EFFECTS OF PIEZOELECTRIC (PZT) SENSOR BONDING AND  
THE CHARACTERISTICS OF THE HOST STRUCTURE ON  
IMPEDANCE BASED STRUCTURAL HEALTH MONITORING**

Prepared by:	Abdul Jalloh
Academic Rank:	Assistant Professor
Institution and Department	Mechanical Engineering Department Alabama A&M University Normal, AL 35762
NASA/MSFC Directorate:	ED 27
MSFC Colleagues:	John Lassiter

## **Summary**

This study was conducted to investigate the effects of certain factors on the impedance signal in structural health monitoring. These factors were: the quality of the bond between the sensor and the host structure, and the characteristics of the host structure, such as geometry, mass, and material properties. This work was carried out to answer a set of questions, related to these factors, that were developed by the project team. The project team was comprised of Dr. Doug Ramers and Dr. Abdul Jalloh of the Summer Faculty Fellowship Program, Mr. Arnaldo Colon-Perez, a student intern from the University of Puerto Rico of Turabo, and Mr. John Lassiter and Mr. Bob Engberg of the Structural and Dynamics Test Group at NASA Marshall Space Flight Center (MSFC).

This study was based on a review of the literature on structural health monitoring to investigate the factors referred to above because there was not enough time to plan and conduct the appropriate tests at MSFC during the tenure of the Summer Faculty Fellowship Program project members.

The surveyed literature documents works on structural health monitoring that were based on laboratory tests that were conducted using bolted trusses and other civil engineering type structures for the most part. These are not the typical types of structures used in designing and building NASA's space vehicles and systems. It was therefore recommended that tests be conducted using NASA type structures, such as pressure vessels, to validate the observations made in this report.

## **Introduction**

The electromechanical impedance method using piezoelectric (PZT) sensors is one of the most recent developments in the field of structural health monitoring. This damage monitoring method is based on the electromechanical coupling between the host structure and the bonded PZT sensor. Damage alters the stiffness, damping and mass of the host structure, which results in changes in the mechanical impedance of the structure. This in turn modifies the effective electrical impedance of the sensor, which is then used to identify incipient damage in the host structure [5, 6]

There are several factors that could affect the performance of the PZT sensor. These include the quality of the bond between the sensor and the host structure, and the characteristics of the host structure, such as geometry, mass, and material properties [13]. It is therefore necessary to understand how these factors affect the quality of the impedance signal that is obtained from the sensor. This work was carried out to answer a set of questions, related to these factors, that were developed by the project team. The project team was comprised of Dr. Doug Ramers and Dr. Abdul Jalloh of the Summer Faculty Fellowship Program, Mr. Arnaldo Colon-Perez, a student intern from the University of Puerto Rico of Turabo, and Mr. John Lassiter and Mr. Bob Engberg of the Structural and Dynamics Test Group at NASA Marshall Space Flight Center (MSFC). The questions are listed in the next section.

This report addresses the following issues that are related to the factors mentioned above:

1. Effects of the quality of sensor bonding on the signal
2. Sensor bonding techniques
3. Sensor geometry
4. Sensitivity of the sensing region
5. Effects of host structure geometry, and material properties on impedance measurements.

This work was based on a review of the literature on Structural Health Monitoring to investigate the factors referred to above because there was not enough time to plan and conduct the appropriate tests at MSFC during the tenure of the Summer Faculty Fellowship Program project members. The surveyed literature documents works on structural health monitoring that were based on laboratory tests that were conducted using bolted trusses and other civil engineering type structures for the most part. These are not the typical types of structures used in designing and building NASA's space vehicles and systems. It is therefore recommended that tests be conducted using NASA type structures, such as pressure vessels, to validate the observations made in this report.

### **Project Questions**

The project questions are listed below. The first four questions were assigned to Dr. Ramers for investigation. His work is documented in his Summer Faculty Fellowship Program Report [12]. The last two questions, questions 5 and 6, were assigned to Dr. Jalloh, and they are addressed in this report.

1. Is there a significant difference in the information provided between the PZT and SCP sensors?
2. Which bands are needed to characterize the PZT and SCP signals?
3. Is there an adequate parsimonious characterization of the piezo signal?
4.
  - a. What are the metrics that can be used for detecting change in the PZT signal indicating change
  - b. What methods and metrics can be used to determine if the PZT is operating correctly?
5. What are the appropriate procedures for attaching PZTs to structures

- a. How does surface area contact affect sensitivity of signal?
  - b. How does quality and type of bond have an effect of the nature of the signals?
  - c. Does gradual degradation (or changes) in the bonding material have an effect on the nature of the signal?
6. In general, how do we size the sensor (length, width, thickness)?

### **Sensor Bonding**

The bonding effects of a PZT sensor significantly affect the estimation of the resonant frequencies of the host structure [15]. Bonding the PZT sensor to the host structure is of utmost importance because the PZT actuation/sensing process depends on the effective electromechanical coupling of the sensor with the host structure being monitored. Bond quality determines the quality of the electromechanical coupling between the sensor and the host structure. As such a study to optimize the quality of the bond between the PZT sensor and the host structure deserves special attention. In the literature, several research teams have documented their work in this area [1, 2, 3, 7, 8, 9, 13, 14, 15].

In their study, which investigated the effects on the bonding layer of the dynamic interaction between a PZT patch and a host structure, Xu and Liu [15] suggested that the bonding effects of PZT sensors should be included to obtain more accurate results.

Ong et al. [8, 9] suggested that adhesives with high modulus should be used in order to obtain maximum repeatability and consistency of the impedance signature.

Bhalla et al. [2] suggested the use of double-sided adhesive tape to bond PZT sensors to host structures.

Giurgiutiu and Zagari [7] demonstrated that the integrity and consistency of the sensor can be assessed by the imaginary component of the impedance measurement. A well-bonded sensor shows a smooth curve while a dis-bonded sensor shows a very strong resonance in the imaginary part. It is therefore possible to determine whether the sensor is perfectly bonded to the host structure or not by tracing the imaginary component. The authors, however, point that qualitative assessment or estimation of the bonding stiffness is a very difficult task.

Berman et al. [1] conducted a set of tests to study the quality of bonding between PZT sensors and graphite reinforcements of a host structure. Different bonding procedures were used in the tests. The test results are summarized in Table 1 below.

Table 1. Procedures investigated for bonding PZT sensors to graphite reinforcement.

	<b>Bonding Procedure</b>	<b>Bond Quality</b>
1	Applied to wet resin, no pressure applied.	<b>Poor.</b> Thick layer of epoxy between sensor and graphite reduces actuation performance.
2	Applied to wet resin, pressure (5 psi) applied.	<b>Mediocre.</b> Layer of epoxy is thinner, but actuation performance still not acceptable.
3	Applied after two hours of curing, no pressure applied.	<b>Poor.</b> Thick layer of epoxy between sensor and graphite reduces actuation performance.
4	Applied after complete curing using cyano-acrylate adhesive, pressure applied.	<b>Acceptable.</b> Layer of cyano-acrylate adhesive much thinner than epoxy, good actuation performance.
5	Applied after complete curing using cyano-acrylate adhesive, fiberglass mesh removed, pressure applied.	<b>Best.</b> Thinnest layer of cyano-acrylate adhesive for optimum actuation performance.

Park et al. [10, 11] observed that brittle piezoceramic sensors can only withstand very small bending. This imposes difficulties in handling and bonding of the sensor into the host structure. Also conformability of piezoceramic sensors to curved surfaces is extremely poor. This makes it necessary to undertake extra treatment of the surfaces before bonding the sensor to the host structure.

### **Sensor Bonding Techniques**

The three main methods used to attach PZT sensors to host structures for structural health monitoring are:

1. **Clamping:** This method is often found to be unreliable since the function of the sensor is to move and it is very difficult to stop the minute vibrations that will sometimes allow the sensor from “walking” out of the clamp.
2. **Soldering:** This method has the advantage of giving a conductive connection. A major drawback is that the movement will cause fatigue in the bond.
3. **Gluing:** This is usually the best approach. Modern epoxy- or acrylate glues, in particular, provide strong, yet flexible bonds. The bond does not experience any

fatigue. Since electrical contact is always required between the sensor and host structure, one possibility is to use conductive glue, usually an epoxy filled with particles. One drawback with these glues is that they are so heavily loaded with conductive particles that the glue line is often weak.

The Structural and Dynamics Testing Group at MSFC have been using the gluing technique to attach sensors to test articles in structural health monitoring tests. The adhesive used is “super glue”, a commercially available product. This seems to be an effective bonding technique, although tests need to be conducted to study the effects on the impedance signal that would result from damage to or deterioration of the bond.

One of the tests conducted by Berman et al. [1] used a vacuum-assisted sensor-mounting technique that provided the tightest possible bond while using the thinnest feasible layer of adhesive. The technique consists of the following steps:

1. A PZT sensor, a square strip of porous release film, a square strip of 0.05 in. thick porous foam, and nylon bagging film were stacked into a four-layer assembly.
2. The mating surfaces of the sensor and composite were cleaned thoroughly with acetone.
3. A one-part cyano-acrylate epoxy was applied to the sensor surface.
4. The assembly was immediately placed on the composite material.
5. A vacuum setup, comprising of a compressor, tubes, and sealant tape wrapped around the sensor assembly, was used to establish a vacuum around the sensor.

The vacuum field forces the sensor tightly against the composite surface and yields a good bond within two hours.

### **Sensitivity of the Sensing Region**

The sensing range of an impedance sensor in general, is closely related to the frequency ranges used, the material properties and geometry of the host structure, and the properties of the sensor [10, 11]. This report will address issues related to the properties and geometry of the host structure.

It has been demonstrated experimentally that the sensing area is localized to a region close to the PZT sensor [1, 4]. This characteristic enhances the sensing ability of PZT sensors to detect damage without being affected by far field boundary conditions, external loading, or normal operational vibrations of the system. Depending on host structure material properties, it has been estimated that the sensing area of a single PZT sensor can vary anywhere from 0.4 m (sensing radius) on composite reinforced concrete structures, to 2 m on simple metal beams.

Several factors affect the sensing region of the host structure in structural health monitoring. Some important factors and their effects are given in Table 2 below [4]. It should be noted that the conclusions in Table 2 were deduced for the most part from tests conducted on bolted truss structures.

The factors in Table 2 should be taken into account when attaching PZT sensors to host structures. The rating scheme shown in the right-hand column of Table 2 indicates the factor's importance: 0 corresponds to a factor of no importance, while 5 would be the most important factor.

Table 2. Factors to consider when attaching PZT sensors to host structures.

<b>Factors</b>	<b>Important Effects</b>	<b>Rating</b>
Material stiffness and density	Impedance shifts to the right and up for stiffer materials	1
Energy absorbent materials	Decrease in amplitude for softer intermaterials. Significantly larger for highly damped materials	2
Material damping	More damped materials give shallower peaks	3
Discontinuity in cross-section	Important attenuation at large cross-section discontinuities	3
Bolted joints	Size of bolt more important than its material. Shearing force at the interface is the most important factor. Major source of energy loss	5

In his study, Esteban [4] made the following conclusions based on the information in Table 2:

1. The impedance shifts to the right and has an increased amplitude for stiffer materials, while most damped materials would tend to give more shallow signals. These factors must be taken into considerations if sensors are to be attached close to areas of different materials.
2. For intermaterials that are softer than the host material, the area of material discontinuity acts as an energy absorbent. This characteristic brings the amplitude of the response down. Conversely, if the intermaterial is harder than the host material, the opposite effect is observed.

3. The sensing range of the PZT sensor will be affected by the internal damping of the material of the host structure. As such, the number of sensors needed to monitor the system should vary accordingly.
4. Cross-sectional discontinuities in the host structure are a source of signal attenuation. This characteristic was observed even for relatively small cross-sectional discontinuities. The number of sensors in this region should also vary accordingly.
5. The size of the bolt in bolted joints plays a great role in the attenuation of the propagating wave, while the bolt material was less critical.

### **Sensor Geometry**

Certain PZT sensor geometries are more favorable than others in conducting structural health monitoring. Laboratory tests [1] have shown that:

1. Increasing the thickness of the sensor (bonded to the host structure) decreases the capacitive contribution of the sensor, thereby decreasing the heights of the peaks in the impedance signature.
2. Increasing the contact area of the sensor causes an increase in the sensor's capacitive contribution, thereby increasing the height of the peaks in the impedance signature. This implies a greater dynamic interaction between the sensor and the host structure
3. Sensor plates as small as 0.50 in. square and 0.01 in. thick are sufficient for structural health monitoring.

It should be pointed out that no information was found in the surveyed literature that directly relates the size of a PZT sensor to the geometry and/or properties of the host structure. However, effective structural health monitoring can be accomplished even with very small PZT sensors.

### **Conclusions and Recommendations**

Although this work was not based on tests conducted at MSFC as was originally envisioned, the review of the literature on structural health monitoring has yielded some very useful information that addresses the project questions that were assigned to the author. Based on this review, it was concluded that:

1. The quality of the bond between the PZT sensor and the host structure has a significant effect on the quality of the signal. Also, several bonding procedures, the resulting quality of the bond and the effect on the signal in each case were reviewed

2. The thickness of the sensor, the size of the contact area of the sensor and the size of the sensor were all found to have effects on the impedance signal.
3. The sensing area was found to be localized to a region close to the PZT sensor. Depending on the material properties and geometry of the host structure, the sensing region can extend anywhere from 0.4 m (sensing radius) on composite reinforced concrete structures to 2 m on metal beams.
4. Several factors that must be considered when attaching PZT sensors to host structures. Some of these factors include material stiffness and density, energy absorbing capacity of materials, material damping, discontinuity in cross-sections, and bolted joints. The effects of these factors on the impedance signal and the relative importance of each factor were reviewed.

This work was based on a review of the literature on Structural Health Monitoring to investigate the factors that relate to the project questions to above. The conclusions in the surveyed literature were made, in the most part, from tests conducted on bolted trusses and other civil engineering type structures. These are not the typical type of structures that are employed in designing and building NASA type space vehicles and systems. It is therefore recommended that tests which replicate those in the surveyed literature be conducted using NASA type structures. The purpose of these tests will be to investigate the effect on the impedance signal in structural health monitoring from the factors related to the project questions.

Additionally, is recommended that tests be conducted to study the characteristics of PZT sensor bonding in cryogenic temperature environments and also on the effect of cryogenic temperatures on the impedance signal.

## **References**

1. Berman, J, Quattrone, R., Averbuch, A., Lalande, F., Cudney, H., Raju, V., and Cohen, G. L., (1999). "Piezoelectric Patch Sensors for Structural Integrity Monitoring of Composite-Upgraded Masonry and Concrete Structures", *Construction Engineering Research Laboratory Technical Report 99/72, US Army Corps of Engineers*.
2. Bhalla, S., Naidu, A. S. K., Ong, C. W., and Soh, C. K., 2002. " Practical Issues in the Implementation of Electromechanical Impedance Techniques in NDE." *Proceedings of SPIE International Symposium on Smart Materials, Nano-, and Micro-Smart Systems, December 16-18, Melbourne, Australia (paper no 4935-77)*.
3. de Faria, A. R., 2003. "The Impact of Finite-Stiffness bonding on the Sensing Effectiveness of Piezoelectric patches." *Technical Note, Smart Materials and Structures 12, N5 – N8*

4. Esteban, J., 1996. "Modeling of the Sensing Region of a piezoelectric actuator/sensor." *Ph.D. Dissertation, Virginia Polytechnic Institute and State University, Blacksburg, Va.*
5. Giurgiutiu V., and Rogers C. A., 1997. "Electromechanical (E/M) Impedance Method for Structural Health Monitoring and Non-destructive evaluation." *Proc. 1<sup>st</sup> Int. Workshop on Structural Health Monitoring (California: Stanford University, 433-444)*
6. Giurgiutiu V., and Rogers C. A., 1998. "Recent Advancements in the Electro-Mechanical (E/M) Impedance Method for Structural Health Monitoring and NDE." *Smart Structures and Materials Conf. (San Diego, California, Proc. SPIE 3329 536-547)*
7. Giurgiutiu V., and Zagari, A. N., 2002. "Embedded Self-Sensing Piezoelectric Active Sensors for Online Structural Identification," *ASME Journal of Vibration and Acoustics, Vol. 124, 116-125.*
8. Ong, C. W., Lu, Y., and Soh, C. K., 2002a. "The Influence of Adhesive Bond on Electromechanical Admittance Response of a PZT Patch Coupled Smart Structure." *Proceedings of the 2<sup>nd</sup> International Conference on Structural Stability and Dynamics, December 16-18, Singapore.*
9. Ong, C. W., Yang, Y., Wong, Y. T., Bhalla, S., Lu, Y., and Soh, C. K., 2002b. "The effects of adhesive on the Electromechanical response of a Piezoceramic transducer Coupled Smart Structure." *Proceedings of ISSS-SPIE 2002 International Conference on Smart Materials and Systems, December 12-14, Bangalore, India (ISSS2002/SA-592).*
10. Park, G., Inman, D. J., Farrar, C. R., 2003. "Recent Studies in Piezoelectric Impedance-Based Structural Health Monitoring," *4<sup>th</sup> International Workshop on Structural Health Monitoring, September 15-17, Stanford, California, 1423-1430.*
11. Park G., Sohn, H, Farrar, C. R., Inman, D. J., 2003. "Overview of Piezoelectric Impedance-Based Health Monitoring and Path Forward." *The Shock and Vibration Digest, Vol. 35, No. 6, 451-463.*
12. Ramers, D. L., 2004. "Analysis of Piezoelectric structural Sensors with Emergent Computing Techniques," *NASA Faculty Fellowship Program Report.*
13. Tseng, K. K-H., and Naidu, A. S. K., 2002. "Non-Parametric Damage Detection and characterization using Smart Piezoelectric Material." *Smart Materials and Structures II, 317-329*
14. Wang, B., Jiang, Y., Li, Y., Wang, X., and Xiong, K., 2003. "Experimental Research on the Response Characteristic of Piezoelectric Transducers Debonding from Composite Beam." *Proceedings of the 4<sup>th</sup> International Workshop on Structural Health Monitoring, Stanford, CA, 1416 – 1422.*

15. Xu, Y. G., and Liu, G. R., 2002. "A Modified Electromechanical Impedance Model of Piezoelectric Actuator-Sensors for Debonding Detection of Composite Repair Patches." *Journal of Intelligent Material Systems and Structures*, Vol. 13, No. 6, 389-405.

**2004**

**NASA FACULTY FELLOWSHIP PROGRAM**

**MARSHALL SPACE FLIGHT CENTER**

**THE UNIVERSITY OF ALABAMA  
THE UNIVERSITY OF ALABAMA IN HUNTSVILLE  
ALABAMA A&M UNIVERSITY**

**STUDY OF A 30-M BOOM FOR SOLAR SAIL-CRAFT:  
MODEL EXTENDIBILITY AND CONTROL STRATEGY**

Prepared By:	Leehyun Keel
Academic Rank:	Professor
Institution and Department:	Tennessee State University Center of Excellence in Information Systems & Department of Electrical Engineering
NASA/MSFC Directorate:	Transportation
MSFC Colleague:	Dr. Mark Whorton

## **Introduction**

Space travel propelled by solar sails is motivated by the fact that the momentum exchange that occurs when photons are reflected and/or absorbed by a large solar sail generates a small but constant acceleration. This acceleration can induce a constant thrust in very large sails that is sufficient to maintain a polar observing satellite in a constant position relative to the Sun or Earth. For long distance propulsion, square sails (with side length greater than 150 meters) can reach Jupiter in two years and Pluto in less than ten years.

Converting such design concepts to real-world systems will require accurate analytical models and model parameters. This requires extensive structural dynamics tests. However, the low mass and high flexibility of large and light weight structures such as solar sails makes them unsuitable for ground testing. As a result, validating analytical models is an extremely difficult problem. On the other hand, a fundamental question can be asked. That is whether an analytical model that represents a small-scale version of a solar-sail boom can be extended to much larger versions of the same boom. To answer this question, we considered a long deployable boom that will be used to support the solar sails of the sail-craft. The length of fully deployed booms of the actual solar sail-craft will exceed 100 meters. However, the test-bed we used in our study is a 30 meter retractable boom at MSFC. We first develop analytical models based on Lagrange's equations and the standard Euler-Bernoulli beam. Then the response of the models will be compared with test data of the 30 meter boom at various deployed lengths. For this stage of study, our analysis was limited to experimental data obtained at 12ft and 18ft deployment lengths. The comparison results are positive but speculative. To observe properly validate the analytic model, experiments at longer deployment lengths, up to the full 30 meter, have been requested. We expect the study to answer the extendibility question of the analytical models.

In operation, rapid temperature changes can be induced in solar sails as they transition from day to night and vice versa. This generates time dependent thermally induced forces, which may in turn create oscillation in structural members such as booms. Such oscillations have an adverse effect on system operations, precise pointing of instruments and antennas and can lead to self excited vibrations of increasing amplitude. The latter phenomenon is known as thermal flutter and can lead to the catastrophic failure of structural systems. To remedy this problem, an active vibration suppression system has been developed. It was shown that piezoelectric actuators used in conjunction with a Proportional Feedback Control (PFC) law (or Velocity Feedback Control (VFC) law) can induce moments that can suppress structural vibrations and prevent flutter instability in spacecraft booms. In this study, we will investigate control strategies using piezoelectric transducers in active, passive, and/or hybrid control configurations. Advantages and disadvantages of each configuration will be studied and experiments to determine their capabilities and limitations will be planned. In particular, special attention will be given to the hybrid control, also known as energy recycling, configuration due to its unique characteristics.

## **UTF Mast Load-Deflection/Load Deflection Cut Wire Test Configurations**

Figure 1 shows UTF mast load-deflection cut wire test configuration. The displacement data collected from the tip position of the boom was used for preliminary model comparison.

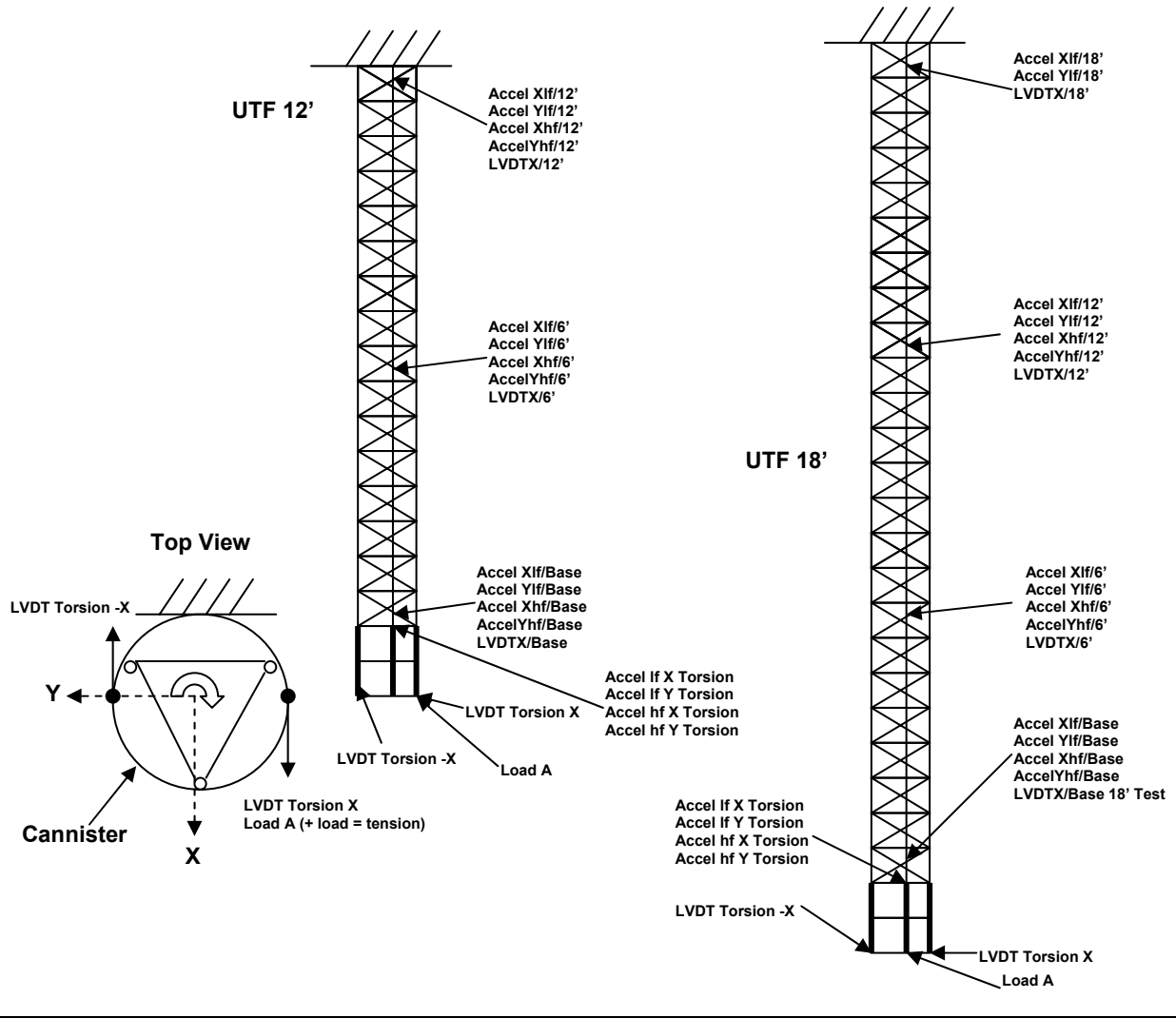


Figure 1: UTF Mast Torsion Load-Deflection Test/Cut Wire Torsion Load-Deflection Test Configurations

### Analytical Models

Consider a beam in transverse vibration. Under the assumption that the cross-sectional dimensions are small compared with the length of the beam, both the shear and rotary inertia effects can be neglected. Then kinetic energy  $T(t)$  and potential energy  $V(t)$  are:

$$T(t) = \frac{1}{2} \int_0^L \left[ \frac{\partial y(x,t)}{\partial t} \right]^2 m(x) dx + \frac{1}{2} \left[ \frac{\partial y(L,t)}{\partial t} \right]^2 m_p \quad (1)$$

$$V(t) = \frac{1}{2} \int_0^L EI(x) \left[ \frac{\partial \varphi(x,t)}{\partial x} \right]^2 dx \quad (2)$$

To determine the transverse displacement  $y(x,t)$ , we assume separation of variables, that is,

$$y(x,t) = \sum_{j=1}^n \phi_j(x) q_j(t). \quad (3)$$

*Remark:* The beam is assumed to be uniform, that is,  $EI(x)=\text{constant}$ ,  $m(x)=\text{constant}$ .

Substituting for the expressions above in Lagrange's equation, a state space model was developed and (A,B,C,D) matrices were computed for both 12ft and 18ft boom lengths under the following assumptions.

*Model 1:* Though inconsistent with eq. (1), we derived mode shape functions  $\phi_j(x)$  assuming (for simplicity) the boom is an Euler-Bernoulli beam with *no tip mass*.

*Model 2:* To improve the accuracy of the model (Model 1), we derived alternative mode shape functions  $\phi_j(x)$  assuming the boom is an Euler-Bernoulli beam with a short tip mass  $m_p$ .

## Results

Two different  $EI$  values were used for each boom length.  $EI = 20 \times 10^6$  lb-in<sup>2</sup> was read from the graph provided by the boom manufacturer, ABLE, Inc. Another value of  $EI$  used was estimated from experimental data. Figure 2 shows the response comparison (analytical model predictions and experimental data) of the 12ft booms for each  $EI$  value.

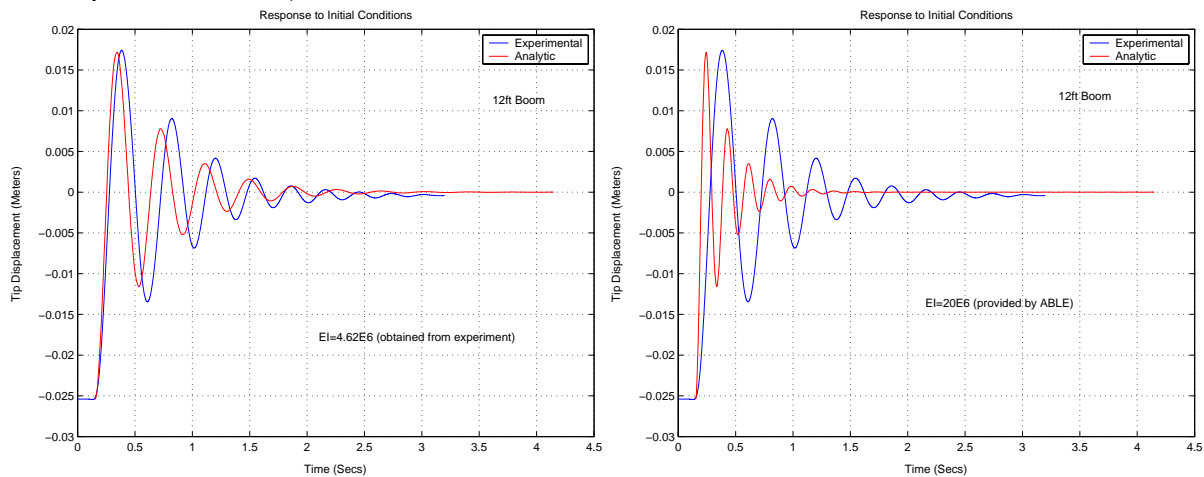


Figure 2. Responses of 12ft boom

Similarly, Figure 3 shows the response comparison (analytical model predictions and experimental data) of the 18ft booms for each  $EI$  value. In both cases, the  $EI$  values estimated from the experimental data yielded an analytical model predicted response that is closer to that of the experimental data. The results are not conclusive and more data at longer beam lengths is needed to reach firm conclusions. Note that all Figures are based on Model 1.

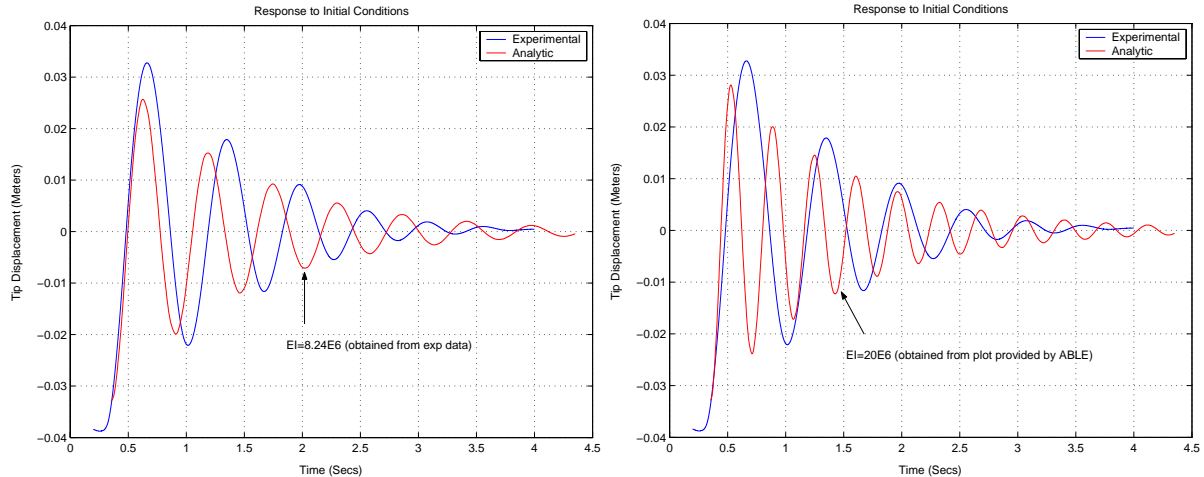


Figure 3. Responses of 18ft boom

### **Control Configuration Using Piezoelectric Transducers**

A theoretical study of active, passive, and energy recycling (hybrid) control configuration has been conducted. Since the structure does not permit excessive added weights due to cabling, mass, and/or an external power source, the energy recycling control configuration may be the “best” if feasible. Laboratory studies are needed to confirm capabilities, limitations and feasibility of this approach.

### **Resources**

The project requires one software tool. Matlab with appropriate toolboxes was the main software tool for verification of models. A laboratory engineer at MSFC provided the experimental data from the boom.

### **Future Works**

More experiments at longer boom lengths have been requested. Once the data is available, the response comparison procedures will be repeated and we expect more conclusive evidence will be found. To evaluate the control strategy, a new test-bed consisting of a long rod with piezoelectric transducers will be constructed. Using that test-bed, the capabilities and limitations of each potential control configuration will be studied. Eventually, the “best” control configuration will be installed on the 30 meter boom for ground testing.

### **Acknowledgements**

The author would like to thank Dr. Mark Whorton of TD54 for providing an opportunity to participate in cutting edge research at NASA, and many hours of valuable discussion and guidance.

2004

NASA FACULTY FELLOWSHIP PROGRAM

MARSHALL SPACE FLIGHT CENTER

THE UNIVERSITY OF ALABAMA  
THE UNIVERSITY OF ALABAMA IN HUNTSVILLE  
ALABAMA A&M UNIVERSITY

**MODELING AND TESTING OF NON-NUCLEAR, HIGH-  
POWER SIMULATED NUCLEAR THERMAL ROCKET  
REACTOR ELEMENTS**

Prepared By:	Daniel R. Kirk
Academic Rank:	Assistant Professor
Institution and Department:	Florida Institute of Technology Mechanical and Aerospace Engineering Department
NASA/MSFC Directorate:	Transportation
MSFC Colleague:	Dr. Charles Schafer

## **Introduction**

When the President offered his new vision for space exploration in January of 2004, he said, “Our third goal is to return to the moon by 2020, as the launching point for missions beyond,” and, “With the experience and knowledge gained on the moon, we will then be ready to take the next steps of space exploration: human missions to Mars and to worlds beyond.” A human mission to Mars implies the need to move large payloads as rapidly as possible, in an efficient and cost-effective manner. Furthermore, with the scientific advancements possible with Project Prometheus and its Jupiter Icy Moons Orbiter (JIMO), (these use electric propulsion), there is a renewed interest in deep space exploration propulsion systems. According to many mission analyses, nuclear thermal propulsion (NTP), with its relatively high thrust and high specific impulse, is a serious candidate for such missions.

Nuclear rockets utilize fission energy to heat a reactor core to very high temperatures. Hydrogen gas flowing through the core then becomes superheated and exits the engine at very high exhaust velocities. The combination of temperature and low molecular weight results in an engine with specific impulses above 900 seconds. This is almost twice the performance of the LOX/LH<sub>2</sub> space shuttle engines, and the impact of this performance would be to reduce the trip time of a manned Mars mission from the 2.5 years, possible with chemical engines, to about 12-14 months, [1, 3, 4, 6, 8, 11, 17, 23].

Nuclear rocket engines are not a new concept, and were designed, built and tested under the Rover/NERVA (Nuclear Engine for Rocket Vehicle Applications) program from 1956-1972, but were never implemented into the space program. An excellent summary of the Rover/NERVA program is given in Reference [8], with many more details about the program contained in References [1, 4, 7, 23, 26]. An example of a nuclear thermal rocket and cross-section of the reactor core developed during the NERVA project are depicted in Figure 1. Many of the reactor and system concepts that are the subject of contemporary interest are similar to those depicted in Figure 1, although new advancements in materials fabrication and geometries have arisen since the NERVA Project, [3, 21, 23, 25]. Unfortunately, despite the nearly \$10 billion (1992 constant dollars) invested, the promises of aerospace nuclear propulsion remained unrealized. The past four decades have witnessed repeated episodes in which nuclear propulsion projects are initiated and development and testing take place, only to be followed by growing doubts about the merit or utility of the proposed applications, and ultimately the project's cancellation. However, with a new, energetic, clearly thought out vision for space exploration, NTP may finally prove itself a “superior capability in the space domain” and “the day is not far off when nuclear rockets will prove feasible for space flight,” [6].

The work presented herein qualitatively and quantitatively defines a non-nuclear test program to characterize the heat transfer processes attendant to a single fuel-element, and a single cooling channel in a nuclear thermal rocket. A model employing the current understanding of heat transfer processes taking place within the reactor core has been developed to facilitate the design of an experimental test bed. The goal of the experiment is to provide NASA MSFC with a capability for assessing and evaluating candidate NTP materials over a range of conditions relevant to nuclear rocket missions.

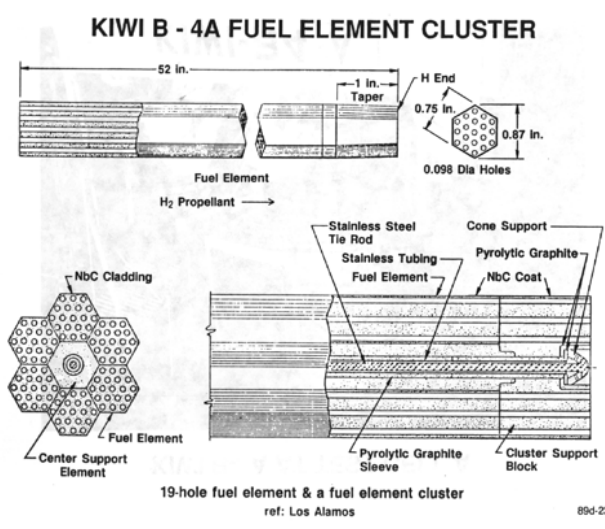
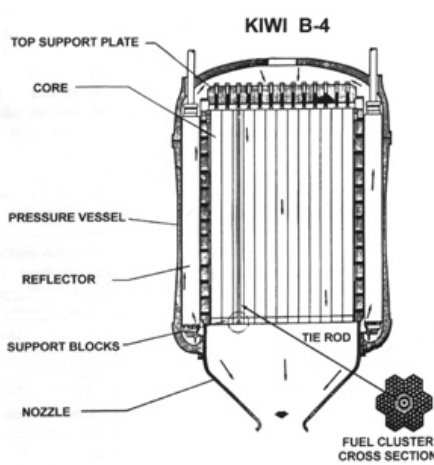
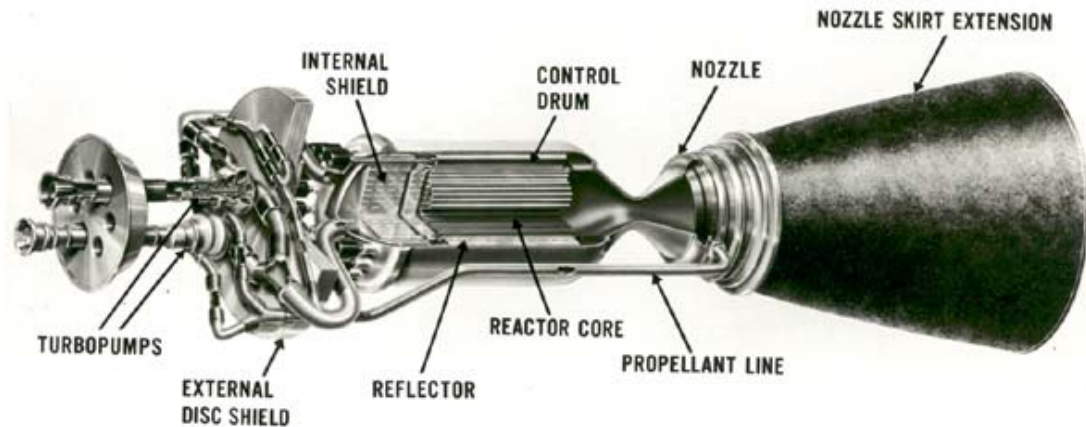


**Figure 1: Typical Rover/NERVA Nuclear Reactor Configuration and Core Cross-Section.**

As indicated in Reference [17], “One of the key questions that has arisen... is [how] to test a nuclear rocket engine in the current societal environment. Unlike the Rover/NERVA programs in the 1960’s, the rocket exhaust can no longer be vented to the open atmosphere.” Additionally, since the nuclear and heat transfer processes taking place within a NTP device are essentially decoupled, there exists compelling motivation to learn as much as possible through a non-nuclear test program. Such non-nuclear experiments would be a safe, cost-effective, and beneficial precursor to nuclear testing.

**Heat Transfer and Fluid Dynamics Modeling Results**

Among the research issues attendant to the development of a nuclear thermal rocket engine is the need to have a detailed understanding of the high temperature, high power heat transfer issues associated with extracting thermal energy from a nuclear power source with hydrogen as the

working fluid. An important first step in gaining this understanding is developing analytical models of simulated nuclear thermal reactor cooling elements to help understand the heat transfer processes taking place. Furthermore, it is critical to accurately model the hydrogen thermal and transport properties at these elevated temperatures and pressures, [18, 19, 20, 22, 24]. An example of results from a model, which simulates the heat transfer mechanisms taking place in a typical cooling channel, is depicted in Figure 2. The upper figure illustrates reactor power distribution as a function of axial location along (solid line) and the integrated power level versus axial position along the reactor (dashed line). The integrated power level is computed from reference data, [1, 3, 8, 11] for a single element, single cooling channel by taking the total reactor power and dividing by the number of cooling holes. This value is then used as an input for actual reactor power distribution based on reactor physics. For the case examined here, a 5 GW reactor was selected, with an equivalent power per cooling channel of about 55 kW.

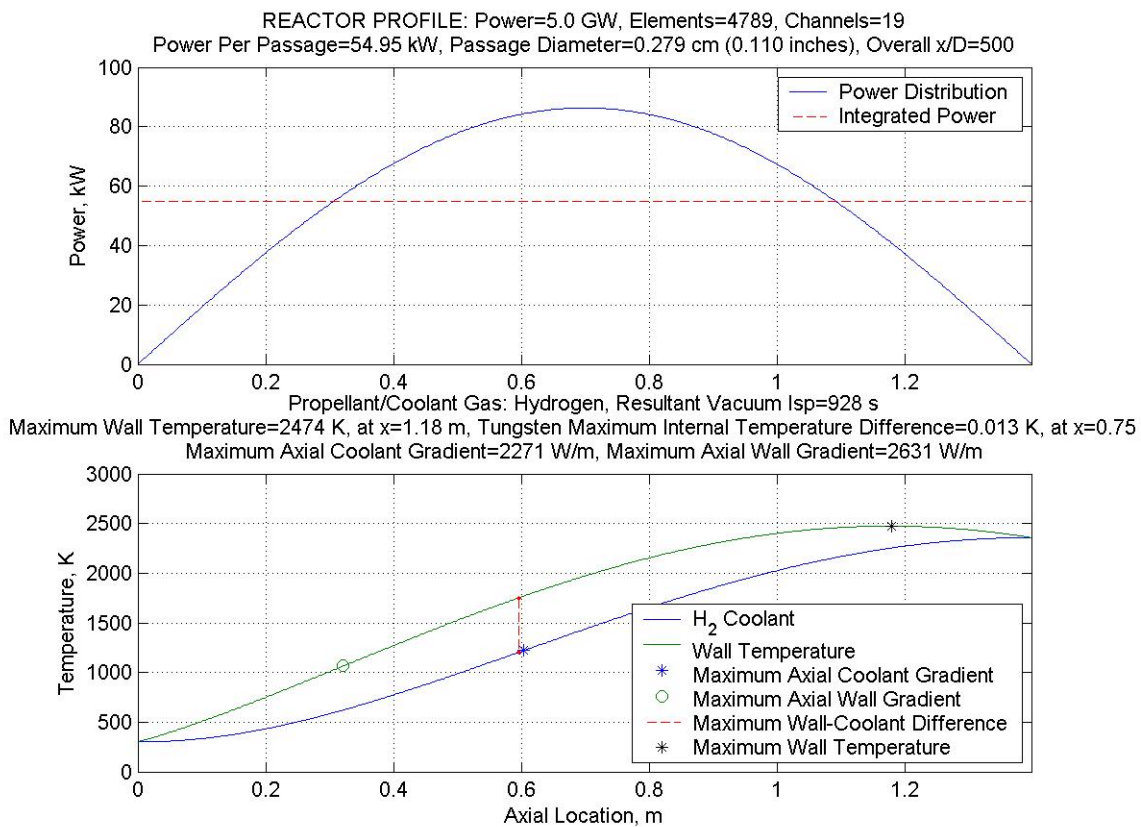


**Figure 2: Example of Heat Transfer Model Results for a Single Cooling Channel of a NERVA-Type NTP Rocket**

The lower plot depicts the H<sub>2</sub> coolant/propellant temperature and the inner wall temperature. The location of the maximum H<sub>2</sub> temperature is at the exit of the channel, whereas the maximum wall temperature is typically located about 80 percent downstream. Also shown are the location and value of the maximum axial gradients in coolant temperature and in wall temperature, and the location of the maximum axial difference between the wall and fluid temperatures. Both of these regions have experienced material failures in prior NERVA experiments, and are important to capture in an experimental simulation.

## **Experimental Design Considerations**

Although the ultimate goal of the experiment is to investigate candidate nuclear materials in hot hydrogen flow, the use of hot hydrogen introduces handling, safety and cost issues that must be carefully addressed. Significant knowledge may be gained through the use of inert, surrogate test gases such as helium, nitrogen and argon. In such experiments, non-dimensional temperatures and heat transfer coefficients may be matched with actual hot hydrogen tests and the behavior of materials and the physical processes taking place at these evaluated conditions may be explored, [9, 18]. Validation of data acquisition, instrumentation and diagnostic capabilities of the facility can be completed prior to the additional complexities associated with hot hydrogen. Furthermore, less costly test articles, made of materials such as steel or tantalum, which do not have to be impervious to hydrogen, may be utilized. A model to provide the appropriate scaling parameters (mass flow, geometry, power settings, pressure, etc.) was developed to guide a test program using substitute fluids.

In order to meet the requirements of an experiment with flowing hot hydrogen, a series of preliminary safety, storage, handling and venting concerns were addressed. Fortunately, preliminary tests will utilize relatively low flow rates of hydrogen (1-2 g/s) and will not require additional complexities such as a dedicated storage facility, post-test hydrogen collection or burn stacks. Readily available, standard bottles will be utilized for preliminary investigations.

The experiment will be located in a 15 x 15 x 10 m dedicated test cell at the Propulsion Research Laboratory. The simulated elements will be housed in a 2 m long and 23 cm diameter cooled vacuum chamber, which contains multiple viewing and instrumentation ports. Due to elongation of the test article at high temperature, bellows fittings to relieve thermal expansion stresses will be located at each end. A 100 kW inductive heating system, which is available at the PRL, will be utilized to generate the intense thermal boundary conditions. Heating coils will be designed to provide a power input profile similar to that shown in the upper diagram of Figure 2 (recall that each cooling channel removes ~ 55 kW from the reactor), [27]. Because of the thermal molecular and transport properties of argon, an entire cooling element (19 cooling holes) may be simulated at these power levels at actual temperatures and heat fluxes. Diagnostics for temperature measurement will include non-intrusive optical pyrometers, which are capable of measuring external and internal surface temperatures along axial locations of the test article.

## **Future Applications for the PRC**

The data obtained from these experiments will be utilized to gain valuable knowledge about the heat transfer processes taking places at elevated temperatures and pressures. The proposed experiment will be the first ever to operate at such extreme thermal conditions and large length-to-diameter ratios ( $L/D \sim 500$ ) with hot hydrogen flow. The data will be compared with known convective heat transfer correlations and appropriate coefficients will be determined. Furthermore, valuable data about materials integrity and suitability as a reactor fuel will be gained. The structural degradation and mass loss impact due to flowing hot hydrogen on

candidate materials will also be assessed. These data will be critical in guiding the design of a next generation nuclear thermal rocket system.

### **Resources**

This project utilized MATLAB for the heat transfer and fluid mechanic analyses, as well as for establishment of a hot hydrogen database. Numerous texts, reports, publications, workshop summaries, etc. were used to establish a technical and historical context of previous NTP technologies and to form the reference comparison cases. Expertise and exchange of ideas from several MSFC directorates (TD 06, TD 40, SD 46, and ED 33) was established to foster collaboration and expedite specification of appropriate diagnostic and instrumentation.

### **Conclusion**

The Propulsion Research Laboratory at NASA Marshall Space Flight Center is uniquely suited to lead in the development of a next generation nuclear thermal rocket engine. To facilitate this process, a non-nuclear, safe, cost-effective experimental program has been developed with the ultimate goal of providing valuable information on heat transfer and material properties in a flowing hot hydrogen environment. When completed, the experiment will be capable of simulating conditions inherent to NTP systems, but never before investigated in a laboratory setting.

### **Acknowledgments**

The author would like to thank Dr. Charles Schafer, Dr. William Emrich, Harold Gerrish, and Dr. Stephen Rodgers, as well as the entire team of engineers and scientists at the Propulsion Research Laboratory. Additionally, the advice and expertise in the areas of materials science and diagnostics from Dr. Binayak Panda and Dr. Jan Rogers is very much appreciated. I look forward to working with each of you in the future to bring this promising experiment to fruition. Finally, sincere gratitude to Dr. Michael Freeman, Dr. Razi Hassan, Dr. Gerald Karr, and Dr. Jeanelle Bland Day for their superior efforts in directing and coordinating the NASA Summer Faculty Fellowship Program.

### **Selected References**

1. Angelo, J.A., and Buden, D., Space Nuclear Power. Orbit Book Company. © 1985.
2. Anghaie, S. Personnel Communication at NASA MSFC on July 20, 2004.
3. Blevins, J.A., Patton, B., Rhys, N.O., Schmidt, G.R., "Limitations of Nuclear Propulsion for Earth to Orbit," AIAA 2001-3515.
4. Bussard, R.W. and DeLauer, R.D., Fundamentals of Nuclear Flight. © 1965, McGraw-Hill, Inc.
5. CHEMKIN Collection III: Thermodynamic Database User Manual.
6. Crouch, H.F., Nuclear Space Propulsion. © 1965, Astronuclear Press.

7. El-Genk, M.S., A Critical Review of Space Nuclear Power and Propulsion. American Institute of Physics. © 1994.
8. Finseth, J.L., "Rover Nuclear Rocket Engine Program: Overview of Rover engine Tests, Final Report," Contract NAS 8-37814.
9. Fowler, J.M. and Warner, C.F., "Measurements of the Heat Transfer Coefficients for Hydrogen Flowing in a Heated Tube." ARS Journal, p.266-267, March 1960.
10. Furman, E. "Thermal Hydraulic Design Analysis of Ternary Carbide Fueled Square-Lattice Honeycomb Nuclear Rocket Engine," in 16th Symposium on Space Nuclear Power and Propulsion, edited by M.S. El-Genk et al., New York, AIP Conference Proceedings, 1999.
11. Given, J.A. and Anghaie, S., "A Computational Model For Thermal Fluid Design Analysis of Nuclear Thermal Rockets," Nuclear Technology, Vol. 117, Jan. 1997, pp. 87-108.
12. Glasstone, S. and Sesonske, A., Nuclear Reactor Engineering. ©, 1967, Litton Educational Publishing, Inc.
13. Hill, P. and Peterson, C., Mechanics and Thermodynamics of Propulsion. 2<sup>nd</sup> Edition, © 1992, Addison-Wesley Publishing Company, Inc.
14. Howe, S.D., "Assessment of the Advantages and Feasibility of a Nuclear Rocket for a Manned Mars Mission," Proceedings from Manned Mars Mission Workshop, Marshall Space Flight Center, Huntsville, Alabama. June 10-14, 1985.
15. Howe, S.D., "High Energy Density Propulsion – Reducing the Risk to Humans in Planetary Exploration."
16. Howe, S.D., "Reducing the Risk to Mars: The Gas Core Nuclear Rocket." Los Alamos National Laboratory.
17. Howe, S.D., Travis, B., and Zerkle, D.K., "SAFE Testing Nuclear Rockets Economically," Los Alamos National Laboratory.
18. Incropera, F.P., and De Witt, D.P., Introduction to Heat Transfer. 2<sup>nd</sup> Edition, © 1990, John Wiley & Sons, Inc.
19. King, C.R., "Compilation of Thermodynamic Properties, Transport Properties, and Theoretical Rocket Performance of Gaseous Hydrogen." NASA TN D-275. April 1960.
20. Kubin, R.F. and Presley, L.L., "Thermodynamic Properties and Mollier Chart for Hydrogen from 300 °K to 20,000 °K." NASA SP-3002. 1964.
21. Lawrence, T.J., Witter, J.K., Humble, R.W., Nuclear Rocket Propulsion Systems. Space Propulsion Analysis and Design, Chapter 8.
22. McCarty, R.D., "Hydrogen Technological Survey – Thermophysical Properties," NASA SP-3089, 1975.
23. Nuclear Thermal Propulsion: A Joint NASA/DOE/DOD Workshop. NASA Conference Publication 10079. 1991.
24. Patch, R.W., "Thermodynamic Properties and Theoretical Rocket Performance of Hydrogen to 100,000 K and  $1.01325 \times 10^8 \text{ N/m}^2$ ." NASA SP-3069. 1971.
25. Powell, J., et al., "MITEE: An Ultra Lightweight Nuclear Engines for New and Unique Planetary Science and Exploration Missions," Plus Ultra Technologies, Inc. Report No. PUR-1, July 24, 1998.
26. Schmidt, H.R. (Chairman), Guidebook for the Application of Space Nuclear Power Systems. Report of the Committee on The Nuclear Space Program. January 1969.
27. Zinn, S., and Semiatin, S. L., "Coil Design and Fabrication: Basic Design and Modifications." Journal of Heat Treating. June 1988, p.32-36.

2004

**NASA FACULTY FELLOWSHIP PROGRAM**

**MARSHALL SPACE FLIGHT CENTER**

**THE UNIVERSITY OF ALABAMA  
THE UNIVERSITY OF ALABAMA IN HUNTSVILLE  
ALABAMA A&M UNIVERSITY**

**In Situ Resource Utilization (ISRU) Experiments for  
Mars Exploration**

Prepared By:	Matt Marone
Academic Rank:	Associate Professor
Institution and Department:	Mercer University Department of Physics
NASA/MSFC Directorate:	Science
MSFC Colleague:	Dr. Palmer Peters

## Introduction

In situ resource utilization can best be described as living off the land. In our case the “land” is the planet Mars. ISRU is based on the idea that some fraction of the consumables, life support and propellant materials do not have to be flown from earth. Rather, they can be manufactured or extracted from resources already present on Mars. The primary resources on Mars are the atmosphere, polar caps and regolith. The atmosphere of Mars is mostly carbon dioxide as shown in the table below. The proportion of oxygen on the other hand is quite small. Still, there is quite a bit of oxygen in the Martian atmosphere, but it is unfortunately tied up with carbon. Thus, one of the goals of ISRU is the separation of breathable oxygen from the carbon dioxide. Several means of separation have been proposed. We have begun experiments on another approach for production of oxygen with carbon monoxide as a useful by product. Our work on a CO<sub>2</sub> separator is described later in this report.

Gas	Proportion (%)
CO <sub>2</sub>	95.3
N <sub>2</sub>	2.7
Ar	1.6
O <sub>2</sub>	0.15
H <sub>2</sub> O	0.03

Table 1: Approximate composition of Mars’ atmosphere at the surface

Regolith melting is another means of obtaining materials. Two materials of interest are iron and silicon. Iron oxide is plentiful on Mars and is of obvious importance for structural components. Silicon is the foundation of solid state devices. Power generation on Mars may be accomplished using silicon solar cells. There is discussion of the feasibility of in situ production of solar cells. This would require a means of extracting silicon from the regolith. We have conducted several experiments concerning melting and glassification of the Mars soil simulant. Other summer faculty fellows have tried various means of processing the stimulant material. These include furnace melting, microwave melting and laser ablation. We have conducted several furnace melting experiments in both air and carbon dioxide environments. We have also carried out experiments to test spark melting in a carbon dioxide atmosphere. These experiments suggest the possibility of using arc melting in a reducing atmosphere. It is important to keep in mind that we are working with a soil stimulant. Any simulant, no matter how chemically similar it is to Martian regolith, may differ in mineralogy. The underlying assumption in this work is that once a glass is formed, any differences between simulant and regolith are unimportant. The exact means of forming the glass do, however, depend on the mineralogy of the regolith. A sample return mission is required to help answer these questions.

## Experiments

Melting experiments were carried out using JSC MARS-1 simulant. This material has been well characterized [1]. JSC MARS-1 is widely accepted among the scientific community. The simulant is derived from the weathered volcanic ash of the Pu'u Nene cinder cone on the Island of Hawaii. The composition of the simulant is known to be richer in  $\text{Al}_2\text{O}_3$ ,  $\text{TiO}_2$  and water compared to the compositions determined by the Viking landers and the Mars Pathfinder.

In order to conduct melting experiments the simulant was first vacuum dried and then milled. Simulant was vacuum dried at  $120^\circ\text{C}$  for several days and then milled. Small particle size and proper mixing help to form a uniform glass and influence melting point of the material. JSC Mars-1 simulant is very coarse grained and one can clearly see different colored grains. A device for milling the simulant was constructed. An agate vial ( Spex #8014) with two agate balls is used. The vial is agitated using a modified paint shaker (Tornado II 51000). The vial is held in place by two wooden end caps that were machined to fit into the shaker frame. The wooden end caps are held together with "missile tape". Tape on the wooden end caps keeps the ends of the vial under compression prevents material from being lost while handling. The loaded paint shaker/mill is shown below.

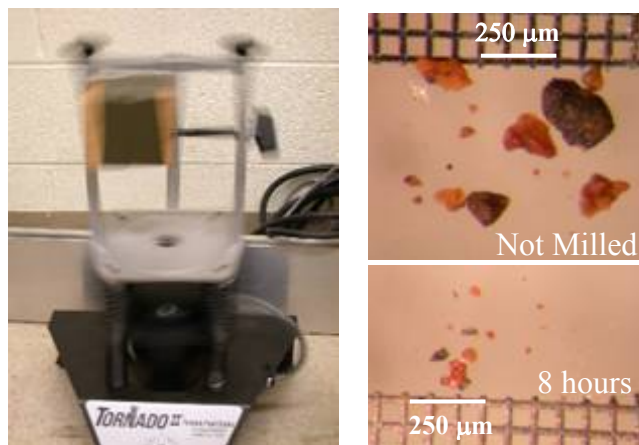


Figure 1: Milling apparatus

Eight hours of dry milling produces a very fine powder as show in figure 1. The particles shown in these photographs were dispersed by mixing simulant with methanol and spraying the mixture onto glass slides. The maximum particle size was limited by the orifice. Particles in the  $500\mu\text{m}$ - $1000\mu\text{m}$  range can be found in the simulant, but they do not pass through the atomizer.

Vacuum dried and milled powders were pressed into pellets using a hydraulic press. The pellets were 1inch in diameter and had a typical thickness of about 1/8 inch. A pressure of 10Kpsi was applied to the pellet. Smaller disks and fragments were prepared by

drilling the pellets with a stainless steel core drill. All melting experiments were carried out in HBC high grade boron nitride crucibles that were machined in our furnace shop. Melted simulant has been found to stick to alumina and so boron nitride was used. Table 2 shows a summary of all melted samples produced. In each run the temperature was ramped up at a rate of 10°C/min and then held at a constant dwell temperature for 60 minutes. The temperature was ramped down at 5°C/min to a level of 500°C. Below 500°C, the sample was allowed to furnace cool by reducing the setpoint below room temperature. Samples processed in CO<sub>2</sub> had a pressure of 5-7mbar at the dwell temperature and about 1.3mbar at room temperature. This is comparable to the atmospheric pressure on Mars. Carbon percentages are by weight of initial simulant not total weight. The carbon source is an arc lamp rod made of spectroscopic grade carbon (Ultra Carbon type C7314) that was shaved with a knife blade.

### Samples Melted in Air

A Sample melted in air at 1200°C is shown below in figure 2. Figure 2a shows the surface which is full of bubbles. This surface is a thin crust with a large cavity below. The sample in figure 2b shows a translucent glass like material that was formed inside a cavity beneath the surface of the melted sample. There are obvious inclusions in this material. We interpret this result as an indication that some of the material in the simulant did not melt. The unmelted material may have been surrounded by other phases that did melt. Electron microprobe analysis shows the presence of some FeTi oxides.



Figure 2: 1200°C Air (a) Surface, (b) Glass in cavity

Since there appeared to be some unmelted phases, we increased the processing temperature to 1300°C. We also added a cap to some of the crucibles to see if it would prevent loss of volatile materials. All of the samples processed at 1300°C were vesicular as shown in figure 3. The addition of carbon to the simulant did not reduce iron to the metallic state. Unlike samples that were laser melted or microwave melted, there does not seem to be any plagioclase or other silicates.



Figure 3: Typical sample is vesicular

### Samples Melted in CO<sub>2</sub>

Processing samples in air will not be very likely on Mars. Since the atmosphere on Mars is approximately 95% CO<sub>2</sub>, we decided to process our samples in a furnace filled with CO<sub>2</sub>. The Engineering Directorate (ED12) allowed us to use a high temperature tube furnace they have in building 4475. A vacuum system is connected to the furnace which is shown below in figure 4.



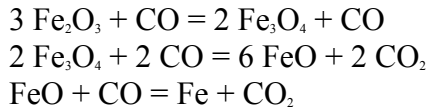
Figure 4: High temperature furnace and vacuum system

Prior to heating the sample, the furnace was pumped out with a roughing pump and then back filled with CO<sub>2</sub>. In order to remove as much air as possible, the furnace was pumped and back filled several times. Room temperature pressure was adjusted to about 1.3mbar. At 1300°C the pressure would then be in the 5-7mbar range, typical of the Martian atmosphere. Unfortunately, the furnace malfunctioned on our first run. The temperature shown on the controller fluctuated. An auxiliary thermocouple indicated that the temperature was 1310°C. The temperature controller actually showed a decrease in temperature with full heater power applied. The furnace was shut down and allowed to cool. We doubt that the sample went much higher than 1310°C but we do not know how long it was at the maximum temperature. The cooling rate is also unknown but it appeared to be much faster than the programmed value (5°C/min.). When the furnace was turned off, the auxiliary thermocouple showed a drop of several degrees in a second. This faster cooling rate and possibly shorter time at the maximum temperature may account for the differences observed in the two sets of samples melted in CO<sub>2</sub>.

Some of the samples melted in CO<sub>2</sub> contained magnetically separated simulant and were pressed into a rod rather than a disk shape. Since one of the desired results is the production of iron from regolith, we decided to use a permanent magnet to do some post processing. Magnetic separation was accomplished by placing a rare earth magnet on top of a Petri dish containing milled simulant. Shaking the dish caused some of the magnetic

material to be attracted to the magnet. The magnet produced a field of about 2.5kG. Sliding the magnet across the top of the dish helped to remove nonmagnetic dust that simply adhered to the magnetic material. This technique separated out about 5-6% of the mass of the original simulant. The magnetically depleted simulant showed only a few weakly magnetic grains remaining. This magnetically separated material was mixed with a small amount of methanol and pressed into a rod. Pressing was accomplished by pouring the material into a glass tube and tamping with a tight fitting solid rod.

The JSC MARS-1 simulant is known to contain Ti-magnetite [1] and our microprobe results show FeTi oxides, possibly ilmenite ( $\text{FeTiO}_3$ ). JSC-Mars-1 simulant is derived from volcanic ash. Varying ratios of Ti-magnetite and ilmenite are found in volcanic ash. Ti-magnetite is a solid solution that lies between magnetite ( $\text{Fe}^{2+}\text{Fe}^{3+}_2\text{O}_4$ ) and Ulvospinel  $\text{Fe}^{2+}_2\text{TiO}_4$ . Hemiteite ( $\text{Fe}_2\text{O}_3$ ) can easily be reduced to metallic iron (Fe) by carbon monoxide (CO). Several reduction reactions are shown below.



Many of our samples were prepared with carbon. We thought that the carbon might help to reduce the iron oxide. In fact, many of the ISRU papers published state that the iron in Martian regolith can easily be extracted by this simple process. However, if the iron is in a more complex oxide the simple CO reduction process might not work.

Two of the samples melted in  $\text{CO}_2$  were reagent grade iron oxides. Red  $\text{Fe}_2\text{O}_3$  and black  $\text{Fe}_3\text{O}_4$  were pressed into rod shapes and heated in  $\text{CO}_2$ . The heating and cooling rates were the same as those used for melting all our other samples. The red  $\text{Fe}_2\text{O}_3$  is not magnetic and the black  $\text{Fe}_3\text{O}_4$  is very strongly magnetic. After melting, neither oxide retained its original color. Both samples became gray and the  $\text{Fe}_2\text{O}_3$  became magnetic. Both Oxides are so strongly magnetic that they can support the weight of the crucible. This experiment seems to indicate that processing in  $\text{CO}_2$  caused the iron oxide reagent to experience a change in its oxidation state.

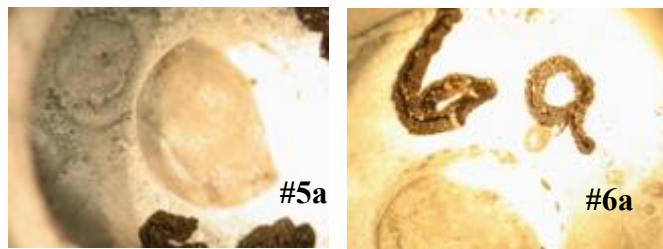


Figure 5: Iron oxides processed in  $\text{CO}_2$  (#5a)  $\text{Fe}_3\text{O}_4$ , (#6a)  $\text{Fe}_2\text{O}_3$

As mentioned previously, there was a furnace malfunction during the first  $\text{CO}_2$  run. We know, from our measurements with the auxiliary thermocouple, that the cooling rate was much faster than the programmed rate. What is not known is the maximum temperature the samples reached or how long they were at this temperature. The samples have not yet undergone microprobe analysis. We can only compare the physical characteristics of the

two batches of samples processed in CO<sub>2</sub>. There are however some very striking difference which are outlined below. Samples identified with only a number are in the first run in which the malfunction occurred. Samples with a number and then a letter (i.e. #1a) indicate that the sample was prepared in the second CO<sub>2</sub> run. Samples in the second run underwent the same heating and cooling rates as those samples processed in air. Table 2 shows a summary of all samples processed in either CO<sub>2</sub> or air.

Figure 6 shows an example of the dramatically different results obtained in these experiments. Both samples are made from magnetically separated simulant. Sample #1 was produced when the furnace malfunctioned and sample #1a was produced with the programmed heating and cooling rates. The magnetic properties of these two samples is as difference as their appearance. Sample #1 is magnetic while sample #1a is not magnetic. Perhaps the faster cooling rate enabled sample #1 to form a glass like ball. No gas bubble can be seen in this sample unlike the structure of sample #1a. Sample #1 may have reached a high enough temperature to thoroughly out gas and then quickly cool to form the glass.

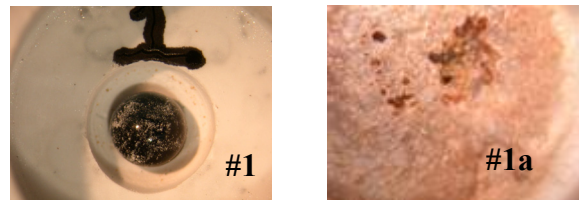


Figure 6: Magnetically separated simulant (#1) magnetic ball of glass, (#1a) not magnetic

Figure 7 shows what happened when carbon was added to the simulant. Again the sample that was formed when the furnace malfunctioned has a glassy appearance to it and the sample for which the material that was cooled slowly has a crust. Both #1a and #2a are similar in appearance and have reduced magnetic properties when compared to samples #1 and #1a. The black glassy part of sample #2 is more strongly magnetic than the glass produced in sample #1.



Figure 7: Magnetically separated simulant with 10%C added (#2) magnetic glass, (#2a) few chips slightly magnetic

Figure 8 show the results for two disks of simulant that has not been magnetically separated. Both samples are similar in appearance. Their surface is full of bubbles. The interior is composed of a vesicular material that has black and dark honey colored regions. Both of these samples contain chips of material that are slightly magnetic. Since these are not made from magnetically separated material they contain all the components of the simulant. This in turn means that there is more material to out gas and contribute to the formation of bubbles and voids.

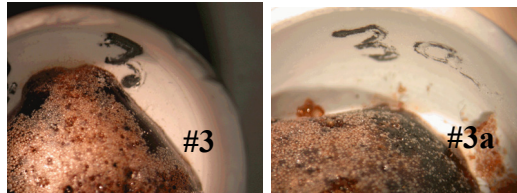


Figure 8: Simulant disks without carbon (#3) and (#3a) contain some magnetic chips

The samples shown in figure 9 are both made from simulant with 10% carbon added. Compared to samples #3 and #3a, both of these samples show enhanced magnetic properties. Again, they have a crusty surface and show considerable bubbles. Sample #4 contains a strongly magnetic chunk that appears to contain some black glassy areas. Sample #4a is magnetic, but not as strong as #4. The magnetic chunk in sample #4 will stick to a magnet and support its own weight.



Figure 9: Simulant disks with 10% carbon added (#4) has a strongly magnetic chunk, (#4a) not as strongly magnetic

These results do seem to show a pattern. In terms of their magnetic properties, samples that contain carbon (#2, 2a, 4, 4a) do seem to be more strongly magnetic than those that do not contain carbon. The samples that were heated in the furnace that malfunctioned (#2, 4) are more glass like and have stronger magnetic properties compared to those that were cooled slowly.

### Oxygen Separation

The Martian atmosphere contains quite a bit of oxygen that is, unfortunately, tied up with carbon. As part of our ISRU we have considered the problem of oxygen separation. Oxygen is important for both life support and propellant. Solid Oxide electrolysis has been suggested by Sridhar as a method for oxygen production [2]. This technique relies on oxygen ion conduction in yttria-stabilized zirconia (YSZ). The YSC cell is a ceramic

material. Oxygen separation is accomplished by ionic conduction that occurs in the 750°C-900°C range. It is well known that silver oxide dissociates and produces atomic oxygen at about 285°C. Thin silver foils have been used in the production of atomic oxygen from molecular oxygen. Collisions between atoms of oxygen can then cause the atomic oxygen to be converted back to molecular oxygen. In order to produce oxygen from the Martian atmosphere, one needs to dissociate the carbon dioxide into carbon monoxide and free oxygen. The free oxygen can then be separated from the carbon monoxide by allowing it to diffuse through a thin silver film. Something similar has been tried by Vuskovic *et al.* [3], in which an RF discharge was used to dissociate the CO<sub>2</sub>. However, the RF technique needs a low pressure to establish the discharge. An RF power source is also required. We envision a device, which would use a UV lamp or a spark source to dissociate the CO<sub>2</sub>. UV light of wavelength  $\lambda < 170\text{nm}$  has sufficient energy to break the carbon-oxygen bond. This would produce carbon monoxide and oxygen. The carbon monoxide exhaust would be used for the reduction of iron from the Martian regolith. Oxygen would diffuse through the silver film and can be used for life support and propellant. We have begun building a prototype of this apparatus as shown in figure 10. In our device, the silver film is heated by an electric heater. Since the temperature is rather low, we may be able to use a solar furnace to replace or supplement the electric heating element.



Figure 10: Prototype of O<sub>2</sub> production device

### Spark Melting

Our final ISRU experiments were based on the idea of arc or spark melting. Furnace melting experiments showed that we were able to convert non-magnetic iron oxide (Fe<sub>2</sub>O<sub>3</sub>) into a magnetic state. Instead of using a furnace to melt regolith, one might be able to use an arc melter. Arc melting provides a high temperature with very rapid heating and cooling. Our spark melting experiments were conducted in a CO<sub>2</sub> atmosphere. The energy of the spark, no doubt produced some CO, providing a reducing atmosphere. These experiments were conducted in a resealable zipper bag that was purged with CO<sub>2</sub>. A carbon arc lamp rod was mounted inside the bag and held in place with a Cajon type fitting. The high voltage source was a Tesla coil that was attached to the fitting. Iron oxide was mixed with methanol to produce thick slurry. This slurry was then coated onto a carbon disk. A sheet of copper was connected to a water pipe with a heavy gauge wire. The copper sheet provided a ground plane in the bag. Between the carbon disk and the ground plane, we placed a rare earth magnet. Sparks from the carbon

electrode produced holes in the iron oxide coating. When observed with a microscope, these holes show melted edges and glassy reflections. Adjacent to many of the holes are small bits of magnetic material. Sparking is a very violent process and material can be ejected from the surface. The magnet placed under the disk helped to retain any magnetic grains that were produced. Sparks striking the disk and the resulting surface features are shown in figure 12. Observation of the surface after sparking revealed magnetic grains standing up from the surface. If a magnet is passed over the surface, these small magnetic grains can be seen moving in response to the magnetic field. No such movement can be observed before spark melting. .

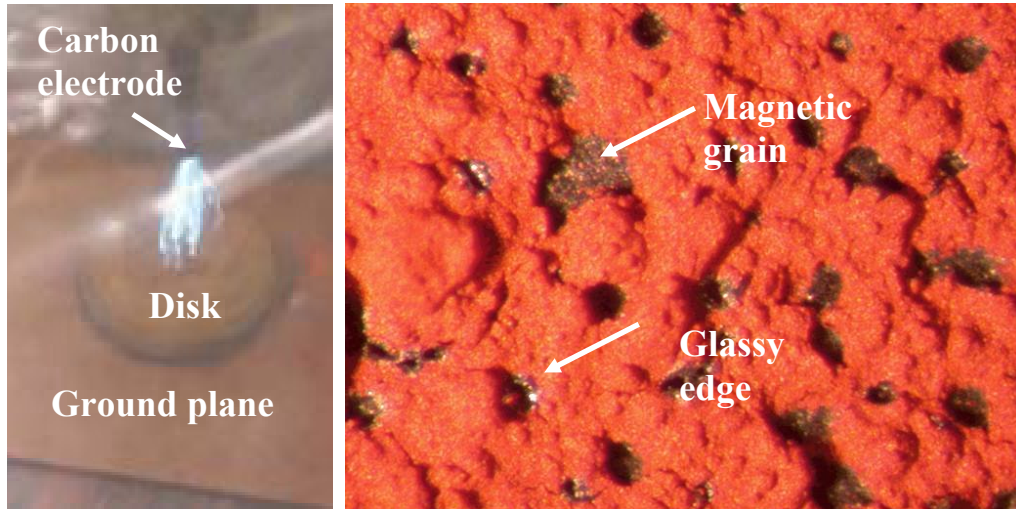


Figure 12: Spark melting  $\text{Fe}_2\text{O}_3$

From these observations, we can conclude that the process is reducing some of the iron in the oxide. We have not yet conducted this experiment with simulant. We plan to try spark melting raw simulant as well as magnetically separated and magnetically depleted simulant. These experiments suggest the possibility of processing regolith in an arc melter equipped with a magnet trap to catch the reduced iron.

DwellTemp. (°C)	Crucible ID	Crucible Type	Atm.	Comp.	Comments
1200	M4, 1	BN No cap	Air	M4 sim.	Simulant disk, 8hr grind, 0%C
1300	M4,2 NC NCP	BN No Cap	Air	M4 sim	Simulant disk, 8 hr grind, 0%C
1300	M4,2 WC Cap	BN Cap	Air	M4 sim	Simulant disk, 8 hr grind, 30%C
1300	M4,2 NC Cap	BN Cap	Air	M4 sim	Simulant disk, 8 hr grind, 0%C
1300 (?)	1	BN No cap	CO <sub>2</sub>	M4 Mag Sep.	Furnace Malfunction max temp near 1300°C uncertain time. Furnace cool. Magnetically separated from M4 powder, 8hr grind. Pressed rod
1300 (?)	2	BN No cap	CO <sub>2</sub>	M4 Mag sep +10%C	Furnace Malfunction max temp near 1300°C uncertain time. Furnace cool. Magnetically separated from M4 powder, 8hr grind +10%C. pressed rod
1300 (?)	3	BN No cap	CO <sub>2</sub>	M4 sim	Furnace Malfunction max temp near 1300°C uncertain time. Furnace cool. Simulant disk, 8 hr grind
1300 (?)	4	BN No cap	CO <sub>2</sub>	M4 sim. +10%C	Furnace Malfunction max temp near 1300°C uncertain time. Furnace cool. Simulant disk, 8 hr grind +10% C
1300	1a	BN No cap	CO <sub>2</sub>	M5 Mag Sep.	Magnetically separated from M5 powder, 8hr grind. Pressed rod
1300	2a	BN No cap	CO <sub>2</sub>	M5 Mag Sep.	Magnetically separated from M5 powder, 8hr grind + 10% C. Pressed rod
1300	3a	BN No cap	CO <sub>2</sub>	M4 sim.	Simulant disk, 8 hr grind
1300	4a	BN No cap	CO <sub>2</sub>	M4 sim. +10%C	Simulant disk, 8 hr grind +10% C
1300	5a	BN No cap	CO <sub>2</sub>	Fe <sub>3</sub> O <sub>4</sub> Black	Pressed rod, strongly magnetic
1300	6a	BN No cap	CO <sub>2</sub>	Fe <sub>2</sub> O <sub>3</sub> Red	Pressed rod, not magnetic

Table 2: Summary of Samples Produced

## **Future Research**

Our work has raised a number of questions that need to be answered. JSC MARS-1 simulant is chemically different than the composition suggested by Viking and Path Finder data. Reformulation of this material seems to be necessary. However, the most recent Mars Exploration Rover (MER) data has not yet been released. Once this data becomes available the simulant should be reformulated. Sample return missions are about a decade in the future. Only then will we have the ability to know the mineralogy of Martian regolith. The question of reducing iron from TiFe oxides should be dealt with in the near term. It seems reasonable to think that Martian volcanism should mirror that on Earth. If not TiFe oxide, then perhaps some other complex oxides exist in the regolith. Terrestrial soil undergoes weathering which appears to be largely absent on Mars.

Experiments conducted in CO<sub>2</sub> yielded very different results. We would like to experiment with cooling rates, processing time and temperature. Whatever occurred when the furnace malfunctioned produced dramatically different results and this needs to be investigated further. Electron microprobe analysis needs to be conducted so that we can understand the chemistry of the materials produced. Melting experiments need to be conducted under different atmospheric conditions. Melting in a CO atmosphere would be the next step.

There are two experiments that can be continued at Mercer University. Our oxygen separation experiments require much less expensive equipment. There are many questions to be answered about the design of our prototype device. Film thickness, substrates, operating temperature and yield all need to be explored and optimized. We also need to experiment with different dissociation mechanisms and determine which approach will make the most efficient use of electrical power. These experiments will provide excellent student research projects. Experiments with spark/arc melting also need to be continued. Again, students can conduct these experiments.

## **Conclusions**

Transformation of iron oxides indicates reduction but, comparable results were not achieved with simulant. This suggests that more complex TiFe oxides will be difficult to reduce or will require a different method. It is difficult to draw any conclusions from our spark melting experiments. They do suggest that arc melting in a magnetic field could be an alternative to furnace melting. This is certainly worth exploring.

## **Acknowledgements**

I would like to thank my NASA colleagues Dr. Palmer Peters and Dr. Don Gillies for their guidance and for the valuable resources they provided. Dr. Ahad Nasab, a faculty fellow from MTSU has been a valuable co-worker and helped me to clarify ideas. Paul Carpenter has provided microprobe analysis. Curtis Bahr and Jeff Quick were kind enough to allow me access to the furnace shop. They provide useful equipment and advice. Thanks to Sheryl Gallop for expert sample preparation. Martin Johnson from the

Engineering Directorate (ED12) provided access to the equipment that made our CO<sub>2</sub> furnace melting experiments possible.

### **References**

[1] C. C. Allen et al., *Martian Regolith Simulant JSC Mars-1*, Proceedings of Lunar and Planetary Science 29<sup>th</sup> Meeting, 1998.

[2] L. Vuskovic et al., *Oxygen Production and Separation for Martian Atmosphere by the Radio Frequency Discharge*, Proceedings of Lunar and Planetary Science ISRU II 28<sup>th</sup> Meeting 1997.

[3] Sridhar, K. R., Finn, J. E., and Kliss, M. H., *In-Situ Resource Utilization Technologies For Mars Life Support Systems*, Adv. Space Res., Vol. 25, No.2, pp. 249-255, 2000

**2004**

**NASA FACULTY FELLOWSHIP PROGRAM**

**MARSHALL SPACE FLIGHT CENTER**

**THE UNIVERSITY OF ALABAMA  
THE UNIVERSITY OF ALABAMA IN HUNTSVILLE  
ALABAMA A&M UNIVERSITY**

**CONVERGENCE ACCELERATION AND  
DOCUMENTATION OF CFD CODES FOR  
TURBOMACHINERY APPLICATIONS**

Prepared By:	Jed E. Marquart, Ph.D., P.E.
Academic Rank:	Professor
Institution and Department:	Ohio Northern University Mechanical Engineering Department
NASA/MSFC Directorate:	Space Transportation
MSFC Colleague:	Dr. Daniel Dorney

## **Introduction**

The development and analysis of turbomachinery components for industrial and aerospace applications has been greatly enhanced in recent years through the advent of computational fluid dynamics (CFD) codes and techniques. Although the use of this technology has greatly reduced the time required to perform analysis and design, there still remains much room for improvement in the process. In particular, there is a steep learning curve associated with most turbomachinery CFD codes, and the computation times need to be reduced in order to facilitate their integration into standard work processes.

Two turbomachinery codes have recently been developed by Dr. Daniel Dorney (MSFC) and Dr. Douglas Sondak (Boston University) [1]. These codes are entitled Aardvark (for 2-D and quasi 3-D simulations) and Phantom (for 3-D simulations). The codes utilize the General Equation Set (GES), structured grid methodology, and overset O- and H-grids. The codes have been used with success by Drs. Dorney and Sondak, as well as others within the turbomachinery community, to analyze engine components and other geometries.

One of the primary objectives of this study was to establish a set of parametric input values which will enhance convergence rates for steady state simulations, as well as reduce the runtime required for unsteady cases. The goal is to reduce the turnaround time for CFD simulations, thus permitting more design parametrics to be run within a given time period. In addition, other code enhancements to reduce runtimes were investigated and implemented.

The other primary goal of the study was to develop enhanced users manuals for Aardvark and Phantom. These manuals are intended to answer most questions for new users, as well as provide valuable detailed information for the experienced user. The existence of detailed user's manuals will enable new users to become proficient with the codes, as well as reducing the dependency of new users on the code authors. In order to achieve the objectives listed, the following tasks were accomplished:

- Parametric Study Of Preconditioning Parameters And Other Code Inputs
- Code Modifications To Reduce Runtimes
- Investigation Of Compiler Options To Reduce Code Runtime
- Development/Enhancement of Users Manuals for Aardvark and Phantom

## **Parametric Study Of Preconditioning Parameters And Other Code Inputs**

The Aardvark and Phantom codes both incorporate a form of 'preconditioning' to enhance the convergence of steady state solutions, as well as to speed the analysis of unsteady solutions, for low speed and incompressible flow problems [2]. This methodology, although very useful and effective, is not an 'exact science', in that no one set of parameter values will result in the lowest required CPU time for all flow cases. Therefore, it is essential that various preconditioning parameter values be examined to determine their effect on the solution time for certain typical flow/geometry cases. In addition, the values and effects of some parameters that are not directly associated with preconditioning were examined. In particular, the following parameters were examined:

- `ivp_parm` – used for selection of velocity for the preconditioning velocity term

- `lpmax` – number of Newton iterations to be run at each timestep
- `upw` – order of accuracy of inviscid fluxes
- `ifreeze_prop` – whether or not thermodynamic property values should be ‘frozen’ at inlet conditions

The values of these parameters were examined in terms of their effects on convergence time required and also accuracy of the solution. An example of one of the sample cases, illustrating pressure contours, is shown in Figure 1.

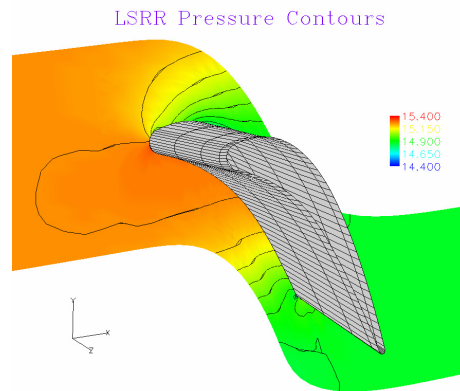


Figure 1: Pressure Contours for Sample Case

From the study, it was determined that the value of the preconditioning velocity parameter (`ivp_parm`) had very little effect on the number of iterations required for convergence. In a similar fashion, the number of inner iterations had negligible effect on the convergence rate, but fewer outer iterations could be run if more inner iterations were used. The order of the inviscid fluxes had very little effect, other than the fact that higher order should be used if vortex shedding studies are performed. Freezing the values of thermodynamic properties, however, did have a positive (reduction) effect on the runtime required, with negligible effect on the results for essentially isothermal cases.

### **Code Modifications to Reduce Runtimes**

Since the overall goal of this effort was to reduce the runtimes required for flow solutions, it was also obvious that the codes should be examined to determine if there might be some methods to speed the solutions by recoding or ‘streamlining’ portions of the codes. It was determined that this was indeed possible. The following changes were made to the codes:

- matrix multiplications were ‘unrolled’, and calls to matrix multiplication routines eliminated
- the ability to ‘turn off’ the energy equation for isothermal cases was created
- 2<sup>nd</sup> order NIST thermodynamic property value determination was installed
- superfluous calls to thermodynamic property value routines were eliminated

Through the restructuring of the codes as listed above, improvements in runtime speeds of 6% to 21% over the baseline code were achieved for Aardvark, and 13% to over 50% for Phantom. The precise amount of improvement depended upon the configuration being run, as well as the

platform on which it was run. For both codes, the decrease in required runtime was dramatic, and a welcome occurrence.

### **Investigation Of Compiler Options To Reduce Code Runtime**

In addition to code restructuring and streamlining, another method used to increase the speed of the codes was to investigate the effects of various compiler options when creating the executable code. Each platform has its own set of compiler options available, with a corresponding anticipated increase in code speed, and thus reduced required runtimes.

Specifically, the platforms on which the compiler options were evaluated included SGI and Sun workstations, with both 2-D and 3-D test cases. It was interesting, and pleasing, to find that, simply by altering the compilation options, a speed increase of over 2% to over 8% was achieved. It was determined that the “-ipa -Ofast” (or its equivalent) compiler option produced the best results in most cases.

### **Development/Enhancement of Users Manuals for Aardvark and Phantom**

Prior to this effort, basic manuals did exist for both the Aardvark and Phantom codes. These documents consisted primarily of copies of variable descriptions, variable default values, some input/output descriptions, and a basic procedure for running the codes. The variable information was taken directly from the codes.

Although providing a start for the user, the documents left something to be desired as far as getting new users up and running quickly and with few or no questions. In particular, there were no sections addressing grid generation and post-processing within the document, although basic documentation did exist separately for these codes. Since the codes which accomplish grid generation and post-processing are not commonly used in industry, the need for their documentation to be incorporated into the Aardvark and Phantom users manuals became apparent. By including documentation for all packages necessary to create a grid, obtain a flow solution, and post-process the solution within one manual, the package becomes ‘complete’. Users have one source of information necessary for the entire package, and the need to contact the code developers for questions is reduced.

In order to make the Aardvark and Phantom users manuals complete and self-sufficient, the following sections were added and/or enhanced:

- Licensing information
- Files required by the codes – including file types and descriptions/uses
- Grid generation – including input/output variables descriptions, hints for use, and a sample case
- Input parameter sets – including full variables descriptions, types, default values, etc.
- Parameter definitions – definition of basic code parameters
- Output description – including output file variables descriptions
- Post-processing – including output variables descriptions and basic use of the post-processing code

Upon completion of the first revision of the manuals, they were distributed to existing users for comments. Response was favorable, and returned comments were incorporated to develop more refined manuals. The manuals will continue to evolve and be updated as the codes change or as it becomes apparent that additional information would be beneficial to the users.

### **Future Applications**

Code development/enhancement is, of course, an ongoing task. Methodology and coding improvements to increase the speed and accuracy of the CFD codes are anticipated. With the improvements made as a part of this study, the turbomachinery community can make tremendous use of these CFD codes in their present form for analysis purposes. As new methods and coding structures emerge, the time required to perform accurate and timely analyses will continue to be reduced, thus providing the community with even more cost effective and useful tools to develop the turbomachinery of the future. This effort has provided a step in the direction of this future work. In the future, CFD analysis will continue to grow in popularity as an analysis tool for not only turbomachinery applications, but all sorts of fluid mechanics applications. It will provide an extremely cost- and time-effective mechanism for analysis, thus reducing the investment in both time and dollars to achieve a successful and efficient design.

### **Conclusions**

The CFD turbomachinery codes, Aardvark and Phantom, have been enhanced to decrease the time required for steady state or time-dependent flow solutions. This was accomplished by determining the values of input parameters which reduced the number of iterations required to achieve steady state, as well as lowering the CPU time per iteration. In addition, the users manuals were enhanced to provide additional information, thus making it possible for new users to get up to speed with the codes quickly, as well as providing current users with information not previously included.

### **Acknowledgements**

The author would like to express his appreciation to the members of the Space Transportation Directorate, Fluid Dynamics Analysis Group (TD-64) for the opportunity to participate in this program. In particular, special thanks are in order to Dan Dorney, Lisa Griffin, and Robert Garcia. Their assistance made this effort a fantastic experience for the author, as well as a successful venture for NASA and the turbomachinery community.

### **References**

- [1] Sondak, D. L., and Dorney, D. J., "General Equation Set Solver for Compressible and Incompressible Turbomachinery Flows", AIAA Paper 2003-4420, 39<sup>th</sup> AIAA/ASME/SAE/ASEE Joint Propulsion Conference and Exhibit, July 20-23, 2003, Huntsville, AL
- [2] Venkateswaran, S., and Merkle, C.L., "Analysis of Preconditioning Methods for the Euler and Navier-Stokes Equations", Von Karman Institute Lecture Series, March 8-12, 1999.

**2004  
NASA FACULTY FELLOWSHIP PROGRAM**

**MARSHALL SPACE FLIGHT CENTER  
THE UNIVERSITY OF ALABAMA  
THE UNIVERSITY OF ALABAMA IN HUNTSVILLE  
ALABAMA A&M UNIVERSITY**

**THE PLUNGE PHASE OF FRICTION STIR  
WELDING**

Prepared by:	John C. McClure
Academic Rank:	Professor
Institution and Department:	University of Texas El Paso, Metallurgical and Materials Engineering Department
NASA/MSFC Directorate:	Engineering
MSFC Colleague:	Dr. Arthur Nunes

## **Introduction**

The many advantages of Friction Stir Welding<sup>1</sup> have led to a relatively rapid acceptance in the often conservative welding community<sup>2, 3</sup>. Because the process is so different from traditional fusion welding, with which most investigators are most familiar, there remain many aspects of FSW for which there is no clear consensus.

For example, the well known onion rings<sup>4</sup> seen in transverse sections have been variously interpreted as grain size variations<sup>5</sup>, variation in density of second phase particles<sup>6</sup> and parts of the “carousel” of material rotating with the pin that have been shed from the carousel<sup>7</sup>. Using Orientation Imaging Microscopy, Schneider<sup>8</sup> has recently noted that the onion rings have a different orientation (and hence etch differently) than the surrounding material, and this orientation is consistent with slip plane orientations at the edge of the carousel.

Likewise, the forces and torque exerted by the FSW tool on the work piece largely remain unaccounted for. Although these forces are routinely measured by investigators with commercial instrumented welders, they are rarely reported<sup>9</sup> or even qualitatively analyzed.<sup>10</sup>

This paper will introduce a model based on a “carousel” or disk of material that rotates with the tool to estimate the torque and plunge force required to plunge a tool into the work piece. A stationary tool is modeled rather than the moving tool because effects such as thermal transients and metallurgical changes in the sample (primarily aging in aluminum) can be more easily accounted for. It is believed, however, that with some modifications the model should be applicable to a moving tool also.

## **Experimental Procedure**

Plunging penetrations were made on the horizontal weld tool at Marshall Space Flight Center on 2219 aluminum (nominal composition 6.3 % Cu, .3% Mn balance aluminum). The work piece was 0.40in (1.0 cm) thick. The pin tool was threaded (20/in or 7.8/cm) and was 0.490 in (1.24cm) in diameter and .375 in. (0.95cm) long with a flat bottom. The tool shoulder was 1.20 in. (3.0 cm) in diameter and slightly concave to the work piece. Penetrations were made to various plunge depths, measured from the tip of the pin, of 0.1 in (0.25 cm) to 0.388 in (0.98cm). The latter plunge submerged the shoulder and is typical of the plunge that would have been used to make a weld. After the desired plunge depth was attained, the welder was emergency stopped to freeze the pin in the sample. The sample was then unscrewed from the pin to preserve the structure.

Plunge speeds were 0.1 in/min or 0.2 in/min (0.0042 to .0084 cm/sec) and the tool rotational speed was varied from 200 rpm to 400 rpm with most plunges made at 300 rpm. Motor torque, plunge force, and plunge depth were recorded during the experiment.

Samples were cut, polished, and etched with Keller’s Solution for metallographic inspection.

## Results and Discussion

Fig. 1 shows plunge force versus plunge depth for 200 rpm, 300 rpm, and 400 rpm plunges all made at 0.1 in/min (0.042 cm/sec). Also included is a plunge at 300 rpm made twice as fast at 0.2 in/min. (0.0084 cm/min).

The cooler welds (made at 200 rpm and the fast plunge at 300 rpm) require the greatest plunge force because they have undergone the least heating and the weld metal has the highest flow stress. The first thin piece of extruded metal (seen on the left side of Fig. 2) does not appear until a plunge depth of approximately 0.07 in. Beyond this depth, all plunge forces decreased or remained nearly constant (in the case of the 400 rpm sample) as thermal equilibrium was established and material properties stabilized and flow stress decreased. Thus, only the 400 rpm sample exhibited steady state behavior and will be the focus of this work.

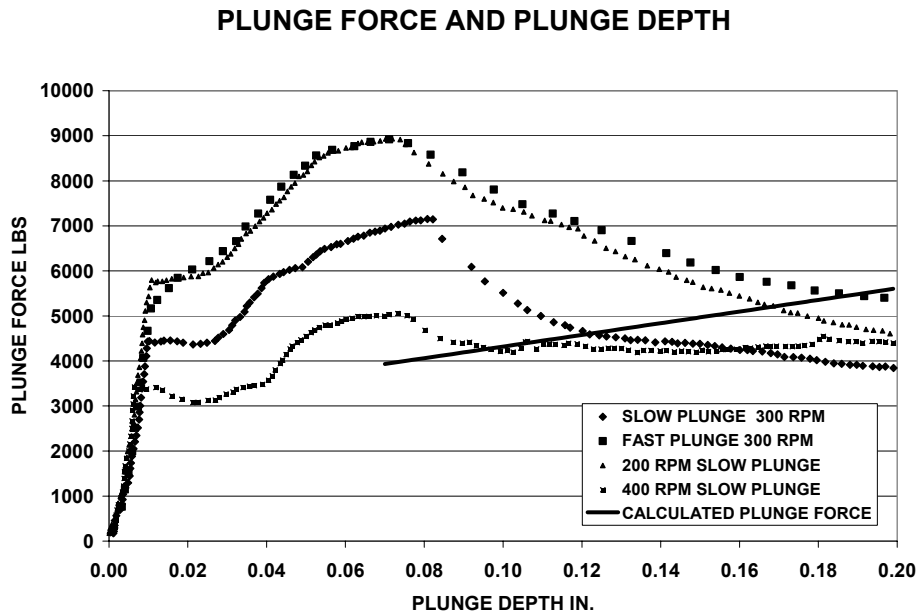


Figure 1: Plunge force versus plunge depth for plunges of 200, 300, and 400 rpm all made at 0.10 in/min. Also shown is a plunge at 300 rpm made twice as fast at .20 in/min. Note that the 400 rpm sample has approximately constant plunge force beyond .08 in. The Calculated Plunge Force is discussed later and should be compared to the 400 rpm data at plunges greater than 0.08 in.

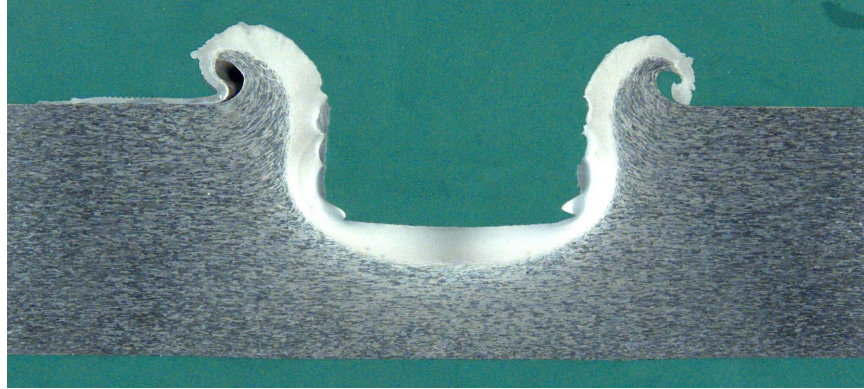
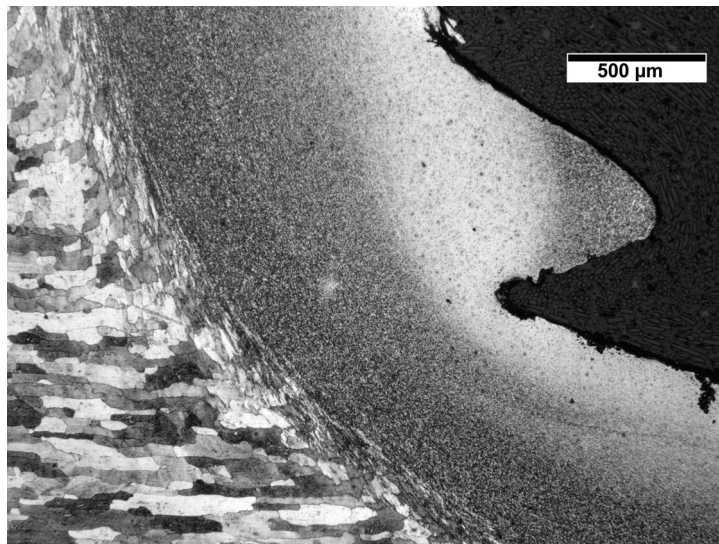
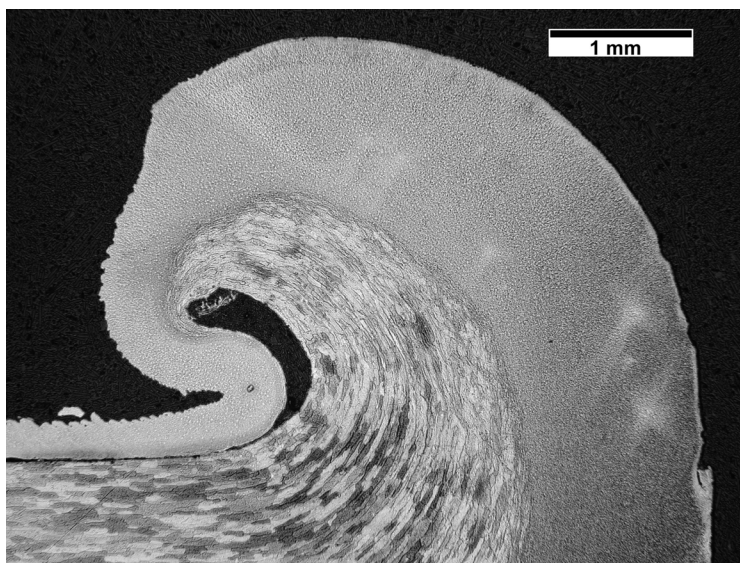


Figure 2: Low magnification cross section of sample plunged to 0.2 inches. Note light etching material surrounding pin fossil some of which is extruded onto the surface. The thin "tail" of metal seen on left side of pin fossil was the first part extruded. Sample is 0.40 in thick.

Fig. 2 shows a low magnification micrograph of the 400 rpm sample after the pin tool was stopped and removed. It is seen that the pin fossil is surrounded by a shiny, fine grained region of recrystallized grains. This is similar to the carousel<sup>7,11</sup> seen on fully plunged welds. Fig. 3 shows higher magnification micrographs of regions around the weld fossil.





**Figure 3: Higher magnification micrographs of Fig. 2 showing lower corner of fossil (above) and extruded material on left side. Note both deformed unrecrystallized grains and fine recrystallized grains that have been extruded by the tool. The fine grains are equiaxed and about 5 microns in size.**

The “tail” seen on the left side of Fig. 3 bottom is the first material extruded as the tool is plunged and is a record of the thickness of the fine grained region as plunge advanced. This material is easily seen by the welder during plunge and does not rotate with the tool.

Fig. 4 shows the pin tool torque (not motor torque) as a function of weld depth. Again the 400 rpm sample shows approximately depth independent torque after 0.07 inches of plunge and appears to be at steady state. The other cooler samples require more torque, and the slope of their curves decreases as temperature increases because steady state conditions are reached more rapidly by the hotter samples. The initial rapid increase in torque (Fig. 4) and plunge force (Fig. 1) below 0.01in of plunge is thought to be of mechanical origin as the welder engages the work piece.

## TORQUE VERSUS PLUNGE DEPTH

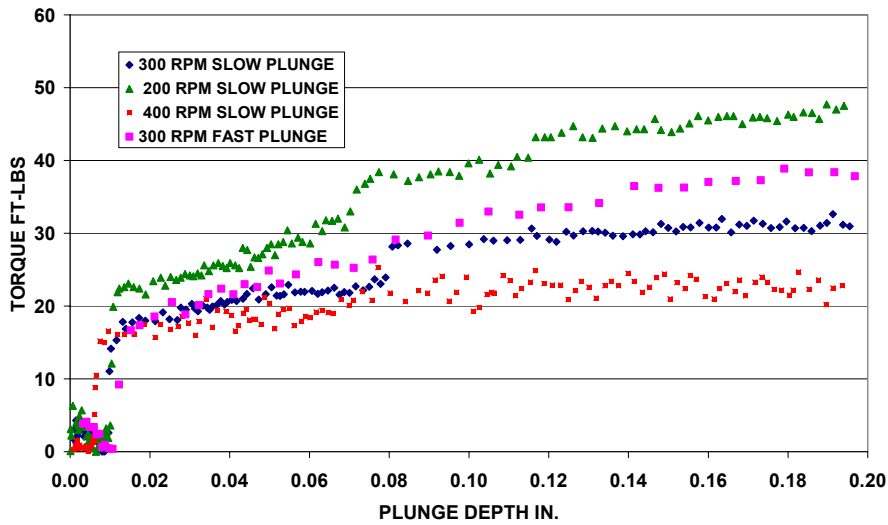


**Figure 4: Measured torque during plunge for various rotational rates and plunge speeds.**

The metal flow configuration around the initially penetrating friction stir welding tool is sketched in Figure 5. The fine grained material seen surrounding the pin tool fossil in Fig. 2 is evidence that material has undergone a very large deformation to promote this recrystallization. According to the model presented in this work, all this deformation takes place in a circular disk of material below the pin tool. This disk rotates with the pin tool and accretes material into the disk as the pin tool plunges. At the same time, material is squeezed out from the edges of this disk and rises along the sides of the pin tool. Only the region directly below the pin tool actually rotates. As mentioned above, material extruded during weld is seen to remain fixed to the work piece and does not rotate with the tool.

That there is a shear surface (the plane dividing the recrystallized and non-recrystallized material) below the tool is apparent from the sharply defined onset of recrystallized metal below the tool. This surface seen in Figure 2 is curved, but for simplicity will be represented as flat. Note that shear between rotating disk below the pin takes place between the rotating disk and the non-recrystallized material both on the flat surface of the disk and on its curved outer periphery.

As the tool descends the shear surface descends, and metal enters the rotating disk to be recrystallized and squeezed out at the sides and up along the tool to the free surface. In Figure 2 the extruded annular cylinder has roughly the same thickness as the rotating plug of metal and comprises chiefly recrystallized metal. The extruded cylinder does not rotate, at least at the upper surface, where it can be observed. It is assumed that the lower

threads deflect the upward flow so that contact between metal and tool is limited and negligible on the inside (the side against the pin tool) of the annular cylinder.

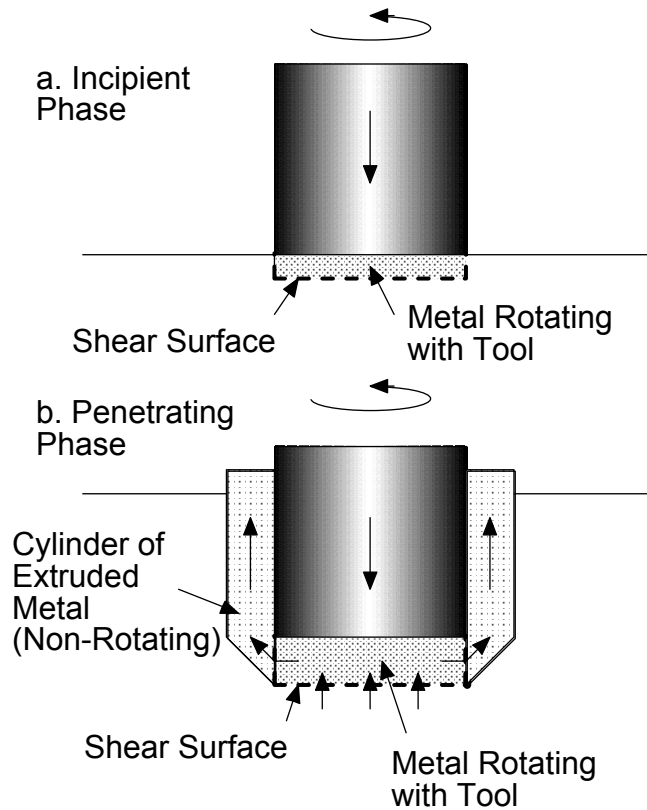


**Figure 5: Idealization of weld metal flow configuration in the vicinity of the penetrating friction stir tool.**

The shear stress  $\tau$  opposing motion at a shearing interface is a function of temperature and strain rate. To simplify the analysis, we will assume that the temperature is the same over all the shearing surfaces. The spindle torque  $M$  can be roughly estimated according to the relation:

$$M = \int_0^R 2\pi r^2 \tau dr + 2\pi R^2 h \tau = \frac{2\pi R^3}{3} \left( 1 + 3 \frac{h}{R} \right) \tau \quad (1)$$

$M$  is the torque,  $R$  is the pin tool radius,  $h$  is the thickness of the rotating disk, and  $\tau$  is the shear stress of the material.

The first term comes from torque due to motion of the flat circular face of the disk and the second term comes from shear between the circumference of the disk and the surrounding material. If  $R$  is 0.25-inches and  $h/R$  is approximately 0.3 (from Figure 2) then for the steady state torque of 22.5 ft-lbs of the 400 rpm data in Fig. 4,  $\tau$  is approximately 4,500 psi. (31 Mpa).

Colder penetrations (lower RPM and faster plunge speeds) show some increase in torque with penetration depth as well as the anticipated higher  $\tau$ . This is thought to be due to

increased friction between tool and work piece at the threads. Colder and harder material is more difficult to deflect from the threads. In situations where the rise in torque with penetration is greater, the imprint of the threads in sections such as shown in Figure 2 is more defined.

There are several forces that the pin tool must overcome in order to penetrate. In particular, the plunge force must be able to squeeze the material in the rotating disk below the pin out to the sides. This requires overcoming a radial shear force between the pin tool and the disk as well as expanding the disk itself which requires overcoming a hoop force within the disk. An additional force is required to bend the disk around the corner of the tool so that it can rise. Lastly, the force necessary to push the material upward along the shear surface between the cylindrical annulus of recrystallized material and the parent metal must be supplied.

To calculate the plunge force, free body diagrams with stresses (not forces) are shown in Figure 6 which permits a calculation of the plunge force  $F_z$ . This Vertical equilibrium on the annular extruded cylinder requires that

$$\pi [(R+h)^2 - R^2] P_1 = 2\pi(R+h)\delta\tau \quad (2a)$$

or

$$P_1 = 2 \left( \frac{1 + \frac{R}{h}}{1 + 2\frac{R}{h}} \right) \frac{R}{h} \frac{\delta}{R} \tau \quad (2b)$$

Equilibrium of the corner element requires

$$P_2 \left( \frac{1}{\sqrt{2}} \right) = P_1 \left( \frac{1}{\sqrt{2}} \right) + \sqrt{2} \tau \quad (3)$$

or

$$P_2 = P_1 + 2\tau = 2\tau \left[ 1 + \left( \frac{1 + \frac{R}{h}}{1 + 2\frac{R}{h}} \right) \frac{R}{h} \frac{\delta}{R} \right] \quad (4)$$

Equilibrium of a ring element of radius  $r$ , height  $h$  and thickness  $dr$  of the cylindrical plug of metal requires:

$$2rhdP = -2(2\tau)hdr - 2r(2\tau dr) \quad (5)$$

The first term on the right is the plastic hoop stress; the second, shear resistance to flow at the bottom surface of the disk. Hence

$$P = P_2 + 2\tau \ln \frac{R}{r} + 2\tau \left(1 - \frac{r}{R}\right)$$

This pressure must be integrated over the area of the disk to obtain a force.

$$F_z = \int_0^R 2\pi r \left[ P_2 + 2\tau \ln \frac{R}{r} + 2\tau \left(1 - \frac{r}{R}\right) \right] dr$$

$$= 2\pi R^2 \left( \frac{1}{2} P_2 + \frac{5}{6} \tau \right) = 2\pi R^2 \tau \left[ \frac{11}{6} + \left( \frac{1 + \frac{R}{h}}{1 + 2\frac{R}{h}} \right) \frac{R}{h} \frac{\delta}{R} \right] \quad (7)$$

(6)

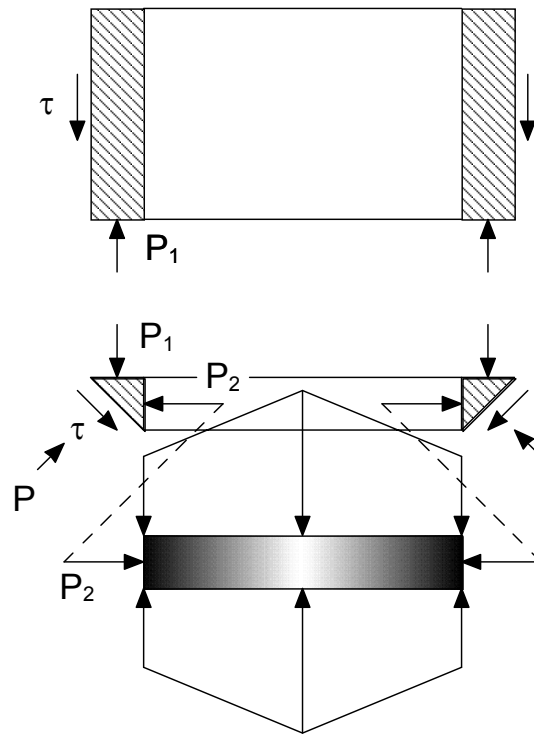


**Figure 6: Free body diagrams for flow elements in the vicinity of the penetrating friction stir tool.**

If the same value of shear stress calculated from the torque (4500 psi) is inserted in (7) a value of plunge force in good agreement with experimental results is obtained. See “Calculated Plunge Force” in Fig. 1.

Note that if  $h$  (the thickness of the recrystallized disk) is very small, the second term in Eq. 7 can dominate and the plunge force will be dependent on the plunge distance,  $\delta$ . Such dependence is seen from 0.01 inch plunge to 0.08 inch in Fig. 1. The material extruded in the “tail” seen in Fig. 2 is only 0.001 in. (0.0025 cm) thick and is probably

representative of the thickness of the rotating disk in the early stages of plunge, so the sharp increase at low plunges in Fig. 1 is not unexpected.

### **Conclusions**

1. The FSW plunge phase torque is that required to rotate a disk of material which rotates with the pin directly below it.
2. This disk is formed of recrystallized metal that was deformed by the pin tool abrasion against the parent metal. As plunge continues, more material is added to this layer until an equilibrium thickness sets in after about .08 in. of plunge.
3. The plunge force required in FSW is the force needed to deform in an outward direction this disk so that it can rise along the pin and eventually be expelled at the surface of the work piece.
4. The shear stress calculated from torque measurements and separately from plunge force measurements agree quite well, and is typical of metals a few hundred degrees below their melting point.

---

<sup>1</sup> W.M. Thomas, E.D. Nicholas, L.C. Needham, M.G. Murch, P. Templesmith, and J.C. Dawes: International Patent Application No. PCT/GB92/02203; G.B. Patent Application No. 9125978.8, 1991 and U.S. Patent No. 5,460,317, 1995.

<sup>2</sup> O.T. Midling, J.S. Kvale, and O. Dahl, *Proc. 1<sup>st</sup> Int. Symposium on Friction Stir Welding*, Thousand Oaks, CA, June 1999.

<sup>3</sup> The Welding Institute web site keeps a current list of applications. See [http://www.twi.co.uk/j32k/unprotected/band\\_1/fswapp.html](http://www.twi.co.uk/j32k/unprotected/band_1/fswapp.html)

<sup>4</sup> K.N. Krishnan, *Mater. Sci. Eng.*, 2002, Vol. A327, pp. 246-251.

<sup>5</sup> H. Jin, S. Saimoto, M. Ball, P.L. Threadgill, *Mat. Sci. and Tech.*, 2001, vol 17, pp 1605-1614.

<sup>6</sup> M.A. Sutton, B. Yang, A.P. Reynolds, Taylor, R., *Mat. Sci. & Engr.*, Vol. A323, 2002, pp. 160-166.

<sup>7</sup> Guerra, M., *op cit.*

<sup>8</sup> J.A. Schneider, A.C. Nunes Characterization of Plastic Flow and Resulting Micro Textures in Friction Stir Welds, *Mat. & Met. B*, April 2004.

<sup>9</sup> Tang, W., *op cit*

<sup>10</sup> M. Melendez, J.C. McClure, A. Nunes, "Forces During Friction Stir Welding", International Materials Conference, Cancun, Mexico, 2002.

<sup>11</sup> Coronado, E., "Effect of Pin Tool Shape on Friction Stir Welds" M.S. Thesis, University of Texas El Paso, 2002.

**2004**

**NASA FACULTY FELLOWSHIP PROGRAM**

**MARSHALL SPACE FLIGHT CENTER**

**THE UNIVERSITY OF ALABAMA  
THE UNIVERSITY OF ALBAMA IN HUNTSVILLE  
ALABAMA A&M UNIVERSITY**

**VISUALIZATION METHODS FOR VIABILITY STUDIES OF  
INSPECTION MODULES FOR THE SPACE SHUTTLE**

Prepared by:	Amir A. Mobasher
Academic Rank:	Assistant Professor
Institution and Department:	Alabama A&M University
NASA/MSFC Directorate:	Science
MSFC Colleague:	Dr. Kenneth Fernandez

## **Introduction**

An effective simulation of an object, process, or task must be similar to that object, process, or task. A simulation could consist of a physical device, a set of mathematical equations, a computer program, a person, or some combination of these. There are many reasons for the use of simulators. Although some of the reasons are unique to a specific situation, there are many general reasons and purposes for using simulators. Some are listed but not limited to (1) Safety, (2) Scarce resources, (3) Teaching/education, (4) Additional capabilities, (5) Flexibility and (6) Cost.

Robot simulators are in use for all of these reasons. Virtual environments such as simulators will eliminate physical contact with humans and hence will increase the safety of work environment. Corporations with limited funding and resources may utilize simulators to accomplish their goals while saving manpower and money. A computer simulation is safer than working with a real robot. Robots are typically a scarce resource. Schools typically don't have a large number of robots, if any. Factories don't want the robots not performing useful work unless absolutely necessary. Robot simulators are useful in teaching robotics. A simulator gives a student hands-on experience, if only with a simulator.

The simulator is more flexible. A user can quickly change the robot configuration, workcell, or even replace the robot with a different one altogether. In order to be useful, a robot simulator must create a model that accurately performs like the real robot.

A powerful simulator is usually thought of as a combination of a CAD package with simulation capabilities. Computer Aided Design (CAD) techniques are used extensively by engineers in virtually all areas of engineering. Parts are designed interactively aided by the graphical display of both wireframe and more realistic shaded renderings. Once a part's dimensions have been specified to the CAD package, designers can view the part from any direction to examine how it will look and perform in relation to other parts. If changes are deemed necessary, the designer can easily make the changes and view the results graphically. However, a complex process of moving parts intended for operation in a complex environment can only be fully understood through the process of animated graphical simulation.

A CAD package with simulation capabilities allows the designer to develop geometrical models of the process being designed, as well as the environment in which the process will be used, and then test the process in graphical animation much as the actual physical system would be "run". By being able to operate the system of moving and stationary parts, the designer is able to see in simulation how the system will perform under a wide variety of conditions. If, for example, undesired collisions occur between parts of the system, design changes can be easily made without the expense or potential danger of testing the physical system.

The simulation component of CAD also opens the door to users of the equipment as well as the equipment designers. For example, a robotics workcell designed for assembling parts by arc welding [1] may be simulated and the motion sequences required for the welding operation tested in simulation prior to actually performing the operation. Unanticipated collisions between the welding robot and the parts being joined or other parts of the workcell can be detected, and the system can be reprogrammed to provide collision-free motion. Thus, simulation adds a new

dimension to CAD by extending its usefulness from design to the manufacturing process, i.e., Computer Aided Manufacturing (CAM).

### **Historical Background of Robosim**

ROBOSIM is a graphical simulation system used for three-dimensional geometrical modeling of robot manipulators and various objects in their workspace, and for the simulation of action sequences performed by the manipulators. ROBOSIM was originally conceived and developed between 1985-88 by NASA-MSFC and Vanderbilt University as a means of rapid prototyping of robotics systems [2]. This early version of the simulation system was written in FORTRAN and was developed for DEC VAX mainframe computers with TEKTRONIX 4014 terminals and also Evans & Sutherland graphics terminals. Robots and other objects in the simulated environment were specified through a program that the user wrote. After a robot had been designed, the user could solve the inverse kinematics problem for a set of points and store the results in a file. This file could then be read back in and used to display the robot at the stored points. This early version of ROBOSIM could only display wire frame models and was basically a robot modeling tool. It also did not contain collision detection capabilities, and it did not possess any advanced features of artificial intelligence-based collision avoidance or path planning capabilities. Despite these shortcomings, ROBOSIM was used at the MSFC in a number of space related activities including: development of off-line welding programs for robots used in fabricating the Space Shuttle Main Engine (SSME), integration of a vision sensor into a robotics workcell used for Solid Rocket Booster (SRB) refurbishment, and planning of a robot mechanism to be mounted on the Orbital Maneuvering Vehicle (OMV) [3].

In the early 1990s Springfield abandoned completely the basic architecture of the earlier versions of ROBOSIM and compatibility with earlier versions to create the current version called ROBOSIM II, [4]. The underlying architecture of the software was redesigned to integrate the desirable features of the earlier versions of ROBOSIM into a common package. The new architecture designed by Springfield provided for an open platform upon which additional features can be more easily added.

The objectives of current effort is two fold: First to utilize the ROBOSIM II simulation environment in the development of an additional module (Boom) for the space shuttle as means of inspection, and second to incorporate the ROBOSIM II into the engineering curriculum at Alabama A&U University.

### **Simulation Results**

The Use of ROBOSIM II was demonstrated in a class project in the academic year 2003-2004 in EE490 Fundamentals of Robotics in AAMU within the school of engineering and technology. The class was taught by Dr. Ken Fernandez of NASA- MSFC. As part of the class project students were presented with a real world scenario of designing and simulation of boom for the shuttle. The project was presented in the following manner:

Shuttle Columbia Accident Investigation Board: Recommendation 3.4-3 Provide a capability to obtain and Downlink high-resolution images of the underside of the Orbiter Wing leading edge and forward section of both wings' Thermal Protection System.

***NASA's Implementation Plan for Space Shuttle Return to Flight and Beyond Response to 3.4-3: "...sensors will be mounted on the end of a 50 foot extension boom which will be carried in the Shuttle payload bay and grappled by the Shuttle's robotic arm."***

Class Project Objective were set as follows: To Apply Computer Simulation Techniques to the Preliminary Concept Verification of the Inspection Boom Planned by NASA in Response to the CAIB Recommendations. In the first trial the design specifications were given as: (1) Boom Length 50 ft, (2) RMS Docking Adapter Fwd, (3) Camera Mounted Aft, (4) Video Linked via RF, (5) Controls via RF link, (6) Boom/RMS Interface Passive, (7) Boom Power Self-Contained, (8) Comm. Via Std. Shuttle Sys.

### ***Verification of the Design Model***

#### ***Stowage Verification:***

Check for interference with cargo bay and other elements

#### ***Deployment Verification:***

Ability for Remote Manipulator System to Grasp Boom

Remove Boom from Stowage Position

Position for examination of wing sections

#### ***Functional:***

Ability of boom mounted cameras to view all critical areas

#### ***Re-Stowage Verification:***

Ability to remove boom from wing area and place in cargo bay

Ability to re-position in stowage area

Ability for Remote Manipulator to release and be stored

Figure 1 depicts the shuttle manipulator and the inspection boom. Figure 2. depicts the front view of the system in which collision detection and relative clearance distance between the shuttle and the arm maybe investigated.

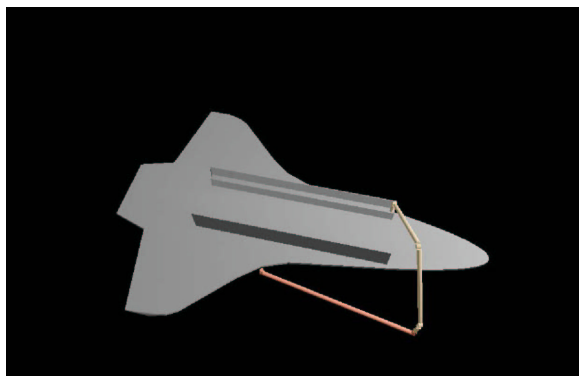


Figure 1. Demonstration of ROBOSIM II Kinematic manipulator Models of the Shuttle, RMS and the boom.

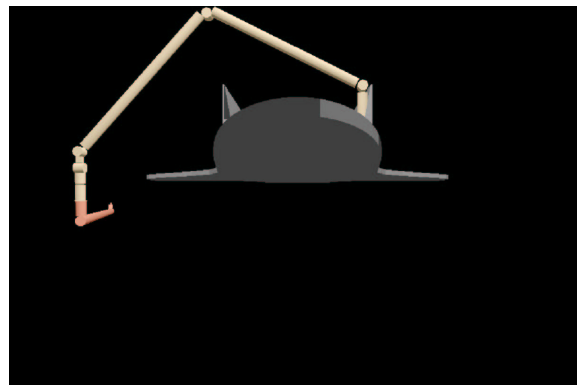


Figure 2. Front view of the shuttle with the Inspection Boom

## **Resources**

Recommended hardware for the Windows version is a 486 CPU, or higher, with 16 Mbytes of RAM. The speed of animation will depend on the processor speed. For best performance, a Pentium processor with processing speed of at least 1.2 GHz is recommended. A graphical accelerator is also recommended. Software requirements include Microsoft Windows 2000.

## **Conclusion**

ROBOSIM II is considered to be a valuable research tool. With a little investment in time and manpower many of the hidden costs involved in the design process maybe eliminated and the safety featured of the design maybe investigated. Those features of this simulation tool are demonstrated in the class project for EE490- Fundamentals of Robotics. In that it was shown that an inspection boom maybe safely installed on board of the shuttle. Future courses that will utilize the ROBOSIM II in AAMU are ME 320- Kinematics and Dynamics of Machines and ME 432-Design for Manufacture and Reliability.

## **Acknowledgements:**

The author wishes to extend his thanks Dr. Kenneth Fernandez for his patience and guidance and mentoring throughout the research. His selflessness and availability through out the course of this project made this research effort a truly pleasant experience. Special thanks goes to Mr. Willie Love for his support in this research.

## **References**

1. George E. Cook, Kenneth R. Fernandez, and Peter C. Levick, "Robot Simulation," *Exploiting Robots in Arc Welded Fabrication*, Ed.: J. Weston, The Welding Institute, Cambridge, England, pp. 132-135,
2. Kenneth Randolph Fernandez, *Robotic Simulation and a Method for Jacobian Control of a Redundant Mechanism with Imbedded Constraints*, Ph.D. Dissertation, Vanderbilt University, 1988.
3. Kenneth R. Fernandez, "The Use of Computer Graphic Simulation in the Development of Robotic Systems," *ACTA Astronautica*, Vol. 17, No. 1, Pergamon Press, New York, NY, pp. 115-122, 1987.
4. James F. Springfield, Jr., *An Open, Extensible System for Robot Simulation*, Ph.D. Dissertation, Vanderbilt University, 1993.

2004

**NASA FACULTY FELLOWSHIP PROGRAM**

**MARSHALL SPACE FLIGHT CENTER**

**THE UNIVERSITY OF ALABAMA  
THE UNIVERSITY OF ALABAMA IN HUNTSVILLE  
ALABAMA A&M UNIVERSITY**

**Elemental Analysis of the JSC Mars-1 Soil Simulant using  
Laser Ablation and Magnetic Separation**

Prepared By:	Ahad S. Nasab
Academic Rank:	Professor
Institution and Department:	Middle Tennessee State U Engineering Technology
NASA/MSFC Directorate:	Science
MSFC Colleague:	Dr. Palmer Peters

## Introduction

Future long-duration missions to Mars require capabilities in terms of manufacture of structures and chemical compounds essential for human habitat and exploratory activities. Currently, it is not feasible to import all the required raw and finished materials from Earth. In fact, essential items such as structural members as well as various gases for human consumption and material processing need to be largely extracted from the available planetary resources. The resources on Mars include its soil and rocks, its atmosphere and the polar caps. Mars atmosphere consists of 95% carbon dioxide and the balance contains small percentages of oxygen, nitrogen, and argon. The Mars regolith contains many metal oxides in various mineralogical forms. Presently, Martian soil samples are not available. However, a closely matched Martian soil simulant developed by the Johnson Space Center has been available for scientific research and engineering studies. The chemical makeup of this simulant is compared with the data from Viking Lander and Path Finder missions in Table 1.

<b>Oxide</b>	<b>JSC Mars-1</b>	<b>Pathfinder</b>	<b>Viking Lander</b>
SiO <sub>2</sub>	43.5	40.9	48.4
TiO <sub>2</sub>	3.8	0.7	0.74
Al <sub>2</sub> O <sub>3</sub>	23.3	10.4	8.2
Fe <sub>2</sub> O <sub>3</sub> /FeO	15.6	21.2	20.8
MnO	0.3	0.5	
MgO	3.4	8.7	6.7
CaO	6.2	6.1	6.6
Na <sub>2</sub> O	2.4	3.2	
K <sub>2</sub> O	0.6	0.5	<0.17
P <sub>2</sub> O <sub>5</sub>	0.9	0.9	
SO <sub>3</sub>		6	7.4
Cl		0.7	0.8

**Table 1:** Percent (by weight) chemical composition of the JSC Mars-1 simulant compared to soil data from Pathfinder and Viking Lander – from Allen, C. C., et al, Johnson Space Center [1].

Martian soil, rich in many metal oxides, can be processed to yield various elements such as Si, Fe, Al, Ti and oxygen. Reduction of these oxides to a metallic form with techniques employed on earth is not feasible at this time due the weight and complexity of such processing plants as well as other chemical reagents used in such processes. In this study, it is proposed that Martian soil simulant be irradiated with a high energy source such as a laser and the products of ablation, usually in the form of ions and excited atoms, magnetically separated and collected on substrates as thick films for further processing and packaging.

Laser ablation techniques have been used by others [2] to separate trace elements from geological specimens. Such studies have used quadrupole mass spectrometers which are not

suitable for separation and production of any significant amounts of elements for manufacturing purposes. Instead, a magnetic sector in conjunction with an optional ionizing source promises to yield adequate amounts of elements suitable for further processing and forming.

In the proposed process, the soil sample is ablated with a high fluence pulsed excimer laser to produce excited atoms and ions of the elements comprising the soil. Assuming that majority of the ablated material is in ionic form, an applied external magnetic field will divert the path of the ions based on their cyclotron radius which in turn depends on the momentum of the ablated ion. The cyclotron radius is defined as

$$R_c = \frac{mv}{zB}, \quad \text{where} \quad v = \sqrt{\frac{2eV}{m}}$$

and  $m$  is the mass of the ion,  $z$  is the ionic charge,  $B$  is the magnetic field strength,  $V$  is potential, and  $v$  is the ion velocity.

Assuming an ionic ejection energy corresponding to 20 eV, and a magnetic field strength of 1.5 kG, the cyclotron radii for ions of various atomic masses can be calculated and plotted as shown below;

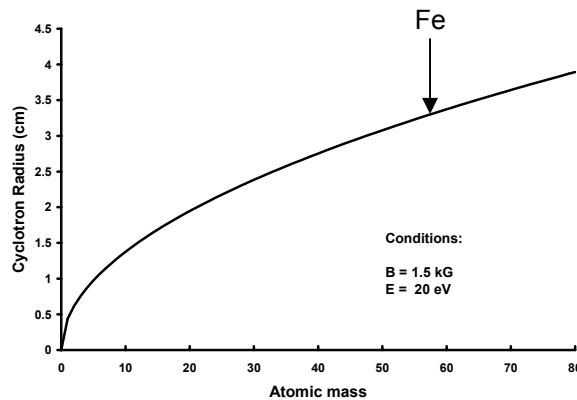


**Figure 1:** Cyclotron radii of singly ionized elements with various atomic masses

This chart indicates that singly ionized particles of iron traveling with a kinetic energy of 20 eV will follow a circular path with a radius of approximately 3 cm when subjected to a magnetic field of 1.5 kG.

The kinetic energy of the ablated particles is not well known for these conditions. Other investigations [3] performed under conditions from which our conditions can be extrapolated estimate the ion energies to range from 10 eV to 100 eV. A separate investigation is required to map the energy distribution of the ablated particles.

As part of the general ISRU experiments, we also studied the effect of annealing and external magnetic fields on glass prepared by melting of the simulant constituents as listed in Table 1 in reagent form. It is desirable to form glasses with significant magnetic properties for use in many applications such electric motors, heat production, and radiation shielding.

## Experiments

The JSC Mars-1 soil simulant, provided by the Johnson Space Center, was processed in different ways to study its chemical and physical transformations under various conditions. The following sections describe the four separate experimental activities that contributed to improved understanding of our abilities to extract elements of interest from the Martian soil simulant by in-situ techniques.

### Experiment 1- Laser Ablation of Soil

In the following series of experiments which constituted the majority of the efforts undertaken as part of the SFFP program, JSC Mars-1 soil simulant was heated in a vacuum furnace at 120 °C for 24 hours and pressed under 10,000 psi to form a pellet of approximately 1 in. diameter and 1/8 in. thickness. The pellet form was preferred to loose soil form due to its ability to retain its shape when undergoing the laser ablation process. An excimer laser (Lambda Physik LPX-100) with 200 mJ pulse energy, 20 ns pulse duration, and 248 nm wavelength (with Kr-F gas mixture) was used for these experiments. The laser radiation was focused using a magnesium fluoride lens on the surface of the soil sample which was centrally placed in a 30-cm cylindrical vacuum chamber. The excimer laser was operated at 10 Hz which provided an average power of 2.0 W with peak powers of 10.0 MW per pulse.

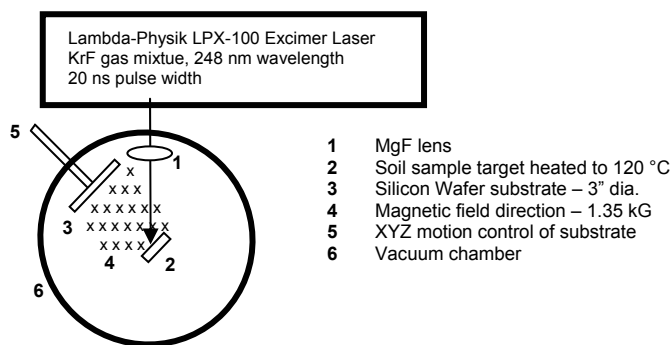


**Figure 1:** Schematic of the experimental setup

Silicon wafers (3 in. dia.) were used as substrates for their sub-nanometer surface polish which facilitated film thickness measurements as well as for their purity which helped in isolation and identification of the deposited material. Carbon tapes were used to mask a small area of the silicon wafer to provide a reference plain for film thickness measurements. A resistance coil

heater using AERO-COAX 1HR063F6.5 wires was manufactured and placed directly behind the soil sample holder and used to heat the soil to 120 °C for several hours under vacuum conditions to ensure any water vapor absorbed from the environment would be vaporized and evacuated before laser ablation resumption. The heating of the sample continued during the laser ablation process.

The pressure in the chamber was maintained at about  $4 \times 10^{-5}$  Torr using a roughing pump (Edwards-18-Two Stage) and a turbomolecular pump (Leybold TurboVac 151C) to provide mean free paths much longer than the radius of the chamber. Chamber pressure was monitored by a thermocouple gauge (Teledyne DV-6M) and a Penning gauge (Edwards CP-25-EK). To investigate the extent of ionization in the plasma produced by laser ablation, two permanent magnets with dimensions of 4 cm by 6.5 cm were placed on opposite sides of the plasma generated by laser ablation. The magnets were separated by 20 mm. The field strength of the magnets was measured to be 1.35 kG at the center which uniformly decreased to 1.1 kG near the edges. If considerable fraction of the plasma were ionized, the path of the ionized particles would be deflected under the influence of a magnetic field perpendicular to the direction of motion of the ionized particles.



**Figure 2:** Experimental setup showing the excimer laser and the vacuum chamber

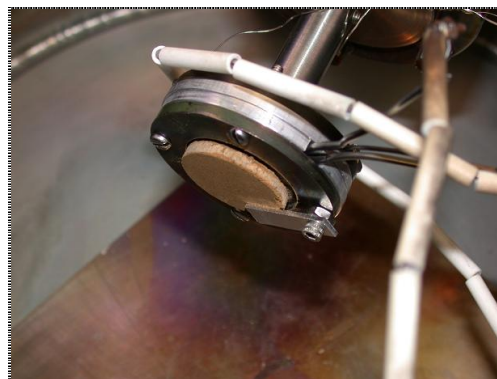


**Figure 3:** Soil sample mounted on an electrically heated target holder

In each case, the soil sample was ablated for 35 minutes at 10 Hz with approximately 200 mJ per pulse. The silicon wafer substrate was placed parallel to the soil sample at a distance of 5 cm from the soil sample. Experimental facilities and the target holder are shown in figures 2 and 3.

The deposited film on the silicon wafer was examined using a stylus profilometer (Tencor Alpha-Step 200) which has a vertical resolution of 5 angstroms.

### Experiment 2 – Ionization Extent of Silicon

In order to investigate the ionization stage of the ablation plasma, an experiment was set up using the facilities at University Alabama, Huntsville under the direction of Dr. Andrew Pakhomov. In

these experiments a glycol cooled array detector (Princeton Instruments IRY-512G/RB) was used in conjunction with a 1200 lines/mm grating spectrometer to study the atomic as well as ionic emission lines of silicon which was the dominant constituent of the soil. The radiation from a pulsed Nd:YAG laser (Molelectron MY32-10) was focused on a small piece of high purity silicon wafer. The emission from the plasma generated as a result of the surface ablation of the silicon wafer was focused on the spectrometer which was set to observe the 500.6059 nm line of the atomic silicon and the 504.1024 nm emission line of the ionic silicon. . As of the writing of this document, the emission data has not yet been collected on the silicon wafer nor the soil sample. However, it is planned that the emission data be collected at various delay times relative to the laser pulse generation. Emission spectrum will be collected at delay times of 20, 30, 50, 100, and 1000 nanoseconds to observe the relative particle densities of the silicon ions compared to the atomic silicon. Once such preliminary data is processed, the JSC Mars-1 simulant will undergo the same experiments to observe the emission lines belonging to other elements such as iron and aluminum. The ultimate goal of these set of experiments is the study of the ionization extent of some of the elements comprising the soil simulant.

### Experiment 3 – Oven Melting of Reagents

The sample under study in these series of experiments was prepared by mixing the oxide constituents of the JSC Mars-1 soil as reagents and heated at 1500 °C for 6 hours. The molten mixture was then cooled down to room temperature. The provided sample has a dark gray color similar to an iron magnet. The sample is also slightly magnetic and responds to an applied magnetic field. Three pieces from the provided sample were cut to study the effect annealing and applied external magnetic field on this sample. The cut pieces had dimensions of 4 mm by 14 mm with a typical thickness of 2 mm. One of the pieces was subjected to resistive heating in an oven which was continuously purged by argon for the entire duration of the heating and cooling processes. The oven temperature was raised to 800 °C at a rate of approximately 20 °C/min. The maximum temperature of 800 °C was then maintained for 4 hours before the oven was cooled at a rate of 50 °C/hr to 100 °C. In a separate experiment, another piece of the sample was heated in the oven as described above except that in this case an external magnetic field of nearly one Tesla was applied for the entire duration of heating and subsequent cooling of the specimen. A summary of the processed pieces and their respective labels are shown below,

<b>Sample label</b>	<b>Oven max. T</b>	<b>Ext. Mag. Field</b>	<b>Notes</b>
Re-Cont	n/a	n/a	<i>Control piece</i>
Re-A	800 °C	0.0	<i>Annealed with no applied magnetic field</i>
Re-B	800 °C	1.0 Tesla	<i>Annealed with applied magnetic field</i>

**Table 2:** List of specimens processed for magnetic property studies

The magnetic properties of each of the specimens as labeled above were measured using a Vibrating Sample Magnetometer (VSM) system. The VSM produced the Hysteresis curves for

each sample. The samples were further examined by polishing their surface to 1  $\mu\text{m}$  and applying a small quantity of a ferrofluid (FerroTec EMG 909) to their surface. The ferrofluid used in this case had particle sizes of 10 nm and viscosity of less than 5 cp. The ferrofluid is generally used to reveal the possible magnetic domain structure of a sample. This method is a well recognized tool in the field of magnetic domain analysis and is known as the Bitter method.

#### Experiment 4 – Laser Melting of Soil

Experiments involving the melting of JSC Mars-1 were previously conducted by the author at Middle Tennessee State University. In these experiments the Martian soil simulant was placed in a metal container with dimensions of approximately 2 in. by 4 in. and 1 in. deep. A CO<sub>2</sub> laser was used to melt a 0.25 in by 0.5 in. area in central area of the sample. The laser light, with a spot size of 0.005 in. was focused at the surface level of the soil. The soil was at room temperature and atmospheric pressure. The experiments were performed in air. The laser scan rate was set at 0.3 in/min. In one experiment the soil as received from JSC was processed using the procedure outlined above. In another experiment 10% (by weight) graphitic carbon was added to the soil to study its effect on the reduction of iron oxides present in the soil to metallic iron. The use of the surrounding soil as the crucible in these experiments alleviated the problems associated with selection of suitable containers which could tolerate the temperatures and high rates of heating and cooling encountered in these cases. The processed soil samples were sectioned, mounted in epoxy and polished at NASA-MSFC and submitted to Mr. Paul Carpenter of BAE Systems for electron beam microanalysis. The discussion of these analyses is included in the next section.

#### Results

Energy deposited by the excimer laser on the soil sample caused ablation of neutral and ionic particles from the sample surface. Since the ablation process is temporally separated from absorption of the laser radiation energy, the ablation materials are ejected in the direction normal to the surface of the sample, regardless of the direction of the incident beam as shown in figure 4. There is, however, a certain degree of asymmetry which is believed to be caused by the shape of the cavity formed by laser ablation after a few hundred pulses. Figure 5 shows that the cavity becomes increasingly deeper at the distal location which forms a wall which in turn inhibits the plasma from expanding in that direction.

It is further noted that under adequate magnification, a cone-like structure is observed to form in the ablated area of the soil sample (Figure 6). The cones are about 100 microns in width and generally point in the direction of the incident beam. We believe that these cones are similar to those observed by many researchers [4, 5] in the field of thin film coating using laser ablation. Foltyn, *et al* [5] suggest that vaporization-resistant impurities are responsible for the cone formation. They demonstrated that the cone tips are much richer in certain elements compared to other parts of the sample.

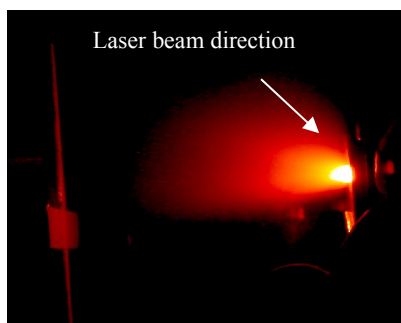


**Figure 4:** Formation of plasma by the ablated material. Silicon substrate is shown on far left

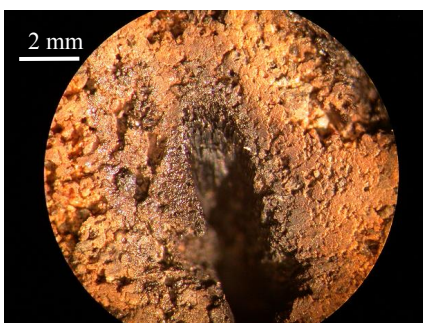


**Figure 5:** Crater formed by mass removal from the soil sample by laser ablation

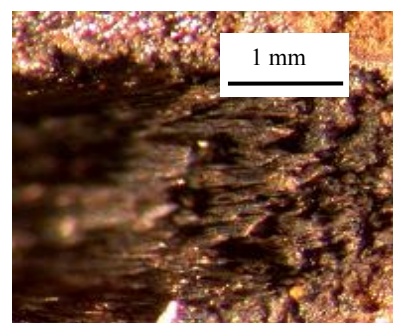


**Figure 6:** Cones formed in the direction of incoming laser radiation

The thin film formed on the surface of the silicon wafer shows a ringed color pattern which is believed to be caused by interference of light from the film surface and the reflective substrate. This is not unlike the colors observed from a thin film of oil on water. The colors observed on the substrates are consistent with film thickness measurements using a stylus-based instrument. It is also noted that more than one order of interference is present.

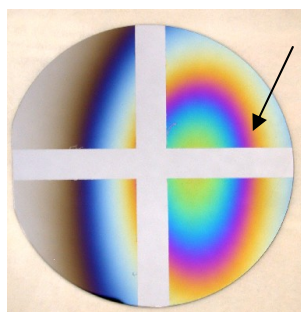


**Figure 7:** Thin film deposit on silicon wafer showing interference patterns

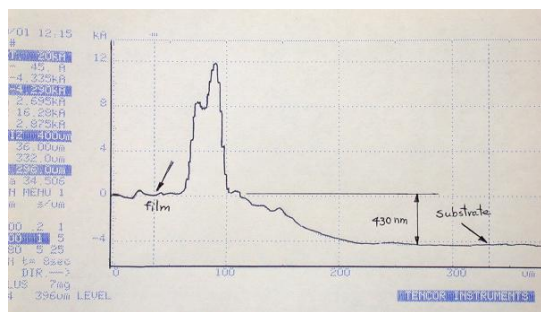


**Figure 8:** Film thickness measured at the point marked in figure 7

The film shown in figure 7 has a maximum thickness of approximately 500 nm which is consistent with the film thickness measurements conducted by the stylus profilometer. The film demonstrates some level of graininess not unlike those observed for crystals of table salt (Figure 9). It is our intention to analyze the deposited film to determine its composition. We believe that the majority of the film consists of silicon dioxide since silicon is the most abundant element in the soil sample. Moreover, film of other elements such as iron, aluminum, or titanium would have created an opaque film and not caused the interference pattern observed on the substrate. Experiments conducted with an applied magnetic field of 1.35 kG in the direction perpendicular

to the direction of particle motion resulted in similar deposited films and film thicknesses as shown in figure 10.

The presence of the magnets above and below the plasma and the presence of magnet housing on the sides of the plasma created a cold wall confining the plasma to the center portion of the passage formed by the magnet and the magnet housing. The resulting pattern is not conclusive concerning the deflection of the plasma by the applied magnetic field. Even though, there seems to be a more convex shape to the pattern towards the right direction, which would be consistent with deflection of positive ions to the right, the effect could as well be due to the wall confinement.

We plan to devise an experiment where the effect of magnetic field on the pattern formed on the substrate could be demonstrated on the same substrate. This could be accomplished by coating an area of the substrate in the presence of external magnetic field and then masking the coated area and coating an adjacent area with ablated material in the absence of the magnetic field. We are also planning to take advantage of electromagnets for this purpose to fix the experiment geometry and only alter the field strength.

Lack of detailed knowledge of the plasma constituents and their average kinetic energy remains the biggest obstacle in the progress of these experiments. Experiments being conducted at UAH are not completed as of the writing of this report.

Studies of the magnetic properties of the cast pieces from oxide reagent are also in progress at this time. The specimens listed in Table 2 have been polished to 1 micron and observed at magnification of 1000X after the surface was treated with a thin film of ferrofluid. No domain structure has been observed from our preliminary analysis as of this writing. We plan to conduct detailed susceptibility and domain analysis studies on these specimens.

Soil samples which were processed by a CO<sub>2</sub> laser at MTSU were analyzed using a microprobe. The two samples that were studied in detail were the laser-processed sample as received (sample a) and the soil sample with 10% by weight graphitic carbon (sample b). As shown in figure 11 sample (a) does not display any granular structure which is an indication of a homogeneous glass structure with some uniform convection lines apparent. On the other hand, sample (b) exhibits many features such as various grains and crystal growth.

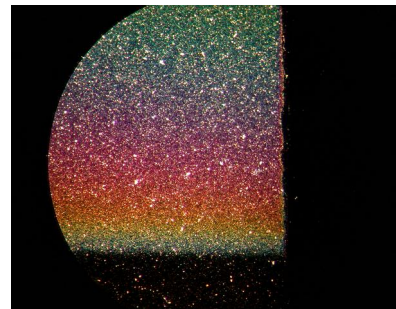


**Figure 9:** Grain-like structure of the thin film deposit

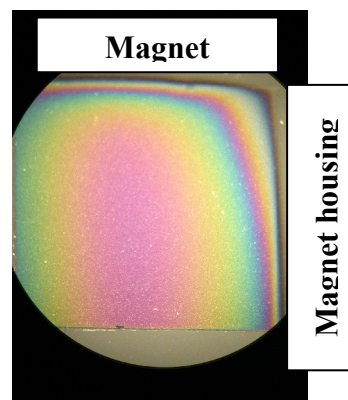
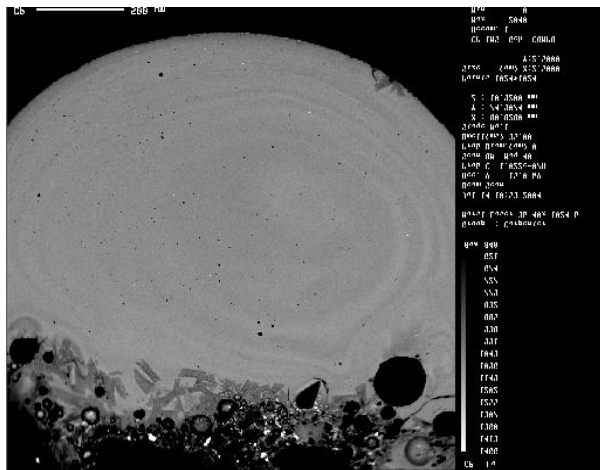
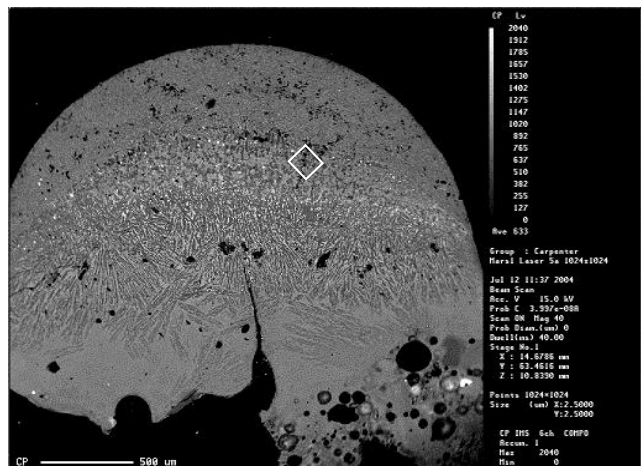


**Figure 10:** Interference pattern of the film in the presence of a magnetic field



(a)



(b)

**Figure 11:** BSE images of the laser-processed samples. (a) JSC Mars-1 soil as received, (b) JSC Mars-1 with 10% (wt) graphitic carbon added.

Further element-specific analysis of various areas of the cross section shown in figure 12 points out the presence of metallic iron at some intermediate locations within the cross sections.

The addition of solid carbon has apparently caused reduction of iron oxides present in the soil to metallic iron. Figure 12 shows the elemental analysis of the area indicated in figure 11(b) for iron. Other prominent structures shown in figure 11(b) were found to be mostly glass, plagioclase, FeTi oxides, CaTiFeAl oxides, as well as several other oxides.

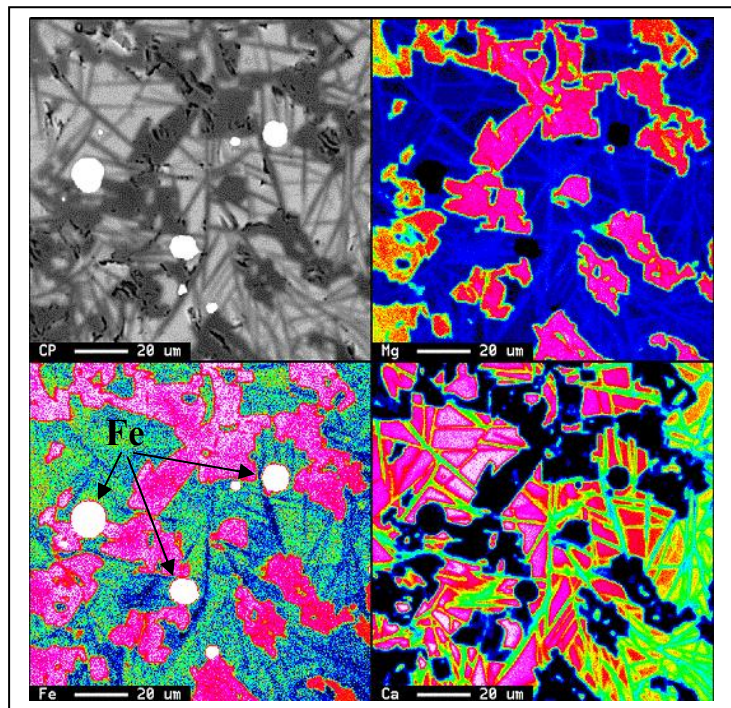


**Figure 12:** BSE images of the area shown in fig. 11 (b) for Mg, Fe, and Ca.

## **Conclusions**

Martian soil stimulant JSC Mars-1 was ablated by an ultraviolet excimer laser in order to separate the constituent elements for *in-situ* resource utilization purposes. It was found that applied external magnetic field had some effect on the path of the ablated particles which could indicate that some of the excited particles forming the plasma are in ionic form. This aspect of the study will be further investigated to determine the extent of ionization in the laser induced plasma. The thickness of the ablated material on a silicon substrate followed the cosine relationship which is typical for film deposition by laser ablation.

The electron beam microanalysis of the soil samples processed by a 30 W CO<sub>2</sub> laser revealed that some iron oxides had reduced to elemental iron in the presence of carbon. Samples with no carbon added did not display any iron oxide reduction.

Study of the magnetic properties of the samples processed under various annealing and external magnetic field condition are still in progress and have not produced any results as of this writing.

## **Future Directions and Recommendations**

Many aspects of the preceding investigations remain unresolved requiring further experimentation and analysis. In particular, the laser-supported plasma formed due to laser ablation of the soil simulant needs to be characterized more precisely in terms of ionization extent and the identification of the major constituents of the plasma at various times and distances from the target. The results of such studies will guide efforts in designing supplemental ionization chambers as well as specification for the magnetic sector stage. It is recommended that an emission spectrometry system with a time delay controller be an integrated part of future laser ablation experiments. Such a system will provide continuous, time resolved and detailed information about the laser-supported plasma.

Experiments that utilized a CO<sub>2</sub> laser to melt the soil sample would benefit from construction of a controlled environment where cover gases and their pressures could be varied. Others have noted that presence of CO during the melting process of iron oxides leads to production of metallic iron. It is recommended that experiments in CO environments under pressures representative of the Martian atmosphere be conducted to study the effect of such environments on the yield of various elements.

## **Acknowledgements**

The author is deeply indebted to his MSFC Colleague, Dr. Palmer Peters for his unwavering support, guidance and encouragement throughout the course of this project. The author would also like to thank Dr. Mathew Marone, a summer faculty fellow, for his help and guidance with many aspects of the project. Many scientists and professionals at the NASA-MSFC Science Directorate contributed to this project. Mr. Paul Carpenter of BAE Systems provided electron beam microanalysis, Ms. Sheryl Gallop prepared samples for analysis, Mr. Curtis Bahr and Mr.

Jeff Quick provided machining and other support services, and Drs. Laurent and Sen of BAE Systems participated in project discussions with the author. Dr. Narayanan Ramchandra guided the experiments involving the magnetic characterization of the sample produced from reagents.

## **References**

- [1] Allen, C. C., *et al.*, ***JSC Mars-1: Martian Regolith Simulant***, Proceedings of Lunar and Planetary Science XXVIII, 1997. No. 1797.
- [2] K. E. Jarvis, J. G. Williams, S. J. Parry and E. Bertalan, ***Quantitative determination of the platinum-group elements and gold using NiS fire assay with laser ablation-inductively coupled plasma-mass spectrometry (LA-ICP-MS)***, Journal of Chemical Geology, Volume 124, Issues 1-2, p. 37-46 (25 July 1995)
- [3] Claeysens, F. *et al.*, ***Comparison of the ablation plumes arising from ArF laser ablation of graphite, silicon, copper, and aluminum in vacuum***, Journal of Applied Physics, Vo. 94, No. 4, p. 2203, 15 Aug. 2003
- [4] Ibrahim, N. B., Edwards, C., Palmer, S. B. ***Yttrium iron garnet surface modification during pulsed laser ablation deposition***, Materials Science-Poland, Vol. 22, No. 2, 2004
- [5] Foltyn, S. R., R. C. Dye, K. C. Ott, E. Peterson, K. M. Hubbard, W. Hutchinson, R. E. Muenchausen, R. C. Estler, and X. D. Wu, ***Target modification in the excimer laser deposition of  $YBa_2Cu_3O_{7-x}$  thin films***, Applied Phys. Lett., vol. 59., no. 5, p. 594, 1991

2004

NASA FACULTY FELLOWSHIP PROGRAM

MARSHALL SPACE FLIGHT CENTER

THE UNIVERSITY OF ALABAMA  
THE UNIVERSITY OF ALABAMA IN HUNTSVILLE  
ALABAMA A&M UNIVERSITY

**WHISPERING-GALLERY MODE AT MSFC: EXCITATION OF  
FUSED-SILICA MICRO-RESONATORS VIA TAPERED  
OPTICAL FIBERS**

**REPORT NOT AVAILABLE**

Prepared By:	Jamiu (Ade) Odutola, Ph.D.
Academic Rank:	Associate Professor
Institution:	Alabama A. & M. University
Department:	Department of Chemistry
NASA/MSFC Directorate:	Science
MSFC Colleague:	Dr. Don Frazier

2004

**NASA FACULTY FELLOWSHIP PROGRAM  
MARSHALL SPACE FLIGHT CENTER**

**THE UNIVERSITY OF ALABAMA  
THE UNIVERSITY OF ALABAMA IN HUNTSVILLE  
ALABAMA A&M UNIVERSITY**

**MECHANICAL CHARACTERIZATION OF A  
MULTIFUNCTIONAL COMPOSITE MATERIAL**

**REPORT NOT AVAILABLE**

Prepared By: Juan A. Román Pagán  
Academic Rank: Graduate Student, B.S.  
Institution and Department: University of Puerto Rico  
Mayagüez Campus  
Department of Civil Engineering and Surveying  
NASA/MSFC Directorate: Engineering  
MSFC Colleague: Raj K. Kaul

**2004**  
**NASA FACULTY FELLOWSHIP PROGRAM**

**MARSHALL SPACE FLIGHT CENTER**

**UNIVERSITY OF ALABAMA**  
**UNIVERSITY OF ALABAMA IN HUNTSVILLE**  
**ALABAMA A&M UNIVERSITY**

**Investigation of Integrated Vehicle Health Management  
Approaches**

Prepared by:	Deidre Paris
Institution:	Clark Atlanta University Department of Engineering
NASA/MSFC Directorate:	Engineering Directorate, ED 10
MSFC Colleague:	Dr. Luis Trevino

This report is to present the work that was performed during the summer in the Advance Computing Application office. The NFFP (NASA Faculty Fellow Program) had ten summer faculty members working on IVHM (Integrated Vehicle Health Management) technologies. The objective of this project was two-fold: 1) to become familiar with IVHM concepts and key demonstrated IVHM technologies; and 2) to integrate the research that has been performed by IVHM faculty members into the MASTLAB (Marshall Avionic Software Test Lab).

IVHM is a NASA-wide effort to coordinate, integrate and apply advanced software, sensors and design technologies to increase the level of intelligence, autonomy, and health state of future vehicles. IVHM is an important concept because it is consistent with the current plan for NASA to go to the moon, mars, and beyond. In order for NASA to become more involved in deep exploration, avionic systems will need to be highly adaptable and autonomous.

### **IVHM Activities**

The first major initiative took place for IVHM was an IVHM testbed workshop. Attendees of this workshop included representatives from the aerospace industry, from governmental agencies, academia, and other NASA centers. The purpose of IVHM is to increase the safety, affordability, and sustainability of Exploration missions through Integrated Systems Health Management of complex, mission-critical vehicles and systems. Some of the objectives of IVHM includes 1) automated pre-flight readiness checkout, 2) built-in test functionality, 3) automated ground processing, 4) automated systems health assessment, 5) failure management and report, 6) integrated real-time fault diagnosis, and 7) trending and prognostics. These objectives will enable GN & C capabilities, advanced mission planning and flight operations, advanced crew escape & survival/payload recovery, advanced automated rendezvous and capture, and advanced checkout, control and maintenance system.

### **Vehicle Health Management History**

One of the things that were identified at the IVHM testbed workshop was that IVHM has a history of having many different paradigms.

- *FDRI (Fault Detection, Isolation, and Reconfiguration)* was a paradigm that was used in the aerospace industry in the 60s and 70s.
- *Autonomy*-some believed that IVHM was a subset of autonomy and there are those who believe that autonomy is a subset of IVHM.
- *VHM<sub>a</sub>(Vehicle Health Monitoring)*- evolved from FDIR.
- *SHM (Systems Health Management)*- this was the first attempt to integrate safety, reliability, fault management, testability and cost benefit analysis into a common framework. This is also defined independently as Structural Health Management.
- *VHM<sub>b</sub>(Vehicle Health Management)*-management aspect spans autonomous reconfigurations well as the resources required to safely and most cost effectively achieve mission goals.

- *IM(Informed Maintenance)*-this is also referred to as condition based maintenance.*RSO(Resilient Systems & Operations)*-this is Level 2 IVHM project under the Design for Safety Program).
- *IIVM (Intelligent Integrated Vehicle Management)*-this is a paradigm that has been developed from the CRAI activities.

There is a difference between VHM<sub>a</sub> and VHM<sub>b</sub>. It is considered among many that the only way to assure the goals of IVHM will be to include an integrated capability for automating the maintenance and operation of vehicles. That would mean a significantly different use of avionics systems as opposed to the way they are now employed. This is the concept of vehicle health management as opposed to simply vehicle health monitoring. Such a concept implies the ability to fully monitor the operational functions of the target vehicle and to have built-in systems abilities to do something with the information derived from that monitoring. Another critical aspect of IVHM is that information is generated and acted upon rather than merely acquiring data and presenting it for later manipulation and use. The integrated system will require many modules as subcomponents such as structural surveillance systems, active structural controls and adaptation, flight controls and control surfaces, propulsion management and surveillance, guidance and navigation.

### **IIVM for NFFP Project**

As a part of the overall goal of developing Integrated Vehicle Health Management (IVHM) systems for aerospace vehicles, the NASA Faculty Fellowship Program (NFFP) at Marshall Space Flight Center has performed a pilot study on IVHM principals which integrates researched IVHM technologies in support of Integrated Intelligent Vehicle Management (IIVM). The framework integrates advanced computational techniques with sensor and communication technologies for spacecraft that can generate responses through detection, diagnosis, reasoning, and adapt to system faults in support of IIVM. These real-time responses allow the IIVM to modify the affected vehicle subsystem(s) prior to a catastrophic event. Furthermore, the objective of this pilot program is to develop and integrate technologies which can provide a continuous, intelligent, and adaptive health state of a vehicle and use this information to improve safety and reduce costs of operations. Recent investments in avionics, health management, and controls have been directed towards IIVM. As this concept has matured, it has become clear the IIVM requires the same sensors and processing capabilities as the real-time avionics functions to support diagnosis of subsystem problems. New sensors have been proposed, in addition, to augment the avionics sensors to support better system monitoring and diagnostics. As the designs have been considered, a synergy has been realized where the real-time avionics can utilize sensors proposed for diagnostics and prognostics to make better real-time decisions in response to detected failures. IIVM, as shown in figure 1, provides for a single system allowing modularity of functions and hardware across the vehicle. The framework that supports IIVM consists of 11 major on-board functions necessary to fully manage a space vehicle maintaining crew safety and mission objectives: Guidance and Navigation; Communications and Tracking; Vehicle Monitoring; Information Transport and Integration; Vehicle Diagnostics; Vehicle Prognostics; Vehicle mission Planning; Automated Repair and Replacement; Vehicle Control; Human Computer Interface; and Onboard Verification and Validation. Furthermore, the presented framework provides complete vehicle management which not only allows for

increased crew safety and mission success through new intelligence capabilities, but also yields a mechanism for more efficient vehicle operations. The representative IVHM technologies for IIVM includes: 1) robust controllers for use in re-usable launch vehicles, 2) scalable/flexible computer platform using heterogeneous communication, 3) coupled electromagnetic oscillators for enhanced communications, 4) Linux-based real-time systems, 5) genetic algorithms, 6) Bayesian Networks, 7) evolutionary algorithms, 8) dynamic systems control modeling, and 9) advanced sensing capabilities.

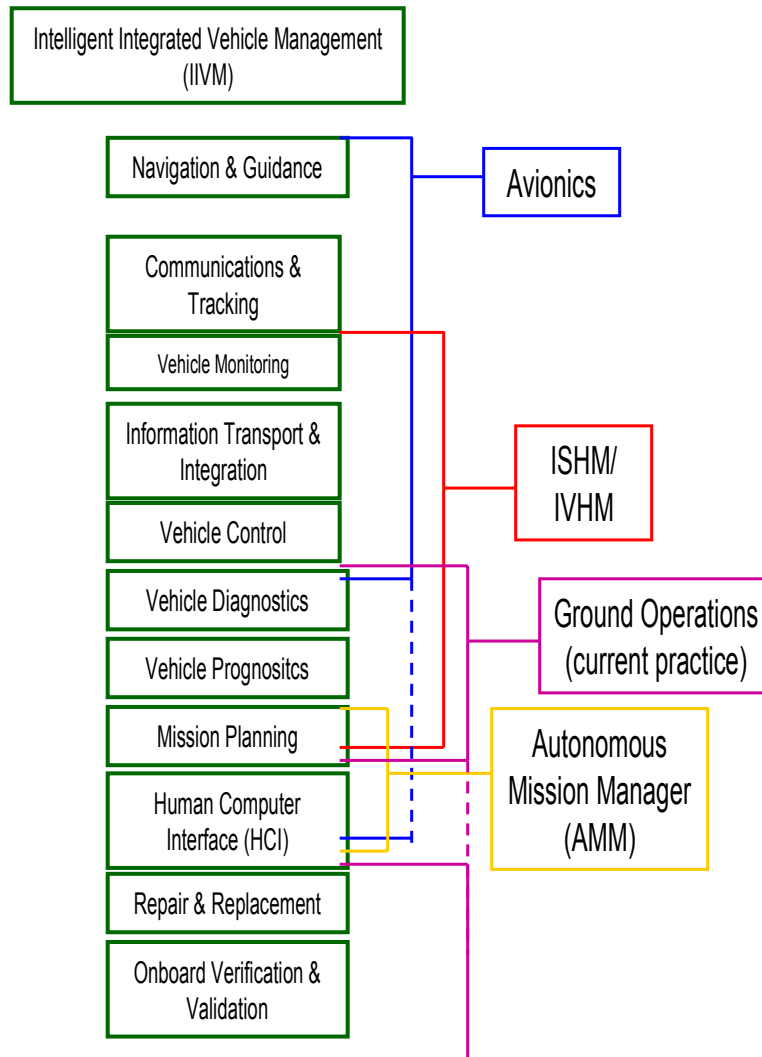


Figure 1: Proposed Intelligent Integrated Vehicle Health Management Framework

### **IVHM TECHNOLOGIES**

The automotive industry is leading the development of on-board and ground-based diagnostics. Nissan has developed a system called the Electronic Concentrated Control System (ECCS) which provides Diagnostic Trouble Codes (DTCs) for technicians to reference in the Diagnostic Manual via CD-ROM. Similarly, Ford states that 70,000 technicians are using their two volume

“ultimate toolbox” Service Manual by referencing on-board provided Service Codes to obtain test procedures, test guides and wiring diagrams for all unique engine configurations<sup>1</sup>.

Integrated Diagnostics (ID) was developed by the Boeing and Honeywell Corporations for the 777 aircraft called the Aircraft Information Management System (AIMS)<sup>2</sup>. This integrated a number of aircraft functions, previously in separate Line Replaceable Units (LRUs), into a single central computer system including the Central Maintenance Computer (CMC). Boeing Phantomworks is developing the Informed Maintenance and Support System (IMSS) which is a maintenance concept that integrates the vehicle, maintenance scheduling, maintenance technicians, technical data, support equipment and logistics system into a tightly managed support system.

Lockheed-Martin is developing the Joint Distributed Information Systems (JDIS) for the Joint Strike Fighter (JSF)<sup>3</sup>. It includes on-board Mission Systems and Vehicle Maintenance System (VMS) as well as ground based Prognostics Health and Management (PHM). JSF will integrate on-board status with ground based logistics and training databases to optimize vehicle availability. Lockheed-Martin Skunkworks’ Integrated Health Management and Data Advisory Tool (IHMDAT) for X-33 is a ground-based system engineering support tool that provides console operators significant added capability for making Launch Commit Criteria (LCC) and maintenance decisions.

Informed Maintenance for the Space Shuttle has focused on Predictive Health and Reliability Management (PHARM)<sup>4</sup>. This system collects and analyzes sensor data, trend failures, and notifies logistics when a replacement part will be required. For X-34, the NASA IVHM Technology Experiment for X-vehicles (NITEX) was to have monitored main engine parameters throughout all mission phases using detailed diagnostic algorithm to detect degraded component performance as well as a system-level health monitoring system that integrates information from multiple components to perform real-time fault detection, isolation and recovery. In addition, the experiment would have demonstrated the use of an advanced, user friendly ground station that combines information provided by the on-board IVHM software with information obtained while the vehicle was on the ground to provide high-level status information on the health of the vehicle along with the ability to access more detailed information when required.

X-37 IM is being developed by Boeing and NASA<sup>5</sup>. This system will focus on the health summary information provided by the IVHM flight experiment as well as additional information already available in the vehicle’s telemetry stream. It will be included into an overall rapid vehicle turnaround demonstration plan utilizing a wireless work documentation system and a wireless communication system for maintenance personnel.

#### IVHM Software

Livingstone was developed at Ames Research Center. It performs system-wide fault detection and isolation; and it can detect sensor faults and multi-point failures. This software compares values with what they should be according the model and the command stream. When the values do not match the software will signal a fault to find one that matches the data; it also searches the space of possible actions to find a recovery action sequence. This software was used on Deep Space One; it was also applied to X-34, X-37 and ISS. It will also fly on EO-1.

SHINE is a rule-based high speed inference system developed at JPL. This is a reusable knowledge base software tool for the real-time monitoring, diagnosis, prognosis and analysis of complex systems through forward and backward inferencing. This software outperforms most commercial products by at least two orders of magnitude. Some of the benefits of SHINE is that it provides a 100x to 1000x improvement in inference, and up to 10,000x reduction in execution environment. Inferencing speed is achieved from a sophisticated mathematical transformation based on graph-theoretic data flow analysis. This reduces the complexity of the conflict-resolution match cycle by the transforming of the knowledge base into a data flow diagram. The data flow diagram is automatically translated to various target programming languages for efficient representation and execution.

BEAM was also developed at JPL. BEAM monitors a signal and learns the normal behavior of a signal; it flags anything that is out of the norm. It also can be programmed, for instance, to turn on a valve so that the pressure can be at a designated psi. It also knows what pressure should be in the valve at a position, x. BEAM has been used as a monitor to interface with modeled-based reasoners like Livingstone.

TEAMS is a modeled-based reasoner that was developed by QUALTECH Systems based out of Connecticut using NASA SBIR/STTR funding. This software was tested by Ames Research Center. This software only models failure models, and has been applied to X-33.

Data mining is a tool to help analyze data from anomalous conditions and significant features both supervised (examples of faults) and unsupervised (only nominal).

### **ON-GOING IVHM ACTIVITIES**

This research work will be continued throughout the year under the NAFP (NASA Administrators fellowship program). The next step is to integrate the IVHM technologies that were researched during the summer into the MASTLA.

### **ACKNOWLEDGEMENTS**

The author will like to thank and acknowledge Jack Bullman (Manager, Avionics Department), Luis Trevino (Staff, Advance Computing Applications Office; Colleague, NFFP program, and Technical Monitor, NAFP program), NFFP Directors (Michael Freeman (UA), Gerald R. Karr (UAH), Razi Hassan (Alabama A & M), and Jeanelle Bland, Amelia O'Neal, Karen E. Grant (Flight Software Group, Mainthia Technology), and LD Wallace (BD Systems).

---

<sup>1</sup> Product Descriptions, Automotive Diagnostics, [www.marketplace.com/descr.htm](http://www.marketplace.com/descr.htm), July 2000.

<sup>2</sup> Smith, R. and Murray, F., "Open Systems Approach to Integrated Diagnostics Demonstration Study Program, Case Study Report, Boeing 777," ARINC Inc, September 1998.

<sup>3</sup> Joint Strike Fighter Intelligent Vehicle and Information Systems Integrated Product Teams Overview, [www.jast.mil/html/header\\_infosys.htm](http://www.jast.mil/html/header_infosys.htm), July 2000.

<sup>4</sup> Parker, J., "Predictive Health and Reliability Management (PHARM) Project Plan," Kennedy Space Center, February 2000.

<sup>5</sup> Green, S., "Informed Maintenance Support System," presented at X-37 Informed Maintenance planning meeting, May 2000, Boeing St. Louis, Kennedy Space Center.

2004

**NASA FACULTY FELLOWSHIP PROGRAM**

**MARSHALL SPACE FLIGHT CENTER**

**THE UNIVERSITY OF ALABAMA  
THE UNIVERSITY OF ALABAMA IN HUNTSVILLE  
ALABAMA A&M UNIVERSITY**

**CFD Multiphysics Tool**

Prepared By:	Dr. Eric R. Perrell
Academic Rank:	Assistant Professor
Institution and Department:	Embry-Riddle Aeronautical University Department of Aerospace Engineering
NASA/MSFC Directorate:	Space Transportation
MSFC Colleague:	Robert B. Adams

## **Introduction**

The recent bold initiatives to expand the human presence in space require innovative approaches to the design of propulsion systems whose underlying *technology* is not yet mature. The space propulsion community has identified a number of candidate concepts. A short list includes solar sails, high-energy-density chemical propellants, electric and electromagnetic accelerators, solar-thermal and nuclear-thermal expanders. For each of these, the underlying *physics* are relatively well understood. One could easily cite authoritative texts, addressing both the governing equations, and practical solution methods for, e.g. electromagnetic fields, heat transfer, radiation, thermophysics, structural dynamics, particulate kinematics, nuclear energy, power conversion, and fluid dynamics. One could also easily cite scholarly works in which “complete” equation sets for any *one* of these physical processes have been accurately solved relative to complex engineered systems.

The Advanced Concepts and Analysis Office (ACAO), Space Transportation Directorate, NASA Marshall Space Flight Center, has recently released the first alpha version of a set of computer utilities for performing the applicable physical analyses relative to candidate deep-space propulsion systems such as those listed above. PARSEC, Preliminary Analysis of Revolutionary in-Space Engineering Concepts, enables rapid iterative calculations using several physics tools developed in-house. A complete cycle of the entire tool set takes about twenty minutes.

PARSEC is a level-zero/level-one design tool. For PARSEC’s proof-of-concept, and preliminary design decision-making, assumptions that significantly simplify the governing equation sets are necessary. To proceed to level-two, one wishes to retain modeling of the underlying physics as close as practical to known *applicable* first principles. This report describes results of collaboration between ACAO, and Embry-Riddle Aeronautical University (ERAU), to begin building a set of level-two design tools for PARSEC. The “CFD Multiphysics Tool” will be the propulsive element of the tool set. The name acknowledges that space propulsion performance assessment is primarily a fluid mechanics problem. At the core of the CFD Multiphysics Tool is an open-source CFD code, HYP, under development at ERAU.

ERAU is renowned for its undergraduate degree program in Aerospace Engineering – the largest in the nation. The strength of the program is its applications-oriented curriculum, which culminates in one of three two-course Engineering Design sequences: Aerospace Propulsion, Spacecraft, or Aircraft. This same philosophy applies to the HYP Project, albeit with fluid physics modeling commensurate with graduate research. HYP’s purpose, like the Multiphysics Tool’s, is to enable calculations of real (three-dimensional; geometrically complex; intended for hardware development) applications of high speed and propulsive fluid flows.

## **Grid Generation**

Resident grid generation capability is a goal of the CFD Multiphysics Tool Project. A number of rudimentary code fragments previously written by the author were assembled into a baseline grid generator. The tool is described in some detail, and a tutorial is presented, in reference [1]. A brief summary is given here.

The user specifies, through namelist input: the overall dimensions in each coordinate direction; the coordinates of the eight corner points of a structured hexahedral blocking topology; the types of segments defining the edges of the block. Currently these types are limited to line segments and circular arcs, each with options for equal grid spacing, or clustering via geometric progressions, for resolution of boundary, free shear, or mixing layers, for example.

The tool employs linear trans-finite interpolation for the surface mesh fill-in on each of the six block sides. There is also an elliptical smoothing option. Similarly, the volume mesh is initially filled with 3-D linear TFI, and a 3-D elliptic smoothing option exists.

A present limitation is that the surface mesh utilities do not have the ability to constrain the mesh to a general geometry. That is, whereas surfaces are *topologically* two-dimensional, they are *geometrically* three-dimensional in general. At present, contoured surfaces cannot be reliably captured without hardwiring the code to do so. For example, in one trial, the outer surface mesh for a converging/diverging rocket combustor and nozzle configuration was generated by hardwiring the code to rotate the block edge contour about the centerline - this in lieu of the usual TFI procedure.

### **General Description of the CFD Code**

More detailed descriptions of the governing equations solved by the code are given in references [3] and [4]. HYP solves the conservation law equations in general coordinates, for a set of conserved variables specified by the user. The fundamental governing equation is

$$\frac{\partial \bar{Q}}{\partial t} + \frac{\partial \bar{E}'}{\partial \xi} + \frac{\partial \bar{F}'}{\partial \eta} + \frac{\partial \bar{G}'}{\partial \zeta} = \bar{W} \quad (1)$$

where  $\bar{Q}$  denotes the vector of conserved variables,  $\bar{E}'$ ,  $\bar{F}'$ ,  $\bar{G}'$  denote the fluxes of conserved variables in the coordinate directions  $\xi, \eta, \zeta$  respectively, and  $\bar{W}$  is the vector of source terms. In a relatively simple calculation, the conserved variables might be a number of chemical species mass densities, three momentum components, and total energy.

$$\bar{Q} = [\rho_1 \quad \dots \quad \rho_{ns} \quad \rho u \quad \rho v \quad \rho w \quad E_T]^T \quad (2)$$

$$E_T = \sum_{s=1}^{ns} \rho_s \left( h_s(T) + h_{s_0}^f - \frac{R_u}{M_s} T \right) + \rho \frac{u^2 + v^2 + w^2}{2} \quad (3)$$

The code uses a finite volume formulation. Mathematically, this means that the spatial derivatives are evaluated according to the divergence theorem. Physically, this approach can be thought of as simple accounting for the conserved variables comprising the  $\bar{Q}$  vector: mass, momentum, and energy. The flow field is divided into a computational mesh, with a number of small hexahedral “cells.” The rate of change of the  $\bar{Q}$  variables within each cell (the leading term in equation (1)) is equal to the rates at which quantities flow in, minus the rate at which they flow out. This difference is the divergence of the fluxes. The source vector  $\bar{W}$  contains terms for the rate of production of the conserved variables within the cell.

## **Electromagnetic Field Modeling**

This involves addition of the magnetic induction equation to the set of conservation equations. The magnetic induction equation is derived from Maxwell's electromagnetic field equations. It adds the three components of a "magnetic flux" to the conserved variables. The wave speeds of the equation set thus extended now include the convective velocity as before, plus two Alfven waves, four magneto-acoustic waves, and one magnetic flux wave [5]. Deriving these wave speeds and the associated flux magnitudes was a primary task of this research. Progress to date is reported in reference[2].

## **Internal Energy Modeling**

The default method of treating the molecular internal energies is according to the equilibrium assumption. That is, one temperature characterizes all of the internal energy states – vibrational, rotational, and electrical. In this case, the internal energy is given by the summation in equation (3).

The specific enthalpies  $h_s(T)$  are calculated as cubic splines, fit to the values in the JANAF Thermochemical Tables in increments of 100 K.

For calculations of high speed flows, HYP has an option to treat molecular vibrational energy independently of the molecular translational energy. We say that the gas is in "vibrational non-equilibrium," meaning that the gas translational and vibrational energies are characterized by two different temperatures. The vibrational energy is

$$E_{vib} = R_u \sum_{s=1}^{ns} \frac{\rho_s}{M_s} \sum_{m=1}^{nm} \frac{g_{sm} \theta_{vsm}}{\exp\left(\frac{\theta_{vsm}}{T_{vib}}\right) - 1} \quad (4)$$

Under construction are options for rotational and electron/electronic non-equilibrium. These energies are

$$E_{rot} = R_u T_{rot} \sum_{s=1}^{ns} \frac{\rho_s}{M_s} \frac{r m_s}{2} \quad (5)$$

$$E_{elec} = R_u \sum_{s=1}^{ns} \frac{\rho_s}{M_s} \theta_{elec,s} \frac{\frac{g_{1,s}}{g_{0,s}} \exp\left(\frac{-\theta_{elec,s}}{T_{elec}}\right)}{1 + \frac{g_{1,s}}{g_{0,s}} \exp\left(\frac{-\theta_{elec,s}}{T_{elec}}\right)} + \frac{3}{2} \rho_e \frac{R_u}{M_e} T_{elec} + \rho_e e_k \quad (6)$$

The summation term in equation (7) is the energy of the electron cloud – the ground and first excited states only - surrounding the molecular nuclei. The last two terms are the free electron translational, and kinetic energies, respectively. Considering Hatfield's findings [1], we adopt the

practice of holding the free and bound electrons in equilibrium (at the same temperature), rather than conserving their energies independently.

## **Conclusions**

A CFD code for aerospace propulsion applications under development at Embry-Riddle Aeronautical University, is being adapted for use by the Advanced Concepts and Analysis Office, as the core of the CFD Multiphysics Tool, the propulsive element of a level-two iterative design software package intended for analyzing deep space propulsion concepts. The entire level-two tool set will be incorporated into PARSEC, the recently operational package of level-zero and level-one tools.

## **Future Work**

The continuation of this project during summer 2005 is anticipated. Much of the basic code modification for an MPD Thruster application is being pursued as a Master's thesis project under the author's supervision. A completion date in December 2004 is expected. Discussions are ongoing about possible funding of additional Master's thesis projects, and Graduate Student Research Program (GSRP) topics, related to the Multiphysics Tool. A proposal for advanced MPD computational work and experimental benchmarking in collaboration with UAH and ACAO is in preparation, in response to the recent Human and Robotic Technology Broad Agency Announcement.

## **Acknowledgments**

I am grateful to the following participants in this project: Robert B. Adams, NFFP Colleague, ACAO; Caroline C. Liron, graduate research assistant, ERAU; Jason Cassibry, Research Scientist, University of Alabama Huntsville; John A. Hatfield, Research Engineer, ISSI.

## **References**

- [1] Hatfield, J.A., "Modeling Thermo-Chemical Nonequilibrium Effects in an Ionized Nitrogen Shock Tube Flow," Ph.D. Thesis, North Carolina State University, Raleigh, NC, 1995.
- [2] Liron, C.C., "*Developing a Multi-Physics Tool for In-Space Propulsion Systems - Application of Numerical Methods and Computational Fluid Dynamics*," Final Co-op Report to The Graduate School, Embry-Riddle Aeronautical University, Daytona Beach, FL, August 2004.
- [3] Perrell, E.R., "Computation of Combustion Heated Hypersonic Wind Tunnel Flows in Phase Nonequilibrium," Ph.D. Thesis, North Carolina State University, Raleigh, NC, 1995.
- [4] Perrell, E.R., Erickson, W.D., Candler, G.V., "Numerical Simulation of Nonequilibrium Condensation in a Hypersonic Wind Tunnel," *Journal of Thermophysics and Heat Transfer*, Vol. 10, No. 2, April-June, 1996, pp. 277-283.
- [5] Powell, K.G., Roe, P.L., Myong, R.S., Gombosi, T., and De Zeeuw, D., "An upwind Scheme for Magnetohydrodynamics," *AIAA paper No. 95-1704*, 1995.

**2004**

**NASA FACULTY FELLOWSHIP PROGRAM**

**MARSHALL SPACE FLIGHT CENTER**

**THE UNIVERSITY OF ALABAMA  
THE UNIVERSITY OF ALABAMA IN HUNTSVILLE  
ALABAMA A&M UNIVERSITY**

**ON STRUCTURAL DESIGN OF A MOBILE LUNAR  
HABITAT WITH MULTI-LAYERED ENVIRONMENTAL  
SHIELDING**

Prepared By:	Masoud Rais-Rohani
Academic Rank:	Professor
Institution and Department:	Mississippi State University Department of Aerospace Engineering
NASA/MSFC Directorate:	Flight Projects
MSFC Colleague:	David V. Smitherman, Jr.

## **Introduction**

The future human lunar missions are expected to undertake far more ambitious activities than those of the Apollo program with the possibility of some missions lasting up to several months. Such extended missions require the use of large-size lunar outposts to accommodate living quarters for the astronauts as well as indoor laboratory facilities.

The greatest obstacle to the prolonged human presence on the Moon is the threat posed by the harsh lunar environment that is plagued with multi-source high-energy radiation exposure as well as frequent barrage of meteoroids. Hence, for such extended missions to succeed, it is vital that the future lunar outposts be designed to provide a safe habitat for the astronauts.

Over the past few years, a variety of ideas and concepts for future lunar outposts and bases have been proposed. With shielding as the primary concern, some have suggested the use of natural structures such as lava tubes while others have taken a more industrial approach and suggested the construction of fixed structures in the form of inflatable, inflatable with rigid elements, and tent-style membrane. For evaluation of these structural design concepts, Drake and Richter<sup>1</sup> have proposed a rating system based on such factors as effectiveness, importance, and timing. While all of these designs, in general, benefit from in-situ resource utilization (i.e., lunar regolith) for shielding, they share a common disadvantage of being fixed to one particular location that would limit exploration to the region in close proximity of the outpost.

As an alternative to the fixed-base concepts, some have suggested mobile lunar outposts (reminiscing of recreational vehicles). While providing a self-contained habitat, such mobile units can offer the future lunar explorers and workers the freedom to travel from one location to another, and to enhance the exploration and scientific activities on the Moon. At the forefront of such concepts is the notional architecture of HARMONY (Human And Robotic MODular iNfrastructures/sYstems) proposed by Mankins.<sup>2</sup> As part of his HARMONY architecture, Mankins suggests the use of Modular Integrated Lunar Outpost (MILO) with each module representing a blend of habitat and robotics design referred to as a “Hab-Bot”. The idea is to launch these Hab-Bots, ahead of astronauts, to a desired spot on the Moon. Operating in the autonomous or remotely operated control mode, these modules will link up together to form a larger integrated outpost. As a mission comes to an end and the crew has departed, these modules will walk to another location and establish a new outpost prior to the arrival of the next group of astronauts and space workers.

While mobility and integration of multiple units are the main advantages of the Hab-Bot design, the greatest drawback to this and all other proposed concepts is the need for the habitat wall to provide the necessary environmental shielding. This requirement poses a serious challenge to the design of the structure, and demands the use of innovative solutions.

As part of this research, a Hab-Bot inspired concept for a Mobile Lunar Habitat (MLH) is proposed, which makes use of advanced composite materials to reduce the habitat’s mass and to seek a viable solution to the shielding problem. A modular design is presented for environmental shielding. In addition, a finite-element model of MLH design is developed and analyzed under an operational loading condition.

## **Environmental Considerations**

### **Radiation Shielding**

Unlike the Earth's surface that is protected by a relatively dense atmosphere and the geomagnetic field, the lunar surface is completely deprived of any natural shielding against harmful space radiation. The ambient radiation environment of the lunar surface consists of energetic ionized particles of solar and galactic origins.<sup>3</sup>

The Solar Energetic Particles (SEP) are released from the Sun through sporadic flare events, which are correlated with the periods of increased solar activity. They mostly consist of hydrogen and helium ions (protons and alpha particles) with a much smaller, but biologically more damaging, heavy-ion component (atomic number,  $Z > 2$ ) that can vary from one event to another.

The most energetic form of radiation in free-space as well as on the lunar surface is that associated with the nearly constant Galactic Cosmic Rays (GCR). Reaching energies of 10 GeV, GCR particles travel at nearly the speed of light through the very thin gas of interstellar space. By some estimates, the GCR spectrum consists of approximately 90% hydrogen, 9% helium, and 1% heavier nuclei such as iron (Fe,  $Z = 26$ ) and nickel (Ni,  $Z = 28$ ).<sup>4</sup>

Without any shielding, an astronaut in free space would receive a blood-forming-organ (BFO) dose-equivalent of 0.6 Sv/yr from GCR at solar minimum conditions. This amount is greater than NCRP's limit of 0.5 Sv/yr.<sup>5</sup> For a large solar flare event such as that of August 1972, the free-space BFO dose is estimated at 4.11 Sv (in a span of few days) as compared to NCRP's limit of 0.25 Sv for a 30-day exposure.

Because of its smallest atomic weight and lack of neutrons in its nucleus, liquid hydrogen is considered as the best radiation shielding material. However, hydrogen-rich polyethylene has been studied as a more practical shielding material, and that is the material considered for shielding the MLH against harmful radiation at a linear thickness of approximately 10 cm.

### **Meteoroid Impact Shielding**

The meteoroid environment near earth and the Moon consists mainly of ice particles of cometary sources. Meteoroids are classified into periodic streams (nearly identical orbits to the source comet) and sporadic (random orbits). The sporadic meteoroids can hit the lunar surface from different trajectories relative to the ecliptic plane. In the interplanetary space, the meteoroids travel at speeds between 11.1 to 72.2 km/s.<sup>6</sup> With the average mass density of 0.5 g/cm<sup>3</sup> and mean speed of approximately 30 km/s, meteoroids and micrometeoroids pose a serious threat to the MLH and the crew working on the lunar surface. At such high velocities, meteoroids can easily penetrate the habitat's wall if it is not adequately designed. Hence, shielding against meteoroid impacts is a major design requirement.

Ground-based projectile testing facilities have been able to shoot meteoroid-size projectiles at speeds reaching no higher than 11 km/s. Therefore, there is significant uncertainty about shield

performance at impact speeds beyond 11 km/s, as the shield performance predictions obtained from various hydrodynamic codes cannot be experimentally verified.

More advanced meteoroid shielding designs incorporate a double or multiple-wall configuration.<sup>7</sup> Once a meteoroid crashes into the front wall, it will melt and vaporize. If the front wall is penetrated, then a cloud of hot gas and debris from the front wall is generated. The objective of the rear wall is to stop this high-energy debris cloud from damaging or penetrating the pressure wall of the habitat.

Previous research involving hypervelocity impact testing of composite shielding shows that neither the number of plies in the laminate nor the impact angle has any significant influence on the diameter of the entry crater in the front wall. However, the Nextel layer is shown to be very effective in stopping the debris fragments coming from the front wall, and that its effectiveness increases as it is moved farther behind the front shield.<sup>8</sup>

In design of MLH, a modular meteoroid-impact-shielding (MIS) configuration is used; its front wall is made of Kevlar-reinforced polymer-matrix composite, and its rear wall—at approximately 10 cm away—is made of two tightly woven blankets of Nextel (primary layer) and Kevlar that are stitched together to enhance the rear wall’s penetration resistance. The MIS is covered on the inside by multi-layer insulation. A more detailed computational analysis is necessary to determine the exact thickness of individual MIS layers as well as the wall spacing.

### **Conceptual Design of MLH**

The proposed design for MLH, as shown in Fig. 1 (b), is derived from the ISS US Lab module with a diameter (pressure vessel only) of 4.22 m (166 in) and length of 8.66 m (341 in). For greater mobility over the lunar terrain, MLH is equipped with six independently controlled mechanical legs. The overall size of MLH is constrained by the interior dimensions and clearances of the single-manifest payload fairing of the Delta IV family of rockets. One of many possible options for an expanded lunar outpost is shown in Fig. 1(a). A closer view of the modular MIS design is shown in Fig. 1(c).

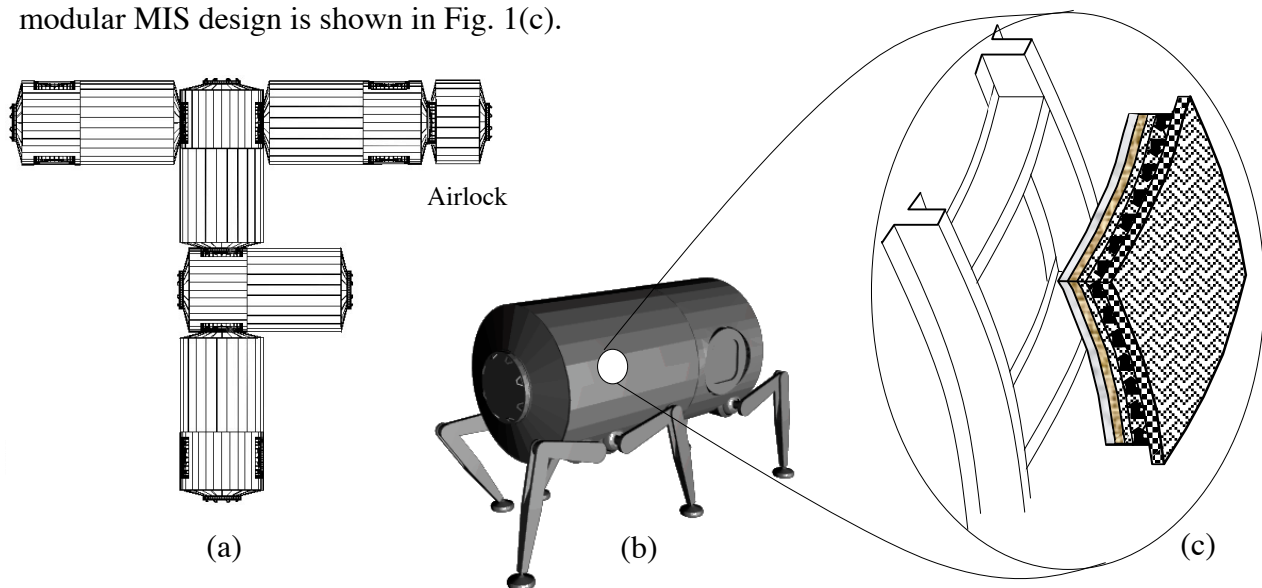


Figure 1: (a) Multi-unit lunar outpost, (b) MLH module, (c) MIS panel

## **Finite-Element Structural Analysis**

Space structures encounter severe vibration and dynamic loads during launch and the initial flight phase. In most instances, these transient mechanical loads are more critical than the operational loads. However, in the absence of launch-specific loads data at this time, the internal pressure of 14.7 psi, as a representative operational loading condition, was used for the preliminary structural analysis.

The FE model, as shown in Fig. 2, was obtained by modifying a previously developed model of ISS US-Lab module. The major modification task involved the extension of its length and addition of two lateral ports. The design geometry of the lateral ports was taken from the ISS Node 1 model. The new model has a diameter of 4.5 m and a length of 9.3 m.

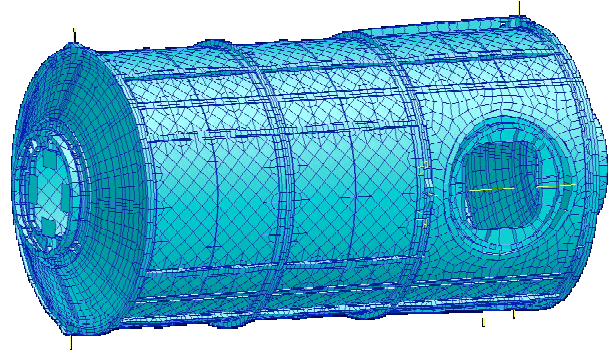


Figure 2: FE model of the MLH structure.

As a baseline design, the model (without the lateral ports) was analyzed for strain energy using 2024-T3 aluminum properties and the specified loading condition. The material in the cylinder portion of the habitat was then changed to AS4-3502 carbon-epoxy with quasi-isotropic properties, and the wall thickness was adjusted until the strain energy nearly matched (< 1% diff.) that of the baseline design. Having nearly the same structural stiffness, the hybrid model was found to weigh 16,435 lb, 2.4% lighter than its aluminum counterpart.

## **Acknowledgments**

The author wishes to thank David Smitherman and Joe Howell of Advanced Projects Office (FD02) for their sponsorship of this research activity through NFFP. A special gratitude goes to Scott Taylor of Morgan Research Corp. for his development of the FE model based on separate models of US Lab module and Node 1 courtesy of the Boeing Co.

## **References**

1. Drake, R.M. and Richter, P.J., "Concept Evaluation Methodology for Extraterrestrial Habitats," *Journal of Aerospace Engineering*, Vol. 5, No. 3, July 1992.
2. Mankins, J., "Modular Architecture Options for Lunar Exploration and Development," *Space Technology*, Vol. 21, No. 1-2, pp. 53-64, 2001.
3. Simonson, L.C. and Nealy, J.E., "Radiation Protection for Human Missions to the Moon and Mars," NASA TP-3079, 1991.
4. Wilson, J.W., Cucinotta, F.A., Miller, J., Shinn, J.L., Thiebaeault, S.A., Singleterry, R.C., Simonson, L.C., and Kim, M.H., "Materials for Shielding Astronauts from the Hazards of Space Radiations," *Material Research Society Fall Meeting*, Boston, MA, Nov. 30 – Dec. 4, 1998.
5. National Council on Radiation Protection and Measurements, "Guidance on Radiation Received in Space Activities," NCRP Report No. 98, July 31, 1989.
6. Anderson, J. and Smith, R.E., "Natural Orbital Environment Guidelines for Use in Aerospace Vehicle Development," NASA TM-4527, 1994.
7. Hayashida, K.B. and Robinson, J.H., "Double-Plate Penetration Equations," NASA TM-2000-209907, 2000.
8. Lamontage, C.G., "Hypervelocity Impact Damage to Polymer Matrix Composite Structures in Space," Ph.D. Thesis, Department of Aerospace Science and Engineering, University of Toronto, 2003.

2004

**NASA FACULTY FELLOWSHIP PROGRAM**

**MARSHALL SPACE FLIGHT CENTER  
THE UNIVERSITY OF ALABAMA  
THE UNIVERSITY OF ALABAMA IN HUNTSVILLE  
ALABAMA A&M UNIVERSITY**

**ANALYSIS OF PIEZOELECTRIC STRUCTURAL SENSORS  
WITH EMERGENT COMPUTING TECHNIQUES**

Prepared By:	Douglas L. Ramers
Academic Rank:	Assistant Professor
Institution and Department:	UNC Charlotte Department of Engineering Technology, College of Engineering
NASA/MSFC Directorate:	ED10
MSFC Colleague:	Luis Trevino

## **Introduction**

The purpose of this project was to try to interpret the results of some tests that were performed earlier this year and to demonstrate a possible use of emergence in computing to solve IVHM problems. The test data used was collected with piezoelectric sensors to detect mechanical changes in structures. This project team was included of Dr. Doug Ramers and Dr. Abdul Jallob of the Summer Faculty Fellowship Program, Arnaldo Colon-Lopez - a student intern from the University of Puerto Rico of Turabo, and John Lassister and Bob Engberg of the Structural and Dynamics Test Group. The tests were performed by Bob Engberg to compare the performance two types of piezoelectric (piezo) sensors,  $\text{Pb}(\text{Zr}_{1-x}\text{Ti}_x)\text{O}_3$ , which we will label PZT, and  $\text{Pb}(\text{Zn}_{1/3}\text{Nb}_{2/3})\text{O}_3\text{-PbTiO}_3$ , which we will label SCP. The tests were conducted under varying temperature and pressure conditions. One set of tests was done by varying water pressure inside an aluminum liner covered with carbon-fiber composite layers (a cylindrical "bottle" with domed ends) and the other by varying temperatures down to cryogenic levels on some specially prepared composite panels. This report discusses the data from the pressure study. The study of the temperature results was not completed in time for this report.

The particular sensing done with these piezo sensors is accomplished by the sensor generating an controlled vibration that is transmitted into the structure to which the sensor is attached, and the same sensor then responding to the induced vibration of the structure. There is a relationship between the mechanical impedance of the structure and the resulting electrical impedance produced in the in the piezo sensor. The impedance is also a function of the excitation frequency. Changes in the real part of impedance signature relative to an original reference signature indicate a change in the coupled structure that could be the results of damage or strain.

The water pressure tests were conducted by pressurizing the bottle on a test stand, and running sweeps of excitations frequencies for each of the piezo sensors and recording the resulting impedance. The sweeps were limited to 401 points by the available analyzer, and it was decided to perform individual sweeps at five different excitation frequency ranges. The frequency ranges used for the PZTs were different in two of the five ranges from the ranges used for the SCP. The bottles were pressurized to empty (no water), 0psig, 77 psig, 155 psig, 227 psig in nearly uniform increments of about 77psi. One of each of the two types of piezo sensors was fastened on to the bottle surface at two locations: about midway between the ends on cylindrical portion of the bottle and at the very edge of one of the end domes. The data was collected in files by sensor type (2 cases), by location (2 cases), by frequency range (5 cases), and pressure (5cases) to produce 100 data sets of 401 impedances.

After familiarization with the piezo sensing technology and obtaining the data, the team developed a set of questions to try to answer regarding the data and made assignments of responsibilities. The next section lists the questions, and the remainder of the report describes the data analysis work performed by Dr. Ramers. This includes a discussion of the data, the approach to answering the question using statistical techniques, the use of an emergent system to investigate the data where statistical techniques were not usable, conclusions regarding the data, and recommendations.

## **Project Questions to Answer**

The questions and summary answers are listed below. The first four questions (in bold) were assigned to Dr. Ramers to investigate. Time did not permit the direct analysis of the data for question 4b. However, approaches to this task already exist that are based on monitoring changes in the imaginary part of the impedance. One technique was discussed in the course presented at MSFC by Los Alamos Dynamics [1], a company specializing in structural dynamics and mechanical vibration consulting.

- 1) Is there a significant difference in the information provided between the PZT and SCP sensors with the given tests?**

*Yes, the SCP type sensor appears to be more sensitive and a better discriminator of pressures, but additional testing is needed.*

- 2) Which bands are needed to characterize the PZT and SCP signal?**

*The results correspond to the literature. The higher frequencies are better. For the better SCP, the 180 – 190kHz frequency band was the best at discriminating between the test pressures.*

- 3) Is there an adequate parsimonious characterization of the piezo signal?**

*The nonparametric metrics, which reduce a set of impedances comparisons to a single number, are parsimonious. The readings of  $Re(Z)$  at 30-50 contiguous excitation frequencies provided good results. A granularity of 400 Hz between frequencies was sufficient for the SCP sensor in the 180 – 190 kHz range to provide good discrimination between the test pressures.*

- 4a) What are metrics that can be used for detecting change in the PZT signal indicating strain?**

*Of the four metrics tested [2], the Root Mean Square Deviation and the Mean Absolute Percentage Difference performed well and were better than the two covariance based metrics at discriminating between the test pressures.*

- b) What are methods and metrics that can be used to determine if the PZT is operating correctly? – SEE REFERENCE ABOVE FOR KNOWN METHOD**

- 5) What are the appropriate procedures for attaching PZTs to structures and attaching leads to PZTs?**

- a) How does surface area contact affect sensitivity of signal?
- b) How does quality and type of bond have an effect on the nature of the signals?
- c) Does gradual degradation (or changes) in the bonding material have an effect on the nature of the signal?

- 6) In general, how do we size the sensor (length, width, thickness)?**

## Discussion of the Data for the Composite Bottle

Because impedance is a function of frequency, each set of five sweeps over the different frequency ranges really constitute one sample. Each of four experiments was conducted with a location-sensor type combination for which one sample was taken at each of the five pressure levels. One trace (all five frequency ranges) at each level is one sample (see Figure1 for example). Table 1 below summarizes the experiments. A consequence of the lack of multiple samples is that statistical techniques may not be used to answer several of the questions.

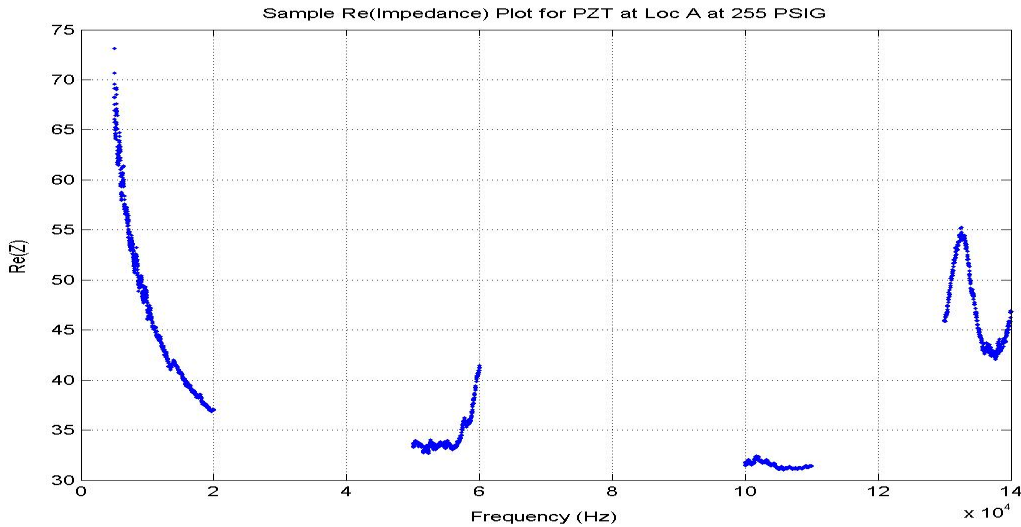


Figure 1 PZT Re(Z) at Location A (Center) Sample

Sensor	Location	<u>Number of Samples</u>				
		Empty	Pressure Level			
			0psig	77psi	155psig	227psig
Pzt	A	1	1	1	1	1
Scp	A	1	1	1	1	1
Pzt	B	1	1	1	1	1
Scp	B	1	1	1	1	1

Sample Frequency Sweeps (kHz):  
401 points ea. Range

<u>Pzt</u>	<u>Scp</u>
5-10	50-60
10-20	100-110
50-60	130-140
100-110	180-200
130-140	250-250

Table 1 Summary of Experiments and Samples

However, some interpretations of the data can be made through qualitative examination of the data and through use a factor analysis for experiments with one trial at each level. Analysis

experiments were also conducted using evolutionary programming techniques that provided answers as reasonable heuristics for this particular set of data. Qualitative analysis of the data and the factor analysis are discussed in the next section and the evolutionary computing analysis is discussed in the section after.

**Qualitative and Factor Analysis of Available Data**

**Which bands are needed to characterize the sensor signal?**

This essentially questions which frequency ranges provide more discriminatory power. The literature, and the model relating impedance to frequency, suggests higher frequencies more sensitive [3]. Each line in each plot in Figure 2 is the real part of the impedance at a pressure level. The plots seem to indicate, in accord with the literature, that the higher frequency result in more distinct separation of pressure related signals.

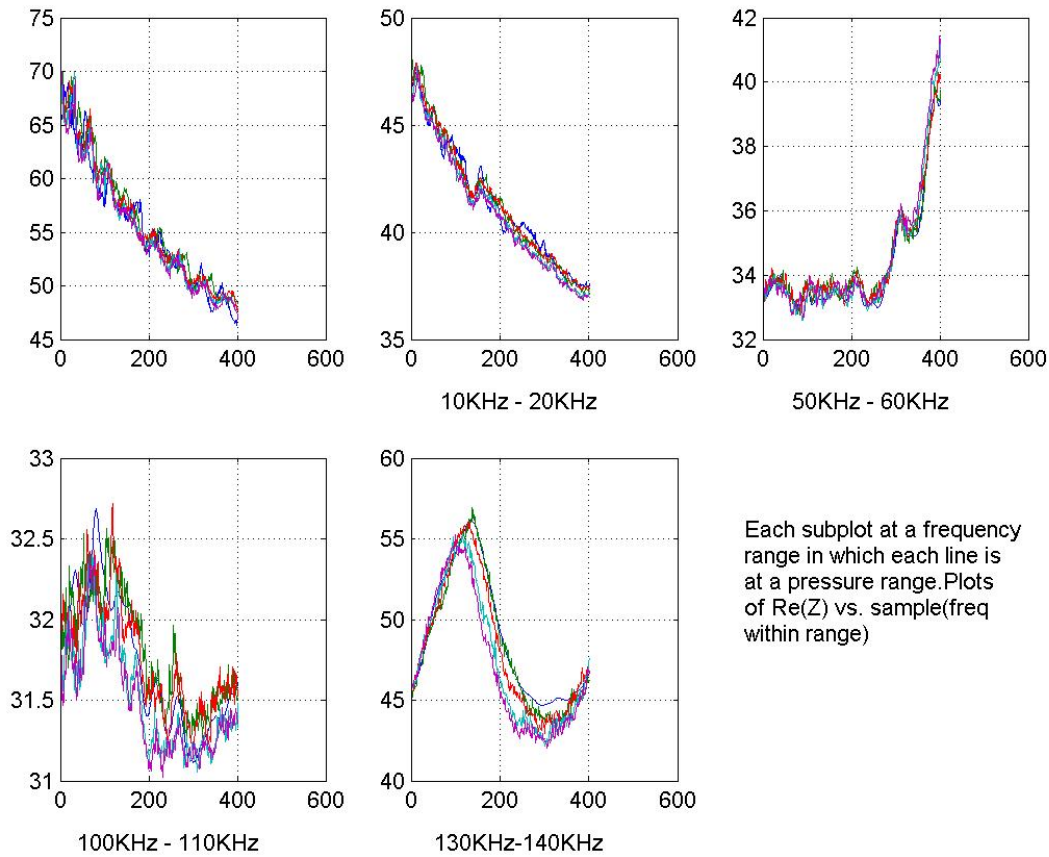


Figure 2 Subplots by Frequency Range for a PZT Type

To help verify this, an analysis of variance test was conducted to see if the mean impedance for each pressure level were the same in each band. If they were, then the band did not discriminate pressures well. However, this statistical test is not valid, because the mean impedance is

calculated using the impedance for each frequency in the band, but the impedance is a function of frequency so the observations are not independent samples. Regardless, the ANOVA indicated that if the samples had been independent, the higher frequency bands were better discriminators, particularly bands 4 (110-110kHz) and band 5 (130-140 kHz) for the PZT.

**Is there a significant difference in the information provided between the PZT and SCP sensors with the given tests?**

A factor analysis using the Root Mean Square Difference (RMSD) metric was used for this analysis. The RMSD metric is calculated as the sum of the squares of the difference between a trace of interest (e.g., at a specific pressure) and a reference trace. The appropriate state for the reference trace the Re(Z) of the bottle filled with water at 0 psig. The Re(Z) for the empty bottles was not used as a reference because the bottle is a different structure with and without water. The mechanical properties that influence mechanical impedance are significantly different for a full or an empty bottle. The metric reflects the change in electromechanical impedance in the sensor, which should be related to the change in mechanical impedance of the structure to which the sensor is attached. The RMSD was calculated for the full 802 frequencies in bands 4 and 5 to get a qualitative indication and order of magnitude of the metric value. The Re(Z) for bands 4 and 5 were chosen because they appear to discriminate between the pressures more than the lower frequency bands do, and measurements were made in the these ranges for both the PZT and SCP type sensors. The results are shown in Table 3. Comparative traces for bands 4 and 5 are shown in Figures 3 and 4.

RMSD Bands 4&5 Sensor	RMSD for		
	(77-0)psig	(155-0)psig	(227-0)psig
PZT at Location A	1.3991	3.0605	4.0084
SCP at Location A	3.7697	6.5325	8.4372
PZT at Location B	2.4018	15.3351	<b>85.74</b>
SCP at Location B	4.5771	12.2303	11.6556

Table 3 RMSD for Bands 4 and 5.

The RMSD metric appears to indicate that the SCP type sensor is more sensitive. For Location A, the RMSD range for the SCP sensor is 4.667 over 155 psi range while it is only 2.6093 over the 155 psi range for the PZT sensor. At location B, that last metric value for the PZT, 85.74, seems inconsistent and may indicate a problem with that sensor. The readings for the SCP sensor at location B appear to be consistent. Examining the traces in figures 3 and 4, we can see that the impedances are lower and relatively flat for the PZT at location B and compared to the corresponding PZT traces for A. The impedances for the lower pressures are also very much lower, and except for the 227 psi trace. Since RMSD is a difference, and the reference was much lower, I suspect a problem with the data from the PZT at location B.

Comparison Pzt and Scp for sweep bands 4 and 5 for all pressures for sensors at location A

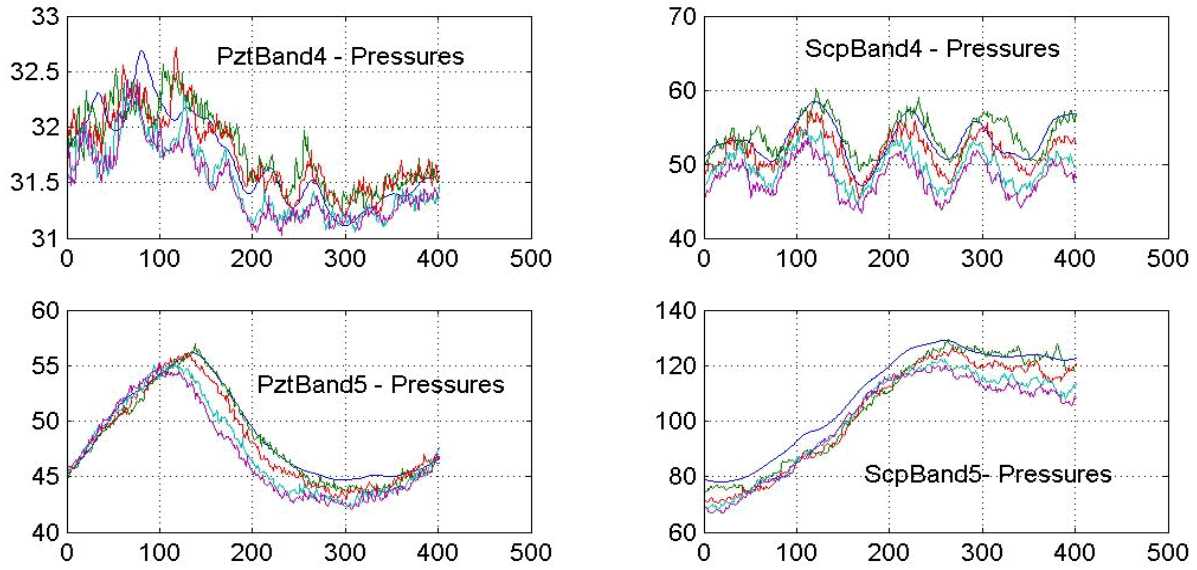


Figure 3 Traces for Location A- Band 4&5

Comparison Pzt and Scp for sweep bands 4 and 5 for all pressures for sensors at location B

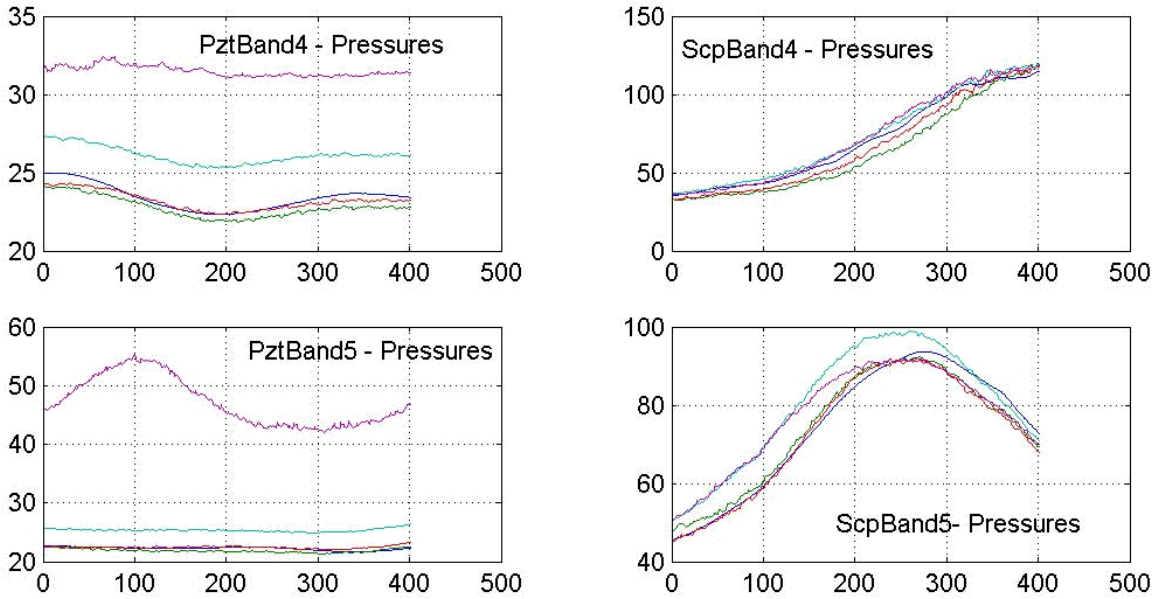


Figure 4 Traces for Location B - Band 4&5

A factor analysis of the above results indicates the same conclusions. The factor plots (Figure 5) comparing the sensors by location show a possible problem at location B. The large increase for the PZT for the high pressure might indicate a problem. Even for the SCP sensor at location B, the increase in RMSD with pressure is not monotonic as it is at location A (see figure 6), indicating a possible problem with the sensor or leads for the SCP at B also. Regardless, these behaviors would not be as desirable for use of these sensors for condition monitoring at location B as the conditions present at location A.

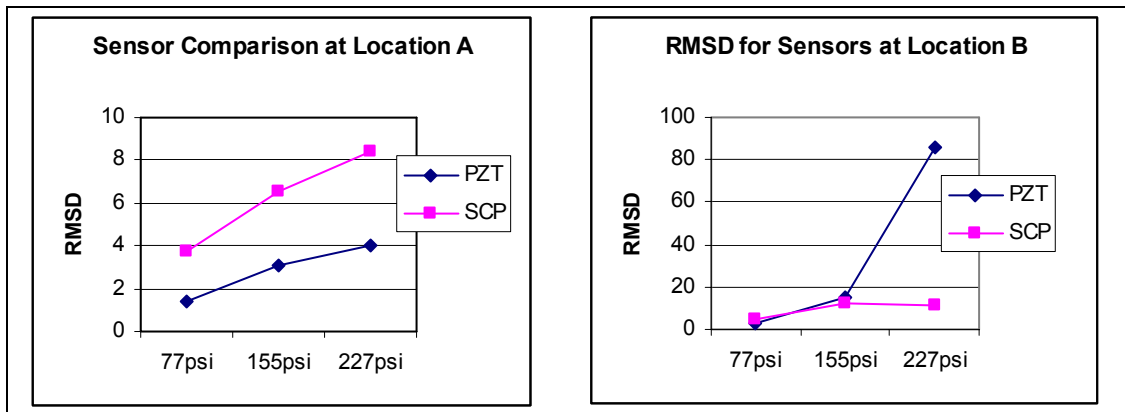


Figure 5 Factor analysis plots for location sensors for pressure levels by sensor

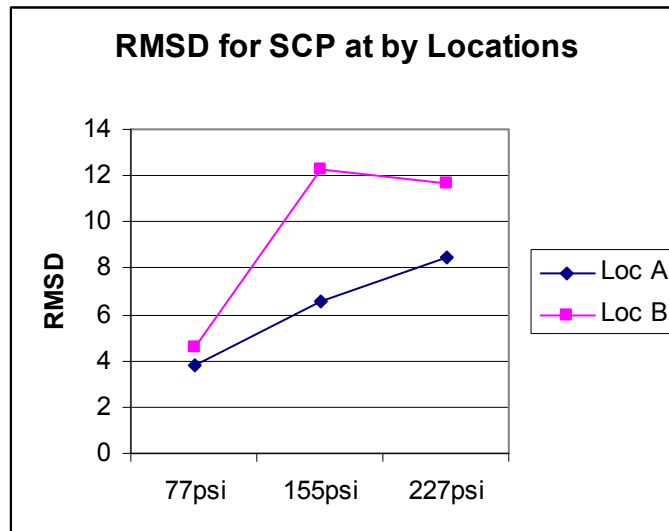


Figure 6 Factor analysis plots for SCP sensor for pressure levels by location

Overall, we could draw no strong conclusions about the sensors or locations. It appears, as expected, that higher frequencies are better. The sensors at location A, though they show more noise, seem to be more consistent. SCP appears to be more sensitive than the PZT. To reinforce the qualitative conclusions made we applied artificial intelligence techniques that facilitate emergence of solutions. The techniques of evolutionary computing and fuzzy logic are useful in situations where there is insufficient data, little is known about the relationships in the data, and there may be ambiguity present in the objectives or measures. These conditions are present in this

problem. These techniques allow the emergence of heuristics with regard to the data collected. The approach and results are discussed in the next section.

## **Evolutionary Computing Analysis of the Data**

### **Introduction**

An experiment was conducted using an evolutionary computing (EC) algorithm with a fuzzy logic rule based evaluation (or fitness) function to determine which sensor at which location in which frequency range using which metric would be “best” to differentiate between the effects of pressure. A second EC experiment was conducted to recommend a reasonable resolution needed to obtain reasonable metric readings. This information could be used to compensate for the 401 sample point limit of the impedance analyzer used for the testing.

Evolutionary computing was well-suited to represent the iterative search over the 28,000 possible combinations of variables. It is useful when there is little known about data or relationships in a problem. It has the advantages of conceptual simplicity, parallelism, self-optimization, simultaneous search over wide and complex solution spaces with multiple minima, and the ability to solve problems with no known solutions [4] [5].

In implementing EC we start with a population consists of N sets (called individuals) that each represent an alternative potential solution to a particular problem. For example, each individual could be composed of values for a set of design variables. The variables for each potential solution are varied somewhat randomly, then each individual set is evaluated with a fitness function (basically, an objective function). The solutions are ranked in some way, and then various methods are applied to the ranked set of possible solutions to generate a new population of potential solutions. The characteristics of good solutions are retained. The new solution set is evaluated and the cycle is repeated. The best characteristics of the solution will emerge over several iterations and we have, hopefully, the best solutions. This approach does not guarantee discovery of the unique optimal solution or convergence to a solution at all. It generally does discover good or reasonable solutions for complex problem that cannot be solve with analytic or statistical models when there is insufficient data or the conditions required to calculate statistics.

Fuzzy logic and fuzzy rule based reasoning are appropriate in an evaluation function with evolutionary computing in our current problem. Fuzzy logic and fuzzy expert systems are particularly useful for representing and reasoning about analog processes when the boundaries between variables are not sharply defined and there may be partial occurrences of events. Fuzzy logic is based on fuzzy set theory developed by Zadeh [6] for incorporating vagueness into decision theory. Variable values are characterized by their degree of membership in sets with linguistic values, such as “high stress” or “low temperature,” and are reasoned over in parallel with a set of antecedent-consequent rules.

### **Problem description for EC Solution**

The variables used for the first EC experiments were SensorLocationFrequencySet, StartFrequency, BandWidthPct, and MetricID. Each individual solution in the population of solutions contained a set of values for the variables described below.

**SensorLocationFrequencySet** are indexes to the data organized as it was collected into 20 sets containing the Re(Z) for each of the pressure levels (0psi, 77psi, 155psi, and 227psi) for a sensor(PZT or SCP) at a location (A or B) for one of the five frequency ranges (see Table 1). The variable is an index into which set to use. The way they were organized also represented classes that could be used to evaluate the best sensor and location and indicated in the table below:

Data Set Indexes	Sensor Type at Location
1 – 5	PZT at Location A
6 – 10	PZT at Location B
11 – 15	SCP at Location A
16 - 20	SCP at Location B

Table 4 Data set indices for EC

**Start Frequency** and **BandwidthPct** are used to select a sequence of frequencies and corresponding Re(Z) within each of the above data sets. The sample starts at a number from one to 350 of the 401 readings in the data set, and the band width is calculated by taking the indicated % of the samples between the start and the 401st sample in sequence. The calculated bandwidth (BW) is on of the solution evaluation parameters (SEPs).

**MetricID** refers to which one of the four nonparametric metrics [ref] to apply to the selected and extracted sample. The four metrics (and the indices) are:

Index	Metric Label and Name	Formula
1	RMSD root mean square deviation	$\sqrt{\frac{\sum_{i=1}^N (y_i - x_i)^2}{\sum_{i=1}^N x_i^2}}$
2	MAPD mean absolute percentage deviation	$\frac{100}{N} \times \sum_{i=1}^N \left  \frac{y_i - x_i}{x_i} \right $
3	COVMETRIC covariance	$\frac{1}{N} \times \sum_{i=1}^N (x_i - \bar{x})(y_i - \bar{y})$
4	CCMETRIC variance normalized covariance	$\frac{Cov(x, y)}{\sigma_x \sigma_y}$

Table 5 Metrics investigated by EC

All of the metrics are measures of differences between a reference set and a measured set. So the  $x_i$  variables represent the reference set values while the  $y_i$  values represent the measured set. The value of N is the number of pairs in the sequences that are being compared. The  $\sigma_x$  and  $\sigma_y$  are the variances of the reference and measured sets respectively

Using the metrics above, the “best” solutions were measured by a fuzzy rule base by considering:

In this problem the first set of computations (shown in Appendix A) were to extract a sequence of impedances for all four pressures (0, 77, 155, 227psig) from the data set and segments identified by the first three variables of each solution. The next calculation is to applying the metric identified by the last variable of the solution (*MetricID*). This calculation results in three numbers that are the metrics value for 0-77psi, 0-155, and 0-227psi. These three numbers are then used to calculate the variables to use in determining the quality of each solution. The criteria used to determine the “best” solutions were:

- 1) **monotonicity** – metric values increase or decrease consistently with pressure,
- 2) reasonably **uniform separation** between measures at different pressures, and
- 3) require **fewer**, rather than more, **measurements** to get reasonable values for a metric.

These criteria were represented by fuzzy variables with membership functions and then processed with a fuzzy rule base to calculate a single quality of solution metric to each individual solution on the population.

### The EC system

The EC system used for this analysis was developed by D.L. Ramers over the in 2003 and early 2004, and is described in the recent conference paper [7]. The system was originally developed to study engineering design processes, and consequently the present problem is viewed as the design of measurement system for pressure in the bottle.

A population of 100 individuals was used, and they were varied in parallel over 60 iterations. The resulting track of the fitness statistics and of the population distribution for the 60<sup>th</sup> generation of solutions is shown in figures 7 and 8 respectively.

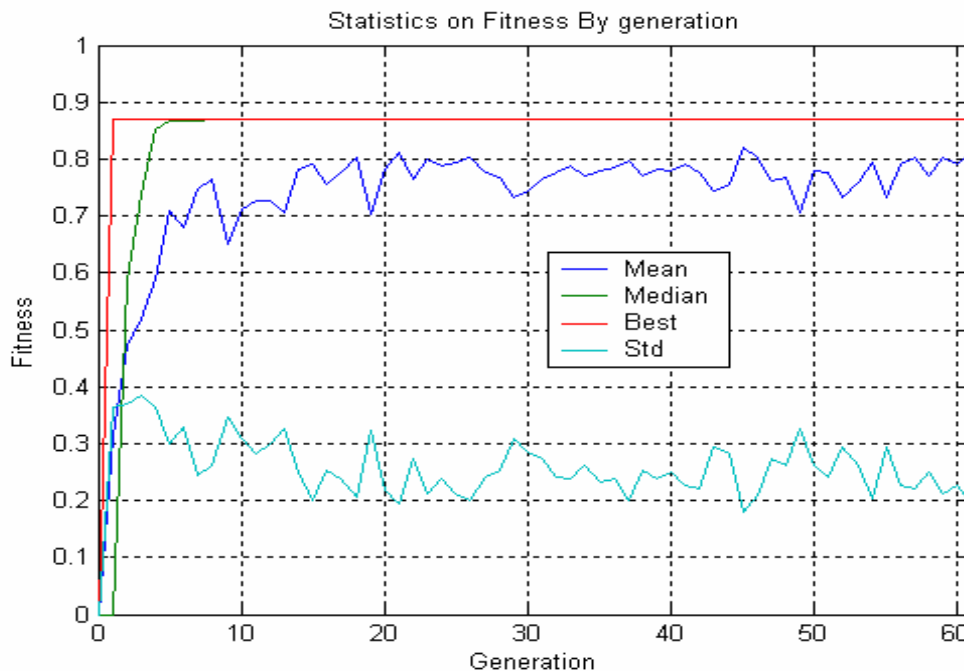


Figure 7 Population fitness progress over 60 generations

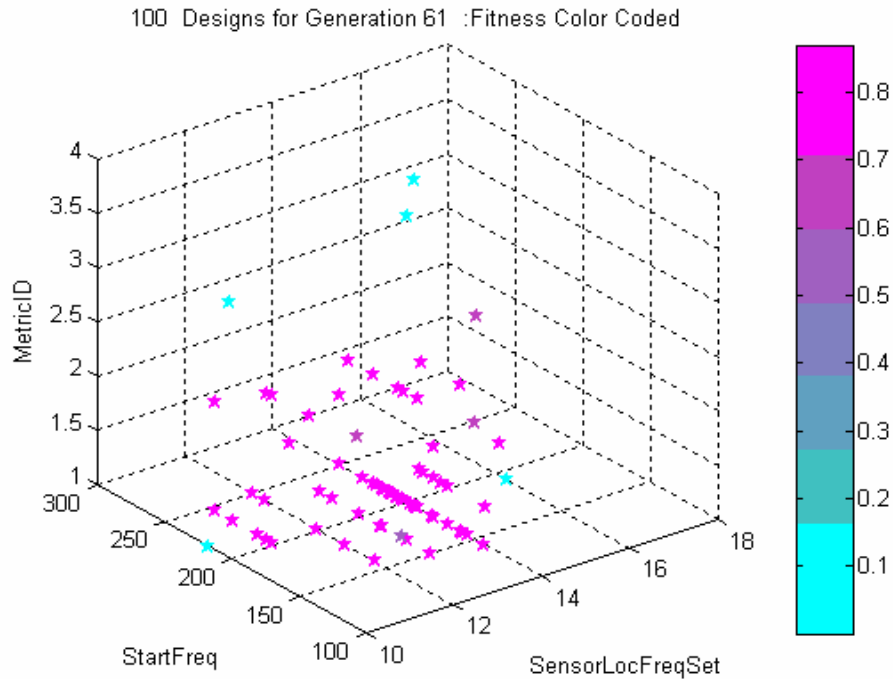


Figure 8 Distribution of alternative solutions of the 60<sup>th</sup> generation

### Discussion of Results

Visual examination of the fitness measures shows that the median population fitness reached the best population fitness by the 10<sup>th</sup> generation (iteration). The mean and the population fitness remained stable over the following generations, showing the intended and forced randomness used with the EC to continue exploring the solution space. The indicated variation was desirable.

From visual examination of the 60<sup>th</sup> generation solution values we can draw the following conclusions:

- Data sets 10-15, representing the SCP sensor at Location A gave the best solutions, and
- Metrics 1 (RMSD) and Metric 2 (MAPD) resulted in the best solutions.

The results also indicate that data set number 14, with a frequency range of 180-200 kHz using metric 1 provide the largest percentage of best solutions. It is important the recall that this last population represents the testing and selection of the best solution combinations from roughly 6000 trials.

Histograms of the combined variable values for only the best individuals (all the of the highest possible score) of the 20<sup>th</sup>, 40<sup>th</sup>, and 60<sup>th</sup> generations, a total of 251 out of 300 individuals, were generated to confirm the visually deduced results, and are shown in the figures below.

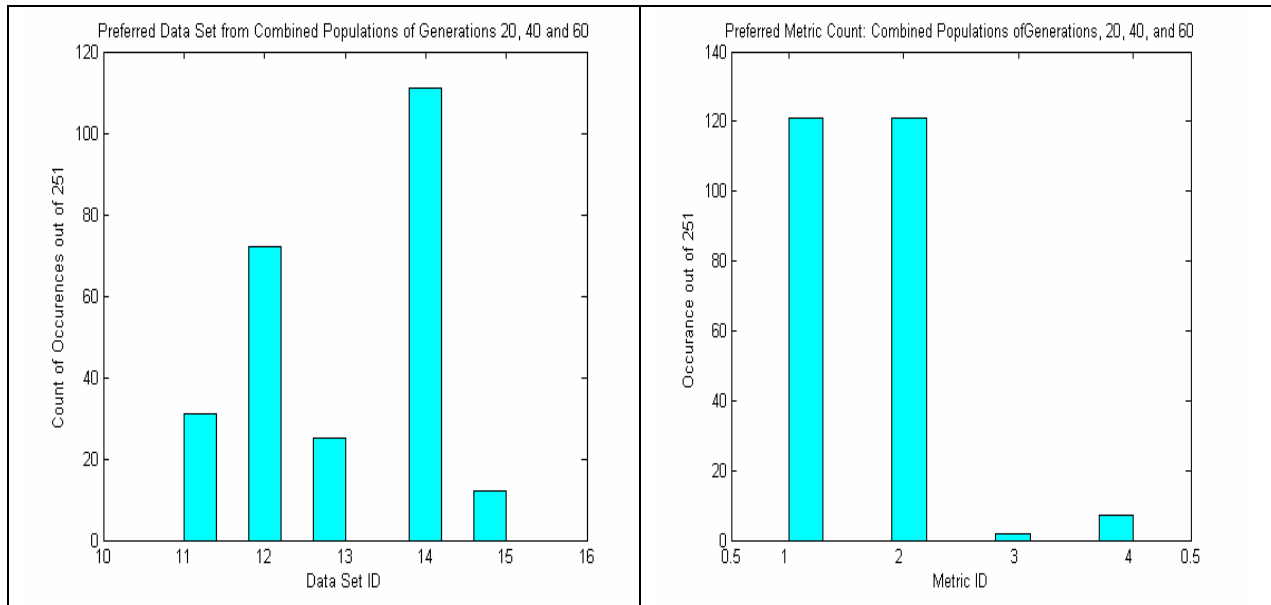


Figure 9 Histogram for Data Sets

Figure 10 Histogram for Metrics

The histogram for the bandwidth (figure 11) indicates that 28 to 52 samples were usually sufficient to give a good indication of pressure with the metrics. The *StartFreq* is not analyzed because its significance is not clearly understood. The results merely show that within the set of frequencies, the ones starting between 140 and 220 seemed to provide the best results. Since the purpose of this variable was to see if we could reduce the number of measurements, it seems that the next experiment that deals with the number of uniformly collected sample to collect, will give a better indication of this factor. This experiment is discussed in the next section.

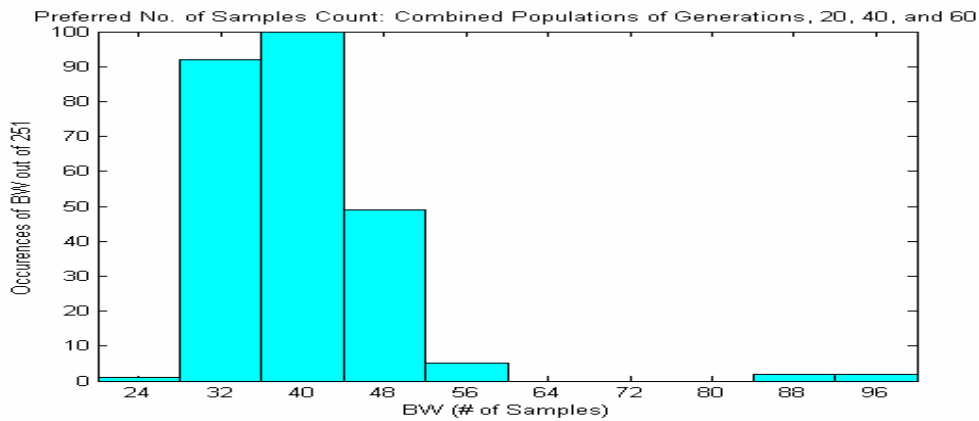


Figure 11 Histogram for Bandwidth

### EC Experiment to Determine Sampling Interval

The EC system was modified so that instead of a start frequency and a bandwidth, each complete 401 data set (for a frequency range) would be considered completely but we would vary a sampling interval to take the impedance at every 1, 2, 3, 4 ... 20th frequency to use for our metric calculation. This means that if we found an adequate quality of pressure differentiation sampling every 10th frequency, we could afford to coarsen the resolution and have the 401 samples that

the instrument could measure take over 10 times the frequency range used in the current samples (about 10kHz typically), which might, in turn, give better results.

A population of 100 individuals was used again, and the distribution of final solutions after 80 generations is shown below (figure 12).

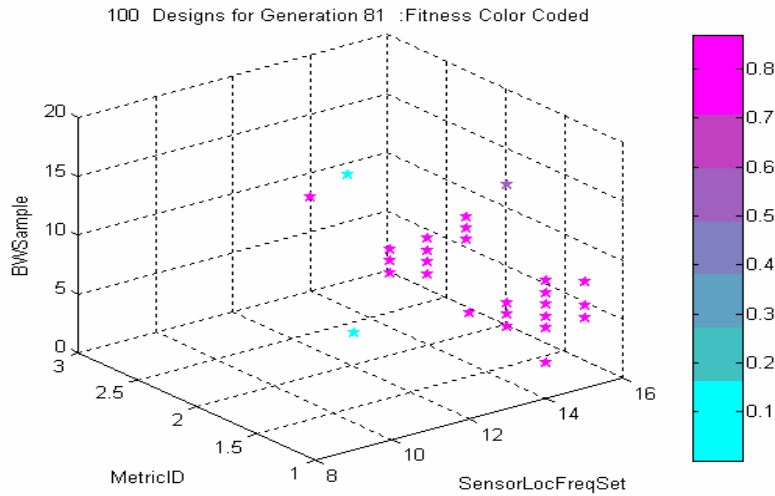


Figure 12 Designs for Last Generation

These results confirm the results of the previous experiment indicating that the RMSD and the MAPD metrics seem to work best, and that data set for the SCP at location A for the higher frequencies, in particularly the 180-200 kHz range, provides the best results for distinguishing pressures through the use of the metrics. The histograms below of the distribution of the best scoring alternatives in the final population show these results. They also show that the sampling resolution could be made coarser by a factor of eight (taking impedance at 400Hz instead of every 50 Hz) and still provide good discrimination. This may permit expanding range or frequencies in a single sweep.

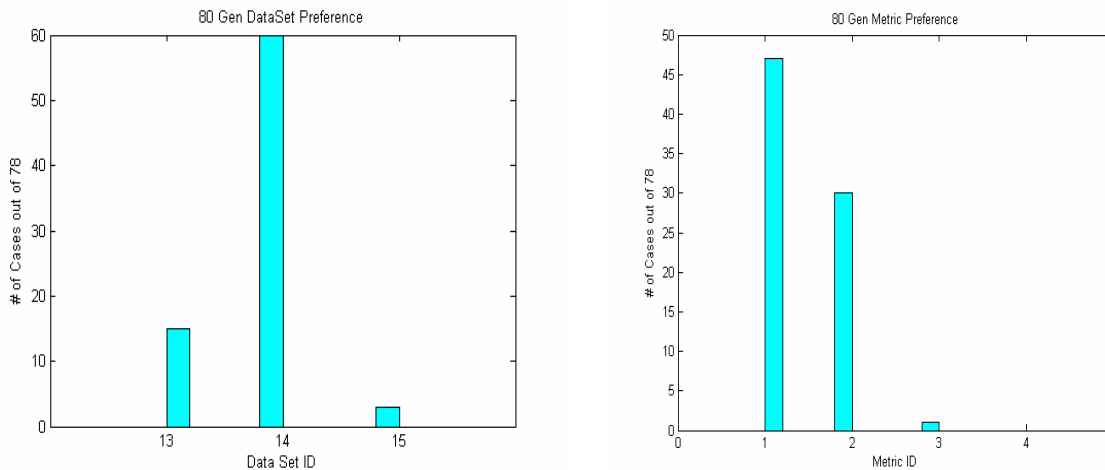


Figure 13 Preferred Data Sets and Metrics in Best of Final Population

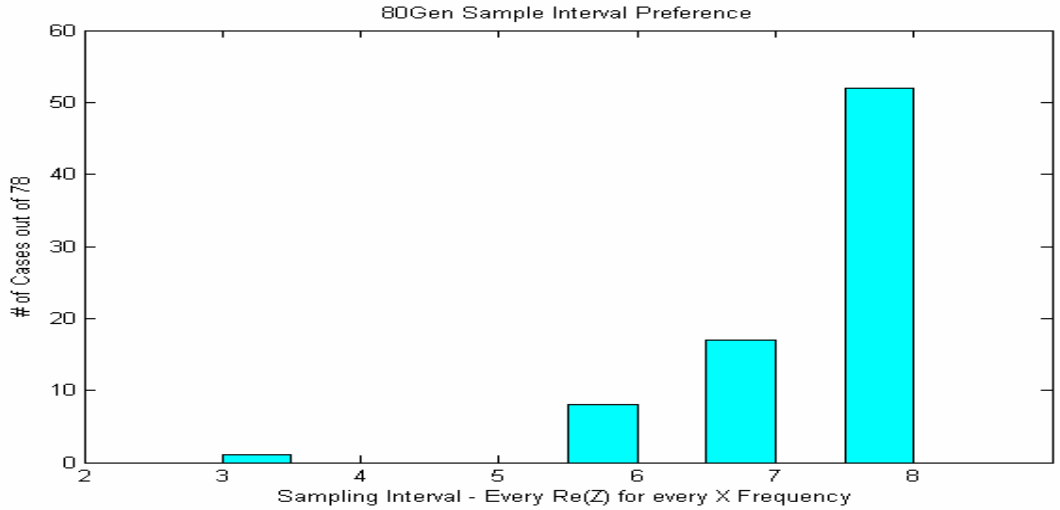


Figure 14 Preferred Sampling Intervals in Best of Final Population

Finally, if we examine the  $\text{Re}(Z)$  traces (Figure 15) for the four pressures in the preferred data set (set #14) we can see that it does do a good job of distinguishing between the pressures, in particular in the 180-190 kHz range.

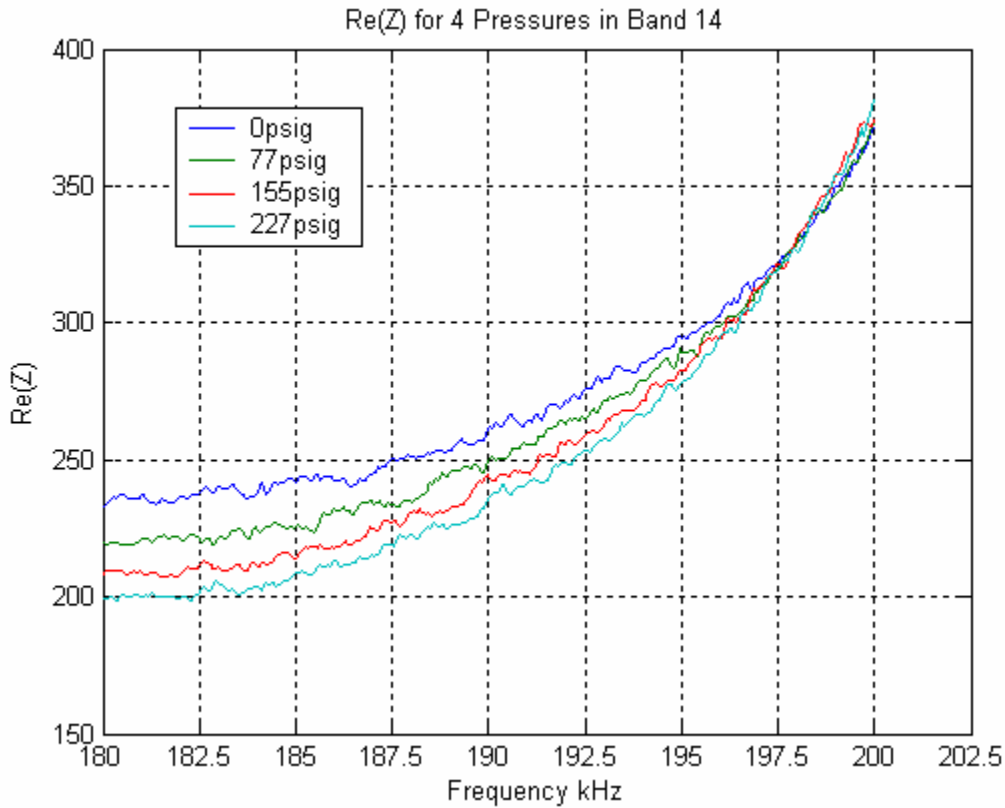


Figure 15  $\text{Re}(Z)$  traces for Dataset 14: SCP at location A 180-200 kHz

## **Conclusions and Recommendations**

Though there was insufficient data to perform statistical modeling on the data, we were able to develop reasonable answers to the initial questions that may be used to guide more specific tests. These conclusions are listed below.

- The SCP type sensor appears to be more sensitive and a better discriminator of pressures.
- The location at the center of the bottle provided better data, but there may have been a failure of the sensor systems on the end of the bottle.
- This type of structural impedance testing seems to be more effective at higher frequencies. For the SCP sensor, the best range was 180 – 190 kHz for discriminating between the test pressures.
- The nonparametric metrics are reasonable and parsimonious representations of the signals. In addition, fewer samples over wider frequency ranges may be sufficient for satisfactory pressure discrimination. These conclusions are based on:
  - \* Re (Z) at only 30-50 contiguous excitation frequencies was sufficient for reasonable metric calculations to discriminate between pressures..
  - \* A granularity of 400 Hz between frequencies was sufficient for the SCP sensor in the 180 – 190 kHz range to provide good discrimination between the test pressures.
- The Root Mean Square Deviation performed the best and the Mean Absolute Percentage Difference performed well at discriminating between the test pressures. The RMSD metric is reasonable to use in testing.

Another conclusion is that it appears that the EC approach worked very well at providing decision making information in an ambiguous, data and knowledge space problem situation. These conclusions can be considered as ad hoc heuristics. In IVHM it is likely that there will be unexpected situations like the one described, and perhaps emergence though EC may be a way to provide some ad hoc heuristics when fairly quick response time is needed. This approach would not work in a short term real time situations, since there must be at least some time allowed for emergence. However, we may want to have emergence based system that observes for emergence of situations and events on monitored systems, and to develop strategies and information to support decision making. In addition, the EC approach is also a tool that could be used for simulations, as it was in this case, to describe emergent states.

For this problem I have listed my recommendations for further testing and analysis.

- 1) Conduct a PZT-SCP test with only one of each sensor at one location, the center of the bottle, to determine the best sensor to use and develop its pressure adjustment relation.

- 2) Run each sample case sweep at a single high frequency range with a 100 to 150 kHz bandwidth for the 401 samples. Convert the results to the RMSD metric and use this as a basis for exploring good starting frequencies before the test.
- 3) A single sample set should consist of a sweep at each of the pressures of a selected range for each of the two sensors. The pressure range should include the min and max pressures on interest. Conduct tests to develop 6-10 sample sets as described above. This would permit calculation of some small sample statistics. If more confidence is desired, develop more sample sets.
- 4) Compare the tests and perform statistical analysis the RMSD as the random variable while trying to its relation to pressure and sensor type. The results should indicate the best sensor to use and provide enough information to develop a model relating the RMSD to the pressure for correction purposes.

I will try to analyze the cryogenic data to explore thermal effects on the sensor over the coming year and report back to John Lassiter.

## References

- [1] "Structural Health Monitoring Using Statistical Pattern Recognition with Emphasis on Embedded Sensing." Short Course by Los Alamos Dynamics, at Marshall Space Flight Center, Huntsville, Alabama, February 25-27, 2004. Contact information: Hoon Sohn, Ph.D., Chief Scientist, Los Alamos Dynamics, P. O. Box 1193, Los Alamos, NM 87544
- [2] Tseng, K.K-H, Naidu, S.K. (2002). "Non-parametric damage detection and characterization using smart piezoelectric material." *Journal of Smart Materials and Structures*, 11 (2002) pp. 317-329, Institute of Physics Publishing, IK, 2002.
- [3] Park, G., Cudney, H.H., Inman, D.J. (2000). "Impedance-Based Health Monitoring of Civil Structure Components." *Journal of Infrastructure Systems*, Vol. 6, No. 4, December, 2002. ASCE.
- [4] Fogel, D. (2000). *Evolutionary Computation, Principles and Practice for Signal Processing*. Bellingham, WA: SPIE Press, 2000.
- [5] Haupt, R.L. and Haupt, S.E. (1998). *Practical Genetic Algorithms*. NY: Wiley Interscience Publications, John Wiley and Sons, Inc., 1998.
- [6] Zadeh, L.A. "Fuzzy Logic," *IEEE Computer*, pp. 83-89, 1988.
- [7] Ramers, D.L. (2004). "Automating and Learning about Engineering Design with Soft Computing," in *Proceedings of the International Conference on Cybernetics and Information Technology, Systems, and Applications*, July 21-25, 2004 in Orlando, FL., 2004.

2004

**NASA FACULTY FELLOWSHIP PROGRAM**

**MARSHALL SPACE FLIGHT CENTER**

**THE UNIVERSITY OF ALABAMA  
THE UNIVERSITY OF ALABAMA IN HUNTSVILLE  
ALABAMA A&M UNIVERSITY**

**Lightning Detection Efficiency Analysis Process:  
Modeling Based on Empirical Data**

Prepared By:	John T. Rompala
Academic Rank:	Professor
Institution and Department:	University of Wisconsin-Stout Physics Department
NASA/MSFC Directorate:	SD-60
MSFC Colleague:	Dr. Richard Blakeslee

## **Introduction**

A ground based lightning detection system employs a grid of sensors, which record and evaluate the electromagnetic signal produced by a lightning strike. Several detectors gather information on that signal's strength, time of arrival, and behavior over time. By coordinating the information from several detectors, an event 'solution' can be generated. That solution includes the signal's point of origin, strength and polarity.

Determination of the location of the lightning strike uses algorithms based on long used techniques of triangulation. Determination of the event's original signal strength relies on the behavior of the generated magnetic field over distance and time. In general the signal from the event undergoes geometric dispersion and environmental attenuation as it progresses. Our knowledge of that radial behavior together with the strength of the signal received by detecting sites permits an extrapolation and evaluation of the original strength of the lightning strike. It also limits the detection efficiency (DE) of the network. For expansive grids and with a sparse density of detectors, the DE varies widely over the area served. This limits the utility of the network in gathering information on regional lightning strike density and applying it to meteorological studies.

A network of this type is a grid of four detectors in the Rondonian region of Brazil. The service area extends over a million square kilometers. Much of that area is covered by rain forests. Thus knowledge of lightning strike characteristics over the expanse is of particular value.

I have been developing a process that determines the DE over the region [3]. In turn, this provides a way to produce lightning strike density maps, corrected for DE, over the entire region of interest. This report offers a survey of that development to date and a record of present activity.

## **Peak Current Distribution**

In an ideal network with a 100% DE, complete information on all lightning strikes is gathered using reliable algorithms. One feature that would be included is the peak strength ( $I_0$ ) of events. Those peak currents cover a wide spectrum of values ranging from below a single (+/-) kiloAmps to a few hundred (+/-) kiloAmps. An example of such a distribution is given in Figure 1. The vertical axis represents the fractional event density, that is, the fraction of all observed events that had a peak current with the range  $I_0 \pm \Delta I$ . The area under the curve is one.

The data set depicted shows Rondonian data for November 23, 2002. It represents a nearly 100% DE since it was restricted to a record of strikes occurring in relatively small region central to the four sites. The shape of the distribution follows the general shape of the gamma probability distribution [4]. The DE Analysis Process under development assumes that this profile is characteristic of the events occurring over the entire region. Though the area density of lightning strikes may vary over the region, it is assumed that this distribution spectrum remains constant.

It examines the operational features of network detectors, and the incoming signal's electromagnetic character to determine the greatest minimum peak current generated at a location needed to produce detections from various combinations of detectors. With these cutoffs determined, it is possible to estimate what fraction of the full peak current spectrum goes undetected at that local. This establishes that location's DE level (which can be a composite result or determined as a function of various detector combinations).

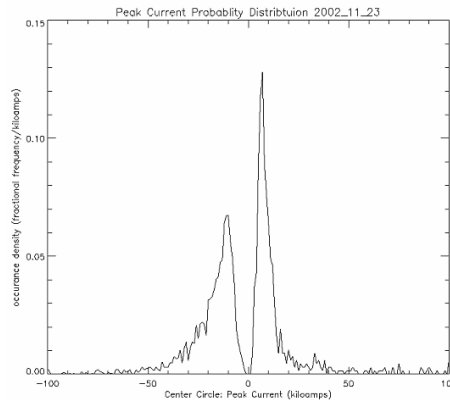


Figure 1: Peak Current Distribution

### **Radial Considerations:**

This greatest minimum detectable peak current comes about, in part, due to range effects. This cutoff is fixed by the range characteristics of the electromagnetic signal and sensitivity of the detector. It is widely accepted that the general dispersion of the signal follows the pattern of a pulsed current in a long straight wire. The resulting functional relation between signal strength and range is inverse ( $1/r$ ). To accommodate variations from this ideal construct, the comparable relation for a lightning event introduces a power value, P,  $(1/r)^P$ .

Signal attenuation due to effects arising from the electrical character of the terrain traversed, is taken to be exponential ( $e^{-a/r}$ ). The attenuation parameter, a, represents the distance a signal must travel before signal drops to  $(1/e)$  of its original value. Operational values vary from a few thousand kilometers to a few hundred thousand kilometers.

These radial characteristics of the electromagnetic signal come into play in two aspects of the development of this DE Analysis Process. The first is the most direct, the determination of the greatest minimum peak current. It is critical that the behavior signal's range behavior be understood before a reliable estimate of the greatest minimum strike strength can be established.

The peak current distribution used, as a model for the entire region is itself produced using algorithms using these interpretations. The subregion used for gathering data for a nearly perfect DE distribution is near all sites thus range issues are not as evident here as they are in remote areas of the service region. Nevertheless, consistency requires that the same values of power and attenuation be used in both steps of the analysis. This becomes an absolute requirement if that analysis is to include an evaluation of those parameters.

Toward that end, the present effort first involved rewriting the algorithms for the DE Analysis Process in a polar format [4]. The central and other subregions now have circular shapes (i.e., circle for central region, rings for outer regions).

### **Reference to Fundamental Data Sets**

In the initial stages of development of the DE Analysis Process, a single data set was employed. That data set already presented processed peak currents and did not reference the sites used in determining solutions. Results were always compared to all solutions since details of those solutions were not part of the data set. Again for consistency, it is important to refer back to raw input signal to the detectors. In this way assurance can be given that the data was processed using the same parameters and techniques used in the application of the DE Analysis Process. To achieve this level of assurance, code was written which refers back to data sets containing the strength of the magnetic field signal received by the sensors and the sites involved in solutions. This was also done to provide a platform for an eventual accommodation and evaluation of the probable data processing technique upgrades.

### **LLP to Peak Current**

The transform from of the magnetic field strength of the incoming signal to the peak current generated in the lightning event is based on a series of triggered lightning experiments carried out by Orville [2]. These experiments involve sending a sounding rocket into an atmospheric electrical environment suitable for producing lightning. A conducting wire trails the rocket into electrically charged clouds. This wire provides a ready path for a lightning strike to follow to ground, while the rocket/wire combination ‘triggered’ lightning events under suitable electric field conditions. The lightning strike so triggered vaporizes the wire but in the process leads to a ground location where instrumentation records the peak current of the strike. These peaks current values were correlated to signals received by detectors at known distances from the lightning strike. The readings, historically expressed in ‘LLP units,’ were normalized, giving the readings of a detector at a ‘normalized’ distance. These experiments indicated a linear relation between normalized LLP signals and the peak current prompting that signal. That data is reviewed periodically with the data spread permitting several interpretations [1]. The data set included strike with a limited peak current. The extrapolation of these triggered lightning results to higher current events and to distant, naturally occurring lightning strikes requires care. The code written for the DE Analysis Process includes interactive features fostering the eventual implementation modifications in these areas.

### **Validation**

Two sample applications of the revised process were carried out. The first dealt with changes in the attenuation factor from  $10^3$  km to  $10^5$  km. Corresponding projected changes in DE for Rondonian network were formulated. The second case monitored the variations in the peak current distribution introduced by various forms of the LLP to peak current relation.

As designed, the DE Analysis Process and assumptions can be evaluated by using it to replicate the empirical data peak current distributions derived from the observed data. Figure 2, compares

empirical data (green) for a subregion about the center of the grid to modeled distribution (black) for the same region under comparable detection conditions

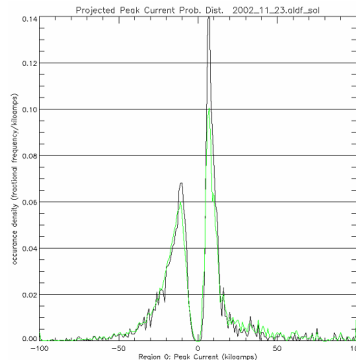


Figure 2: Empirical and Modeled Distributions

## **Conclusion**

Confidence in the validity of the process and in its potential for application grows. It was originally meant to serve as a strictly operational tool for gaining the detection efficiency of the network under various conditions. It has already served a role in the clarification of operational parameters. It has shown potential for an expanded role in this regard. If the validity of the process can be fully established, it can be applied to meteorological studies. Being developed in conjunction with this empirical based modeling of the peak current is an analytical model. That formalism will eventually lend itself to an analysis of peak current distribution physics.

## **Acknowledgements**

The many NSSTC members contributing to this effort and their support is much appreciated especially that of Dr. Richard Blakeslee and Mr. Jeff Bailey. The SFFP staff fostered and facilitated this work during all stages of its development.

## **References**

- [1] Idone V. P., A. B. Saljoughy, R.W. Henderson, P. K. Moore and R. B. Pyle: A reexamination of the peak current calibration of the National Lightning Detection Network, 1993, Journal of Geophysical Research, 98, 18323-18332.
- [2] Orville, R. E., Calibration of a magnetic direction finding network using measured triggered lightning return stroke peak currents, 1991, Journal of Geophysical Research, 96, 17135-17142.
- [3] Rompala J. T.; "Characteristics of the Rondonian Lightning Detection Network"; Report LIV, NASA/MSFC, 2000, Research Reports, NASA/ASEE Summer Faculty Fellowship Program.
- [4] Rompala J. T., R. J. Blakeslee, and J. C. Bailey; "Detection Efficiency Contours for Regions Served by Lightning Detection Networks of Limited Scope"; Poster Presentation, 12<sup>th</sup> International Conference on Atmospheric Electricity.

**2004**

**NASA FACULTY FELLOWSHIP PROGRAM**

**MARSHALL SPACE FLIGHT CENTER**

**THE UNIVERSITY OF ALABAMA  
THE UNIVERSITY OF ALABAMA IN HUNTSVILLE  
ALABAMA A&M UNIVERSITY**

**Development of a Modeling Framework to Support Control  
Investigations of Sailcraft Missions  
A First Cut: ABLE Sailcraft Dynamics Model**

Prepared By:	Dr. Sriprakash Sarathy
Academic Rank:	Associate Professor
Institution /Department:	Clark Atlanta University/ Engineering
NASA/MSFC Directorate:	Transportation (GNC)
MSFC Colleague:	Dr. Mark S. Whorton

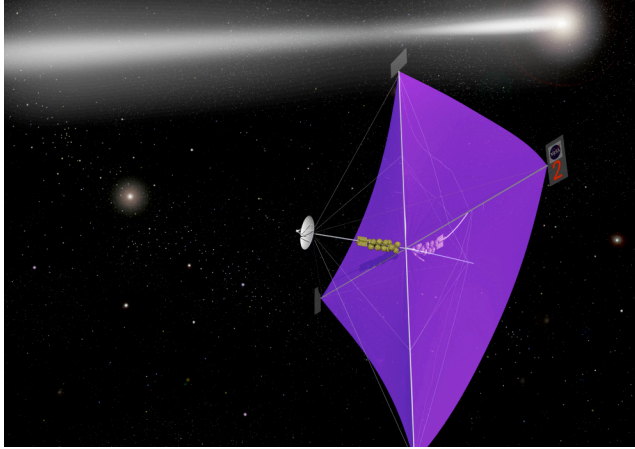


Figure 1: Artist's Depiction of Solar Sailcraft Mission

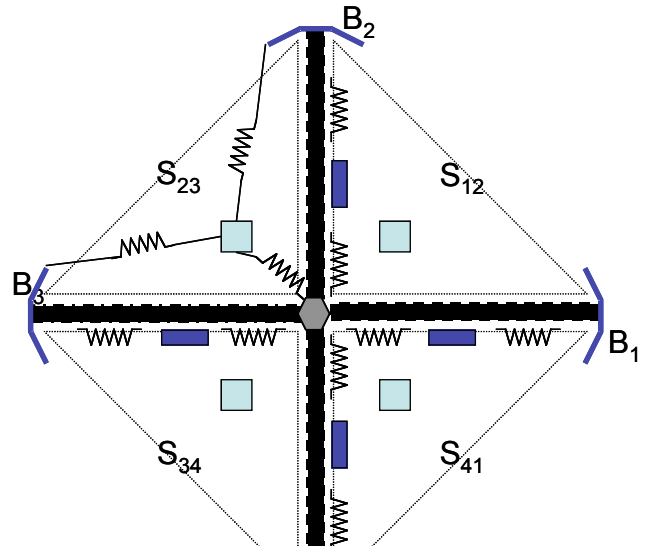


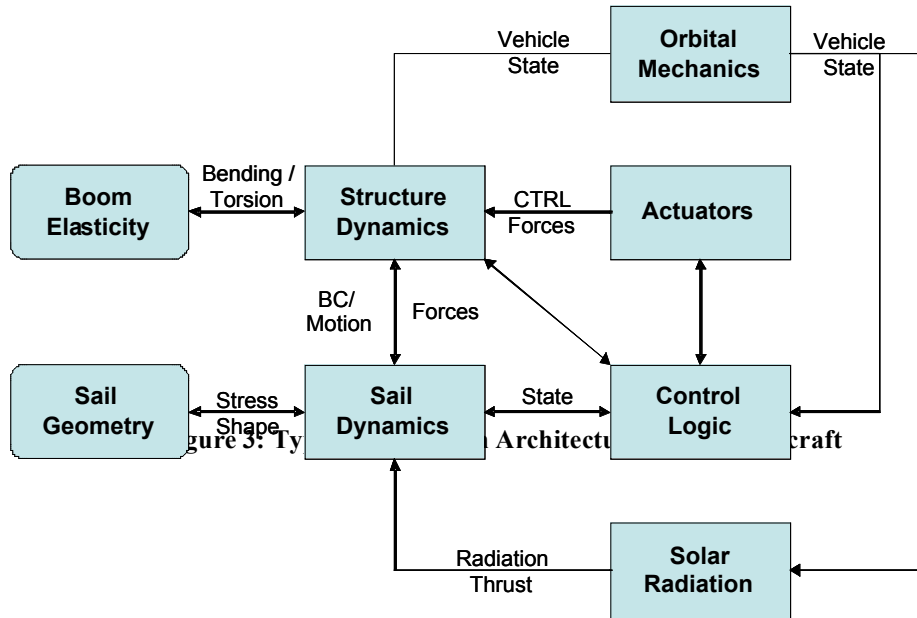
Figure 2: Example of Solar Sail Dynamic Model

## Introduction

Solar Sailcraft, the stuff of dreams of the H.G. Wells generation, is now a rapidly maturing reality. The promise of unlimited propulsive power by harnessing stellar radiation is close to realization. Currently, efforts are underway to build, prototype and test two configurations. These sails are designed to meet a 20m sail requirement, under guidance of the In-Space Propulsion (ISP) technology program office at MSFC. While these sails will not “fly”, they are the first steps in improving our understanding of the processes and phenomena at work. As part of the New Millennium Program (NMP) the ST9 technology validation mission hopes to launch and fly a solar sail by 2010 or sooner.

Though the Solar Sail community has been studying and validating various concepts over two decades, it was not until recent breakthroughs in structural and material technology, has made possible to build sails that could be launched. With real sails that can be tested (albeit under “earth” conditions), the real task of engineering a viable spacecraft has finally commenced. Since it is not possible to accurately or practically recreate the actual operating conditions of the sailcraft (zero- $G$ , vacuum and extremely low temperatures), much of the work has focused on developing accurate models that can be used to predict behavior in space, and for sails that are 6-10 times the size of currently existing sails. Since these models can be validated only with real test data under “**earth**” conditions, the process of modeling and the identification of uncertainty due to model assumptions and scope need to be closely considered.

Sailcraft models that exist currently, are primarily focused on detailed physical representations at the component level, these are intended to support prototyping efforts. System level models that cut across different sail configurations and control concepts while maintaining a consistent approach are non-existent. Much effort has been focused on the areas of thrust performance, solar radiation prediction, and sail membrane behavior *vis-à-vis* their reflective geometry, such as wrinkling/folding/furling as it pertains to thrust prediction. A parallel effort has been conducted on developing usable models for developing attitude control systems (ACS), for different sail configurations in different regimes. There has been very little by way of a system wide exploration of the impact of the various control schemes, thrust prediction models for different sail configurations being considered.



The Vector Graph Object Modeling (VGOM) method offers a simple paradigm to model even complex dynamical systems using a graph-tree representation. By reducing each model to the absolute minimal set of generalized coordinates and by uncoupling any discretization and coordinatization effects, a wide variety of models can be compared and integrated. This would provide a viable framework for evaluating the impact of various choices on the system dynamics, controllability and risk associated with the sail missions.

### Approach

This effort is not aimed at developing new models *per se*, rather the emphasis is on developing a way to bring in different existing models, representing them within a common framework, and being able to compare them. More important is the ability to model, not just components or sub-systems, but an entire spacecraft system. This can be achieved if *any* (physical continuous dynamic) model can be reduced to its essential elements. The graph theoretic approaches that form the basis of the VGOM, allow us to do just that. Simply put, the problem is stripped of the geometry, and specific coordinate frame information, as well as the constraints, leaving only the generalized coordinates represented on a graph through nodes and edges. Such a graph can be shown invariant to coordinate choices, nature of joint interaction models, force driver models or even motion variable choices. This is not to say that these do not affect the model, only that the *graph* remains the same. All the other information such as material, kinematic, geometric and constraint information, is included *after* the graph is formed. A second important advantage is that a *systems-of-systems* approach can be implemented by allowing individual sub-systems or systems to be independently modeled and integrated within this framework. This approach, while not new, is a natural extension of the VG method, and is a manifestation of the principles of *diakoptics*. This implies that, the interactions between different parts of the overall model can be explicitly identified once the sub-parts (for example see Figure 3) are defined. This is critical in managing uncertainty of the overall model, since improper modeling of the interactions between sub-parts can drastically degrade the overall model even if each of the sub-parts are accurately represented.

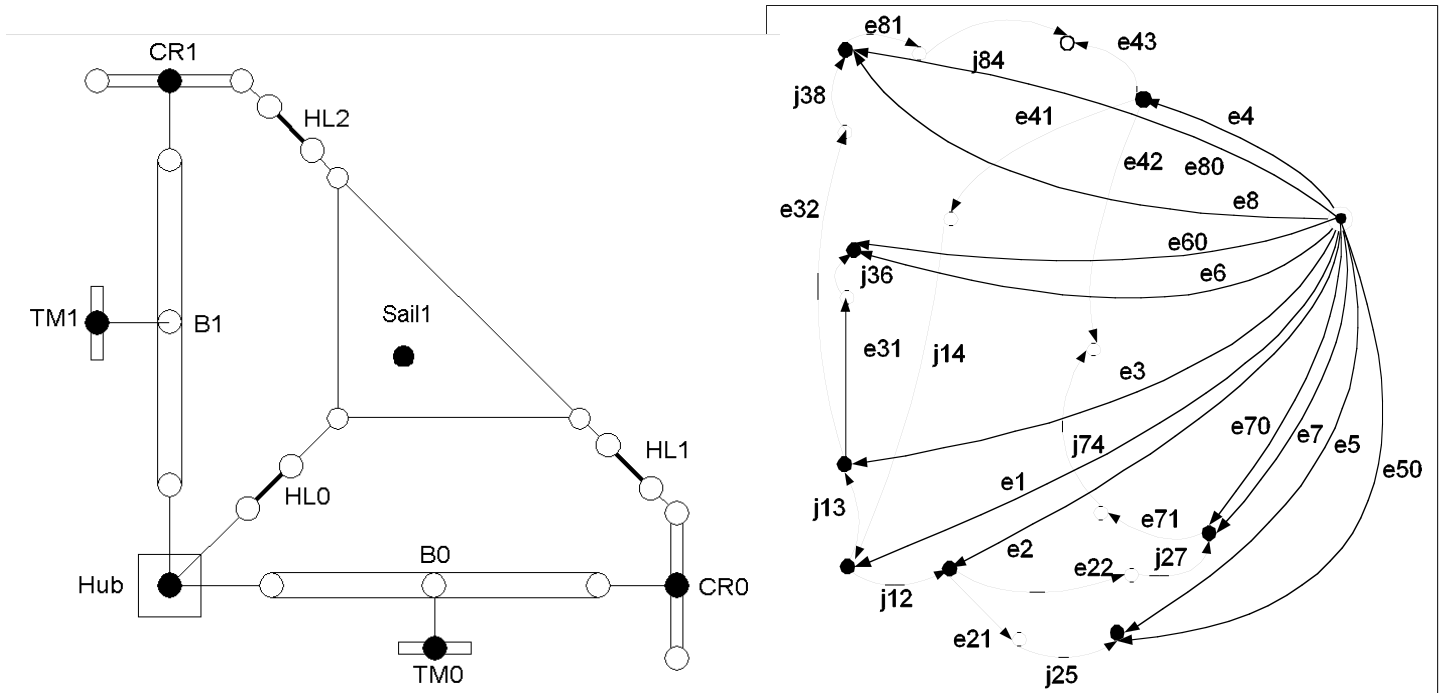


Figure 4 a & b: VGOM based Dynamics Model Development

### Results and Conclusions

This approach can be best appreciated when viewing an example. For this reason a significant portion of this effort is aimed at developing a model representation of an existing sailcraft. The ABLE Engineering Inc. is one of the two vendors developing a 20m sailcraft (Figure 2). Based on the available literature, a first cut at a scalable dynamics model has been developed (Figure 4b). This system graph is obtained by following the process outlined earlier, Figure 4a shows an intermediate step that relates the physical model to the system graph. This model can be refined in a transparent manner, by changing the nature of the joint interactions, definition of the external force drivers, as well as constraints on the system. While these changes do not alter the model topology, changes in choices of generalized coordinates will result in a clear change in the system graph signaling a fundamentally different model abstraction. As this example shows, this approach is capable of modeling complex multi-body interactions. It has the capability of including flexible elements as well as arbitrary joint interactions. A MATLAB™ based toolbox is being developed to support such functionality for Solar Sails.

## Acknowledgements

I would like to thank Dr. Mark Whorton for giving me this unprecedented opportunity to tackle a problem of relevance to NASA and valuable guidance in this area. I also would like to acknowledge my colleagues Dr. Lee Keel and Dr. Wale for their contributions. I would like to specially mention Dr. Young Kim of TD 54 who was invaluable in helping me sound out my ideas and get them right. I wish to thank Jerry Oakley for his discussions on the test data package he performed on the boom structure. Finally, I wish to acknowledge my family, for persevering with my periodic disappearances to Huntsville in the wee hours of the day.

## References

- [1] Andrews G.C. and Kesavan. H.K. "Simulation of Multibody Systems Using Vector-Network Model", *Journal of Dynamics of Multibody Systems*, 1978.
- [2] Blandino, Joseph R., Johnston, John D., Miles, Jonathan J. and Dharamsi, Urmil K. "The effect of asymmetric mechanical and thermal loading on membrane wrinkling". *AIAA/ASME/ASCE/AHS/ASC Structures, Structural Dynamics and Materials Conference*, v 2, p 1282-1292, 2002.
- [3] Leifer, J.Black, J.T., Belvin, W.K. and Behun, V. "Evaluation of shear compliant borders for wrinkle reduction in thin film membrane structures" *AIAA/ASME/ASCE/AHS/ASC Structures, Structural Dynamics and Materials Conference*, v 7, p 5325-5331, 2003.
- [4] McInnes, Colin R. "Passive control of displaced solar sail." *Journal of Guidance, Control, and Dynamics*, v 21, n 6, Nov-Dec, 1998, p 975-982
- [5] McInnes, Colin R. and Brown, John C. "Solar sail dynamics with an extended source of radiation pressure." *Acta Astronautica*, v 22, 1990, p 155-160
- [6] Mikulas, Martin M. and Adler, Aaron L. "Rapid structural assessment approach for square solar sails including edge support cords". *AIAA/ASME/ASCE/AHS/ASC Structures, Structural Dynamics and Materials Conference*, v 1, p 440-453, 2003.
- [7] Murphey, T.W., Murphy, D.M. and Mikulas, M.M. "A Method to Quantify the Thrust Degradation Effects of Structural Wrinkles in Solar Sails." *43rd AIAA/ASME /ASCE/ AHS/ ASC Structures, Structural Dynamics, and Materials Conference* 22-25 April 2002, Denver, Colorado AIAA 2002-1560
- [8] Murphy, D.M., Murphey, T.W. and Gierow, P.A. "Scalable Solar Sail Subsystem Design Considerations", *43rd AIAA/ASME/ASCE/AHS Structures, Structural Dynamics, and Materials Conference*, Denver, Colorado. 22-25 April 2002.
- [9] Sarathy, S. and Shujaee, K. and Cannon, K. "A Coupled Object Based Vector Graph Theoretic Modeling Method For Multi-Body Simulation", *ASTC 2000, MGA Conference*, Washington DC, April 2000.
- [10] Sarathy, S. and Shujaee, K. and Cannon, K. "High Fidelity Real Time Parallel Simulation Modeling of Non Linear Systems", *Inter Service / Industry Simulation, Education Conference I/ITSEC*, Orlando FL Nov 2003.
- [11] Sarathy, S. and Shujaee, K. and Molnar, P. and Cannon, K. "On the Development of a Framework for the Control of Large Scale Unmanned Aerial Vehicles", *World Automation Congress*, Orlando FL. February 2002.
- [12] Wei, B. "Dynamic Modeling And Attitude Control Of Solar Sail Spacecraft: Part I/II", *AIAA Guidance, Navigation, And Control Conference And Exhibit* 5-8 August 2002, Monterey, California
- [13] Wie, Bong and Rothmayr, Carlos M. "Integrated Orbit, Attitude, and Structural Control

Systems Design for Space Solar Power Satellite”, NASA-TM-2001-210854, L-18077,  
2001.

---

**NASA FACULTY FELLOWSHIP PROGRAM**

**MARSHALL SPACE FLIGHT CENTER**

**THE UNIVERSITY OF ALABAMA  
THE UNIVERSITY OF ALABAMA IN HUNTSVILLE  
ALABAMA A&M UNIVERSITY**

**Java-based Graphical User Interface for MAVERIC-II**

Prepared By:	Suk Jai Seo
Academic Rank:	Assistant Professor
Institution and Department:	Middle Tennessee State University Computer Science Department
NASA/MSFC Directorate:	Transportation
MSFC Colleague:	Greg Dukeman

## **Introduction**

A computer program entitled “Marshall Aerospace Vehicle Representation in C II, (MAVERIC-II)” is a vehicle flight simulation program written primarily in the C programming language. It is written by James W. McCarter at NASA/Marshall Space Flight Center. The goal of the MAVERIC-II development effort is to provide a simulation tool that facilitates the rapid development of high-fidelity flight simulations for launch, orbital, and reentry vehicles of any user-defined configuration for all phases of flight.

MAVERIC-II has been found invaluable in performing flight simulations for various Space Transportation Systems. The flexibility provided by MAVERIC-II has allowed several different launch vehicles, including the Saturn V, a Space Launch Initiative Two-Stage-to-Orbit concept and a Shuttle-derived launch vehicle, to be simulated during ascent and portions of on-orbit flight in an extremely efficient manner. It was found that MAVERIC-II provided the high fidelity vehicle and flight environment models as well as the program modularity to allow efficient integration, modification and testing of advanced guidance and control algorithms. In addition to serving as an analysis tool for technology development, many researchers have found MAVERIC-II to be an efficient, powerful analysis tool that evaluates guidance, navigation, and control designs, vehicle robustness, and requirements.

MAVERIC-II is currently designed to execute in a UNIX environment. The input to the program is composed of three segments: 1) the vehicle models such as propulsion, aerodynamics, and guidance, navigation, and control 2) the environment models such as atmosphere and gravity, and 3) a simulation framework which is responsible for executing the vehicle and environment models and propagating the vehicle’s states forward in time and handling user input/output. MAVERIC users prepare data files for the above models and run the simulation program. They can see the output on screen and/or store in files and examine the output data later. Users can also view the output stored in output files by calling a plotting program such as gnuplot. A typical scenario of the use of MAVERIC consists of three-steps; editing existing input data files, running MAVERIC, and plotting output results.

The three steps described are conducted by a sequence of numerous UNIX commands, and it requires users’ considerable amount of knowledge of MAVERIC program and data files. We developed a graphical user interface (GUI) so that it makes MAVERIC much more user-friendly and it allows MAVERIC users more productive. Users select necessary steps required to conduct a flight simulation from the menus that are provided by the GUI instead of invoking multiple, separate UNIX commands. The GUI we developed is written in Java programming language, which has many advantages over other programming environment. Java is free and it is available from [java.sun.com](http://java.sun.com) for all modern platforms with no license restrictions. It is object-oriented and there are a huge amount of pre-written packages available, which are ready-to-use or easily extendable. It is platform independent, so the same program can be run on any environment without recompiling. Java is consistent with traditional MAVERIC philosophy, i.e., all GUI source code is available (provides low-level insight into the GUI) and modifiable by TD54 developers so that improvements can be made.

## User Interaction With MAVERIC ( command-based)

Many input data files are needed to run simulation using MAVERIC. These data files are composed of three segments; the vehicle models such as propulsion and aerodynamics, the environment models such as atmosphere and gravity, and a simulation framework that specifies simulation options. Interaction with MAVERIC is currently command-line based (UNIX commands). Typically MAVERIC users change/modify contents of these input data files before the simulation, execute MAVERIC, and view the simulation results by invoking many different UNIX commands as shown in Figure 1. It requires user's knowledge of name and location of data files and type of data in each data file. Users also should know how to invoke different programs.

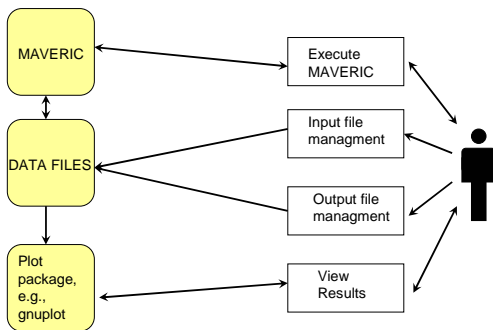


Figure 1: Command-based MAVERIC

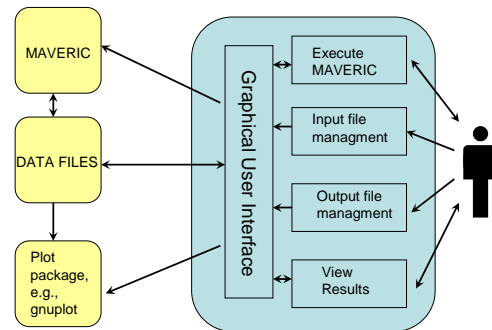


Figure 2: GUI-based MAVERIC

## GUI Architecture(GUI-based MAVERIC)

The GUI we developed provides a more user-friendly environment for the MAVERIC users. Users do not have to invoke any UNIX commands; the GUI is a menu- and mouse-based application. Different menu items in GUI replace the functionalities of most of UNIX commands that used be required for the flight simulation using MAVERIC. Users can manage input/output data files, execute MAVERIC, and view the simulation results by selecting options that are provided in GUI as shown in Figure 2.

## GUI Design

There are three menu categories provided in the GUI; editing, running MAVERIC, and results. The edit menu allows the user to change any input data before the simulation by guiding through the editing process. The run menu provides the user a various options to execute the flight simulation program, MAVERIC. After or during the simulation the user can not only watch the screen output from MAVERIC but also plot the output data that is stored in the output data files produced by running MAVERIC. All of the above functionalities are provided directly from the GUI menu options.

## Features of GUI

In addition to the functionalities described above, the GUI contains the following features. Some of the features are shown in Figure 3.

- Find the appropriate input data files for the case selected by the user
  - Users are not required to know the location of input or output data files
  - Check out (co) files for the user if necessary
- Allows multiple cases of flight simulations
  - GUI dynamically adapts to a new case so that the user doesn't have to remember the 'case' directory or the 'case' file name – important because these names are arbitrary and not always easy to remember
  - Allows user to modify new case data
  - Dynamically updates GUI menu-items
- Provides very useful menu-items for plotting output data
  - Show the output files created by the most recent simulation
  - Easily switch among different output files
  - Show the variables to plot in alphabetical order
  - Invoke plotting program for the user, continually update graphs while MAVERIC is running
- Shows useful message dialog boxes for the user
  - Provides helpful information on MAVERIC
  - Provides appropriate, informative error messages

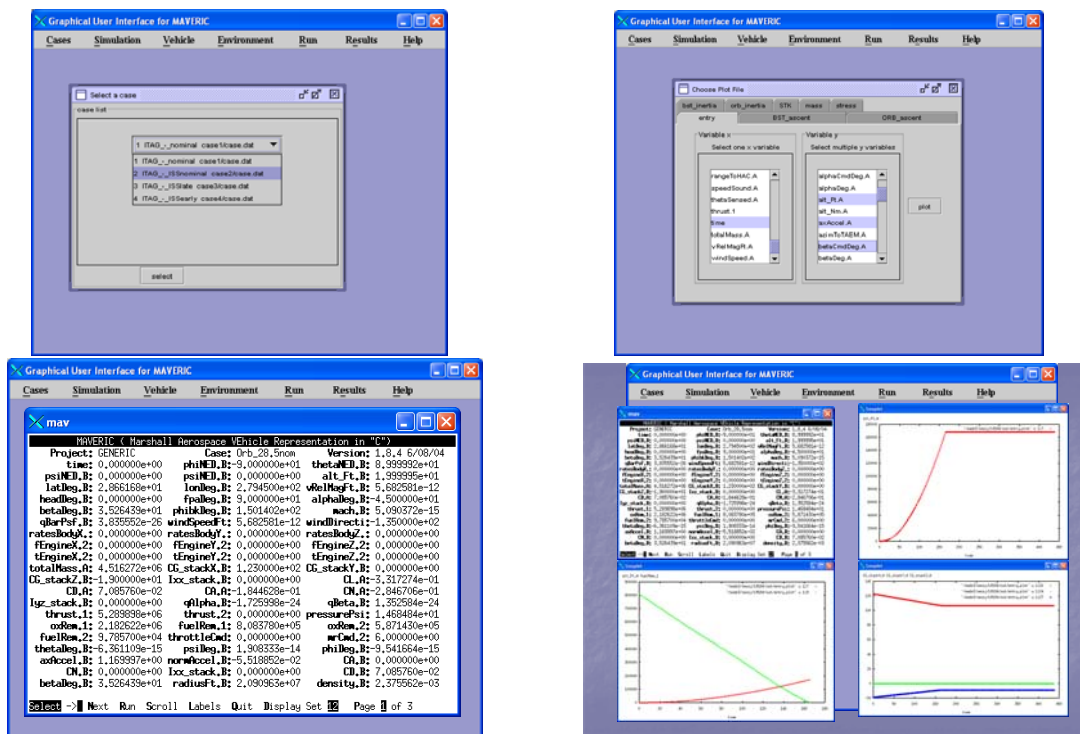


Figure 3: Snap shots of GUI

## **Resources**

The GUI was developed in Java programming language, which can be run on any platforms. However, the GUI uses the gnuplot plotting program, so currently the GUI can be run in UNIX only. MAVERIC is also run in UNIX now, but in the future when MAVERIC is ready to be run on other platforms, plotting option should be replaced by a Java-based plotting package.

## **Conclusion/Future Works**

The Java-based GUI we developed makes MAVERIC-II, an invaluable simulation tool for various Space Transportation Systems, much more user-friendly and much more useful. The project of this summer was focused on reducing the input/output file management burden on the user, and adding features that reduce the learning curve of MAVERIC is recommended in the future. Instead of invoking gnuplot program to view/plot the output, incorporating Java-based plotting package into the GUI will provide GUI developers/maintainers more control over plotting functions and make the GUI more platform-independent. This will be much easier with data file structure enhancements being undertaken by TD54, i.e., any enhancements to data file structure will directly benefit the GUI design.

## **Acknowledgements**

The author would like to thank Greg Dukeman of TD54 for providing an opportunity to participate in the space vehicle simulation area of the Marshall Space Flight Center's Transportation Directorate and many hours of valuable discussion and guidance. The author also appreciates other team members' support on the research including Jim McCarter, John Hanson, and Curtis Zimmerman.

## **References**

- [1] McCarter, J. (2004), "MAVERIC-II Vehicle Flight Simulation Software," NASA-MSFC, Space Transportation Directorate, Vehicle & Systems Development Dept, GN&C Group/TD54, Guidance & Trajectory Team.
- [2] McCarter, J. (2004), "MAVERIC-II User's Guide," NASA-MSFC.
- [3] Deitel & Deitel. (2003), *Java How To Program*, Prentice Hall.
- [4] Sun Microsystems (2004), "The Java Tutorial", <http://java.sun.com/docs/books/tutorial/>
- [5] Sun Microsystems (2004), "The Source for Developers", <http://java.sun.com/docs/>

**2004  
NASA FACULTY FELLOWSHIP PROGRAM**

**MARSHALL SPACE FLIGHT CENTER**

**UNIVERSITY OF ALABAMA  
UNIVERSITY OF ALABAMA IN HUNTSVILLE  
ALABAMA A&M UNIVERSITY**

**NASA Integrated Vehicle Health Management (NIVHM)  
A New Simulation Architecture:  
An Investigation  
PART I**

Prepared by:	Gene Sheppard
Institution:	Georgia Perimeter College Math/Computer Science Dept.
NASA/MSFC Directorate:	ED-19
MSFC Colleague:	Leslie Murphy

## Introduction

The overall objective of this research is to explore the development of a new architecture for simulating a vehicle health monitoring system in support of NASA's on-going Integrated Vehicle Health Monitoring (IVHM) initiative. As discussed in NASA MSFC's IVHM workshop on June 29-July 1, 2004, a large number of sensors will be required for a robust IVHM system. The current simulation architecture is incapable of simulating the large number of sensors required for IVHM. Processing the data from the sensors into a format that a human operator can understand and assimilate in a timely manner will require a paradigm shift. Data from a single sensor is, at best, suspect and in order to overcome this deficiency, redundancy will be required for tomorrow's sensors. The sensor technology of tomorrow will allow for the placement of thousands of sensors per square inch. The major obstacle to overcome will then be how we can mitigate the torrent of data from raw sensor data to useful information to computer assisted decisionmaking.

We can take our cue from the human sensory apparatus. We should consider how the human mind processes and assimilates the large sensor input. For example, consider the following [1, 2, 3, 4, 5]:

- The average human male has about 18,000 cm<sup>2</sup> of skin surface area.
- The number of pressure/pain sensors per cm<sup>2</sup> ranges from 50 on the back to 2,500 on the hand.
- Given an average of 1,000 sensors per cm<sup>2</sup>, there are about 18,000,000 skin sensors constantly sending information to the brain 24/7.
- The human eye has about 125,000,000 photoreceptors constantly simulating the brain 24/7.
- The human nose has about 40,000,000 olfactory sensors sending input directly to the brain 24/7.
- Human nerve impulses travel about 0.1 to 100 meters per second.

For the sake of simplicity, we will presume each sensor sends a one or a zero. Roughly every 200 milliseconds about 183,000,000 bits (22,875,000 bytes) of information is processed. This is simply raw data being pushed around without regard for content or context. The wondrous part of all this is, the conscious mind is presented with only "pertinent" data and in a format easily assimilated. This suggests some intelligent processing occurs before alerting the conscious mind. Processing of sensor data just above the sensors is indicated by the reaction of a hand when fire is encountered. Before the fire-pain message reaches the brain, the hand is beginning to pull away from the fire. Mimicking the human model, IVHM will have the following hierarchy:

Sensors → low level processing → midlevel processing → intelligent decision processing

It is important to note the brain has no central processing unit ("CPU") indicating it is designed for distributed processing.

Beowulf is a distributed processing technology suited for the task of mimicking the human sensory and response apparatus. From a strictly technological perspective, a Beowulf system is

ideal to deal with IVHM. Beowulf also promises tremendous potential for cost reduction associated with simulation of a vehicle health monitoring system. Beowulf technology is proposed as an ideal architecture for this computing problem because it can be easily used to simulate the above model and can be easily copied and used for IVHM simulation.

A brief history lesson is in order. The story of *Beowulf*, an old English poem originally composed in perhaps the early eighth century and put to paper around the year 1016, describes how Beowulf subdues a ferocious monster that has spent twelve years killing and eating people. The name Beowulf is applied to a computing technology intended to defeat of the monstrous cost of supercomputing.

### **Approach**

Utilizing Beowulf techniques will allow design/development of a scalable/flexible platform which will easily accommodate future computer technology using heterogeneous computer systems and a communication infrastructure. Beowulf systems typically use 7 foot racks housing about 16 computing elements each having a 3x24x30 inch footprint. The computing nodes are interconnected via fast network hardware and protocol. The pictures on page 8 are examples of such systems.

In this context, flexible translates to the ability to add homogeneous and heterogeneous computing nodes using the same network hardware and software with minimal effort. Scalable means the ability of the software to adapt, incorporate new computing nodes, and redistribute of computing resources.

We began our research by examining the flexibility component and transfer speeds/latencies of the current network in the MAST lab. We addressed the questions: Can heterogeneous computing nodes be seamlessly integrated (as much as possible)? What transfer latencies are incurred?

Open-source software and network solutions were examined for cost containment purposes. The open-source operating system of choice is Linux. The open-source network software Message Passing Interface (MPI) is supported the best. Both Linux and MPI are also available from commercial resources. The following software variations of MPI were examined: MPICH-1 (implements MPI version 1 - freeware), MPICH2 (implements MPI version 2 - freeware), MPI/RT (RT means real time – freeware and commercial versions), MPI Globus (commercial), Pallas MPI (commercial), LogP-MPI (commercial), and LAM-MPI (Local Area Multiprocessing - freeware).

Of the versions of MPI we examined, the only version we were able to configure and run properly was LAM-MPI. During our tests, the following systems were successfully communicating over an Ethernet network using LAM-MPI:

- 5 SGI single-CPU Octane systems running IRIX 6.5
- 1 SGI four-CPU system running Slackware Linux 2.2
- 1 SGI 10-CPU Origin system running IRIX 6.5 operating system
- 1 Concurrent with two Intel CPUs (4 with hyper-threading) running Redhat Linux

- 1 Dell with a single Intel CPU running Slackware Linux 2.4

It must be noted the SGI implementation of MPI was easily configured and brought up; however, because of SGI's array-services daemon, the systems did not play well with dissimilar computing nodes.

As part of our research, we examined publications, write-ups, and white papers on optical-electrical hardware implementing the reflective memory that would be required in order to significantly lower data transfer latencies between computing nodes. The optical-electrical products we examined were Infiniband, ScramNet, Myrinet, and Memory Channel. Each of the products either has or is planning to implement a version of MPI on its hardware.

Performance tests we conducted proved to be of little value. Ethernet times and functionality were easily overshadowed by optical-electrical reported speeds. For example, moving one byte via Ethernet requires about 500 microseconds and optical-electrical requires less-than or equal to 1 microsecond. Also, reflective memory is not an option on Ethernet. Ethernet will not be a viable option for this environment until speeds matching the optical-electrical systems can be reached implementing reflective memory.

### **Recommendations**

In order to provide NASA with a flexible/scalable simulation system, I recommend utilizing Beowulf technology. My vision for IVHM and future simulation development is pictorially described in Figures 1 and 2. Each node in Figure 1 will have one or more CPUs and collaborate via MPI over an optical-electrical intranet. The nodes can be configured in sub-clusters within a rack or across racks. The sub-clusters can collaborate on a single simulation or execute different simulations. If more computing power is needed, another rack of nodes can be added. I believe the system as depicted in Figure 1 can be expanded to between 2 and 50 computing nodes without extra effort.

Figure 2 shows a Beowulf cluster modeling the human sensory system or IVHM. Each cluster utilizes the same architecture as in Figure 1. This design offers a very flexible/scalable system. As sensor technology advances, computing nodes with the appropriate sensor interface can be added and plugged into the IVHM simulation. Examining and evaluating sensor data as close to the sensor as possible is a paradigm easily incorporated. This is the architecture I highly recommend for IVHM and future simulation.

There are several issues of concern regarding open-source resources and off-the-shelf commodities that must be considered in the planning and design of a simulation system. Those issues include:

- 1) Use of open source technology. Open source is a good place to begin, but reliable support is found internally only. I have noticed as an open-source technology matures, volunteer support begins to diminish and industry will commercialize it provided there is a perceived market. Therefore, I highly recommend adoption of both of the following:
  - a. Development of an in-house knowledge base for supporting the open-source.

- b. Purchase of commercial adaptations of open-source tools allowing for technical support for as long as warranted.
- 2) Off-the-shelf computing nodes may not be acceptable because of their large footprint. I recommend using semi-customized, off-the-shelf computing nodes in order to save space. As indicate in Figure 2, space is a resource requiring constant attention.
- 3) A small 5 to 10 node Beowulf proof-of-concept system should be evaluated for both a simulation and IVHM.
- 4) Ask reflective memory vendors to show their wares on the above system.
- 5) Complete simulation/test of architectures; verify simulation accuracy of systems.
- 6) Verify simulation test-bed against representative workloads.
- 7) Use simulation test bed to study advanced application workloads and to set requirements for IVHM and future simulation.

### **Future Goals**

My future goals for this research include:

- Continue developing proof-of-concept system for three-dimensional memory model using Beowulf
- Use LAM-MPI in three-dimensional memory model development
- Examine MPI operations with optical-electrical networks if money is available
- Examine MPI coupled with OpenMP, an open source software for shared memory management/processing
- Create a prototype system
- Complete simulation/test of architectures; verify simulation accuracy
- Continue to work with NASA MSFC on IVHM

### **Conclusion**

For the purposes of developing a three-dimensional memory model, the time spent at NASA MSFC has provided me with the practical knowledge to begin my research. This opportunity has enabled me to build upon what had been an abstract vision. To start, I will use the Slackware version of Linux and LAM-MPI to lay the communication foundation and then examine OpenMP for the shared memory (between intra-node CPUs) part of the project.

It is interesting to note my research goal will provide benefits for both NASA's IVHM and simulation projects and myself. I believe IVHM will necessarily have an intelligent component and the results of my research will provide the fundamentals for an intelligent IVHM. I look forward to continuing to support NASA's IVHM project after returning to school and far into the future, hopefully even next summer.

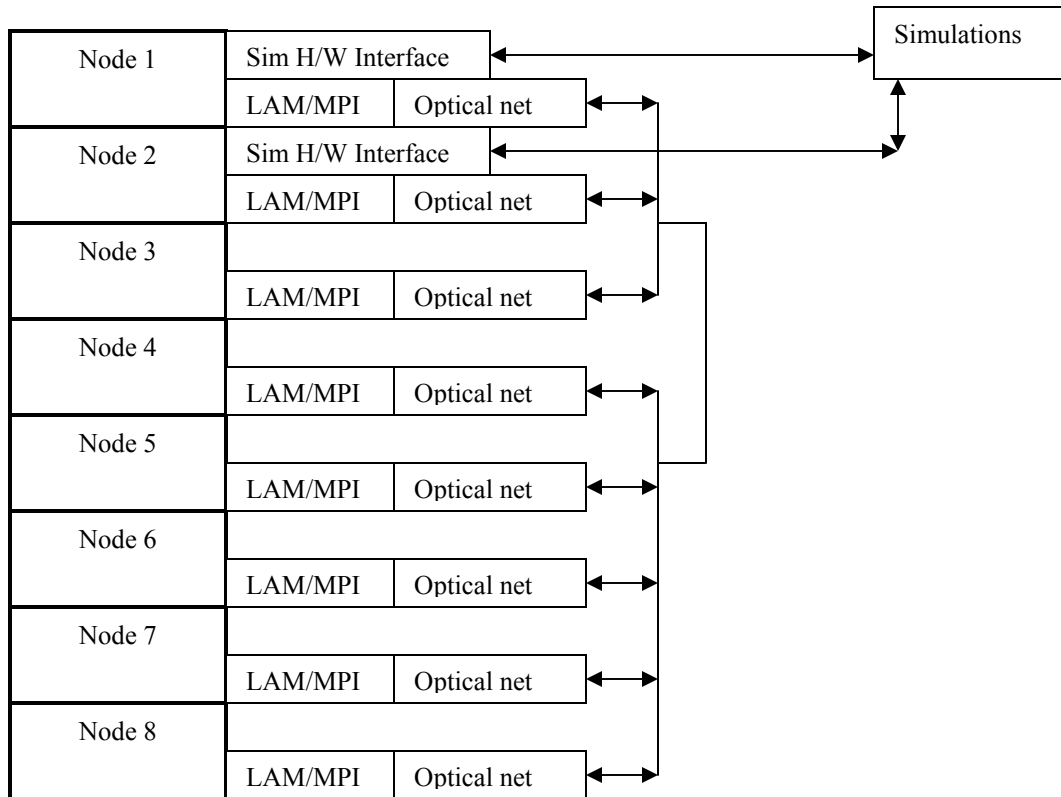


**FIGURE 1**

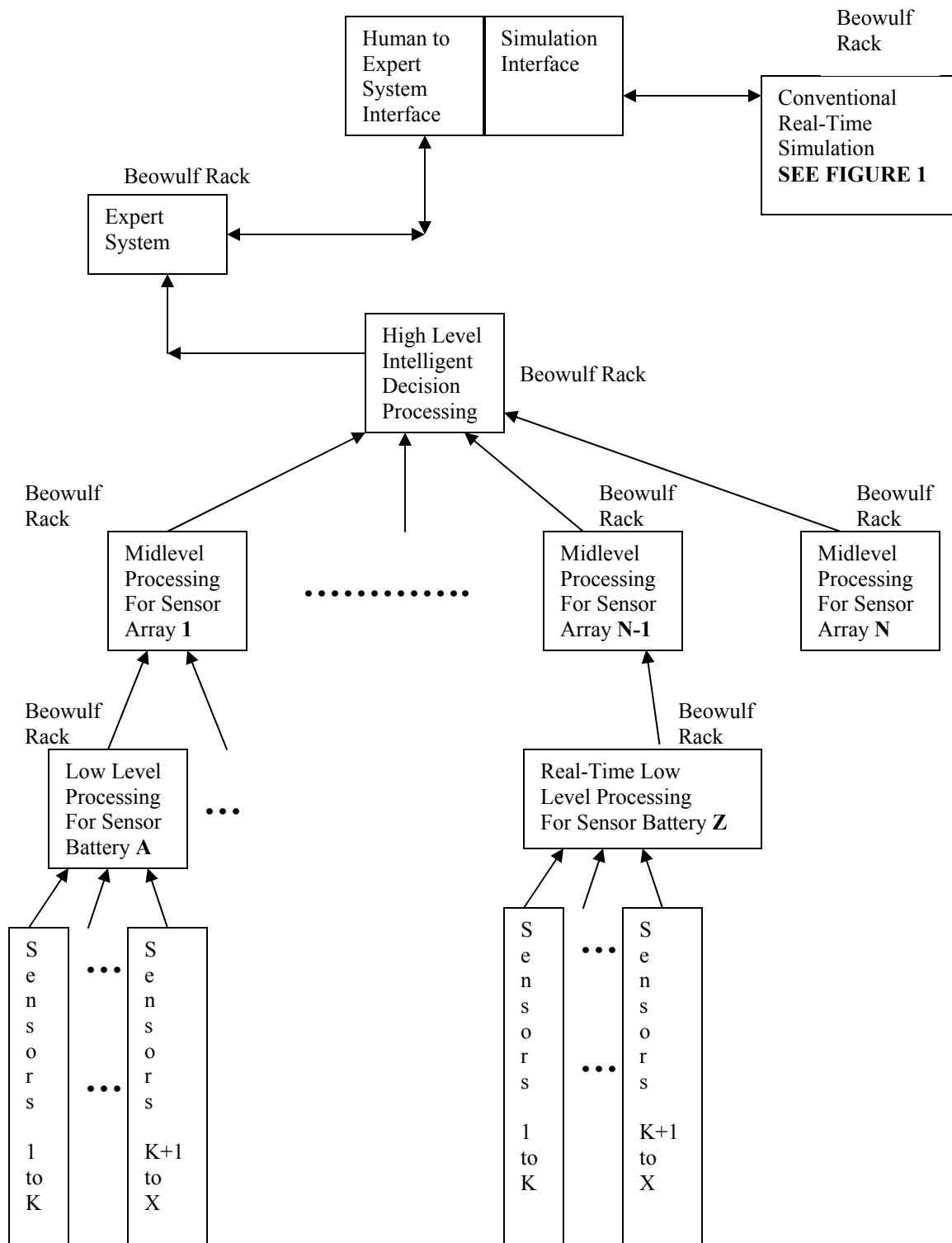
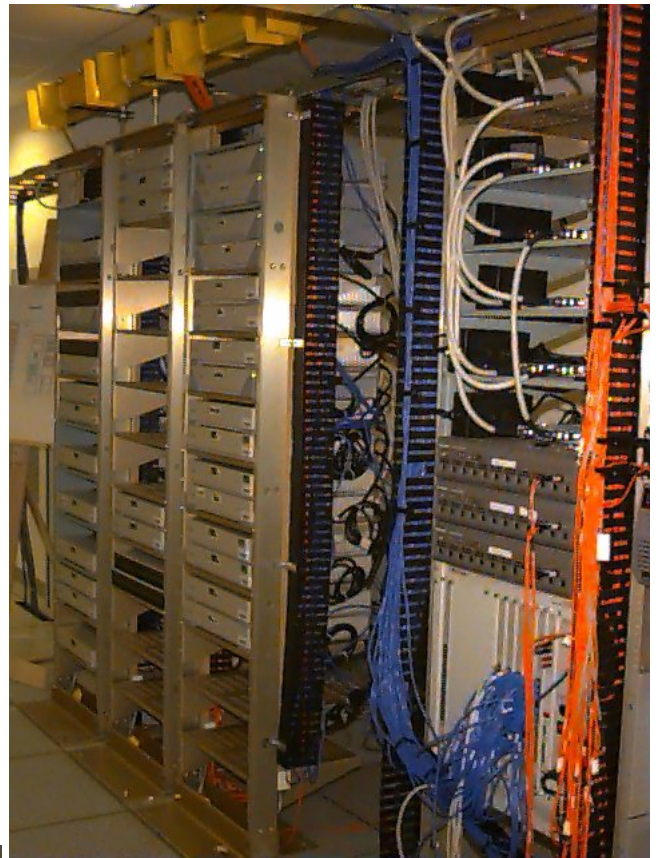


**Figure 2**



## BIBLIOGRAPHY

- [1] Author unknown. (2004, July 16). Skin: a Living Envelope--Protecting, Sensing, Repairing. Skin Science [On-line]. Available: [http://www.skin-science.com/\\_en/\\_ww/loreal-skin-science/proteger/organe.aspx?](http://www.skin-science.com/_en/_ww/loreal-skin-science/proteger/organe.aspx?)
- [2] Nave, Rod. (2004, July 16). Rods and Cones. Hyper Physics Sponsored by Georgia State University [On-line]. Available: <http://hyperphysics.phy-astr.gsu.edu/hbase/vision/rodcone.html>
- [3] Elert, Glenn (Editor). (2004, July 16). Surface Area of Human Skin. The Physics Factbook [On-line]. Available: <http://hypertextbook.com/facts/2001/IgorFridman.shtml>
- [4] Author unknown. (2004, July 16). Nervous System. Biologymad.com [On-line]. Available: <http://www.biologymad.com/master.html?http://www.biologymad.com/NervousSystem/NervousSystem.htm>
- [5] Chudler, Eric H. (2004, July 16). Brain Facts and Figures. Available: <http://www.hallym.ac.kr/~neuro/kns/tutor/facts.html>
- [6] Sterling, T. (Editor). (2002). Beowulf Cluster Computing with Linux. Cambridge, MA: The MIT Press
- [7] Pacheco, P.S. (1997). Parallel Programming with MPI. San Francisco, CA: Morgan Kaufmann Publishers
- [8] Cheng, Albert M. K. (2002). Real-Time Systems Scheduling, Analysis, and Verification. Hoboken, NJ. Wiley-Interscience, John Wiley & Sons, Inc.
- [9] Author unknown. (2004, July) LAM/MPI Parallel Computing [On-line]. Available: <http://www.lam-mpi.org/>

2004

**NASA FACULTY FELLOWSHIP PROGRAM**

**MARSHALL SPACE FLIGHT CENTER  
THE UNIVERSITY OF ALABAMA  
THE UNIVERSITY OF ALABAMA IN HUNTSVILLE  
ALABAMA A&M UNIVERSITY**

**INTEGRATION OF LAUNCH VEHICLE SIMULATION/ANALYSIS  
TOOLS AND LUNAR CARGO LANDER DESIGN (PART 1/2)**

Prepared By:	Yeu-Sheng Paul Shiue George Brian DeJean, Accompanying Student, Undergraduate Senior Jeffrey King, USRP Student, Undergraduate Senior
Academic Rank:	Professor
Institution and Department:	Christian Brothers University Mechanical Engineering Department
NASA/MSFC Directorate:	Engineering
MSFC Colleague:	Mr. Bill Pannell

## Introduction

Simulation and analysis of vehicle performance is essential for design of a new launch vehicle system. It is more and more demand to have an integrated, highly efficient, robust simulation tool with graphical user interface (GUI) for vehicle performance and simulations. The objectives of this project are to integrate and develop launch vehicle simulation and analysis tools in MATLAB/Simulink under PC Platform [2, 3], to develop a vehicle capable of being launched on a Delta-IV Heavy Launch Vehicle which can land on the moon with the goal of pre-implanting cargo for a new lunar mission, also with the capability of selecting other launch vehicles that are capable of inserting a payload into Trans-Lunar Injection (TLI).

The vehicle flight simulation software, MAVERIC-II (Marshall Aerospace Vehicle Representation In 'C'), developed by Marshall Space Flight Center was selected as a starting point for integration of simulation/analysis tools [1]. The goals are to convert MAVERIC-II from UNIX to PC platform and build input/output GUI's in the MATLAB environment, and then integrate them under MATLAB/Simulink with other modules. Currently, MAVERIC-II has been successfully converted from UNIX to PC using Microsoft Services for UNIX subsystem on PC. Input/Output GUI's have been done for some key input/output files. Calling MAVERIC-II from Simulink has been tested.

Details regarding Lunar Cargo Lander Design are described in Part 2/2 of the paper on page X-1.

## Roadmap to the Launch Vehicle Simulation (LVSim)

The possible modules for integration using MATLAB/Simulink with GUI for parameter inputs and outputs are shown in Figure 1.

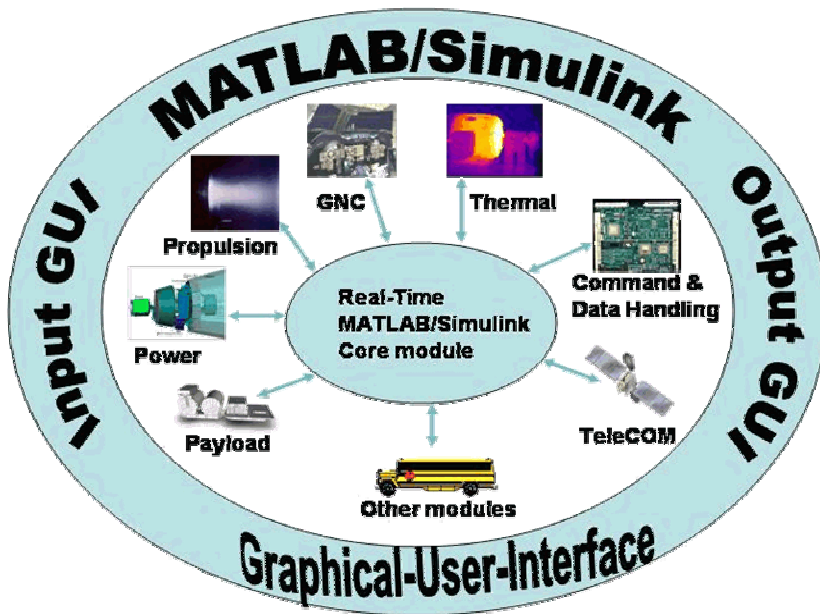


Figure 1: Integration of Launch Vehicle Simulation Tools

The optimal goal is to have all separate modules such as propulsion, GNC (guidance, navigation, and control), thermal, CDH (command & data handling), telecommunication, power, payload, and other modules, developed in MATLAB/Simulink and then integrate with input/output graphical user interface. Currently, propulsion module has been developed by the Transportation Directorate in Marshall Space Flight Center. MAVERIC-II, which was also developed by the Transportation Directorate, is mainly command-line simulation software that includes many modules that are available for integration. Therefore, conversion of MAVERIC-II to PC becomes the first step of this project. Next will be integrating propulsion module with MAVERIC-II. After that, other modules will need to be developed or extracted from MAVERIC-II to make the whole package as native MATLAB/Simulink software.

### Conversion of MAVERIC-II to PC

MAVERIC-II is a UNIX-based ANSI C 3- or 6-DOF Vehicle Flight Simulation Program. It can accommodate any vehicle configuration and flight phases. The main numerical integration engine is the TFrames software. It has become one of NASA's primary tools for simulating space transportation vehicle designs. The source codes of MAVERIC-II consist of 87 program files (77 C, 2 C++, and 8 FORTRAN) and 152 user-defined header files [4,5]. Figure 2 shows a screen shot of MAVERIC-II data screen.

```

Command Prompt - mav
MAVERIC < Marshall Aerospace Vehicle Representation in "G">
Project: GENERIC Case: Orb_28.5nom Version: 1.8.4 6/08/04
FltPhase.A: BST_ascent FltPhase.B: None Insertion: 0
time: 0.000000e+00 thrust.1: 5.289898e+06 thrust.2: 0.000000e+00
alt_Ft.B: 1.999995e+01 alphaDeg.B: -4.500000e+01 fEngineX.1: -5.284023e+06
headDeg.B: 0.000000e+00 betaDeg.B: 3.526439e+01 oxRem.1: 2.182622e+06
latDeg.B: 2.866168e+01 phibkDeg.B: 1.501402e+02 fuelRem.1: 8.083780e+05
lonDeg.B: 2.794500e+02 alphaCmdDeg: 0.000000e+00 oxRem.2: 5.871430e+05
vRelMagFt.B: 5.682581e-12 betaCmdDeg: 0.000000e+00 fuelRem.2: 9.785700e+04
mach.B: 5.090372e-15 phibkCmdDeg: 0.000000e+00 Stage_sep: 0
windSpeed.B: 5.682581e-12 qBarPsf.B: 3.835552e-26 Stage_sep: 0
fpaDeg.B: 9.000000e+01 qAlpha.B: -1.725998e-24 eng1_pwr.1: 1
eng2_pwr.1: 1 eng3_pwr.1: 1 eng4_pwr.1: 1
eng1_pwr.2: 0 eng2_pwr.2: 0 eng3_pwr.2: 0
fEngineX.1: -5.284023e+06 fEngineY.1: 0.000000e+00 fEngineZ.1: 2.492463e+05
axAccel.B: 1.169997e+00 qBeta.B: 1.352584e-24 azimToTAEM.: 9.454096e+01
normAccel.B: -5.518852e-02 alt_Nm.B: 3.291569e-03 rangeToHAC.: 4.911030e+03
totalMass.B: 4.516272e+06 heatLoad.B: 0.000000e+00 rangeToGoNM.: 4.911030e+03
speedSound.: 1.116339e+03 thetaSensed: -6.361109e-15 psiSensed.B: 1.908333e-14
phiSensed.B: -9.541664e-15 thetaNED.B: 8.999992e+01 mrCmd.1: 2.700000e+00
phiNED.B: -9.000000e+01 throttleCmd: 1.000000e+00 mrCmd.2: 6.000000e+00
aeroForceX.: -5.589382e-23 aeroForceY.: 0.000000e+00 aeroForceZ.: -8.625764e-23
Select -> Next Run Scroll Labels Quit Display Set Page 1 of 1

```

Figure 2: MAVERIC-II Data Screen

Since UNIX environment and PC Windows environment are completely different, the authors tried to use different approaches for conversion. MinGW 3.1 was first selected as a compilation tool which includes GNU C and FORTRAN compilers. However, the standard libraries and header files in MinGW are different from those on UNIX. Therefore, compilation was not successful. Cygwin was installed to emulate the UNIX environment on top of MinGW during the next try. Some head files are still not quite compatible. Finally, Microsoft Services for UNIX (SFU) 3.5 was selected as a subsystem on PC [6, 7]. The SFU is an interoperability

designed to streamline interaction between the Windows Server 2003 Family, Windows XP Professional and the Windows 2000 Family of operating systems and UNIX or Linux systems in heterogeneous networks. The Interix SDK that comes with SFU provides support for UNIX threaded applications and updated UNIX utilities and APIs.

With some changes on the MAVERIC-II source codes, all MAVERIC-II source codes were recompiled, linked, and run on PC under Windows XP Professional with SFU installed. Since the standard ASCII text file format on UNIX and PC are different, the source codes for input from a data file had to be modified. The comparisons of computation speed for MAVERIC-II to run on UNIX via Telnet and PC standalone are shown in Figure 3.

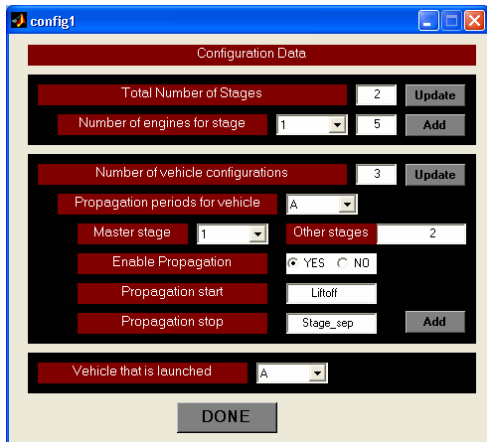
	1st Menu Case Selection	Popup Data Screen	1st Run up to 165.17 sec. w/ 1 sec. refresh	Continue Run up to 437.3695 sec.
MAVERIC on UNIX using Telnet	Immediate	1 sec.	15 sec.	18 sec.
MAVERIC on PC standalone	Immediate	1 sec.	12 sec.	17 sec.
MAVERIC on PC under MATLAB/Simulink	Immediate	1 sec.	12 sec.	18 sec.

Figure 3: Calculation Speed Comparisons

At the time of testing, MAVERIC-II was running on DEC ALPHA with eight 560MHz processors under Compaq Tru64 UNIX v5.1 operating system and Pentium 4 3.06GHz laptop with 512MB memory. The testing results will vary depending on the machines.

**Input/Output GUI**

Input and output graphical-user-interface for key data files has been developed. These GUIs can be standalone or integrated together in MATLAB/Simulink environment. These GUI modules will create exactly the same data files for MAVERIC-II setup and configuration. User can read in existing data and perform modifications. Figure 4 shows an example of input GUI for configuration file and its data file.



```

num_stages 2 # Total number of stages in this simulation.
num_engines 5 3 # Number of engines on each stage respectively.

num_vehicles 3 # Number of vehicle configurations in this simulation
# A Vehicle Configuration is a stack of stages
# to be propagated (can be a single stage).

```

```

-----
I N P U T #2
-----
#
# Vehicle Configurations and Propagation Periods
#
# In the following table, specify the stages that comprise each
# Vehicle Configuration. The first stage listed will be the "Master"
# stage. This is the stage that will be propagated and whose variables
# will be updated during propagation.
#
# Also specify in this table when the trajectory for each vehicle
# configuration is to be propagated. The Name of a mission events
# (see data/events.dat) or a literal time value can be used to indicate
# the propagate start and stop times. When the integration time reaches
# the Start time, the propagation of the stage stack will be triggered
# IF the enable flag is set to "Y" or "1".
#
#

```

PROPAGATION PERIODS FOR EACH CONFIGURATION					
	Stages	Enable	Propagation	Propagation	Propagation
			START	STOP	
vehicle_A	1 2	Y	Liftoff	Stage_sep	\$
vehicle_B	2	Y	Stage_sep	ORB_meco	\$
vehicle_C	1	N	Stage_sep	BST_impact	\$

NOTES: The first stage listed is the "Master" stage for that configuration.  
The Mission Events are defined in dataw/events.dat .

Figure 4: Example Input for Configuration and Data File

Since output data from MAVERIC-II are basically multiple columns data for different sets of output variables. An output GUI was developed to read a certain output data file. It will extract the header of the data file and allow user to select different variables to plot against each other. Figure 5 shows an example of output GUI and its data file.

```

FltPhase.A FltPhase.B Insertion time thrust.1 thrust.2 alt_Ft.B alphaDeg.B f
9999999. 9999999. 0.000000e+00 0.000000e+00 5.289999e+06 0.000000
9999999. 9999999. 0.000000e+00 1.000000e+00 5.925964e+06 0.000000
9999999. 9999999. 0.000000e+00 2.000000e+00 5.920170e+06 0.000000
9999999. 9999999. 0.000000e+00 3.000000e+00 5.920518e+06 0.000000
9999999. 9999999. 0.000000e+00 4.000000e+00 5.921010e+06 0.000000
9999999. 9999999. 0.000000e+00 5.000000e+00 5.921494e+06 0.000000
9999999. 9999999. 0.000000e+00 6.000000e+00 5.922436e+06 0.000000
9999999. 9999999. 0.000000e+00 7.000000e+00 5.923372e+06 0.000000
9999999. 9999999. 0.000000e+00 8.000000e+00 5.924461e+06 0.000000
9999999. 9999999. 0.000000e+00 9.000000e+00 5.925703e+06 0.000000
9999999. 9999999. 0.000000e+00 1.000000e+01 5.927100e+06 0.000000
9999999. 9999999. 0.000000e+00 1.100000e+01 5.928653e+06 0.000000
9999999. 9999999. 0.000000e+00 1.200000e+01 5.930361e+06 0.000000
9999999. 9999999. 0.000000e+00 1.300000e+01 5.932222e+06 0.000000
9999999. 9999999. 0.000000e+00 1.400000e+01 5.934240e+06 0.000000
9999999. 9999999. 0.000000e+00 1.500000e+01 5.936411e+06 0.000000
9999999. 9999999. 0.000000e+00 1.600000e+01 5.938737e+06 0.000000
9999999. 9999999. 0.000000e+00 1.700000e+01 5.941216e+06 0.000000
9999999. 9999999. 0.000000e+00 1.800000e+01 5.943855e+06 0.000000
9999999. 9999999. 0.000000e+00 1.900000e+01 5.946641e+06 0.000000
9999999. 9999999. 0.000000e+00 2.000000e+01 5.949581e+06 0.000000
9999999. 9999999. 0.000000e+00 2.100000e+01 5.952671e+06 0.000000
9999999. 9999999. 0.000000e+00 2.200000e+01 5.955911e+06 0.000000
9999999. 9999999. 0.000000e+00 2.300000e+01 5.959298e+06 0.000000
9999999. 9999999. 0.000000e+00 2.400000e+01 5.962829e+06 0.000000
9999999. 9999999. 0.000000e+00 2.500000e+01 5.966502e+06 0.000000
9999999. 9999999. 0.000000e+00 2.600000e+01 5.970316e+06 0.000000
9999999. 9999999. 0.000000e+00 2.700000e+01 5.974266e+06 0.000000
9999999. 9999999. 0.000000e+00 2.800000e+01 5.978350e+06 0.000000
9999999. 9999999. 0.000000e+00 2.900000e+01 5.982569e+06 0.000000
9999999. 9999999. 0.000000e+00 3.000000e+01 5.986904e+06 0.000000
9999999. 9999999. 0.000000e+00 3.100000e+01 5.991367e+06 0.000000
9999999. 9999999. 0.000000e+00 3.200000e+01 5.995949e+06 0.000000
9999999. 9999999. 0.000000e+00 3.300000e+01 6.000646e+06 0.000000
9999999. 9999999. 0.000000e+00 3.400000e+01 6.005452e+06 0.000000
9999999. 9999999. 0.000000e+00 3.500000e+01 6.010363e+06 0.000000
9999999. 9999999. 0.000000e+00 3.600000e+01 6.015374e+06 0.000000

```

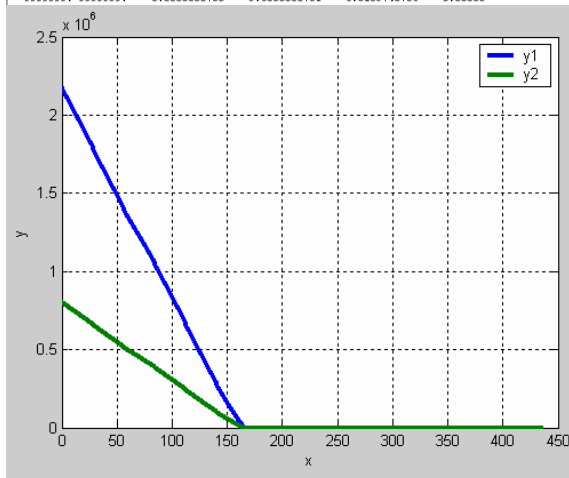
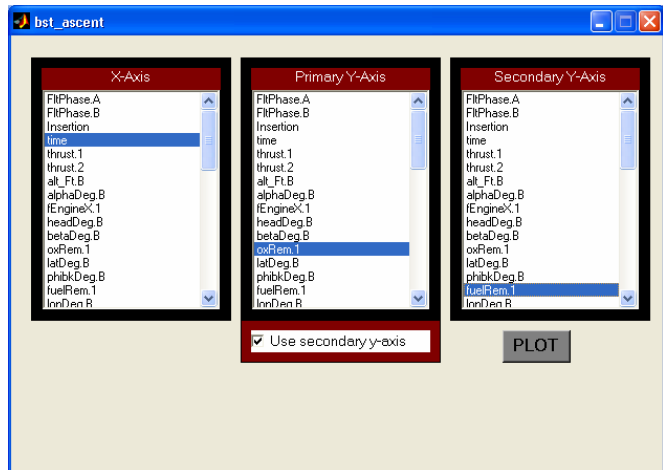


Figure 5: Example Output GUI and Data File

## **Conclusions**

As a result of this project, key input GUI modules for input data files were developed under MATLAB. MAVERIC-II was successfully converted and run on PC. Comparison of the calculation speed has been performed. The testing the existing propulsion module in Simulink and calling MAVERIC-II in Simulink has been done. This project shows great potential for future vehicle simulation and analysis. It provides user-friendly GUIs for input and output. After integrating all modules in Simulink, users can run real-time simulation. Also, data output could be streamed to Satellite ToolKit (STK) for visualization, communications and power analyses. Other modules such as Thermal, GNC, Telecommunication, and Data Handling will be converted to MATLAB/Simulink when they are available. It is found that MATLAB/Simulink is a great tool to create user friendly GUI for real-time simulations in different levels.

Clearly, Microsoft Services for UNIX has great advantages in migrating from UNIX to PC. It provides an UNIX subsystem for PC that will not sacrifice the performance of the PC.

Future works that lead to final integration include testing MAVERIC-II on other PCs, linking propulsion Simulink module to MAVERIC-II, acquiring other Simulink modules to be integrated, and continuing improvement of Input/Output GUI. The process of integration will take place piece-by-piece when necessary modules are available. Details regarding Lunar Cargo Lander Design are presented on page X-1.

## **Acknowledgements**

The authors would like to thank Mr. Bill Pannell, Mr. Bert Dolerhie, Mr. Geoffrey Beech, and all personnel in Engineering Directorate for providing a quiet but stimulating work environment and support. Also, the authors would like to thank the MAVERIC group in Transportation Directorate for their technical support.

## **References**

1. Jim McCarter, "Marshall Aerospace Vehicle Representation In 'C' (MAVERIC-II) User's Guide", 2<sup>nd</sup> Generation, NASA-MSFC.
2. James B. Dabney, "Mastering SIMULINK", Prentice Hall, 2004.
3. Stephen J. Chapman, "MATLAB Programming for Engineers", 2<sup>nd</sup> edition, Brooks/Cole, 2002.
4. Samuel P. Habison III, "C, A Reference Manual", 5<sup>th</sup> edition, Prentice Hall, 2002.
5. Peter Aitken and Bradley, "Teach Yourself C in 21 Days", Sams Publishing, 1994.
6. "Windows Services for UNIX 3.5 Reviewer's Guide", Microsoft Corp., 2004.
7. "Windows Services for UNIX 3.5 White Paper", Microsoft Corp., 2004.

**2004**

**NASA FACULTY FELLOWSHIP PROGRAM**

**MARSHALL SPACE FLIGHT CENTER**

**THE UNIVERSITY OF ALABAMA  
THE UNIVERSITY OF ALABAMA IN HUNTSVILLE  
ALABAMA A&M UNIVERSITY**

**An Open Source Simulation System**

Prepared By:	Thomas Slack
Academic Rank:	Assistant Professor
Institution and Department:	The University of Memphis Department of Engineering Technology
NASA/MSFC Directorate:	Engineering, ED 19
MSFC Colleague:	Drew Hall

## **Doing Real Time, without the Real Royalties**

An investigation into the current state of the art of open source real time programming practices. This document includes what technologies are available, how easy is it to obtain, configure, and use them, and some performance measures done on the different systems. A matrix of vendors and their products is included as part of this investigation, but this is not an exhaustive list, and represents only a snapshot of time in a field that is changing rapidly. Specifically, there are three approaches investigated:

1. Completely open source on generic hardware, downloaded from the net
2. Open source packaged by a vender and provided as free evaluation copy
3. Proprietary hardware with pre-loaded proprietary source available software provided by the vender as for our evaluation

The evaluation was one of two projects done in 10 weeks by two summer fellows of the NASA Faculty Fellowship Program (NFFP) at Marshal Space Flight Center (MSFC) and three undergraduate students all from different schools, two of whom were summer interns on the Visiting Researcher Exchange and Outreach (VREO) program. The third was a summer cooperative student. All of the work done by the group for ED 19 is stored in the Virtual Research Center (VRC) on line. The group will continue to collaborate with this mechanism over the next year and hopefully continue this effort next summer. The investigation was spit into two projects that were each headed by one of the faculty fellows. One was an investigation of collaborating networked computers the second is summarized in this paper.

The members of Division ED 19 had a goal to upgrade the capabilities of the Marshall Avionics System Test-bed (MAST) lab. A review of the capabilities of the lab is instructive. This is composed of hardware in the loop hard real time computer systems and robotic mechanism for simulating attitude adjustments. The robotic system consists of a table with roll pitch and yaw capabilities. Figure 1 shows a general view of how the systems interact to do hardware in the loop simulation. The system to be tested (T) is either strapped to the table, or in the case of some optical systems is positioned to look at an object strapped to the table. There may be additional simulation equipment and software (A) provided by the stakeholders involved in testing T. As much as possible T is placed in the environment and has the same signals that it would have in the real situation. Models of how the physical systems that are interacting with T may be in A, or in the MAST lab computers (M). M has the additional task of controlling the robotics in the lab to maintain whatever attitude that is needed for T to maintain the illusion of being on the mission.

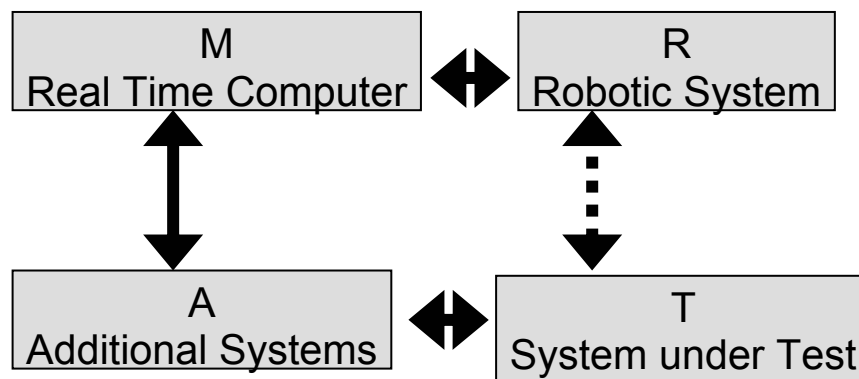


Figure 1: MAST Lab Equipment Configuration

This is a very simple view, but since the project was concerned with the upgrading and replacement of M, it is important to understand the capabilities required, but the details are less important.

The current computational capabilities of the computers, called M, are as follows: The systems, manufactured by Silicon Graphics Inc. (SGI), are called by them “Challenge” or “Origin” computers. They are an Irix OS on a multiple 200MHz MIPS processor shared memory platform. This platform has the capability of doing the functions described above, but should be upgraded as it is 7 years old. Since the upgrade was to be done, a review of the cost history of the MAST labs reveals that they are very expensive to maintain because of the software in the essentially proprietary systems build for NASA by SGI. There were also anecdotal incidences associated with the lack of software source that led personnel to look to systems that are open source.

During the course of the summer, it became apparent that the upgrade of the computer facility was timely because the new systems (particularly Integrated Vehicle Health Maintenance (IVHM)), that need to be simulated are orders of magnitude more complex than the ones simulated in the past. This fact points to using a different architecture for simulation than has been used in the past. More will be said about this in the Results and Conclusions section below.

It turns out that the real-time open source community on the Internet has made significant strides in the last few years, and so this upgrade is an opportunity to move away from more expensive proprietary towards an open source solution.

The goal then simply stated was to:

Define an architecture for open source based simulation systems to support large scale locally distributed simulations in real-time with hardware in the loop.

The part of the goal that this investigation covers is to discover what real time software is available in the open source community, how good is it, and how hard is it to use. We wished to examine and compare different systems from those available, so for the first two weeks of the summer we researched on the Internet to find what was available. The result of that search was collected in a matrix of currently available systems. This matrix, included on VRC, cannot be considered all encompassing.

## **The Test Systems**

### **1. System RTAI**

The first system is a completely open source system on generic hardware, downloaded from the net. This system is called RTAI, because RTAI was the open source real time kernel software used. The computer was placed on the desk of the author for use as a word processing and email tool during the summer. This turned out to be a Pentium 4 single processor system with 256 Mbytes of memory running at 2.523 GHz. This system was called debian after it was installed.

## 2. System RTLinux

The second system was an available Red Hat Linux system, called opus0, which was already in the MAST lab. This turned out to be a Dual processor Pentium 3 (Xeon) system with 1GByte of memory running at 2.795GHz. I turned hyper-threading off in an effort to be as time determined as possible. An evaluation copy of the RTLinuxPro software available from FSMLabs was installed on this system.

## 3. System Concurrent

The third system was provided as an evaluation by Concurrent Computer Corporation. This turned out to be a Dual processor Pentium 4 system with 2GBytes of memory running at 3.0 GHz. This system was provided with a real time clock card that is a key to the real time performance of the system. The other two systems achieved their real time performance by using a dual kernel model. This system used a modified Red Hat Linux 2.6 kernel that they call Red Hawk. Because the 2.6 kernel is fully preemptable, they did not use a dual kernel model to achieve the performance.

## Installation of the Systems

The PC the RTAI system was to be installed on had two partitions already created on its 18 GB disk. It was therefore fairly straightforward to backup the contents of the second partition onto the extra space on the first, and repartition the disk to have four partitions instead of two. The contents were restored to one of the three new partitions on a FAT32 file system volume; the other two became the swap space and root partition of the new Linux system to be installed. This process took about two days. Under ideal conditions it would take about two hours.

The next step was to install the Debian linux system. Once the Linux was installed, it was by default a 2.2.20 kernel. While, on the Debian CDs was source for several kernels none of them was 2.2.20. After discovering which sources were available on the CDs, and which were needed by RTAI, we discovered a match between the 2.4.17 linux kernel which we had a source for and with the 2.4.13 RTAI version. The next step was to rebuild that kernel and reboot with it. Once the new kernel was installed it had to have the RTHAL patch installed. The RTAI then installed without a hitch in a few minutes.

The second system, RTLinux, was a download from FSMLabs. They provided us with the key to a download from their FTP site, and we downloaded and installed their 2.4.18 kernel on Opus0. This first version did not boot at all. Opus0 has SCUZZY disks, which I understand are more difficult to boot from. We consulted with FSMLabs and they provided us with a second download with new drivers on it. This 2.4.25 kernel download booted correctly, but was a beta version of their software and had some other problems that made it hard for us to use. They also had not understood that we had a multiple CPU system. When we mentioned this to FSMLabs they worked for several days and provided us with a third version.

The third system, Concurrent arrived from the vender, fully functional. This provides one end of the spectrum of installation of the systems. The other end is provided by the RTAI system. Between these extremes was the experience of installing the RTLinux system provided by FSMLabs.

## **The Test**

FSMLabs provided a simple piece of code that we decided would be a good program to compare functionality on the different platforms. This code was written with POSIX threads. It creates a thread that has priority zero with the following steps:

1. Calculate a time approx. 1 ms in the future.
2. Ask the system to sleep till then.
3. Wake up and take the time.
4. Calculate how late you woke up.
5. Store the worst number you have found so far, and loop to 1.

This code was chosen and translated to the other two systems with minor changes. On the FSMLabs system, a second thread with very low priority was used to print the numbers each time a new worst case was found. The second thread shared the memory where the worst case was stored. The first thread would signal a semaphore each time it stored a new value in the worst case. The second thread would wake up and print the value sometime while the first thread was sleeping. Also on this system, a recording thread is generated for each CPU available. We added code that would make one CPU exclusively work with one thread. Since there were two CPUs on this system, after we turned hyper-threading off, we allowed the other CPU to handle all of the threads and processes left. In this way we hoped that the exclusive thread would be able to get the best results for this system.

On the RTAI system, the printing program was in a separate process. The programs communicated with FIFOs. Since this was a uniprocessor, the issue of making the CPU exclusively work on one thread did not arise.

On the Concurrent system, the translation was almost directly from the FSMLabs code, without the extra threads for each processor. This system has a special scheduler, which allows you to guard a CPU from interrupts and designate it as being exclusively being used by a single process. We used this scheduler to create two processes running the single thread. We guarded one CPU so that it would exclusively run the one thread. The other CPU was allowed to run the rest of the system. Since this system had hyper-threading turned on, we guarded both the other virtual CPUs so that they would be idle.

## **Results and Conclusions**

The results of the sleep-jitter test program are shown in Figure 2.

	Test duration	CPU0	CPU1
RTAI	89 min	17.4	
RTLlinux	25 min	92.85	158.24
Concurrent	60 min	133.82	

Figure 2: The Results of the Sleep-jitter test

As we look at these results we realize that there are many factors making the comparison weak. First the second two machines are symmetric multiprocessing machines, and the first is a uniprocessor. Second, the RTLlinuxPro system is a Beta release, and may therefore have some things not tested nor tuned. Third the second two machines are networked, and the first one, has

only a loopback interface working. With all of these weaknesses, I believe that the order of the systems would not be changed significantly, only the distance between them.

During my discussions of these technologies with the vendors, I got many numbers for the quickest interrupt latency that could be obtained. As they talked about the different systems that are out there they gave their opinion as to how the systems would fare in comparison. In general, this is the order that they gave. One thing can be said is that the completely open source solution is as at least as good any other available in pure performance.

As far as programming is concerned, when you are programming for RTAI it is certainly disconcerting at first to be continually adding modules to the kernel and removing them as you test software. It is also irritating to discover that under these conditions a normally rock solid Unix OS is as vulnerable to crashing as any Windows or Macintosh OS as you try out your software. After a while you get used to doing a sync before trying any new module just to be sure the disk is clean since you may have to power cycle the machine to get it back.

However, just because you do more programming in the user space, does not mean that you will be less likely to deadlock using RTLinux. It is the nature of real time programming on the edge of what a processor can perform to make an error that deadlocks the system regardless of the mechanism used to do it.

Of the three systems, the concurrent was the least likely to have a programming problem. This was because you could do the entire program in user space and in general test it. They use the fancy scheduler to play with placing it at a higher priority. You must pay a price in performance for this capability. First, it is using processes instead of threads to schedule. This is inherently less efficient. Second, the tools for tracing the operation must have some overhead however small.

Finally, we must consider the IVHM project when considering the upgrade. Such a project will lend itself to simulation by a large number of parallel CPUs working together. A benefit of using open source for real time simulation is that many more processors can be considered in the architecture because you are not paying for the software by the machine.

It is the opinion of the author that perhaps all of these systems be used in the upgrade of the computational facilities of the MAST lab. As a first step, an 8 processor CPU (perhaps with 4 now and upgradable to 8) with the concurrent technology be considered. This would be the development machine. A 16 or 32 node cluster of processors with minimal linux OS and either RTAI or RTLinux might be considered for the next addition. The ability to get the speed you need in the individual processors, at the same time control the whole with a overall system like that proposed by Gene Sheppard in his final report would give you the flexibility to expand to as large a system as you need.

The ability of the development machine to expand to multiple nodes as needed by tying the clock cards together is also a plus.

**2004**

**NASA FACULTY FELLOWSHIP PROGRAM**

**MARSHALL SPACE FLIGHT CENTER  
THE UNIVERSITY OF ALABAMA  
THE UNIVERSITY OF ALABAMA IN HUNTSVILLE  
ALABAMA A&M UNIVERSITY**

**FABRICATION OF 3-D PHOTONIC BAND GAP CRYSTALS VIA  
COLLOIDAL SELF-ASSEMBLY**

Prepared By:	Girija Subramaniam & Shannon Blank
Academic Rank:	Professor (GS), Student (SB)
Department:	Chemistry
Institution:	Penn State University
NASA/MSFC Directorate:	Science
MSFC Colleague:	Andrew Keys

## **Introduction**

The behavior of photons in a Photonic Crystals, PCs, is like that of electrons in a semiconductor in that, it prohibits light propagation over a band of frequencies, called Photonic Band Gap, PBG [1-5]. Photons cannot exist in these band gaps like the forbidden bands of electrons. Thus, PCs lend themselves as potential candidates for devices based on the gap phenomenon. The popular research on PCs stem from their ability to confine light with minimal losses. Large scale 3-D PCs with a PBG in the visible or near infra red region will make optical transistors and sharp bent optical fibers. Efforts are directed to use PCs for information processing and it is not long before we can have optical integrated circuits in the place of electronic ones.

## **Fabrication of PCs via Self-Assembly**

Many methods have been utilized to prepare PCs. Nanomachining [6], lithography [7] and 3-D holography [8, 9] are a few of the most commonly used but they suffer from being involved, complex, and expensive. These drawbacks also include the inability to produce uniform submicron ordering over large area. Self-assembly of colloidal silica spheres leads to opaline crystals with Face Centered Cubic (FCC) close packing.

Calculations and experiments show that these opal structures do not have a complete photonic band. However the inverse structures i.e. air spheres in high refractive index background dielectric material have a complete photonic band gap [10-12]. The goal of this project is to make the metallic inverse opal structure, a PBGM with complete gap. Tungsten inverse opals are of special importance because of their ability to modify thermal radiation [13-19]

The strategies to inverse opals involve the following steps:

Synthesis of Monodisperse silica spheres

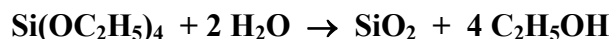
Self-assembly in Face Centered Cubic (FCC) packing to form the opal template

Infiltration of the interstitial air gaps with materials of interest

Removal of the template to form the inverse opal structure

## **Synthesis of Silica Spheres**

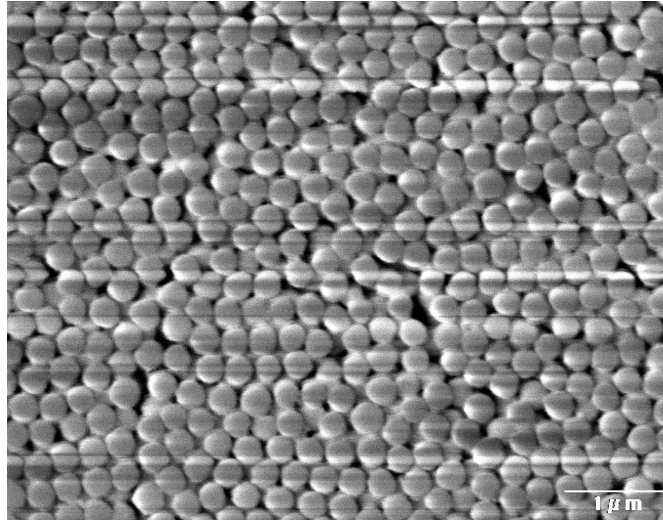
Highly monodisperse silica particles can be obtained by Stober's process [20]. It involves the hydrolysis of tetraethyl orthosilicate, catalyzed by ammonia in aqueous ethanol. Spheres with a diameter of 480nm were prepared successfully with very high monodispersity (reference 2003 report).



To prepare larger silica particles greater than 1 $\mu\text{m}$ , Giesche's continuous growth process [21, 22] was adapted. In the continuous growth process, reactants are added at a constant rate to a "seed," which is a suspension of smaller silica particles. During our trial, the rate of addition was increased many fold for lack of peristaltic pumps. To our surprise, absolutely no growth occurred

using the seed spheres of 1.4 $\mu\text{m}$ , instead the reactants mixed producing 280nm spheres (Figure 1).

**Figure 1: SEM Image of 280nm Spheres**



### **Purification**

Purification was done to decrease the polydispersity of the spheres by repeated wash with ethanol centrifugation. Monodispersity was checked using a Zetapal Size Analyzer and SEM measurements. SEM pictures clearly show that the bigger spheres ( $\sim 1.4 \mu\text{m}$ ) were highly polydispersed (Figure 2) in spite of purification.

**Figure 2: SEM Images of Polydispersed 1.4 and 1.2  $\mu\text{m}$  Spheres**



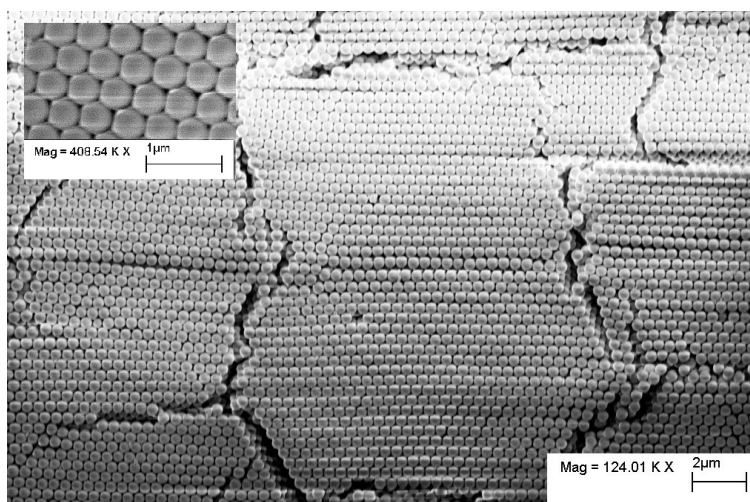
### **PCs via Self-Assembly**

Success of getting a uniform photonic crystal very much depends on the successful self-assembly of templates in FCC arrangement, which in turn, depends solely on the monodispersity of the

silica spheres. Various methods were tried to synthesize monodisperse spheres with partial success. The two primary methods of self-assembly utilized were room-temperature crystallization [23] and electrophoresis [24]. The electrophoretic method is faster than crystallization and produces uniform crystal deposition. Concentrations of 1%, 0.5%, and 0.33% v/v ethanolic suspension were used. The use of higher concentrations led to thicker deposits, but did not affect the uniformity. The spheres were deposited on ITO- glass and silicon-ITO electrodes.

Samples made via electrophoretic deposition tended to dislodge from the substrate easily making it difficult to perform infiltration. Although crystallization is quite slow, it produces stable and uniform crystal deposition, which is better suited for infiltration. The assembly is heated in an oven at 700°C by a 5°C ramp, held at 700°C for four hours and cooled to room temperature to make it robust. Almost all the samples cracked during this process and can be seen in Figure 3.

**Figure 3:** SEM Image of 480nm Spheres Deposited via Crystallization



### **Infiltration of Templates**

Low Pressure Chemical Vapor Deposition (LPCVD) has been shown to infiltrate silicon all the way to the substrate [25]. Since no Chemical Vapor Deposition facilities are available at MSFC, we tried to use:

- a. in *situ* chemical reactions
- b. sputtering for infiltration.

The possibility of using Physical Vapor Transport (PVT) is being explored.

#### **a. in *situ* Chemical Reactions**

Our preliminary trials were concentrated in trying to do in situ precipitations of gold, silver molybdenum and tungsten and were carried out by the general procedure as described below:

A drop of reactant A is placed on the crystals, kept covered for a few hours to ensure infiltration.

The excess A is wicked off; a drop of reactant B is placed to infiltrate and react over a few hours. The excess B is wicked off; a drop of water is placed briefly and wicked off. The crystals were allowed to dry.

One of the major problems encountered by us was the crystals with Si-ITO substrate tend to lift off completely in aqueous solutions; ethanolic solutions, on the other hand do not stay put and spreads immediately and evaporates away before it can infiltrate well into the structure. The reactions used for the precipitation of the metals are tried in vitro to establish the right conditions and to confirm the reduction to Zero oxidation state. X-ray fluorescence spectroscopy of the products from these last three reactions confirm the reduction proceeding to the metal level (Figures 4-6)

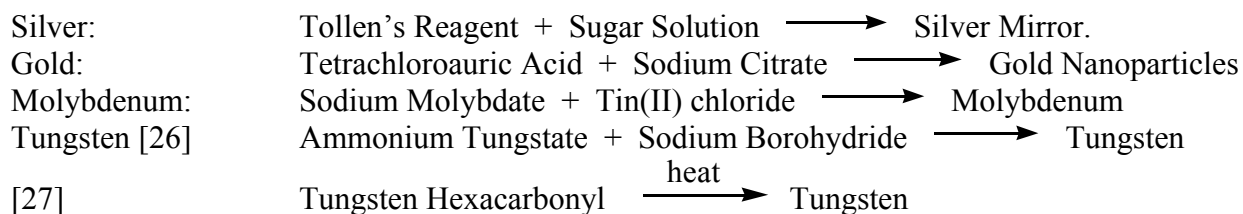


**Figure 4:** X-Ray Fluorescence Spectroscopy of Molybdenum

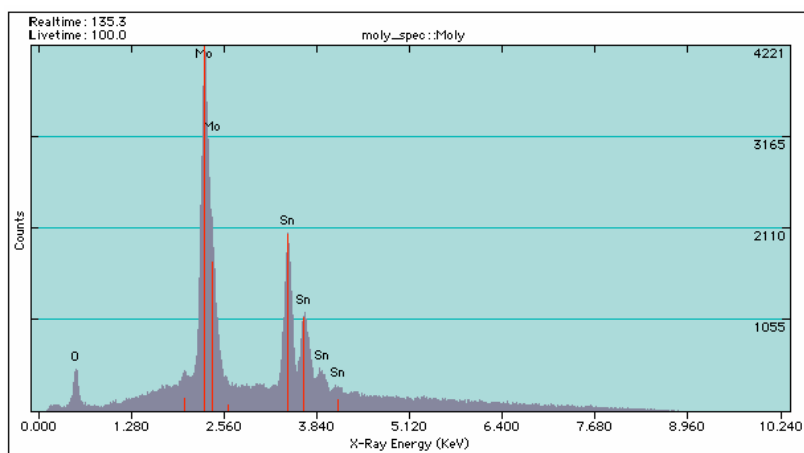


**Figure 5:** X-Ray Fluorescence Spectroscopy of Tungsten

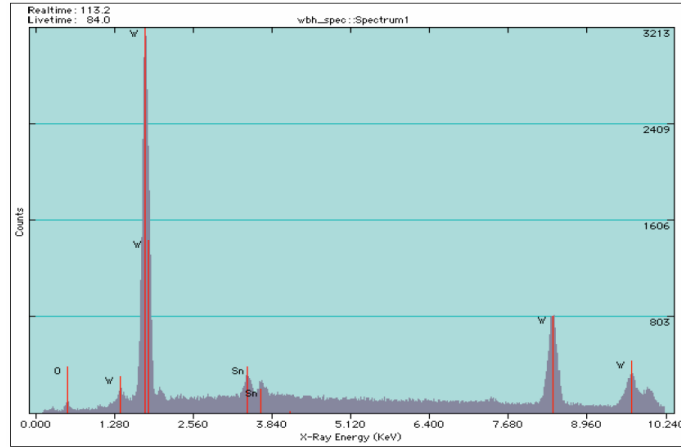
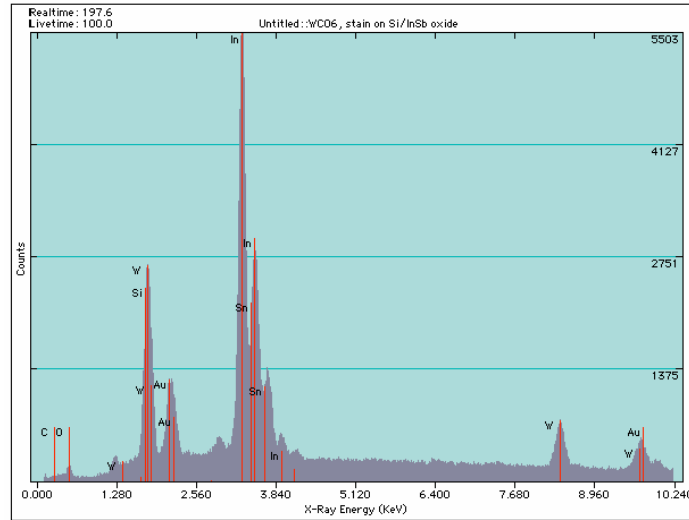
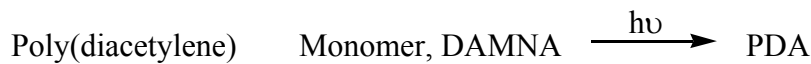


**Figure 6:** X-Ray of Tungsten From the Decomposition of  $W-(CO)_6$



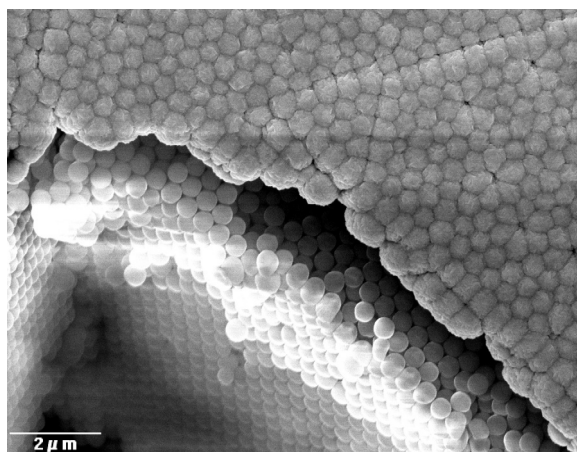
*In situ* polymerization shown below was also attempted:



**b. Sputtering**

The infiltration of silicon into the interstitial spaces was tried by sputtering with tungsten target. The tungsten coating was peeling off from the substrate and seems to hold a little better where on the crystal. Analysis of these samples was done using SEM to see whether tungsten penetrated all the interstitial sites. As Figure 7 clearly shows the tungsten just crystallizes on the first row of spheres, as expected. This may be a good way to make 1-D PCs.

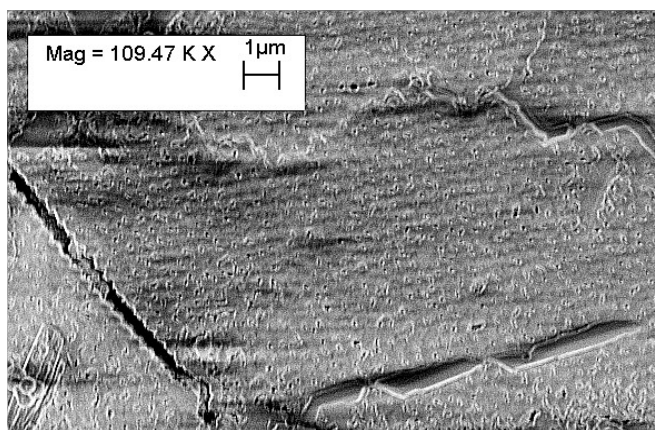
**Figure 7:** 480nm Spheres with Top Layer of Tungsten via Sputtering



### **Results from Infiltration**

Preliminary results indicate that silver grains are successfully infiltrated and we believe that the same is true of gold infiltration also. The infiltration of Molybdenum went very smooth with high efficiency as Figure 8 shows.

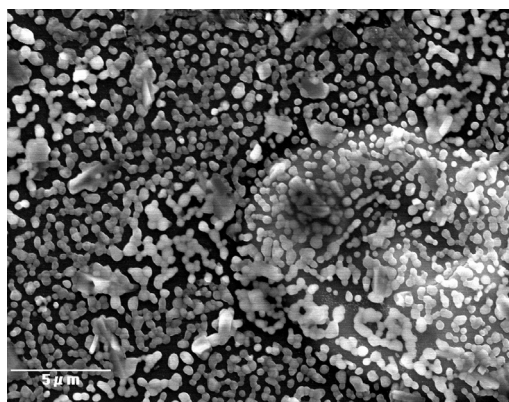
**Figure 8:** Sample Infiltrated by Molybdenum



Sodium borohydride reduction of ammonium tungstate is very fast at ambient temperature; however the tungsten reduction reaction proceeded via famous Tungsten blue in acidic medium and the evolution of gaseous hydrogen destroys the assembly. Non-destructive reduction of solid tungstate with glycerol proceeds at 170° but seems extremely slow with aqueous tungstate.

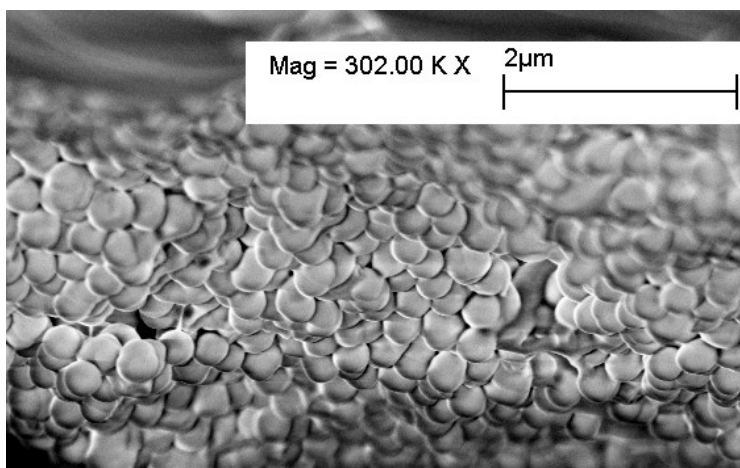
Another more direct route is by the thermal decomposition of tungsten hexacarbonyl, which as Figure 9 shows produces Tungsten at 700° C. We are exploring a very good solvent to dissolve hexacarbonyl for effective infiltration.

**Figure 9:** Tungsten From the Decomposition of  $W-(CO)_6$



The attempts to do *in situ* photochemical polymerization of diacetylene monomer, DAMNA failed. 7 hours of irradiation was unable to give the desired result which suggests that the rate of polymerization is either too low or it does not occur at all. This hurdle was overcome by infiltrating the polymer solution, instead of the monomer. Preliminary results indicate that the polymer does infiltrate through the voids, given enough time (Figure 10). The polymer used in this trial was mixed with 10% of Poly (hydroxymethyl methacrylate) to decrease the brittle nature of the Poly (diacetylene), PDA.

**Figure 10:** Sample Infiltrated by PDA



### **Removal of Template from Molybdenum Opal**

A drop of 1% HF was added over the crystal and allowed to remain for 20 min. It was noticed that after etching, the ITO coating is also etched off the glass substrate. The SEM analysis is yet to be done on the sample to see the success of the etching process to produce Mo inverse opals.

### **Future Efforts**

The project is still in progress. Our future efforts need to be directed in the following areas:

- To standardize synthetic efforts to make monodisperse micron size spheres
- To make the electrophoretic assembly stick to the substrate better
- To refine *in situ* infiltration techniques
- To explore PVT and LPCVD for infiltration

### **Acknowledgements**

The authors gratefully acknowledge Andrew Keys for the sponsorship. Special thanks are to David Smith, SD 46 for the use of the laboratory facilities. Special thanks are to Curtis Banks for help with sputtering. Thanks are due to Curtis Bahr and Sherryl Gallop and all other members of the Science Directorate who made my stay very pleasant at MSFC. The efforts of the NFFP coordinators Mike Freeman, Gerald Karr, Razi Hussan and Jeanelle Bland Day are very much appreciated. Thanks are also to Greg Nordin, Frank Berisford of UAH and Gregory Jerman of MSFC-ED 33 for SEM and X-ray fluorescence spectroscopy.

### **References**

1. S. John, *Phys. Rev. Lett.* **53**, 2169, **1984**.
2. P. W. Anderson, *Phil. Mag.* **B52**, 505, **1985**.
3. S. John, *Phys. Rev. Lett.* **58**, 2486, **1987**.
4. E. Yablonovitch, *Phys. Rev. Lett.* **58**, 2059, **1984**.
5. A. P. Bykov, *Sov. J. Quant. Electron.* **4**, 861, **1975**.
6. Fleming, J. G.; Lin, S.-Y. *Opt. Lett.* **1999**, *24*, 49.
7. Divliansky, I.; Mayer, T. S.; Holliday, K. S.; Crespi, V. H. *Appl. Phys. Lett.* **2003**, *82*, 1667.
8. Miklyaev, Y. V.; Meisel, D. C.; Blanco, A.; von Freymann, G.; Busch, K.; Koch, W.; Enkrich, C.; Deubel, M.; Wegener, M. *Appl. Phys. Lett.* **2003**, *82*, 1284.
9. Campbell, M.; Sharp, D. N.; Harrison, M. T.; Denning, R. G.; Turberfield, A. J. *Nature* **2000**, *404*, 53.
10. A. Moroz, *Phys. Rev. Lett.* **83**, 5274, **1999**.
11. R. Biswas, M. M. Sigalas, G. Subramania, and K.-M. Ho, *Phys. Rev. B* **57**, 3701, **1998**.
12. A. Moroz and C. Sommers, *J. Phys. Condens. Matter* **11**, 997, **1999**.
13. M. U. Pralle, et al., *Appl. Phys. Lett.* **81**, 4685, **2002**.
14. C. M. Cornelius and J. P. Dowling, *Phys. Rev. A*, **59**, 4736, **1999**.
15. Z.-Y. Li, et al., *J. Appl. Phys.* **93**, 38, **2003**.
16. Z.-Y. Li, *Phys. Rev. B*, **66**, **2002**
17. S. Y. Lin, J. G. Fleming, and I. El-Kady, *Opt. Lett.* **28**, 18, 1683, **2003**.
18. S. Y. Lin, J. G. Fleming, and I. El-Kady, *Opt. Lett.* **28**, 20, 1909, **2003**.
19. G. von Freymann and S. John, *Appl Phys. Lett.* **84**, 224, **2004**.
20. W. Stober, A. Fink and J. Bohn, *J. Colloid Interface* **26**, 62, **1968**.
21. H. Giesche, *J. Eur. Ceram. Soc.* **14**, 189, **1994**.
22. H. Giesche, *J. Eur. Ceram. Soc.* **14**, 205, **1994**.
23. P. Jiang, J. F. Bertone, K. S. Hwang and V. L. Colvin, *Chem. Mater.* **11**, 2132, **1999**.

24. A. L. Rogach, N.A. Kotov, D. S. Koktysh, J. W. Ostrander and G. A. Rogoisha, *Chem. Mater.* **12**, 2721, **2000**.
25. Y. A. Vlasov Y. A., X. Bo, Z. Strum and D. J. Norris, *Nature* **414**, 289, **2001**.
26. D. V. Goia, and E. Matijevic, *New J. Chem.* **11**, 1203, **1998**.
27. A. P. Patokin and V. V. Sagalovich, *Russ. J. Phys. Chem.* **50**, 370, **1976**.

2004

**NASA FACULTY FELLOWSHIP PROGRAM**

**MARSHALL SPACE FLIGHT CENTER**

**THE UNIVERSITY OF ALABAMA  
THE UNIVERSITY OF ALABAMA IN HUNTSVILLE  
ALABAMA A&M UNIVERSITY**

**The Effect of Infrastructure Sharing in Estimating  
Operations Cost of Future Space Transportation  
Systems**

Prepared By:	Meenakshi Sundaram
Academic Rank:	Professor
Institution and Department:	Tennessee Tech University Department of Industrial and Systems Engineering
NASA/MSFC Directorate:	Transportation
MSFC Colleague:	Steve Creech

## **Introduction**

NASA and the aerospace industry are extremely serious [1] about reducing the cost and improving the performance of launch vehicles both manned or unmanned. In the aerospace industry, sharing infrastructure for manufacturing more than one type spacecraft is becoming a trend to achieve economy of scale. An example is the Boeing Decatur facility where both Delta II and Delta IV launch vehicles are made. The author is not sure how Boeing estimates the costs of each spacecraft made in the same facility. Regardless of how a contractor estimates the cost, NASA in its popular cost estimating tool, NASA Air force Cost Modeling (NAFCOM) has to have a method built in to account for the effect of infrastructure sharing. Since there is no provision in the most recent version of NAFCOM2002 to take care of this, it has been found by the Engineering Cost Community at MSFC that the tool overestimates the manufacturing cost by as much as 30%. Therefore, the objective of this study is to develop a methodology to assess the impact of infrastructure sharing so that better operations cost estimates may be made.

## **Infrastructures**

Infrastructure in manufacturing refers to resources such as facilities, equipment, engineering and skilled labor, tooling, inspection devices, material handling devices, transportation equipment and methods and other requirements necessary to manufacture, store, and transport launch vehicles, both manned and unmanned. To manufacture launch vehicles, necessary equipment and buildings housing this equipment constituting the physical facility are required. The right engineering skills and critical touch labor skills are absolutely essential to build reliable and cost effective launch vehicles. Tooling in the form of assembly fixtures have to be built and maintained. Because of the low production volume, stringent inspection procedures and quality control measures have to be in place to ensure quality products. Unique inspection, test and other equipment may be necessary for each element of a launch vehicle. Soft tooling may lend some flexibility for manufacturing more than one element. Common tooling and inspection devices will also help reduce program costs and save considerable amount of lead time.

In the commercial world, especially in the automotive industry, it is not uncommon to see centralized design and development before the product design and tooling are passed on to an assembly plant. Automobile assembly plants are routinely built to assemble more than one type of vehicle on the same line. This practice is not very common in commercial aircraft manufacturing. However, aircrafts with different options are assembled on the same line. Due to extremely low volume of production in the case of space launch vehicles, the practice of infrastructure sharing has not taken off. But it is being looked at very favorably in the interest of reducing mission costs. The recent decision by Boeing to move the production of Delta II launch vehicles to the Decatur facility built to make Delta IV launch vehicle is an indication that infrastructure sharing

Will be necessary to realize economy of scale. To achieve cost reduction, it may be necessary to examine a program critically right at the conceptual design stage. Contract regulations may have to be modified to take advantage of infrastructure sharing. Infrastructure sharing will require that the vehicle design have common elements. For example the diameter of core and length may be very similar or the ratio of length /diameter may be very close. The major assumption here is that any required machining of panels is subcontracted and the facility is responsible only for the assembly.

### **Ground Rules**

The following ground rules are used in this study.

- Expendable launch vehicles
- Shuttle derived vehicle with a payload carrier similar to shuttle C
- Both ET and payload carrier are made at the same facility
- Limited production quantities
- Not more than four flights per year
- Units stored until use.
- Six year shelf life
- Shared infrastructure
- Examine only production phase

### **Methodology Used**

Extensive literature search was made using the REDSTAR library resources at Science Application International Corporation (SAIC). A report by Chrysler Corporation [3] describing how best the infrastructure at MAF could be better utilized was found to be invaluable. The report based on a study made in the early 70's is very thorough. It outlined a detailed capacity utilization plan for the manufacturing of orbiter and drop tanks at MAF. Several other documents related to external tank manufacturing and shuttle and shuttle-C were also reviewed. Documents available in the public domain describing the capabilities of MAF were reviewed. The LM-Michoud website was visited to get educated on the capabilities at the facility. MAF was visited with Spencer Hill, a colleague from the Engineering Cost Group at MSFC. The Lockheed Martin personnel that the author interfaced at MAF were very cooperative and provided extremely useful LM proprietary data. The author during the visit also made several interesting observations related to the study. These data were analyzed for the report. None of the data could be included in this report because of the proprietary nature of the data. It was found the facility to be a humongous one occupying over 800 acres. A lot of state-of-the art assembly and welding equipment are operational. The friction stir welding equipment is one-of-a-kind and very impressive. The fiber placement machine for composite materials was awesome. Richard Webb [6] of KT Engineering is another source that

provided data used in this study.

### **Production Rate Curve**

As described in the Parametric Cost Estimating Handbook [2], production rate effect may be explained as changes that can be expected in hours/unit of producing the X-the unit if an item is produced at a given production rate. If the production rate is increased, as can be expected, the hours for the X-the unit will decrease. Taking into account the effect of learning, the production rate curve may be described as below.

$$Y, \text{ Cost for the X-th unit} = A * X^b * Q^r \dots\dots\dots(1).$$

- Where A = Cost of the very first unit or the cost of Theoretical First Unit (TFU)
- X = Unit number
- b = Learning curve slope
- Q = Production Rate / Year
- r = Production rate curve slope

Obviously the net effect of adding the production rate effect (  $Q^r$  ) is to adjust the cost of TFU accounting for the production rate. It is stated in the NAFCOM99 manual [5] that the rate effect may be ignored or treated differently in different models. It is further suggested that the rate curve slope may be derived from historical data holding the learning curve slope constant. There could be a correlation between the production rate and the learning curve.

The author very strongly believes from the available historical production cost data of external tank at MAF, a different approach is required for developing the slope of the production rate curve. The historical ET production data could not be provided in this report in the interest of protecting the data. However, it should be pointed out that the total cost for producing up to four units remains at a constant level. This is due to the fact that a subcontractor doing the machining of aluminum panels would have to amortize most of the tooling and CNC programming cost with the first four units. Since all the fixed costs are to be absorbed in the first four units, it is suggested that a new rate curve slope. Note that this may vary from program to program.

Using the last three data points, the author determined the production rate slope to be 60%. The same approach used by several cost professional was used in developing the rate curve slope. The author is of the opinion that a different approach may be warranted. The rate curve slope computed does not deviate very much from the production rate curve slope being used by Richard Webb [6]. He has come up with a rate curve slope of 63.10% from data available in the public domain. In the judgment of the author based on the available ET production data, a 60% production rate curve slope would be justifiable whenever quantities produced are four or more. It should be cautioned that rate curve

might not be applicable for production quantities of less than four for items like ETs.

### **Effect of Infrastructure Sharing**

To investigate the potential cost savings that could be realized by making use of the available infrastructure and critical skills at MAF for more than one program, the operating contractor, LM was asked during the visit to quantify potential cost savings that can be expected using the concept of shared infrastructure. Since the LM personnel that hosted the visit were apprised of the intent of the visit they were prepared to provide the necessary data and answer many questions that the author had. Three major functional areas were identified. They are: facilities, overhead and management and skilled or touch labor. As a follow up, two of the LM cost personnel made a visit to MSFC and provided additional data in response to the author's request. During this visit meaningful discussions were made related infrastructure sharing. The LM personnel provided several interesting data related to capacity, critical skills, and overhead costs that can be used to justify the production of both ET and payload carrier at the same facility.

From the data collected in person and additional data provided during the follow up visit, the following inferences are made. Note that only general comments are made without disclosing any proprietary data.

- A savings of about 30% per year from the recurring cost may be realized if both ET and payload carrier are built at Michaud making best use of the available infrastructure and critical skills. The estimated savings are based on a build rate of 2/year for each program.
- The total cost (both DD&T and recurring) stabilizes after 2-units/ year.
- By extrapolation, it may be stated that a build rate of 3/year for each of the two programs will minimize the total unit cost.
- Labor costs and other direct costs may substantially be reduced with infrastructure sharing.
- Management and supervision costs may be reduced with shared infrastructure.

Further the following intangible factors may be considered in making a decision about infrastructure sharing.

- Availability of equipment facility without having to spend additional money on production and inspection equipment.
- Availability engineering and skilled expertise to minimize the effect of learning.
- Ease of managing more than one program.
- Better control of programs.

To verify the percentage savings with shared infrastructure claimed by LM, a method was needed. After examining a couple of possible methodologies, it was decided to embark

upon the weight based CER methodology. Weight based CER has been very well accepted and used among the engineering cost group at NASA. It is also documented very well in NAFCOM99 manual [5]. In spite of the fact that the NAFCOM software tool has been offering complexity generators approach to account correctly for a variety of cost drivers; the conventional first pound cost approach has still the merit. For many elements that have well defined geometries, it is possible to determine the weights accurately. The first pound cost approach effectively considers the unique / weight relationship for all hardware items.

Flight hardware cost may be estimated using the first pound cost approach from the equation below.

$$Y = A X^b \dots\dots\dots (2)$$

Where A = First pound cost  
X = Weight of the hardware  
b = slope

Slope values for different hardware items derived based on 100 different weight driven CERs obtained from parametric models developed at MSFC, GSFC, JPL, and NASA HQ are listed in a table in the NAFCOM99 manual.

A similar approach has been used in estimating the cost savings that could be realized if two programs with almost identical geometrical relationships were undertaken at the same facility. The geometrical relationship used to identify similarities is the length / diameter ratio. The two elements compared here are: structures and mechanism of ET and payload carrier.

The weight for the structures and mechanism for ET is 62,993 lbs. The first pound cost and the cost slope are: 0.0116 and 0.7 respectively for this element. Therefore the total cost of this element is computed as below.

$$Y = 0.0116 * 62,993^{0.7} = \$26.5438M$$

The estimated weight of a notional payload carrier is found to be 61,814 lbs. The cost slope for this element is also 0.7. Therefore the cost is computed as below.

$$Y = 0.0116 * 61,814^{0.7} = \$26.1950M$$

If these two elements were made at the same facility, the total weight would be 124,807 pounds. Using the same first pound cost and the cost slope values, the cost if these elements are made in the same facility is determined as below.

$$Y = 0.0116 * 124,807^{0.7} = \$42.8376M$$

If these two elements are made at different facilities, the total cost for making both the elements would be  $26.5438+26.1950 = \$52.7388\text{M}$ . If both of them are made at the same facility based on the total weight of the elements, the cost savings would be about  $\$9.9012\text{M}$ . This results in a percentage cost savings of 19%. The percentage cost savings is in line with the reported [4] cost savings by Lockheed Martin, the operating contractor of the Michoud facility.

## **Conclusion**

Several interesting and useful problems have been investigated, analyzed and reported here. The approach presented for developing the production rate curve slope seems to be very practical and realistic. If applied in practice for items produced at a rate of higher than four, it may prove to be very valuable. The approach indicated for determining potential cost savings that can be realized using shared infrastructure has some merit. It definitely warrants further investigation. The operating contractor of the Michoud facility has provided ample data and convincing percentage savings that could be realized if more than one program is undertaken at Michoud. This has been verified by a very simple methodology developed by the author. Even though, the potential savings estimated is different, the concept of infrastructure sharing has merit. It is prudent for NASA to take a serious look at the available infrastructure at Michoud in pursuit of developing cost effective future space transportation system for exploration of both lunar and mars planets.

## **Acknowledgements**

The author would like to thank the entire team of cost professionals in the Engineering Cost Group in the Transportation Directorate of Marshall Space Flight Center. Special thanks are due to Steve Creech, Barbara Stone-Townsend, Spencer Hill and Charles Hunt. The cooperation and unflinching help extended to the author by the Lockheed Martin personnel at Michoud is very much appreciated. It certainly was a very enjoyable and highly productive summer for the author.

## **References**

- [1] Blair. J.C., R.S. Ryan, Schutzenhofer. L.A., and Humphries. W.A (2001)., Launch Vehicle Design Process: Characterization, Technical Integration, and Lessons Learned
- [2] Booz Allen Hamilton (2003), *Parametric Estimating handbook*, NASA Contract Number: GS-23F-9755H
- [3] Chrysler Corporation Space Division (1972), Michoud Facility Utilization Study for the Orbiter and External LO<sub>2</sub> –LH<sub>2</sub> Drop Tank, Contract NAS 8-4016.
- [4] Lockheed Martin (2004), MSFC Engineering Cost Team Visit Report.
- [5] SAIC (1999), NASA/Air Force Cost Model 99, Version 6, and Contract Number: NAS8-40431
- [6] Webb, R. (2004), Operations Cost Model- Overview, Contract No. NAS8-02076

**2004**

**NASA FACULTY FELLOWSHIP PROGRAM**

**MARSHALL SPACE FLIGHT CENTER**

**THE UNIVERSITY OF ALABAMA  
THE UNIVERSITY OF ALABAMA IN HUNTSVILLE  
ALABAMA A&M UNIVERSITY**

**RACK DISTRIBUTION EFFECTS ON  
MPLM CENTER OF MASS**

Prepared By:	John T. Tester
Academic Rank:	Associate Professor
Institution and Department:	Northern Arizona University Department Mechanical Engineering
NASA/MSFC Directorate:	Flight Projects
MSFC Colleague:	Jon Holladay

## Introduction

This research was in support of exploring the need for more flexible "center of gravity" (CG) specifications than those currently established by NASA for the Multi-Purpose Logistics Module (MPLM). The MPLM is the cargo carrier for International Space Station (ISS) missions. The MPLM provides locations for 16 standard racks, as shown in Figure 1; not all positions need to be filled in any given flight. The MPLM coordinate system ( $X_M$ ,  $Y_M$ ,  $Z_M$ ) is illustrated as well. For this project, the primary missions of interest were those which supply the ISS and remove excess materials on the return flights. These flights use a predominate number of "Resupply Stowage Racks" (RSR) and "Resupply Stowage Platforms" (RSP). In these two types of racks, various smaller items are stowed. Hence, these racks will exhibit a considerable range of mass values as well as a range as to where their individual CG are located.

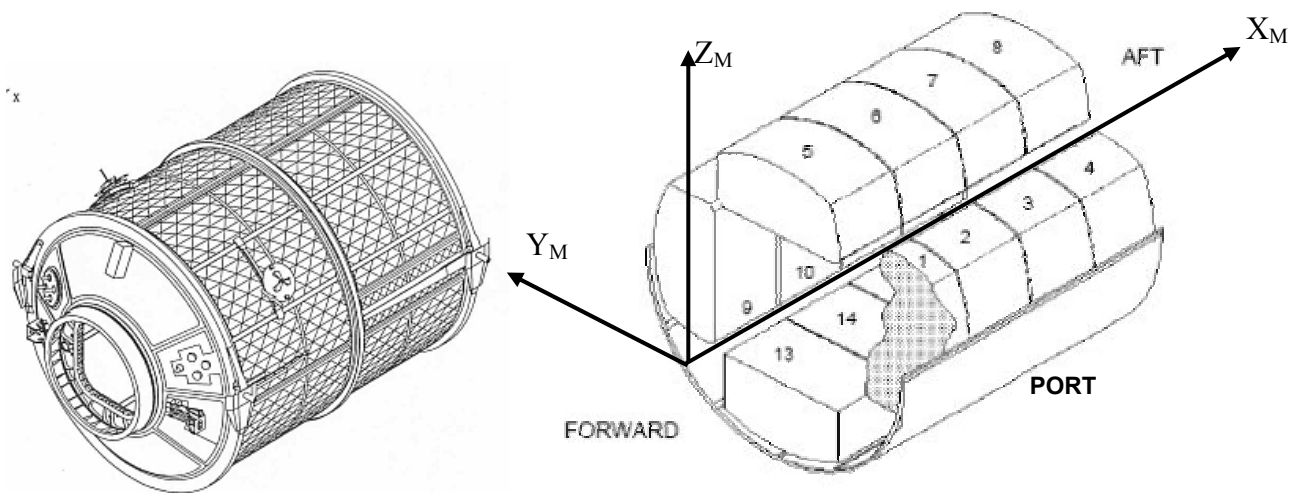


Figure 1: MPLM (left) and schematic of racks arrangement (right).

There are two aspects to this packing problem: Designing the MPLM rack organization such that the  $CG_M$  will exist within a specified allowable space (Figure 2) and ensuring that *calculated*  $CG_M$  and mass will be sufficiently accurate to match the *measured* corresponding values once the MPLM is packed. For this report, the first scenario is termed "packing design;" the second comparison process is termed "packing validation." For the purposes of this summer study, any RSR or RSP can go into any of the 16 MPLM positions for the ISS support missions.

A Manifest Flexibility Task (MFT) study, conducted by the Johnson Space Center (JSC), evaluated a limited number of alternative MPLM payload scenarios for their resulting loads on the individual rack fittings.[3] This study was used as a baseline for establishing numerous  $CG_M$  alternatives based upon variations in individual rack CG. In past flights, the RSR and RSP exhibited a wide range of masses and a relatively wide range of CG. The MFT used a series of analysis categories: Liftoff, Heavy Landing and Light Landing. The Liftoff and Light Landing categories were conducted with the rack masses at (essentially) the same masses as those recorded in previous STS/MPLM flights. The Heavy Landing category used heavier masses for the racks, about 80 – 100 lbm heavier than that used in the true flight record. Within each of

these mass categories, the racks had further alternative settings per computer simulation. These options were established as low and high values of the rack CG within ranges based upon past flight histories; for brevity, a summary of these cases is given in Table 1, and Figure 3 illustrates these CG locations. As historical data was only available for the landing scenarios, the Light Landing and Heavy Landing situations were the only scenarios explored this summer.

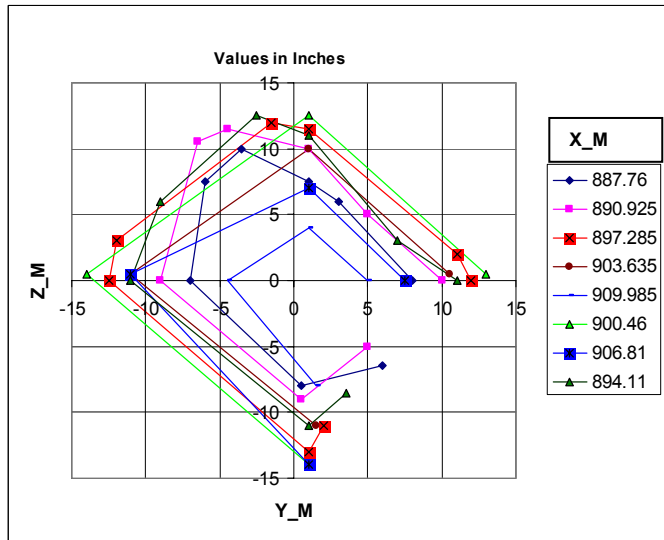


Figure 2: Allowable envelope of  $CG_M$ . [1]

Table 1. Rack CG alternatives for each MFT loads analysis.

CASE →	A	B	C	D	Nominal (Nom)
$X_{rack}$	NOM (RSP)	NOM (RSP)	NOM (RSP)	NOM (RSP)	NOM
	LOW (RSR)	LOW (RSR)	HI (RSR)	HI (RSR)	
$Y_{rack}$	LOW (RSP)	LOW (RSP)	HI (RSP)	HI (RSP)	NOM
	NOM (RSR)	NOM (RSR)	LOW (RSR)	LOW (RSR)	
$Z_{rack}$	LOW	HI	HI	LOW	NOM

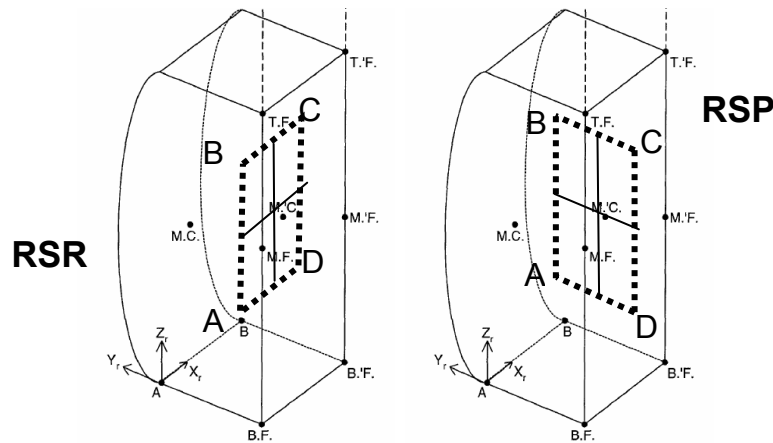


Figure 3: Alternative sub-cases for RSR and RSP local CG.

### Problem Definition

The CM of any object is given at right, , where  $N$  is the number of racks used in the manifest,  $x_i$  is the x-axis position of rack  $i$  in the MPLM frame,  $m_i$  is the mass of rack  $i$ , and  $i = 1, 2, \dots, N$ .

$$CG_{M-X} = \frac{\sum_{i=1}^N x_i m_i}{\sum_{i=1}^N m_i}$$

Equivalent equations are apparent for  $Y$  and  $Z$  of the  $CG_M$ . For the problem at hand, MSFC desired to have many different, discrete alternatives for the CG of the racks examined for trends in overall CG location. Thus, a program was developed in MatLab in order to enumerate combinations of rack locations for a given manifest, based upon Table 1. It is noted that with  $n$  rack positions,  $n$  racks to install, with  $k$  of type RSP (with only RSR being the other type allowed), the number of alternate examinations would be given in the equation below. The number of alternatives for return flight 6A, for example, had  $n = 16$ ,  $m = 8$ , and  $k = 4$ . Such a

situation produced a total of  $2.544 \times 10^{17}$  different  $CG_M$  results. Even if each calculation took only 0.001 second, it would require  $70 \times 10^9$  hours of computer time.

$$alternatives = \left( 3^{3k} \right) \left( \frac{n!}{k!(n-k)!} \right) \left( \frac{k!}{m!(k-m)!} \right)$$

Thus, only variations in the end racks were considered for this summer, as the end racks contained racks with the largest  $x_M$  values, resulting in the greatest moment arm shifts in the  $CG_M$  from the  $CG$  equation.

## Results

Many different computation runs were examined, more that can be illustrated in this summary report. Figure 4 shows the packing difference of the MFT cases. 23 out of 30 results exceeded the 1" specification. One conclusion in this limited study is that varying the racks tolerances significantly in the Verification Loads Analysis (VLA) process will result in a higher potential for larger packing differences. This trend is confirmed in the enumerated studies as well.

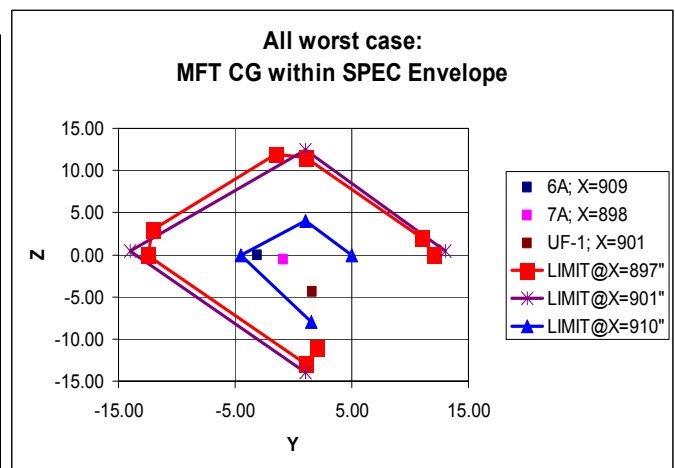
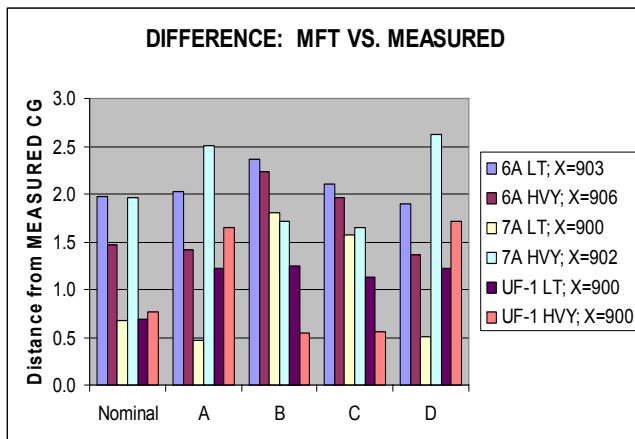


Figure 4: MFT Packing differences.

Figure 5. Worst case  $CG_M$  in envelope.

Figure 5 shows the 6A, 7A, and UF-1 return flight worst-case scenarios for off-axis  $CG_M$  in the enumerated case studies. In the lightest-loaded flight (6A), the  $CG_M$  is trending towards its envelope limit. This chart, along with other data, suggests that lightly-loaded MPLM missions have much more variable potential to be loaded “off-balance.” However, even for the worst case of this specific manifest, the  $CG_M$  is still within the dimensional envelope. Additional data show also that heavier missions tend to have less packing differences than lighter missions.

## Future Applications for the MSFC

In the case studies examined, the center of gravity was calculated in lieu of the maximum loads exerted on the MPLM fittings. This focus was based upon the assumption that the  $CG_M$  position is correlated to such maximum loads. Work from the MFT should have data, not reported, which should allow correlation analyses to be conducted as a preliminary confirmation. If the  $CG_M$  – maximum loads correlation is proved valid, then using the  $CG_M$  as a screening tool for extreme loading cases would be a valuable in STS mission planning and future vehicle design studies.

As part of investigating the VLA process, the author discovered that many different dynamic and structural computer models were required for validating each mission payload.[2] This multi-layered and time-consuming is likely due to limitations of computing power over two decades ago, when the STS was initially developed and deployed. This project, combined with new

computing technology, may encourage streamlining of the VLA process by constructing a single VLA model. Additionally, modern search techniques can be used with the integrated model to examine the safety of multiple missions simultaneously.

### **Resources**

This research utilized routine office personal computer resources available in the Pressurized Carriers Group. Additionally, MatLab was used to conduct the comparisons and enumerations. MatLab was also used to construct plotted data. Microsoft Excel was also used to prepare tables for MatLab input, as well as providing some plotted results. If the correlation analysis were performed in the future, the MatLab Statistics Toolbox module should be purchased for use. Consideration should also be given to access the Engineering Directorate computational resources in the dynamics and structural areas for future research.

### **Conclusions**

The analysis of the MPLM CG is a potentially complex problem to address. By restricting early studies to a few manifest alternatives, the problem becomes manageable, but the results are only valid for those studied manifests. The rationale for restricting such studies is understandable, in light of the literally trillions of alternative scenarios to examine if all possible manifests were considered. However, the MFT report and the results of the CG enumerations conducted by this researcher are only truly valid for the specific manifests under examination. For a more thorough understanding of physical manifest variations (as opposed to the rack variations) to be accomplished, a probabilistic-based analysis is recommended, whereby the discrete factors amongst the racks are assigned estimated values. This approach allows for an estimated  $CG_M$  mean to be determined, with an associated deviation and even confidence level. This data can subsequently be input into a probabilistic dynamics and structures model, enabling far fewer computational runs, yet giving statistically valid results.

In order to study the manifest design problem, advanced computer tools should be surveyed in order to determine the best approach for handling the large number of manifest variations. The use of recent computational design tools, such as genetic algorithms, simulated annealing, or neural networks, may aid in future manifest packing designs.

### **Acknowledgements**

The author thanks the Pressurized Carriers Group in the Marshall Space Flight Center's Flight Projects Directorate. Scott Prichard, from Teledyne Brown Engineering, was especially helpful in providing historical rack data for this project.

### **References**

- [1] MPLM Interface Definition Document, 11/14/2003, ISS-MPLM-IDD-006 Rev E.
- [2] Structural Integration Analysis Responsibility Definition for Space Shuttle Vehicle and Cargo Element Developers, 1/19/01, NSTS 37329 Rev B..
- [3] Gardner, S., Manifest Flexibility Task – Loads Analysis Summary, Technical Memorandum SCIS-TM-03-017, 3/31/03.

2004

**NASA FACULTY FELLOWSHIP PROGRAM**

**MARSHALL SPACE FLIGHT CENTER**

**THE UNIVERSITY OF ALABAMA  
THE UNIVERSITY OF ALABAMA IN HUNTSVILLE  
ALABAMA A & M UNIVERSITY**

**A SUMMARY OF NASA SUMMER FACULTY FELLOWSHIP  
WORK IN THE E.O. OFFICE AND  
IN THE EDUCATOR RESOURCES CENTER**

Prepared By:	H. Wendell Thompson, Sr.
Academic Rank:	Associate Professor
Institution and Department:	Alabama A & M University Department of Secondary Education
NASA/MSFC Directorate:	Equal Opportunity Office/ Educator Resource Center
MSFC Colleague:	Mr. Willie Love

## **Introduction**

The Office of Equal Opportunity supports a number of summer programs which are designed to: 1.) Increase the number of elementary and secondary students and teachers who are involved in NASA-related education opportunities; and 2.) Support higher education research capability and opportunities that attract and prepare increasing numbers of students and faculty for NASA-related careers.

A part of my work in the E.O. office involved the evaluation of several of the programs in order to determine their level of success and to make recommendations for the improvement of those programs where necessary. As a part of the involvement with one of the programs, the PSTI, I had the great opportunity to interact with the students in a number of their sessions which involved problem-based learning in science, mathematics and technology.

A summary of the evaluation of those programs is included in this report.

The second part of my work involved assisting the coordinator of the Educator Resource Center at the Space and Rocket Center. I participated in space science workshops for in-service and pre-service teachers. These educational resources were made available to the participants including many hands-on activities that they could take back to their classes. I participated in the three hour workshops that were offered on Tuesdays and Thursdays of each week, although there were workshops on other days. On Mondays, Wednesdays, and Fridays, I worked in the E.O. office. As a result of my work in the ERC, I developed a Directed Reading PowerPoint Lesson Plan Guide involving remote sensing entitled, "Echo the Bat." This was based on a NASA published children's book entitled Echo The Bat, written by Ginger Butcher. I have included a description of the lesson in this report.

A summary of the evaluations of several of the summer programs supported by the Equal Opportunity office are included in this report.

## **The Pre-Service Teacher Institute (PSTI) –Oakwood College, Sponsor**

The goal of the PSTI is to offer undergraduate and graduate students majoring in Early Childhood or Elementary Education at minority universities in a pre-determined region, an opportunity to spend two residential weeks at NASA and at Oakwood College fully immersed in the procedures and techniques of teaching science, mathematics, and technology to K-8 students. The objectives of the program are: 1.) To gain information about the classroom of the future; and 2.) To teach a lesson plan using problem-based learning to fourth graders. The success level was excellent over-all. The program met and exceeded objectives and measured outcomes. It also met an outside reviewer's indicators of success.

## **The Michael Anderson Research Program—Alabama A & M University, Sponsor**

The goals of the program were: 1.) To boost student enrollment by twenty to thirty percent, at least 50% of which will be minority female; 2.) To increase student retention in the engineering program by 50%; and 3.) To provide a quality learning experience for minority students who

pursue engineering, but are academically unprepared for the demands placed on them by the disciplines of an engineering curriculum. The objectives were: 1.) To encourage high school students to enhance their knowledge of science, mathematics, and technology through “hands-on” experimentation; and 2.) To inform parents of their role in getting their children prepared to study science, mathematics, engineering, and technology. The success level indicated that it is an excellent program. The verbal reports of both faculty and students indicated that the students benefited tremendously. There were a number of projects that were completed by the students including building solar powered boats which they raced across water, heart monitors, small motorized vehicles which had object sensors to enable them to change direction when they encountered an obstacle, and other similar technological products.

### **The I AM SET Project (Individuals With Disabilities in Math, Science, Engineering, and Technology---Alabama A & M University, Sponsor**

The goal of the I AM SET program is to provide educational science, technology and mathematics based opportunities for high school students with disabilities through monthly workshops, career development seminars, and 6-week summer internships in their field of interest at NASA/MSFC. The objectives of I AM SET were: 1.) To match students with professionals in different career fields to shadow them in the work environment for a few hours and heighten awareness of specific careers; 2.) To have industry tours which will help students to become aware of different career opportunities in business and industry; and, 3.) To provide summer jobs for high school and college students. An evaluation of the success level of the program indicated that it has experienced some degree of success in assisting students with disabilities to participate in NASA workplace environments which involve science, mathematics, and technology during the summer term.

### **The G.L.O.B.E. (Girls Leading Others By Example) Program---Lawson State Community College, Sponsor**

The goal of this program is to strengthen the SMET knowledge base of the underserved community and to increase the number of Hispanic and African-American females in grades 6-12 entering colleges/universities. The objectives of this program are: 1.) To involve Hispanic and African-American females in the Birmingham, Alabama area with an emphasis on grade levels 6-12; 2.) To engage local community college females as role models; 3.) To help students learn about different careers in space science and technology and mathematics through field trips and guest lecturers; 4.) To provide computer training workshops ranging in skills development from basic to advanced applications; 5.) To provide leadership/teaming approaches to learning; and 6.) To encourage “out of the box” thought processes. An evaluation of the success level revealed that the program met and exceeded the goals for this year.

### **The MISE (Minorities In Science and Engineering Program)---Oakwood College, Sponsor**

The goal of the MISE program is to increase the number of African-American scientists and engineers attending Oakwood College, Alabama A & M University, and minorities from the University of Alabama School System. The Objective of the program is to provide an opportunity for minority students enrolled at AAMU, Oakwood College, and UAH, to spend ten

weeks at the MSFC working full-time in the laboratories of prominent NASA scientists. This program has met and exceeded expectations. Evidence of the quality of this program may be seen in the success of former participants: Mr. Courtney Pace (a May, 2003 graduate of AAMU) was hired by Lockheed Martin in Sunnyvale, California as an engineer. Ms. Alicia Peters (a May, 2004 graduate of AAMU) was hired as a Computer Science Specialist 1 for United Space Alliance of Houston, Texas (a prime contractor for NASA's Space Shuttle operations.)

### **Project MI FUTURO---Stillman College, Sponsor**

The goal of this project is to provide a new and innovative curriculum for Hispanic students that helps them to study, stay in school, graduate successfully, and pursue higher education. The objectives are: 1.) To offer Hispanic high school students math, science, literature, career development, self-esteem, cultural, and entrepreneurial exploration, leadership and life-skills development through creative activities and the bio-track program; and 2.) To offer non-Hispanic students who are in 10<sup>th</sup> -12<sup>th</sup> grades, the opportunity to participate if certain criteria are met, including being willing to tutor Hispanic students at least two hours per week outside the normal classroom schedule. This program has met and exceeded the goals which were set. There has been a 100% high school graduation rate for the participants.

### **Educator Resource Center**

A major part of my work in the Center was preparing for, and assisting with the workshops on various topics related to space science that were held weekly. Another task involved greeting visitors to the ERC from all over the nation, as well as some international teachers, and supplying them with the materials that they requested, based upon the grade level that they were teaching.

I also developed a Directed Reading Lesson in remote sensing for a fourth grade class entitled, "Echo the Bat." This is from a children's book of the same title written by Ginger Butcher and published by NASA. A copy of the PowerPoint Lesson has been e-mailed to the NFFP office. Mrs. Chanel Leslie has indicated that she will use this lesson next summer with her PSTI students. I will use the lesson at Alabama A & M University in the Reading in the Content Areas course which I teach. An assignment will be given to the students which will require them to make use of the ERC in the development of lesson plans to teach reading skills in science, mathematics and technology.

### **Conclusion**

All of the programs that I reviewed this summer showed evidence of success in helping to inspire the next generation of explorers and should be continued if funding is available.

### **Acknowledgements**

The author would like to thank the entire staff of the Equal Opportunity Office for their assistance in my work this summer. I wish to especially thank Mr. Willie Love, Assistant Director of the EO Office, my Colleague, and Mrs. Chanel Leslie, my Mentor for their support. I

also thank Dr. Alease Sims, Coordinator of the Educator Resource Center and her staff for their patience, assistance, encouragement and support in helping me to become a part of their team of excellence. It may be noted that the staff received an award from NASA for their work in the ERC.

### **Reference**

Butcher, Ginger. (2000), "*The Adventure of Echo The Bat*," <http://imagers.gsfc.nasa.gov/k-4/>

**2004**

**NASA FACULTY FELLOWSHIP PROGRAM**

**MARSHALL SPACE FLIGHT CENTER**

**THE UNIVERSITY OF ALABAMA  
THE UNIVERSITY OF ALABAMA AT HUNTSVILLE  
ALABAMA A&M UNIVERSITY**

**ELECTROFORMED NICKEL-GRAPHITE COMPOSITE**

Prepared By:	Pei Xiong-Skiba
Academic Rank:	Professor
Institution and Department:	Physics and Astronomy Austin Peay State University
NASA/MSFC Directorate:	Space Science (SD 50)
MSFC Colleague:	Dr. Brian Ramsey
UAH Colleague:	Darell Engelhaupt

## Introduction

Future x-ray astronomy will demand larger optics than Chandra, currently in orbit. Ways must be devised to produce cheaper and lighter x-ray mirrors to save the cost of manufacturing and launching this future telescope. One technique, being developed at Marshall Space Flight Center and elsewhere, is electroformed nickel replication technique, wherein mirror shells are electroformed (using pure nickel or a nickel alloy) onto super-polished and figured aluminum mandrels and are subsequently released by cooling. This technique can produce relatively inexpensive mirrors, but is hampered by the high density of nickel ( $8.9 \text{ g/cm}^3$ ). An alternative is to develop a composite, with lower mass density and compatible mechanical properties to the nickel cobalt alloy, as the mirror shell material.

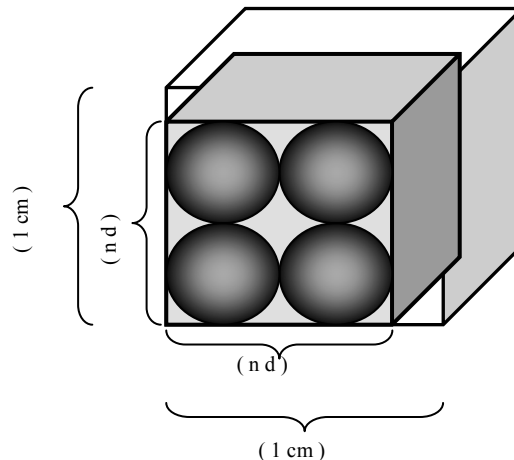
Electrocomposite films can be formed using traditional electroplating techniques in a plating bath mixed with various inert particles.[8,5,7,6] These composites typically have a considerably higher yield strength, hardness, and lower mass density than the pure metals. Assuming a composite is packed with identical spherical particles next to each other and the space between the spheres is filled with metal as shown in Figure 1, the density of this composite can be calculated using equation:

$$\rho_{com} = \frac{\pi}{6} \rho_{particle} + (1 - \frac{\pi}{6}) \rho_{metal} \quad (1)$$

Where  $\rho_{com}$ ,  $\rho_{particle}$ , and  $\rho_{metal}$  are the mass densities of the composite, the particle and the metal matrix, respectively. Figure 2 is a plot of  $\rho_{particle}$  versus  $\rho_{com}$  of the above equation at  $\rho_{met} = 8.90$  (nickel). As shown in figure 2, the mass density of the particle must be less than  $3.3 \text{ g/cm}^3$  for its composite to have mass density below  $6.0 \text{ g/cm}^3$  in this ideal case. In practice, the mass density of a composite would be higher than the value depicted by the graph due to particle size distribution and “poor particle packing”.

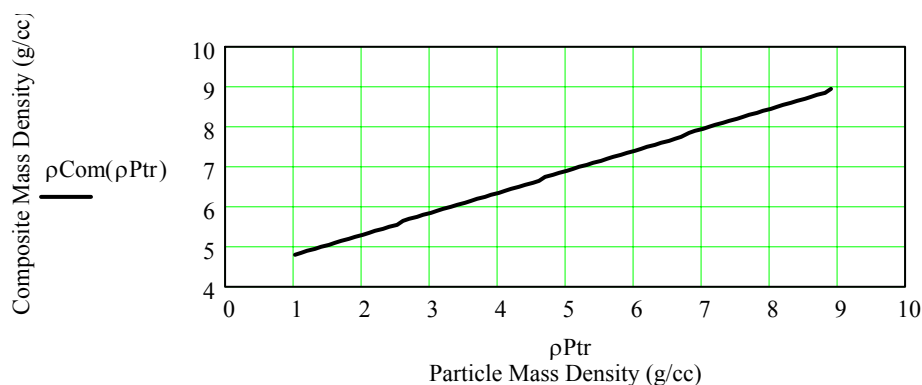
In a previous study [12] involving nickel and  $\gamma$ -phase alumina powder (mass density  $3.3 \text{ g/cm}^3$ ), we reported 23% alumina particle inclusion (by weight) using a special reverse pulse plating waveform. Applying this waveform, the deposit thickness per cycle is

Figure 1: Model for minimum theoretical density at maximum particle inclusion.



approximately the diameter of the particles at low duty cycle, the lowest mass density of the nickel-alumina composite achieved is  $6.4 \text{ g/cm}^3$ . Further reduction in mass density is desirable. Our goal for this study is to explore other composite systems to produce a composite with mass density less than  $6.0 \text{ g/cm}^3$ . Graphite is chosen in this study because of its low mass density,  $1.9 - 2.3 \text{ g/cm}^3$ , and availability (small sized powders, one micrometer or less, are commercially available.) The minimum theoretical mass density of this composite at maximum particle inclusion is  $5.2 \text{ g/cm}^3$ .

Figure 2: The theoretical minimum mass densities of composites as a function of mass densities of incorporated inert particles at maximum particle inclusions.



## Experimental

Nickel composite shells were formed in a 3.5-liter glass beaker. The electrolyte was nickel sulfamate bath as shown in Table 1. Synthetic graphite powder,  $1\text{--}2 \mu\text{m}$ , from Aldrich Chemical Company was used. All of the bath components were mixed with de-ionized water and blended in a blender for 2 minutes. The bath was stirred mechanically with a magnetic stirrer to keep the powder in suspension. The plating temperature was controlled automatically at  $47 \pm 1^\circ\text{C}$ . The pH of the bath was adjusted to  $4.0 \pm 0.2$  using sulfamic acid before plating each sample. The anode is a titanium coil in contact with nickel chips in a cylindrical basket. The cathode is a rotating nickel plated aluminum cone. After each shell was plated, the nickel composite shell (about  $220 \mu\text{m}$  thick) was removed from the cone using a mechanical pusher. The cone was then washed with Micro-90 concentrated cleaning solution and cotton wipes, rinsed with warm water and de-ionized water, dried with compressed air, dipped in  $5 \text{ g/L K}_2\text{Cr}_2\text{O}_7$  solution for 90 seconds to passivate the cone's metal surface, and further rinsed with de-ionized water. The cone was ready to be used again. KEPCO's BOP 20-20M bipolar power supply is used in this experiment to enable reverse pulse plating. This power supply was controlled by Labview software via a PC. The densities of the nickel-graphite composites were determined using Archimedes' principle.

## Results and Discussions

Many models have been developed throughout the years in attempting to understand the mechanisms of metal and inert particle co-deposition process.[4,1,3,9,11] It is understood the amount of particle incorporated is affected by the competition between the charge-transfer controlled metal deposition reaction and the mass-transfer limitation of the inert particle

deposition process. Generally speaking, the amount of particle incorporated increases as the particle loading in the plating bath increases. However, the gain is insignificant at particles loading above 20 g/L.[12,4] Thus, 20 g/L graphite powder loading was used for this study.

Table 1: Chemical composition of the electrolytes.

Nickel Metal as Sulfamate	100 g/L
Boric acid	35 g/L
Sodium Dodecal Sulfate (SDS) (wetting agent)	0.2 g/L
Graphite Powder (1~2 μm)	20 g/L

Unlike composites formed by metal matrix and inert particles, the conducting graphite powder makes it possible for this composite to plate in areas initially nonconductive during long time (more than 10 hours) plating. It is found that at 20 mA/cm<sup>2</sup> plating current density, about 50% of the composite was plated on the sample holder. Lowering the plating current density to 5 mA/cm<sup>2</sup> prevents this to happen completely. The current density threshold inhibiting this to happen lays between 5 mA/cm<sup>2</sup> to 10 mA/cm<sup>2</sup>.

Shell 4 was plated in direct current mode with 20 mA/cm<sup>2</sup> current density. Shell 6 and 10 were plated with reverse pulse plating waveforms. In the cases shell 6 and 10, the anodic current density was chosen twice that of the cathodic current density, as suggested by Tang, et al.[10] Shell 6 was initially plated by direct current at 10 mA/cm<sup>2</sup> current density for two hours followed by reverse pulse plating. Approximately two diameter (2D) of the graphite powder particles is plated and one diameter (1D) of the graphite powder particles is removed in each cycle. Shell 10 was initially plated by direct current at 5 mA/cm<sup>2</sup> current density for ten hours, then followed by reverse pulse plating (plating 3D and removing 2D.) As shown in table 2, mass densities of the composites continuously decrease as the duty cycle decreases.

Table 2 shows the mass densities of the composites plated under various conditions.

Shell #	Plating Mode	J <sub>C</sub> (mA/cm <sup>2</sup> )	T <sub>C</sub> (sec)	J <sub>A</sub> (mA/cm <sup>2</sup> )	T <sub>A</sub> (se <sup>c</sup> )	ρ(g/cm <sup>3</sup> )
4	DC	20	–	–	–	8.3
6	2D/1D	10	560	20	100	7.5
10	3D/2D	8	1050	16	250	5.62

The inner surface of this composite is rough, not suitable for mirrors. Most likely, an x ray mirror shell will require plating a thin layer of metal, such as nickel-cobalt alloy, followed by a thick nickel-graphite composite coating. This will increase the mass density of the mirror shell. The ratio of the composite mass (m<sub>com</sub>) to metal mass (m<sub>met</sub>) can be calculated for a targeted shell mass density using equation:

$$\frac{m_{com}}{m_{met}} = \frac{(\rho_{met} - \rho_{shell}) \cdot \rho_{com}}{(\rho_{shell} - \rho_{com}) \cdot \rho_{met}} \quad (2)$$

where ρ<sub>met</sub>, ρ<sub>com</sub>, and ρ<sub>shell</sub> are the mass densities of the metal, the composite, and the shell, respectively. Using our data, ρ<sub>met</sub> = 8.90 g/cm<sup>3</sup>, ρ<sub>com</sub> = 5.62 g/cm<sup>3</sup>, and ρ<sub>shell</sub> = 6.00 g/cm<sup>3</sup>, the mass ratio (m<sub>com</sub>/m<sub>met</sub>) should be larger than 5.

## **Conclusion**

Reverse pulse plating waveform, plating ND and removing (N-1)D each cycle, can be used in electroplating nickel-graphite composite to obtain low mass density. The lowest mass density of the composite achieved in this study is 5.62 g/cm<sup>3</sup>. This composite appears having sound mechanical properties, compared with brittle copper-graphite composite.[2] To inhibit nickel-graphite composite plating around sample holder, the cathodic current density should be kept below 10 mA/cm<sup>2</sup>, ideally at 5 mA/cm<sup>2</sup>. The roughness of the surface of the composite is not suitable for a mirror surface. Most likely, an x-ray mirror shell will require plating a thin layer of metal covered by a thick layer of nickel-graphite composite.

## **Acknowledgements**

The authors would like to thank William Jones for creating this research opportunity. This work is funded by NASA/SFFP (2004) program.

## **References**

1. J. P. Celis, J. R. Roos, C. Buelens, J. Fransaer, *Trans. Inst. Metal Finish.*, **69** (4), 133, (1991).
2. C.G. Fink and J.D. Prince, *Trans. Am. Electrochem. Soc.* **54**, 315 (1928).
3. J. Fransaer, J. P. Celis and J. R. Roos, *Metal Finishing*, **91** (June), 97 (1993).
4. N. Guglielmi, *J. Electrochem. Soc.*, **119** (8), 1009 (1972).
5. A. Hovestad, L. J. J. Janssen, *J. Appl. Electrochem*, **25**, 519 (1995).
6. D. Landolt, *Journal of the Electrochem. Soc.*, **149** (3), S9 (2002).
7. M. Musiani, *Electrochimica Acta*, **45**, 3397 (2000).
8. R. Narayan and B. H. Narayana, *Reviews on Coating and Corrosion*, **4** (2), 113 (1981).
9. I. Shao, P. M. Vereecken, R. C. Cammarata, and P.C. Searson, *Journal of the Electrochem. Soc.*, **149** (11), C610 (2002).
10. P. T. Tang, H. Dylmer, and P. M. Oslender, *United State Patent* 6,036,833, (March, 2000)
11. Patrick R. Webb and Neil L. Robertson, *J. Electrochem. Soc.*, **141** (3), 669 (1994).
12. P. Xiong-Skiba, D. Engelhaupt, R. Hulguin, R. and B. Ramsey, to be submitted to *J. of the Electrochem. Soc.*

# REPORT DOCUMENTATION PAGE

*Form Approved*  
OMB No. 0704-0188

Public reporting burden for this collection of information is estimated to average 1 hour per response, including the time for reviewing instructions, searching existing data sources, gathering and maintaining the data needed, and completing and reviewing the collection of information. Send comments regarding this burden estimate or any other aspect of this collection of information, including suggestions for reducing this burden, to Washington Headquarters Services, Directorate for Information Operation and Reports, 1215 Jefferson Davis Highway, Suite 1204, Arlington, VA 22202-4302, and to the Office of Management and Budget, Paperwork Reduction Project (0704-0188), Washington, DC 20503

<b>1. AGENCY USE ONLY</b> ( <i>Leave Blank</i> )		<b>2. REPORT DATE</b> January 2005	<b>3. REPORT TYPE AND DATES COVERED</b> Contractor Report	
<b>4. TITLE AND SUBTITLE</b>  The 2004 NASA Faculty Fellowship Program Research Reports			<b>5. FUNDING NUMBERS</b>  NNM04AA08G	
<b>6. AUTHORS</b> J.R. Pruitt, G. Karr,* L.M. Freeman,** and R. Hassan*** (Program Directors) and J.B. Day (Compiler and Editor)				
<b>7. PERFORMING ORGANIZATION NAMES(S) AND ADDRESS(ES)</b>  The University of Alabama in Huntsville, Huntsville, AL 35899 The University of Alabama, Tuscaloosa, AL 35487 Alabama A&M University, Normal, AL 35762			<b>8. PERFORMING ORGANIZATION REPORT NUMBER</b>  M-1137	
<b>9. SPONSORING/MONITORING AGENCY NAME(S) AND ADDRESS(ES)</b>  National Aeronautics and Space Administration Washington, DC 20546-0001			<b>10. SPONSORING/MONITORING AGENCY REPORT NUMBER</b>  NASA/CR-2005-213847	
<b>11. SUPPLEMENTARY NOTES</b> *The University of Alabama in Huntsville; **The University of Alabama, Tuscaloosa; ***Alabama A&M University Prepared for the Education Programs Department, Customer and Employee Relations Directorate				
<b>12a. DISTRIBUTION/AVAILABILITY STATEMENT</b>  Unclassified-Unlimited Subject Category 99 Availability: NASA CASI 301-621-0390			<b>12b. DISTRIBUTION CODE</b>	
<b>13. ABSTRACT</b> ( <i>Maximum 200 words</i> ) For the 40th consecutive year, the NASA Faculty Fellowship Program (NFFP) was conducted at Marshall Space Flight Center (MSFC). The program was sponsored by NASA Headquarters, Washington, DC, and operated under contract by The University of Alabama, The University of Alabama in Huntsville, and Alabama A&M University. In addition, promotion and applications are managed by the American Society for Engineering Education (ASEE) and assessment is completed by Universities Space Research Association (USRA). The nominal starting and finishing dates for the 10-week program were June 1 through August 6, 2004. The primary objectives of the NASA Faculty Fellowship Program are to: (1) Increase the quality and quantity of research collaborations between NASA and the academic community that contribute to the Agency's space aeronautics and space science mission; (2) Engage faculty from colleges, universities, and community colleges in current NASA research and development; (3) Foster a greater public awareness of NASA science and technology, and therefore facilitate academic and workforce literacy in these areas; (4) Strengthen faculty capabilities to enhance the STEM workforce, advance competition, and infuse mission-related research and technology content into classroom teaching; and (5) Increase participation of underrepresented and underserved faculty and institutions in NASA science and technology.				
<b>14. SUBJECT TERMS</b> space transportation; science in low gravity; making use of space; materials and processes; structures; dynamics; conceptual design; large space optics manufacturing; thermal control; testing and experimentation; quality engineering; information and electronic systems/aviation; automation and robotics; astrophysics; Earth science; space science; system analysis and integration			<b>15. NUMBER OF PAGES</b> 357	
			<b>16. PRICE CODE</b>	
<b>17. SECURITY CLASSIFICATION OF REPORT</b> Unclassified	<b>18. SECURITY CLASSIFICATION OF THIS PAGE</b> Unclassified	<b>19. SECURITY CLASSIFICATION OF ABSTRACT</b> Unclassified	<b>20. LIMITATION OF ABSTRACT</b> Unlimited	